UNIVERSITY OF CALIFORNIA

Santa Barbara

Using Ion Mobility-Mass Spectrometry to Understand Amyloid β-Protein Assembly: The Effects of Small Molecule Inhibitors and Familial Mutations

A dissertation submitted in partial satisfaction of the requirements

for the degree Doctor of Philosophy

in Chemistry

by

Xueyun Zheng

Committee in charge:

Professor Michael T. Bowers, Chair

Professor Steven K. Buratto

Professor Mattanjah S. de Vries

Professor Frederick Dahlquist

September 2015

The dissertation of Xueyun Zheng is approved.

_____

Steven K. Buratto

_____

Mattanjah S. de Vries

_____

Frederick Dahlquist

_____

Michael T. Bowers, Committee Chair

August 2015

Using Ion Mobility-Mass Spectrometry to Understand Amyloid β-Protein Assembly:

The Effects of Small Molecule Inhibitors and Familial Mutations

by

Xueyun Zheng

ACKNOWLEDGEMENTS

I would like to thank my advisor Mike Bowers for letting me being part of the group and your endless support through this journey. I have always been inspired by your enthusiasm for science. I still remembered when I visited the lab before joining the group, you introduced those giant instruments to me and called them “babies”. Soon after I joined the group, I quickly fell in love with these instruments and started to enjoy every moment working and playing with the instruments! The research with amyloid β has never been easy, but it is your belief in science that encourages me to keep trying. I also want to thank Mike for bringing me so many collaborations that I have opportunities to work on so many interesting molecules with fantastic scientists. Besides your mentoring on research, I also want to thank you for teaching me how to become a great scientist, including how to give a nice presentation, how to write a great paper and how to communicate effectively. Thank you for supporting me to attend conferences and bringing me to the science community. I can’t express more how I am thankful for every detail that you have done to support me. I am so happy to have you in my life!

I would like to thank all the past and present members of Bowers group. Thank you for creating a wonderful and supportive working environment for me. Megan, thank you for teaching me how to use the instruments and how to work with the complicated aggregation systems. Thomas, thank you for helping me with the instruments all the time. You are a great mentor and always so patient teaching me every detail of the mechanics and engineering which I had zero-knowledge before. It has been so great working together with you on instrumentation. Catie, thank you for being a great friend, listening to me, telling me so

many wonderful stories and sharing me the online kitten videos. Of course, I also want to thank you for helping me improving my writing skills and journal publishing. Thanh, thank you for being a great companion through this journey. Your spirit of hard-working always inspires me that I should work more too. I wish you a great success pursuing an academic career! Erin, I have enjoyed the time we teaching Physical Chemistry together and baking together over the weekends. Stan, Qian, Li, Matt, Alex, Veronica, Jurgen, Priyanka, Micheal and Natalia, I am so happy meeting you and being part of the group here!

I also want to thank my research collaborators. This work would not have been possible without you. Drs. Chun Wu and Shea, thank you for doing theoretical calculations and helping me understanding the theory beyond my experimental results. Drs. Teplow and Roychaudhuri, I really enjoyed our collaborations on the mutant and species projects. Dr. Condron, thank you for preparing great Abeta peptides for my studies all the time. Drs. Bitan, Bahr and Lim, thank you for providing these wonderful small molecules for my studies.

I would like to thank my family for the endless support through this journey. I think my dad and mom are the coolest parents in the world! You never received any education, yet you support all of your kids, us, to finish at least college education. Even you don't know what chemistry or doctor means, you still decided to support me to go abroad and pursue a doctoral degree in Chemistry! Thank you for supporting your daughter without any doubt. I am very proud of you! I also want to thank my elder brother and two younger sisters for staying close to our parents and bringing joy to the family! Thank you for chatting with me from time to time to keep me updated. I love you all!

Lastly I would like to thank my husband, Deyu, for sticking by me through good times and rough times over the last eight years. Thank you for taking the biggest adventure by giving up the cozy life in China and following me to another country to pursue a degree. You

not only take care of my life, but also help me with research taking nice TEM images for my samples. You are such an encyclopedia of chemistry and science that I can always find answers to my puzzles. I believe you will become a great material scientist. You are the best!

VITA OF XUEYUN ZHENG

AUGUST 2015

EDUCATION

University of California, Santa Barbara, CA 03/2011-Present

Ph.D. In Progress, Physical Chemistry, GPA: 3.99/4.0

Ph.D. Candidate, 03/2012-Present

University of California, Riverside, CA 09/2009-12/2010

Environmental Toxicology Graduate Program, GPA: 3.89/4.0 (Transferred)

Xiamen University, Xiamen, China 09/2005-07/2009

B.Sc., Chemical Biology, GPA: 3.7/4.0

RESEARCH EXPERIENCE

Graduate Research Assistant 03/2011-Present

Chemistry Department, UC Santa Barbara

Supervised by Prof. Michael T. Bowers

Dissertation Topic: Using ion mobility-mass spectrometry to understand Alzheimer's disease-related protein aggregation: The effects of small molecule inhibitors and familial mutations

- Develop expertise in ion mobility spectrometry-mass spectrometry (IMS-MS) analysis of protein structure, assembly and interactions
- Develop expertise in IMS and MS instrumentation, maintenance, trouble-shooting and repairing
- Mentor and assist new graduate students, postdoc and undergraduate students to performed experiments in lab

Graduate Research Assistant 09/2009-12/2010

Chemistry Department, University of California, Riverside

Supervised by Prof. Yinsheng Wang

Research Topic: Formation, replication, and repair of halogenated DNA lesion in bacterial and mammalian cells

- Chemically synthesized halogenated oligonucleotides
- Purified oligonucleotides by PAGE and HPLC
- Replicated halogenated DNA in bacterial cells using molecular biology techniques
- Analyzed and quantitated oligonucleotides by MS, LC/MS and LC/MS/MS

Undergraduate Research Assistant 05/2007-07/2009

Department of Chemistry, Xiamen University

Key Laboratory for Chemical Biology of Fujian Province, Fujian, China

Supervised by Prof. Yufen Zhao

Research Topic: Development of non-radioactive assay method for Protein Kinase A using γ-[$^{18}O_4$]-ATP and MALDI-TOF mass spectrometry

- Expressed, purified and characterized proteins using molecular biology techniques and bioanalytical approaches (SDS-PAGE, UPLC, Western Blotting and MS, LC/MS, etc.)
- Established stable isotope labeling and MALDI-TOF MS based methods for protein kinase assay

TEACHING EXPERIENCE

Teaching Assistant: Physical Chemistry 01–06/2012, 01-06/2013

Chemistry Department, University of California Santa Barbara

- Instructed discussion sections for Physical Chemistry lecture series (Chem 113B, C)
- Grade homework and exams, conduct office hours 3 times per week

Teaching Assistant: General Chemistry Laboratory 09/2010-12/2010

Chemistry Department, University of California, Riverside

- Instructed general Chemistry laboratory
- Graded lab reports and exams and conducted office hours

PUBLICATIONS

1. **X. Zheng,** D. Liu, G. Bitan, M. T. Bowers, "The Important Role of Lysine in Amyloid β-protein Assembly: An Ion Mobility Study", *Manuscript in Preparation*

2. **X. Zheng**, C. Wu, D. Liu, B. A. Bahr, J.-E. Shea and M. T. Bowers, "PADK as an Effective Inhibitor of Aβ42 Early Assembly: An Experimental and Theoretical Study", *Manuscript in Preparation*
3. **X. Zheng**, C. Wu, D. Liu, J.-E. Shea and M. T. Bowers, "Mechanism of C-Terminal Fragments of Amyloid β-Protein as Aβ Inhibitors", *Manuscript in Preparation*
4. **X. Zheng**, D. B. Teplow, M. T. Bowers, "Amyloid β-protein Assembly: Differential Effects of A2T and A2V Familial Alzheimer's Disease Mutations", *ACS Chemical Neuroscience,* **2015**, ASAP
5. **X. Zheng**, D. Liu, F.-G. Klärner, T. Schrader, G. Bitan, M. T. Bowers, "Amyloid β-protein Assembly: The Effect of Molecular Tweezer CLR01 and CLR03", *Journal of Physical Chemistry B* **2015**, 119 (14), 4831–4841 (Selected ACS Editors' Choice)
6. **X. Zheng**, M. M. Gessel, M. L. Wisniewski, K. Viswanathan, D. L. Wright, B. A. Bahr and M. T. Bowers, "Z-Phe-Ala-diazomethylketone (PADK) disrupts and remodels early oligomer states of the Alzheimer disease Aβ42 protein", *Journal of Biological Chemistry* **2012**, 287, 6084-6088
7. R. Roychaudhuri, **X. Zheng**, A. Lomakin, P. Maiti, M. M. Condron, G. B. Benedek, G. Bitan, M. T. Bowers and D. B. Teplow, "Role of species-specific primary structure differences in Aβ42 assembly and neurotoxicity", *ACS Chemical Neuroscience, Submitted*
8. S. Lee, **X. Zheng**, J. Krishnamoorthy, M. G. Savelieff, H. M. Park, J. R. Brender, J. H. Kim, J. S. Derrick, A. Kochi, H. J. Lee, C. Kim, A. Ramamoorthy, M. T. Bowers, and M. H. Lim, "Rational design of a structural framework with potential use to develop chemical reagents that target and modulate multiple facets of Alzheimer's disease", *Journal of the American Chemical Society,* **2014**, 136, 299–310
9. T. D. Do, A. Chamas, **X. Zheng**, A. Barnes, D. Chang, T. Veldstra, H. Takhar, N. Dressler, B. Trapp, K. Miller, A. McMahon, S. C. Meredith, J.-E. Shea, K. L. Cantrell, M. T. Bowers, "Elucidation of the aggregation pathways of helix-turn-helix peptides: Stabilization at the turn region is critical for fibril formation", *Biochemistry,* **2015,** 54 (26), 4050–4062
10. R. Roychaudhuri, A. Lomakin, S. Bernstein, **X. Zheng**, M. M. Condron, G. B. Benedek, M. Bowers, and D. B. Teplow, "Gly25-Ser26 Amyloid β-protein structural isomorphs

produce distinct Aβ42 conformational dynamics and assembly characteristics", *Journal of Molecular Biology*, **2014**, 426, 2422–2441

11. D. Liu, X. Peng, B. Wu, **X. Zheng**, T. T. Chuong, J. Li, S. Sun, and G. D. Stucky, "Uniform Concave Polystyrene-Carbon Core-Shell Nanospheres by a Swelling-Induced Buckling Process", *Journal of the American Chemical Society*, **2015**, ASAP
12. B. Wang, J. A. Maciá-Agulló, D. G. Prendiville, **X. Zheng**, D. Liu, Y. Zhang, S. W. Boettcher, X. Ji, and G. D. Stucky, "A hybrid redox-supercapacitor system with anionic catholyte and cationic anolyte", *Journal of The Electrochemical Society*, **2014**, 161 (6), A1090-A1093
13. C. Fu, **X. Zheng**, Y. Jiang, Y. Liu, P. Xu, Z. Zeng, R. Liu and Y. Zhao, "A universal and multiplex kinase assay using γ-[$^{18}O_4$]-ATP", *Chemical Communications* **2013**, 49, 2795-2797

PRESENTATIONS

1. **X. Zheng**, D. B. Teplow, M. T. Bowers, "Ion mobility-mass spectrometry reveals the early assembly of amyloid β-protein: The effects of familial mutations A2T and A2V", Poster Presentation at *63rd American Society of Mass Spectrometry (ASMS) Annual Meeting*, 2015 St. Louis, MO
2. **X. Zheng**, R. Roychaudhuri, D. B. Teplow, M. T. Bowers, "Amyloid β-protein Familial Mutants: A2T and A2V, An Ion Mobility Study", Oral Presentation at *Conference on Ion Chemistry and Mass Spectrometry*, 2015 Lake Arrowhead, CA
3. **X. Zheng**, M. T. Bowers, "Ion Mobility Spectrometry Coupled Mass Spectrometry Sheds Light on Screening Small Molecule Inhibitors for the Alzheimer's Disease Amyloid-β Proteins", Poster Presentation at *American Association of Pharmaceutical Scientists (AAPS) Annual Meeting*, 2014 San Diego, CA
4. **X. Zheng**, D. Liu, G. Bitan, M. T. Bowers, "Ion mobility spectrometry reveals the modulation of early oligomerization of amyloid-β protein by molecular tweezer", Poster presentation at *Isolated Biomolecules and Biomolecular Interactions (IBBI) Conference*, 2014 Porquerolles Island, France

5. **X. Zheng**, D. Liu, G. Bitan, M. T. Bowers, "Molecular tweezer targeting and regulating amyloid β aggregation", Oral presentation at *Conference on Ion Chemistry and Mass Spectrometry*, 2014 Lake Arrowhead, CA
6. **X. Zheng**, M. T. Bowers, "Using ion mobility spectrometry to screen small molecule inhibitors for the Alzheimer's disease Aβ42 protein", Poster Presentation at *61st American Society of Mass Spectrometry (ASMS) Annual Meeting*, 2013 Minneapolis, Minnesota
7. **X. Zheng**, M. T. Bowers, "Using ion mobility spectrometry-mass spectrometry to screen small molecule inhibitors for the Alzheimer's disease Aβ42 protein", Poster Presentation at *Alzheimer's Association Brainwaves Research Symposium*, 2013 Santa Barbara, CA
8. **X. Zheng**, M. H. Lim, M. T. Bowers, "A novel molecule capable of targeting and regulating amyloid β and metal-Aβ species", Oral Presentation at *Conference on Ion Chemistry and Mass Spectrometry*, 2013 Lake Arrowhead, CA
9. **X. Zheng**, B. A. Bahr, M. T. Bowers, "PADK disrupts and remodels the early oligomer states of the Alzheimer's disease Aβ42 protein", Oral presentation at *Conference on Ion Chemistry and Mass Spectrometry*, 2012 Lake Arrowhead, CA

HONORS & AWARDS

- **The First Jean-Pierre Schermann Poster Prize and Student Travel Stipend** 05/2014
  Conference on Isolated Biomolecules and Biomolecular Interactions, Porquerolles Island, France
- **Doctoral Student Travel Grant** 2014
  Graduate Division, University of California, Santa Barbara
- **Prestigious Dean's Distinguished Fellowship** 2009-2010
  Environmental Toxicology Graduate Program, University of California, Riverside
- **Honor of Outstanding Graduate** Xiamen University, Fujian, China 2009
- **National Scholarship for Encouragement** China 2008
- **Chen Zhang'e Scholarship** (the Enterprise Scholarship) Xiamen University 2008
- **Merit Student Award (top 3%)** Xiamen University 2006, 2007&2008
- **The First Class Scholarship (top 3%)** Xiamen University 2006&2007

ABSTRACT

Using Ion Mobility-Mass Spectrometry to Understand Amyloid β-Protein Assembly: The Effects of Small Molecule Inhibitors and Familial Mutations

by

Xueyun Zheng

Amyloid β-protein (Aβ) has been correlated with Alzheimer's disease (AD) which is the most common form of dementia. Aβ proteins assemble into oligomers, large aggregates, protofibrils before growing into fibrils. Recently more and more evidence has shown that the intermediate, oligomeric states of Aβ, rather than the fibrils are correlated with AD pathology. Among them, the 56 kDa dodecamer species was identified as a proximate toxic agent for AD onset. Therefore to understand the early oligomerization of Aβ proteins and to target the early assembly of Aβ are of significance for therapeutic strategy for AD treatment. In this thesis work, we use mass spectrometry coupled with ion mobility spectrometry method (IM-MS) to investigate the early assembly of Aβ proteins.

In the first, we sought to search for small molecule inhibitors for Aβ and understand their binding interactions and the mechanism of inhibitory actions. Several classes of small molecules, including Z-Phe-Ala-diazomethylketone (PADK), two derivatives of the Aβ C-terminal fragment Aβ(39-42), molecular tweezers, and ML, have been studied and shown different effects. These studies of small molecule inhibitors show that ion mobility

spectrometry method has emerged to be a powerful tool for the screening and understanding of small molecule inhibitors for AD and other amyloid diseases.

In the second, we sought to understand the effects of amino acid substitutions on Aβ structure and aggregation. Two recently discovered familial mutations at Ala2 (A2) within Aβ, a protective A2T mutation and a recessive A2V mutation were investigated. Our ion mobility studies reveal different assembly pathways for early oligomer formation for each peptide and provide a basis for understanding how these two mutations lead to, or protect against, AD.

Lastly, we also sought to understand the early assembly of amyloid β-protein (Aβ) from different rodent species. We investigate the biophysical and biological properties of Aβ peptides from humans, mice (Mus musculus), and rats (Octodon degus).

In conclusion, we have successfully applied ion mobility spectrometry method to understand complicated aggregation systems. This provides a powerful tool to screen small molecule inhibitors for Aβ proteins and sheds light onto their inhibitory mechanisms. The studies of Aβ mutants imply that ion mobility method can be used as new tool in developing an understanding of the effect of familial mutations on Aβ assembly in AD and the assembly of other mutated protein systems.

TABLE OF CONTENTS

Chapter 1

Introduction

1.1 Protein Aggregation Diseases

Proteins, which are composed of polypepetide chains of amino acids, are essential and perform a variety of functions within living organisms. Most proteins can function properly only when they are folded into certain specific and stable structure. Protein folding is the process that an unstructured protein undergoes certain conformation changes to reach its native state[1]. To ensure a protein folds appropriately is critical for its proper cellular function. How and whether a protein folds depend primarily on its amino acid sequence and the cellular environment surrounding the polypeptide chains. However, under certain

circumstances, protein misfolding or unfolding can occur[1-2]. When protein folding is unsuccessful, the protein is usually redirected to the proteasome where it is proteolytic degraded[3]. If not cleared appropriately, these misfoled or disordered proteins often aggregate and accumulate intra- or extracellularly and eventually become problematic and cause diseases[4]. Amyloidosis diseases are one of these protein aggregation diseases, which are caused by aggregation and accumulation of amyloid-forming proteins[5-6]. These diseases include Alzheimer's disease, Huntington's disease, Parkinson's disease, etc. (some examples are provided in **Table 1.1**)[7]. The amyloidosis deposits of the protein aggregates can occur in some parts of the body, extracellularly or intracellularly.

Table 1.1 List of some amyloidosis diseases and the corresponding amyloid-forming proteins implicated in each case.

Disease	**Aggregation Protein**
Alzheimer's disease	Amyloid β and Tau protein
Parkinson's disease	α-Synuclein
Prion disease	Prion protein
Frontotemporal dementia	Tau protein
Huntington disease	Huntington with polyglutamine expansion
Type II diabetes	Islet amyloid polypeptide (IAPP)
Cataract	γ-Crystallin

These amyloid-forming proteins exist in a complex dynamic equilibrium between soluble monomeric or oligomeric states and various insoluble states of higher-order aggregates. The aggregation depends on the protein concentration, interactions with other proteins and the cellular environment. Studies showed that the aggregation usually starts with a lag phase which contains oligomers and small aggregates, follows by a rapid

elongation phase and then reaches a stationary phase when the amyloid fibrils are formed[8] (Figure 1.1). A better understanding of the factors that affect this equilibrium is of significance for determining how protein aggregation occurs and for developing effective therapies against the amyloidosis diseases[6]. In this thesis, we aimed to understand the aggregation of amyloid β-proteins that are related to Alzheimer's disease.

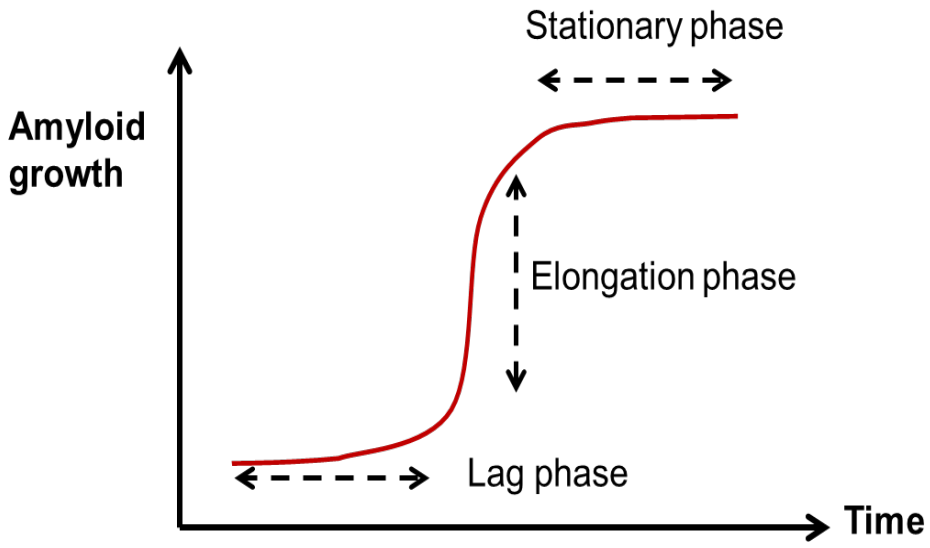

Figure 1.1 Aggregation kinetics for amyloid growth.

1.2 Alzheimer's disease

1.2.1 Alzheimer's Disease and Prevalence

Alzheimer's disease (AD) is a degenerative brain disease and is the most common form of dementia (other forms of dementia include Vascular dementia, Dementia with Lewy bodies, Fronto-temporal dementia which includes Pick's disease, etc.)[9]. It was first described by a German physician Dr. Alois Alzheimer in 1906[10]. He found dramatic shrinkage and abnormal deposits in and around nerve cells in the brain autopsy of his patient Auguste D.

who suffered profound memory loss[10]. AD is characterized by damage of neurons in the brain and causes a decline in memory, language, problem-solving and other cognitive and executive functions that affect daily activities, and eventually leads to death.

Nowadays, there are 47.5 million people having dementia worldwide and there are 7.7 million new cases every year[11]. AD may contribute to 60–70% of cases and therefore it has become one of the most important diseases. AD is an age-related disease and often occurs in senior people with age of 65 years and older. As the population ages and life spans continue to increase, the prevalence will increase. By 2050, the number of patients with AD worldwide is estimated to be 135 million.

Therefore to understand the pathology of AD and develop therapeutic strategy for AD treatment is of significance and it has become one of the hot research topics for scientists.

1.2.2 Symptoms of Alzheimer's disease and Diagnosis

AD and other dementia affect each patient in a different way, which might depend on the impact of the disease and the personality of the patient before becoming ill. The symptoms of AD vary among individuals and the progression of disease varies greatly. People with AD live an average of eight years, but some people may survive up to 20 years. The symptoms linked to AD and other dementia can be understood in three stages.

Earliest Alzheimer's Stage: The earliest stage of AD can began as early as 20 years or more before the symptoms can be detected and they are often overlooked as the changes are gradual. The most common initial symptom in AD is memory decline, a gradually loss of ability to remember new information. This is because the first formation of plaques and

tangles and neuron damages often start from the hippocampus region in the brain that is involved in formation of new memory and learning. The common signs in the earliest stage include forgetfulness, becoming lost in familiar places and losing track of the time, etc[9].

Middle Stage of Alzheimer's: The mid to moderate stage can last from 2 to 10 years. As the plaques and tangles build up more in the hippocampus region and spread to other parts of brain, the neuron damages spread to other regions in the brain which start to display other malfunctions and difficulties. As a result, the patients start to have serious problems with memory or thinking and have difficult with work or social life. As the disease progresses, the patients may experience changes in personality and behavior and have trouble recognizing friends and family members. The signs and symptoms become clearer, and many people with Alzheimer's are first diagnosed in these stages[9,12].

Last stage of Alzheimer's: The last stage of AD may last 1 to 5 years. As the disease advances, the plaques and tangles spread to the whole brain and most of the cortex of the brain is seriously damaged. The brain shrinks dramatically due to widespread cell death. The patients often become totally dependent and inactive. Memory disturbances are serious and the physical signs and symptoms become more obvious. The symptoms include becoming unaware of the time and place, having difficulty recognizing relatives and friends. The patients often experience changes in behavior and personality, including aggression, apathy and depression, etc[11].

AD diagnosis: AD can only be confirmed by brain autopsy after death, by the identification of amyloid plaques and neurofibrillary tangles in the brain[13]. However, a variety of approaches and tools are available to help make a diagnosis of AD. The physician

will ask to obtain a medical and family history, especially psychiatric history and history of cognitive and behavioral changes. Cognitive tests and physical and neurologic examinations, including tests of memory, attention and language, will be conducted.

1.3 Amyloid β-protein and Alzheimer's disease

1.3.1 Amyloid β-protein

AD is a complicated disease and its aetiology has not been fully understood. One of the classical hallmarks of AD histopathology is the extracellular deposits of amyloid plaques, which are primarily composed of the Amyloid β-protein (Aβ) (Figure 1.2A)[6]. A second hallmark of AD is the presence of intracellular neurofibrillary tangles, which are composed of abnormal, hyperphosphorylated tau protein (Figure 1.2B)[6]. In this thesis, we focus on understanding the assembly of Aβ proteins.

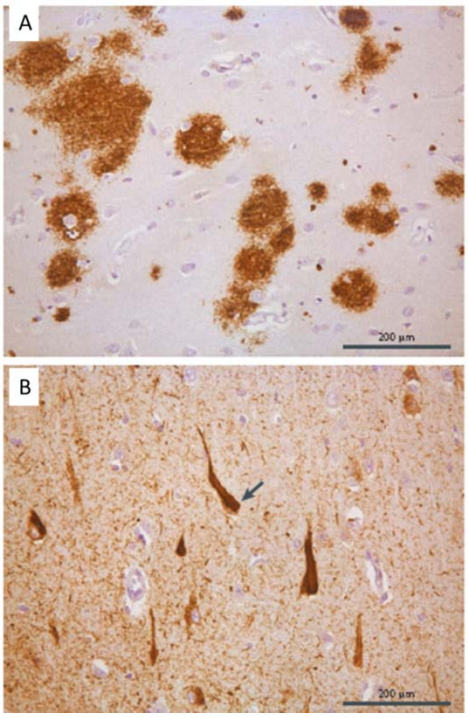

Figure 1.2 Characteristics of Alzheimer's disease. (A) Amyloid plaques. A human cortical section from an AD patient, stained with an amyloid-β (Aβ)-specific antibody. (B) Neurofibrillary tangles (indicated by an arrow). A human cortical section from an AD patient, stained with a phospho-tau-specific antibody. The images are reproduced from reference [6] with permission.

Aβ is, in reality, not one but a group of peptides with various lengths between 36 to 43 amino acid residues (primary sequence is shown in Figure 1.3). Aβ peptides are derived from the type-1 transmembrane protein, amyloid precursor protein (APP), through proteolytic cleavage by β- and γ-secretases[14].

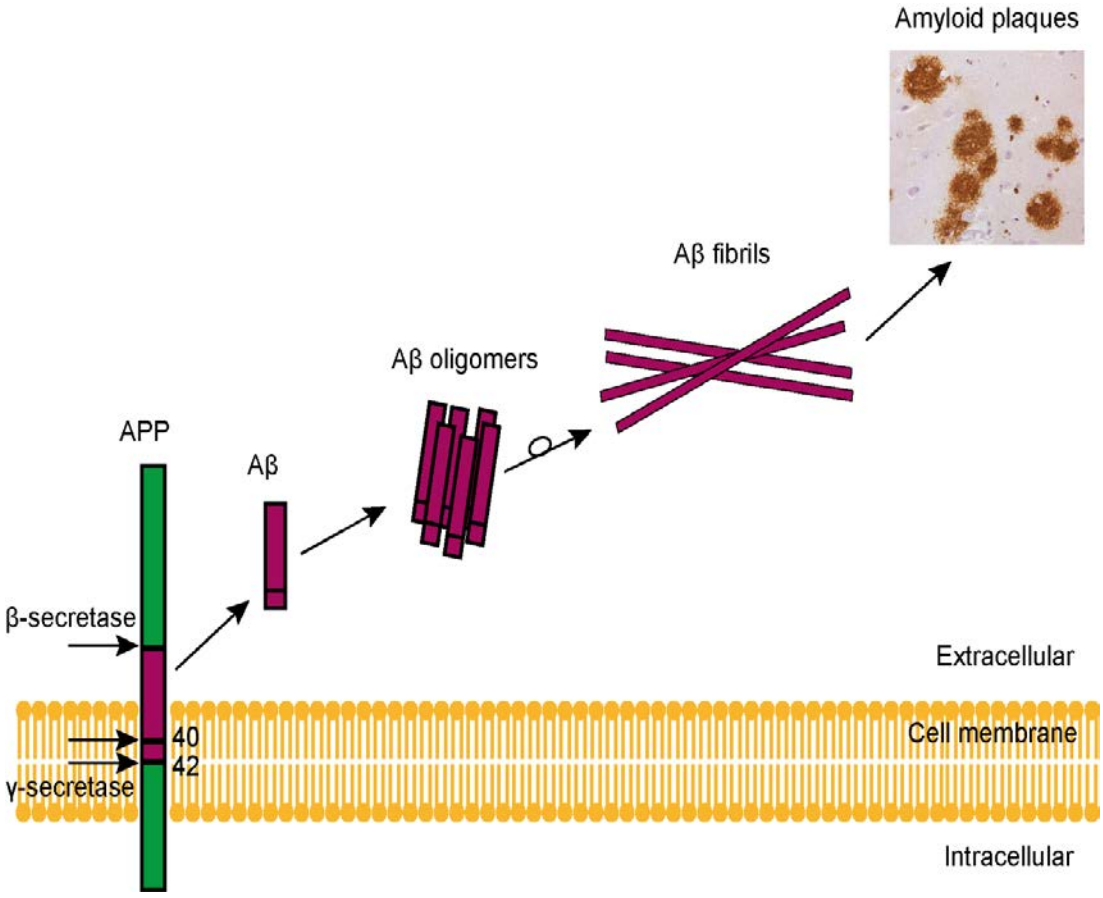

Figure 1.3 The production of Aβ proteins and formation of amyloid plaques *in vivo*. Image of amyloid plaque is adapted from Figure 1-2A which is reproduced from reference [6] with permission.

Aβ exist *in vivo* primarily as 40- or 42-amino-acid long peptides. The most common and abundant form is Aβ40, which constitutes ~90% of all Aβ species.[15] However, it is significantly less toxic in cells. Even though Aβ42 is a relatively minor constituent (~9% of all Aβ species), it is highly neurotoxic and much more aggregation-prone than Aβ40. Aβ42 has been found to be the primary component of amyloid plaques (Amino acid sequence of Aβ42 is provided in Figure 1.4).

Figure 1.4 The primary sequence of Aβ42 peptide. Positively charged amino acid residues are noted in blue and negatively charged residues are noted in red.

The physiological role of APP and Aβ is unclear. However, studies have shown that the onset of AD may be connected with an imbalance of the production and clearance of Aβ[14]. Recently, scientists were able to quantify Aβ production and clearance from cerebrospinal fluid of individuals with and without AD. Compared to the balanced rates for healthy individuals, the AD patients showed an increased ratio of Aβ production over clearance[16].

1.3.2 Amyloid β-protein aggregation

Once released into the extracellular environment, Aβ monomer starts to self-associate with each other to form small oligomers and eventually grow into fibrils. The structure of Aβ fibrils has been well characterized, consisting of β-sheet strands[17].

Formation of Aβ fibrils *in vitro* and *in vivo* is a complex process involving multiple intermediate oligomeric species. More and more evidence showed that these oligomeric

species are highly neurotoxic. It is believed that these intermediate oligomeric states, rather than the final product, fibrils, are the proximal neurotoxins acting in AD.[18-21] Immediately upon dissolution *in vitro*, Aβ42 forms small oligomers, including dimers and tetramers, as well as paranuclei (pentamers and hexamers) that self-associate to form decamers and dodecamers.[22-24] However, Aβ40 forms only dimers and tetramers before slowly self-assembling into fibrils (Figure 1.5). Among these species, the 56-kDa dodecamer has been identified as a plausible cause of memory deficits in the AD brain[25] and in transgenic mice[26].

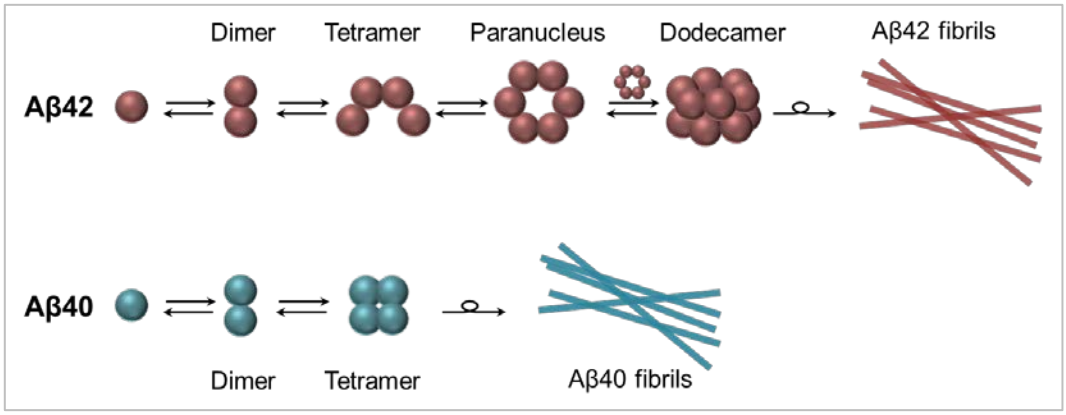

Figure 1.5 Schematic of oligomerization patterns for Aβ40 and Aβ42 proteins. Aβ40 is noted in red and Aβ42 is noted in blue. M, D, Te, H and Do represent monomer, dimer, tetramer, hexamer and dodecamer, respectively.

1.3.3 Amyloid cascade hypothesis of AD

Briefly, in a health brain, neuron cells are connected and communicated through synapses (Figure 1.6). In general, signal or information is carried from one neuron to another through the chemicals called neurotransmitters. The exon sends the signal to another neuron by release the chemical neurotransmitters to its receptors on the dendrites of the other neuron. The dendrites receive the signal and transport the information as an electric signal to the body. However, in the brain of AD patients, this neurotransmission process is disrupted.

Eventually the synapses are destroyed and the neuron cells are killed, as a result, the communication network of the brain is damaged and therefore causes failure of many functions of the brain[27].

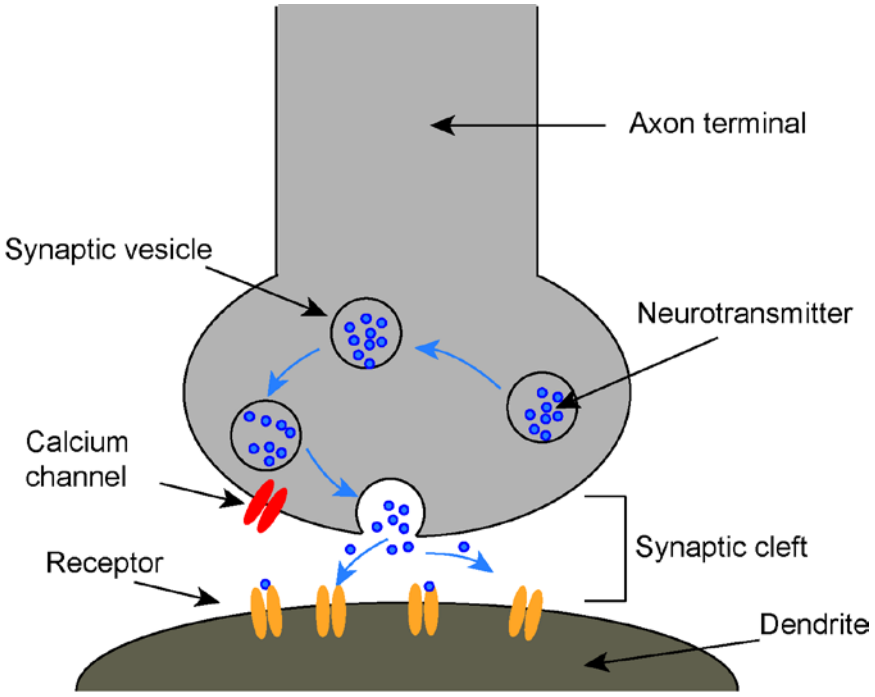

Figure 1.6 Signal transmission between two neurons through a synapse. Neurons send signals through axons and receive signals through dendrites. The junction at which two cells meet is the synaptic cleft. Neurotransmitters are released from the axon of one neuron to the receptors on the dendrite of another.

Currently, the amyloid cascade hypothesis (Figure 1.7) is widely accepted to explain AD pathology[28]. It is suggested that deposition of Aβ peptide in the brain is a crucial step that ultimately leads to Alzheimer's disease. Abnormal high level of Aβ protein present in the brain, which can be resulted from overproduction, decreased clearance or increased Aβ42/40 ratio, and start to assemble and aggregate into soluble oligomers and eventually grow into Aβ fibrils. These intermediate forms, soluble oligomers have been shown be

synaptotoxic and neurotoxic. The deposited Aβ triggers or accelerates Tau phosphorylation and aggregation into tangles, which ultimately leads to neuronal loss[28]. However, how Aβ trigger Tau pathology and how Tau pathology leads to neuronal loss are unclear and remain elusive.

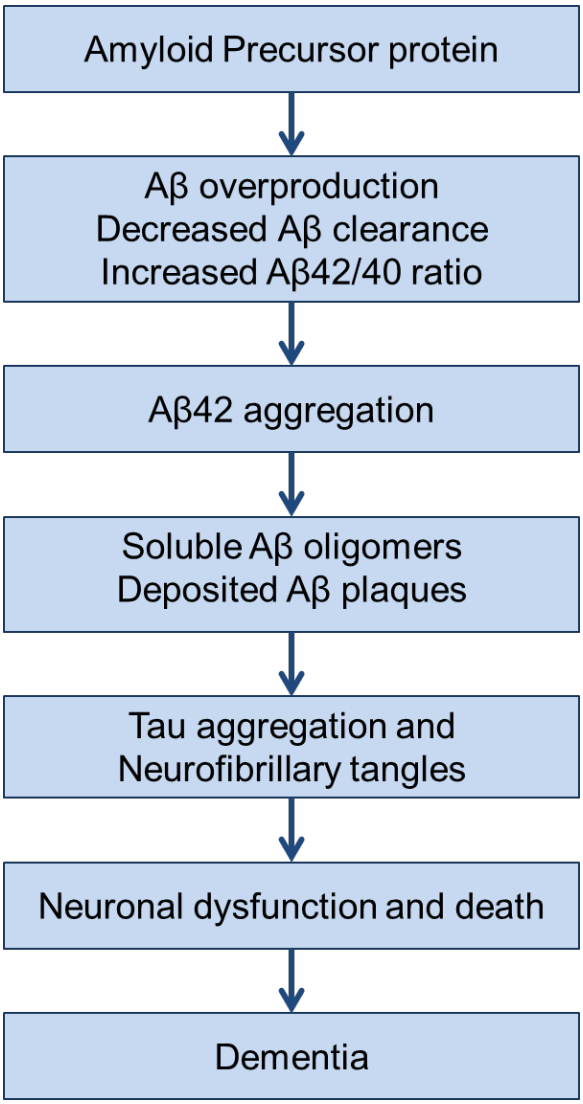

Figure 1.7 Amyloid cascade hypothesis for AD pathology.

Several possible receptors have been proposed for Aβ oligomers or amyloid β-derived diffusible ligands (ADDLs) and mediating their synaptotoxic effects (Figure 1.8)[27].

For example, nerve growth factor receptor, p75NTR, has been shown to play a role in Aβ-induced cell death (apoptosis) through its downstream effectors, such as c-Jun N-terminal kinase. The N-methyl-D-Aspartate (NMDA) receptor, which is a glutamate receptor, can also bind ADDLs. Glutamate is an important neurotransmitter in the brain involved in learning and memory. When glutamate is attached to NMDA receptor, NMDA permits calcium to enter the cell, which is an important process for cell signaling, as well as learning and memory. On the other hand, ADDLs bind to NMDA receptor, and cause imbalance in Calcium homeostasis in the cell, leading to increased oxidative stress and loss of synapses. The Frizzled receptor has also been implicated as a receptor for Aβ oligomers. ADDLs bind to Frizzled receptor and inhibit Wnt signaling, relieving the inhibition on Gsk3b signaling and thereby leading to hyperphosphorylation of Tau protein. APP and Prion protein (PrPC) are also receptors for ADDLs for its mediation of synaptic dysfunction. In addition, Aβ oligomers have been shown to form pores in the membrane and act as ion channels which lead to abnormal ion transport, such as calcium or zinc ions, into the cell and causes cellular dysfunction and synapse loss[27].

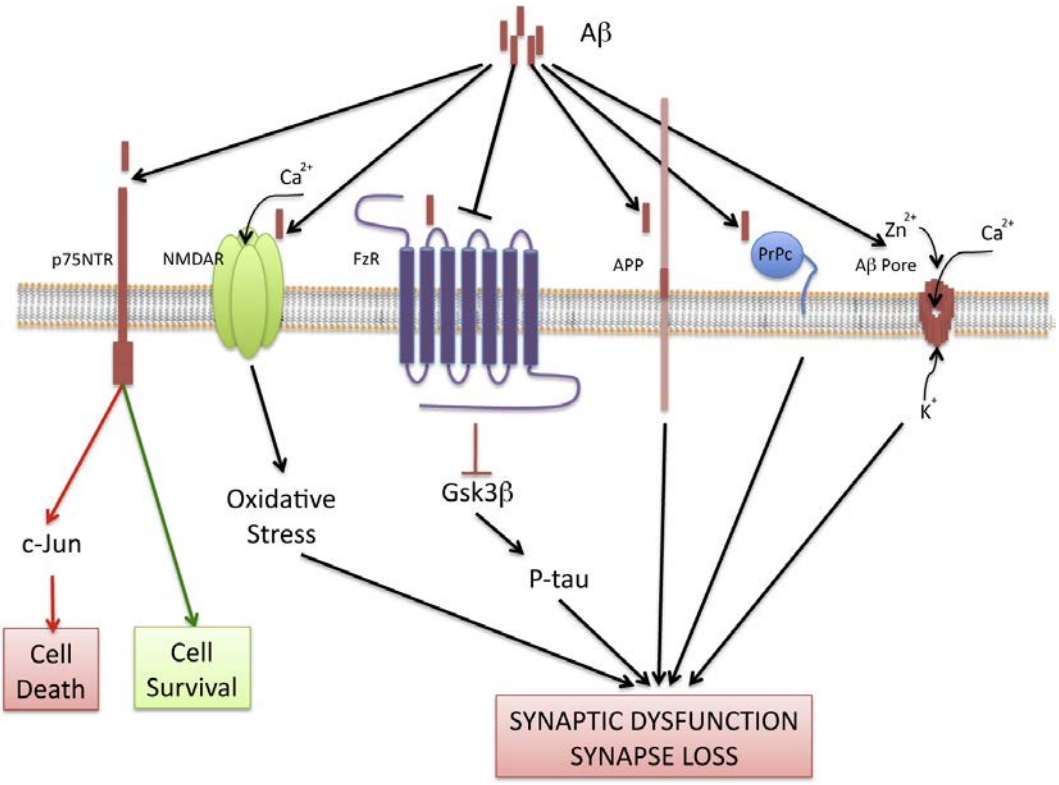

Figure 1.8 Possible receptors for Aβ oligomers and pathways. This figure is reproduced from reference [27] with permission.

1.4 Therapeutic strategy for AD

1.4.1 Current available treatments for AD symptom

There is no cure for AD so far and the treatments aim to slow the AD symptoms. These treatments temporarily improve symptoms of AD by increasing the amount of neurotransmitters in the brain (see Figure 1.8). There are five drugs approved by the U.S. Food and Drug Administration (Table 1.2). These drugs rescue the communication process through two different mechanisms: inhibiting the activity of cholinesterase or slowing down the release of calcium into the cell which thereby slows down the cell damage process. Donepezil, galantamine and rivastigmine are cholinesterase inhibitors and therefore slow

down the process that cholinesterase degrades the neurotransmitter. Memantine, on the other hand, works by regulating the activity of glutamate. In the brain of AD patients, excess glutamate is released from the damaged cells, which results in too much calcium in the cell and thereby facilitates cell damage. Memantine blocks the NMDA receptor and thereby helps prevent this destructive process.

Table 1.2 Current available drugs for AD approved by FDA (Reproduced with permission from Alzheimer's Association, http://www.alz.org/).

Drug name	Brand name	Approved for	FAD approved
1. Donepezil	Aricept	All stages	1996
2. Galantamine	Razadyne	Mid to moderate	2001
3. Memantine	Namenda	Moderate to severe	2003
4. Rivastigmine	Exelon	All stages	2000
5. Donepezil and Memantine	Namzaric	Moderate to severe	2014

However, none of the treatments available today slows or stops the damage of neurons in the brain. Efforts are input in the understanding of AD onset and developing drugs targeting amyloid β and its aggregation, aiming to stop the progress of the disease.

1.4.2 Therapeutic Strategy for AD

Based on the amyloid cascade hypothesis, there are three major strategies for AD therapy and prevention (Summarized in Table 1.3). The first one is preventing Aβ production. This can be achieved by inhibiting or modulating the β- and/or γ-secretase enzymes.[29] However, this approach has been problematic because both secretases cleave substrates other than APP, which play important roles in other functional biological

processes.[30-32] Another potential strategy is enhancing the clearance of Aβ oligomers and aggregates from the brain.[33] This can be accomplished either by facilitating degradation of Aβ by proteases[34] or other clearance mechanisms such as Aβ immunotherapy[35]. The third strategy is directly remodeling the aggregation of Aβ into clearance-prone structures.

Table 1.3 Three strategies for AD therapy.

Approach	**Therapy**
Inhibition of amyloid production	γ-Secretase inhibitors and modulators β-secretase inhibitors
Promotion of amyloid clearance	Aβ immunotherapy
Inhibition of amyloid aggregation	Aβ inhibitors

Small molecule inhibitors for Aβ: Many natural proteins, peptides and small molecules have been discovered to interact with Aβ and modulate Aβ self-assembly[36]. Among them, small molecules are particularly attractive as a direct therapeutic strategy for the treatment of AD[37-38]. For instance, biologically active molecules from green-tea ((–)epigallocatechin-3-gallate, EGCG) or the Indian spice turmeric (curcumin), have been found to prevent Aβ aggregation and inhibit Aβ-induced toxicity[39-40]. Inositol stereoisomers have been found to interact with Aβ and attenuate its neurotoxic effects[41-42]. C-terminal fragments of Aβ42 and many polyphenol molecules have been shown to inhibit Aβ oligomerization, aggregation, and toxicity[43-47]. In this thesis work, we evaluated the effects of several classes of small molecules on Aβ aggregation (Chapters 3-6).

1.5 Familial Alzheimer's Disease

1.5.1 Familial Alzheimer's disease

AD is an age related disease and usually occurs sporadically in senior people above 65 years old (95% of all AD cases). However, 5% of AD cases occur below age 65. These early onset AD cases are often caused by genetic mutations, named familial AD (FAD). These mutations occur primarily in three genes, the APP[48-49], presenilin 1 (PS1)[50-51], or presenilin 2 (PS2)[52] genes (Table 1.4). Missense mutations of PS1 and PS2 genes often cause over production of Aβ42 and therefore lead to early onset of AD, which are the primary cause of autosomal dominant AD[53].

Table 1.4 Confirmed genetic factors related to Alzheimer's disease: relationships to the amyloid-β phenotype[14].

Chromosome	Gene Defects	Phenotype
21	APP mutations	↑ Production of all Aβ peptides or Aβ40
14	Presenilin 1 mutations	↑ Production of Aβ42
1	Presenilin 2 mutations	↑ Production of Aβ42

1.5.2 Genetic mutations in APP

Numerous FAD-related mutations in the APP gene have been identified and many of them are near β- or γ-secretase cleavage sites. This results most commonly in overproduction of Aβ or relative increases in the amount of Aβ42 that is produced relative to Aβ40[14,54]. Moreover, many mutations in the APP gene occur within the Aβ sequence (Figure 1.9), and such single amino acid substitutions in Aβ primary sequence are very likely to

affect the biophysical and aggregation properties of Aβ. Many mutations in the APP gene result in amino acid substitutions within the central region of Aβ, for instance, Flemish (A21G)[55], Arctic (E22G)[56], Dutch (E22Q)[57], Osaka (E22Δ)[58], Italian (E22K)[59] and D23N (Iowa)[60] mutations. The resulting peptides exhibit distinct aggregation propensity and toxicity. The central region of Aβ has been shown to be crucial for the initial nucleation of Aβ folding and assembly[61]. Mutations near this region may disrupt the Aβ conformation, resulting in increased aggregation propensity and formation of toxic oligomers[62].

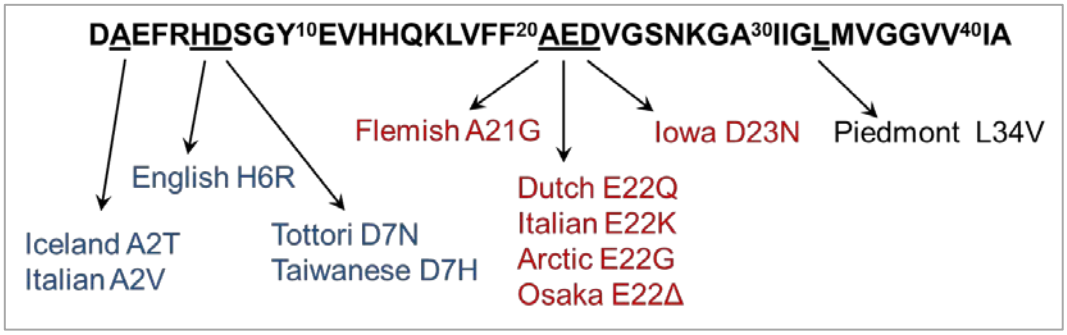

Figure 1.9 Familial mutations in APP gene within Aβ sequence.

A number of APP mutations result in amino acid substitutions at the N-terminus, and these substitutions alter Aβ assembly. These include the English (H6R)[63-64], Tottori (D7N)[63-66], and Taiwanese (D7H)[67] mutations. Most recently, two new APP mutations have been described that result in the substitutions A2T and A2V can be important in Aβ structure and assembly[68-69]. Many of these familial mutations cause early onset of disease. However, A2T is the first one that was found to protect against AD and protect cognitive decline in the elderly without AD[68]. Single mutations in Aβ can cause dramatic effects on AD etiology, therefore to understand the effects of these mutations is of significance for understanding these familial AD and their future therapeutic development. Thus it is another important focus of this thesis work (Chapters 7 and 8).

References

1. Dobson, C. M. Protein folding and misfolding. *Nature* **2003,** *426*, 884-890.

2. Dobson, C. M. Principles of protein folding, misfolding and aggregation. *Seminars in Cell & Developmental Biology* **2004,** *15*, 3-16.

3. Goldberg, A. L. Protein degradation and protection against misfolded or damaged proteins. *Nature* **2003,** *426*, 895-899.

4. Selkoe, D. J. Folding proteins in fatal ways. *Nature* **2003,** *426*, 900-904.

5. Ross, C. A.; Poirier, M. A. Protein aggregation and neurodegenerative disease. *Nat. Med.* **2004,** *10*, 8.

6. Aguzzi, A.; O'Connor, T. Protein aggregation diseases: pathogenicity and therapeutic perspectives. *Nat Rev Drug Discov* **2010,** *9*, 237-248.

7. Chiti, F.; Dobson, C. M. Protein Misfolding, Functional Amyloid, and Human Disease. *Annu. Rev. Biochem.* **2006,** *75*, 333-366.

8. Knowles, T. P. J.; Vendruscolo, M.; Dobson, C. M. The amyloid state and its association with protein misfolding diseases. *Nat Rev Mol Cell Biol* **2014,** *15*, 384-396.

9. Alzheimer's, A. 2015 Alzheimer's disease facts and figures. *Alzheimer's & Dementia* **2015,** *11*, 332-384.

10. Alzheimer, A. Über einen eigenartigen schweren Erkrankungsprozeß der Hirnrinde. *Neurologisches Centralblatt* **1906,** *23*, 1129-1136.

11. World Health Organization, Dementia, Fact sheet. http://www.who.int/mediacentre/factsheets/fs362/en/ 2015).

12. Prince, M.; Albanese, E.; Guerchet, M.; Prina, M. *Alzheimer's Disease International: World Alzheimer Report*; 2014.

13. Gearing, M.; Mirra, S. S.; Hedreen, J. C.; Sumi, S. M.; Hansen, L. A.; Heyman, A. The Consortium to Establish a Registry for Alzheimer's Disease (CERAD). Part X. Neuropathology confirmation of the clinical diagnosis of Alzheimer's disease. *Neurology* **1995,** *45*, 461-466.

14. Selkoe, D. J. Alzheimer's disease: Genes, proteins, and therapy. *Physiol. Rev.* **2001,** *81*, 741-766.

15. Jakob-Roetne, R.; Jacobsen, H. Alzheimer's Disease: From Pathology to Therapeutic Approaches. *Angew. Chem., Int. Ed.* **2009,** *48*, 3030-3059.

16. Mawuenyega, K. G.; Sigurdson, W.; Ovod, V.; Munsell, L.; Kasten, T.; Morris, J. C.; Yarasheski, K. E.; Bateman, R. J. Decreased Clearance of CNS β-Amyloid in Alzheimer's Disease. *Science* **2010,** *330*, 1774.

17. Petkova, A. T.; Ishii, Y.; Balbach, J. J.; Antzutkin, O. N.; Leapman, R. D.; Delaglio, F.; Tycko, R. A structural model for Alzheimer's β-amyloid fibrils based on experimental constraints from solid state NMR. *Proceedings of the National Academy of Sciences* **2002,** *99*, 16742-16747.

18. Klein, W. L.; Krafft, G. A.; Finch, C. E. Targeting Small Aβ Oligomers: The Solution to an Alzheimer's Disease Conundrum? *Trends Neurosci.* **2001,** *24*, 219-224.

19. Walsh, D. M.; Selkoe, D. J. Aβ Oligomers - a decade of discovery. *J. Neurochem.* **2007,** *101*, 1172-1184.

20. Shankar, G. M.; Li, S. M.; Mehta, T. H.; Garcia-Munoz, A.; Shepardson, N. E.; Smith, I.; Brett, F. M.; Farrell, M. A.; Rowan, M. J.; Lemere, C. A.; Regan, C. M.; Walsh, D. M.; Sabatini, B. L.; Selkoe, D. J. Amyloid-β Protein Dimers Isolated Directly From Alzheimer's Brains Impair Synaptic Plasticity and Memory. *Nat. Med.* **2008,** *14*, 837-842.

21. Rahimi, F.; Shanmugam, A.; Bitan, G. Structure–function relationships of pre-fibrillar protein assemblies in Alzheimer's disease and related disorders. *Curr. Alzheimer Res.* **2008,** *5*, 319-341.

22. Bitan, G.; Kirkitadze, M. D.; Lomakin, A.; Vollers, S. S.; Benedek, G. B.; Teplow, D. B. Amyloid β-Protein (Aβ) Assembly: Aβ40 and Aβ42 Oligomerize Through Distinct Pathways. *Proc. Natl. Acad. Sci. U. S. A.* **2003,** *100*, 330-335.

23. Teplow, D. B.; Lazo, N. D.; Bitan, G.; Bernstein, S.; Wyttenbach, T.; Bowers, M. T.; Baumketner, A.; Shea, J. E.; Urbanc, B.; Cruz, L.; Borreguero, J.; Stanley, H. E. Elucidating amyloid β-protein folding and assembly: A multidisciplinary approach. *Accounts Chem. Res.* **2006,** *39*, 635-645.

24. Bernstein, S. L.; Dupuis, N. F.; Lazo, N. D.; Wyttenbach, T.; Condron, M. M.; Bitan, G.; Teplow, D. B.; Shea, J.-E.; Ruotolo, B. T.; Robinson, C. V.; Bowers, M. T. Amyloid-β protein oligomerization and the importance of tetramers and dodecamers in the aetiology of Alzheimer's disease. *Nat. Chem.* **2009,** *1*, 326-331.

25. Gong, Y.; Chang, L.; Viola, K. L.; Lacor, P. N.; Lambert, M. P.; Finch, C. E.; Krafft, G. A.; Klein, W. L. Alzheimer's disease-affected brain: presence of oligomeric Aβ ligands (ADDLs) suggests a molecular basis for reversible memory loss. *Proc. Natl. Acad. Sci. U. S. A.* **2003,** *100*, 10417-10422.

26. Lesné, S.; Koh, M. T.; Kotilinek, L.; Kayed, R.; Glabe, C. G.; Yang, A.; Gallagher, M.; Ashe, K. H. A specific amyloid-β protein assembly in the brain impairs memory. *Nature* **2006,** *440*, 352-357.

27. Pozueta, J.; Lefort, R.; Shelanski, M. L. Synaptic changes in Alzheimer's disease and its models. *Neuroscience* **2013,** *251*, 51-65.

28. Karran, E.; Mercken, M.; Strooper, B. D. The amyloid cascade hypothesis for Alzheimer's disease: an appraisal for the development of therapeutics. *Nat Rev Drug Discov* **2011,** *10*, 698-712.

29. Bateman, R. J.; Siemers, E. R.; Mawuenyega, K. G.; Wen, G.; Browning, K. R.; Sigurdson, W. C.; Yarasheski, K. E.; Friedrich, S. W.; DeMattos, R. B.; May, P. C.; Paul, S. M.; Holtzman, D. M. A γ-secretase Inhibitor Decreases Amyloid-β Production in The Central Nervous System. *Ann. Neurol.* **2009,** *66*, 48-54.

30. Barten, D.; Meredith, J., Jr.; Zaczek, R.; Houston, J.; Albright, C. γ-Secretase Inhibitors for Alzheimer's Disease. *Drugs R&D* **2006,** *7*, 87-97.

31. Imbimbo, P. B.; Giardina, G. A. M. γ-Secretase Inhibitors and Modulators for the Treatment of Alzheimer's Disease: Disappointments and Hopes. *Curr. Trends Med. Chem.* **2011,** *11*, 1555-1570.

32. Ghosh, A. K.; Osswald, H. L. BACE1 (β-secretase) Inhibitors for the Treatment of Alzheimer's Disease. *Chem. Soc. Rev.* **2014,** *43*, 6765-6813.

33. Bates, K. A.; Verdile, G.; Li, Q. X.; Ames, D.; Hudson, P.; Masters, C. L.; Martins, R. N. Clearance Mechanisms of Alzheimer's Amyloid-β Peptide: Implications for Therapeutic Design and Diagnostic Tests. *Mol. Psychiatr.* **2009,** *14*, 469-486.

34. Higuchi, M.; Iwata, N.; Saido, T. C. Understanding Molecular Mechanisms of Proteolysis in Alzheimer's Disease: Progress Toward Therapeutic Interventions. *BBA-Proteins Proteomics* **2005,** *1751*, 60-67.

35. Lemere, C. A.; Masliah, E. Can Alzheimer disease be prevented by amyloid-β immunotherapy? *Nat Rev Neurol* **2010,** *6*, 108-119.

36. Stains, C. I.; Mondal, K.; Ghosh, I. Molecules that target beta-amyloid. *ChemMedChem* **2007,** *2*, 1675-1692.

37. Necula, M.; Kayed, R.; Milton, S.; Glabe, C. G. Small Molecule Inhibitors of Aggregation Indicate That Amyloid β Oligomerization and Fibrillization Pathways Are Independent and Distinct. *J. Biol. Chem.* **2007,** *282*, 10311-10324.

38. Hawkes, C. A.; Ng, V.; McLaurin, J. Small Molecule Inhibitors of Aβ-Aggregation and Neurotoxicity. *Drug Dev. Res.* **2009,** *70*, 111-124.

39. Ehrnhoefer, D. E.; Bieschke, J.; Boeddrich, A.; Herbst, M.; Masino, L.; Lurz, R.; Engemann, S.; Pastore, A.; Wanker, E. E. EGCG Redirects Amyloidogenic Polypeptides into Unstructured, Off-pathway Oligomers. *Nat. Struct. Mol. Biol.* **2008,** *15*, 558-566.

40. Yang, F. S.; Lim, G. P.; Begum, A. N.; Ubeda, O. J.; Simmons, M. R.; Ambegaokar, S. S.; Chen, P. P.; Kayed, R.; Glabe, C. G.; Frautschy, S. A.; Cole, G. M. Curcumin Inhibits Formation of Amyloid β Oligomers and Fibrils, Binds Plaques, and Reduces Amyloid In Vivo. *J. Biol. Chem.* **2005,** *280*, 5892-5901.

41. McLaurin, J.; Golomb, R.; Jurewicz, A.; Antel, J. P.; Fraser, P. E. Inositol Stereoisomers Stabilize an Oligomeric Aggregate of Alzheimer Amyloid β Peptide and Inhibit Aβ-induced Toxicity. *J. Biol. Chem.* **2000,** *275*, 18495-18502.

42. McLaurin, J.; Kierstead, M. E.; Brown, M. E.; Hawkes, C. A.; Lambermon, M. H.; Phinney, A. L.; Darabie, A. A.; Cousins, J. E.; French, J. E.; Lan, M. F.; Chen, F.; Wong, S. S.; Mount, H. T.; Fraser, P. E.; Westaway, D.; St George-Hyslop, P. Cyclohexanehexol Inhibitors of Aβ Aggregation Prevent and Reverse Alzheimer Phenotype in a Mouse Model. *Nat. Med.* **2006,** *12*, 801-808.

43. Fradinger, E. A.; Monien, B. H.; Urbanc, B.; Lomakin, A.; Tan, M.; Li, H.; Spring, S. M.; Condron, M. M.; Cruz, L.; Xie, C.-W.; Benedek, G. B.; Bitan, G. C-terminal peptides coassemble into Aβ42 oligomers and protect neurons against Aβ42-induced neurotoxicity. *Proc. Natl. Acad. Sci. U. S. A.* **2008,** *105*, 14175-14180.

44. Li, H.; Monien, B. H.; Lomakin, A.; Zemel, R.; Fradinger, E. A.; Tan, M.; Spring, S. M.; Urbanc, B.; Xie, C. W.; Benedek, G. B.; Bitan, G. Mechanistic Investigation of the Inhibition of Aβ42 Assembly and Neurotoxicity by Aβ42 C-Terminal Fragments. *Biochemistry* **2010,** *49*, 6358-6364.

45. Gessel, M. M.; Wu, C.; Li, H.; Bitan, G.; Shea, J.-E.; Bowers, M. T. Aβ(39–42) Modulates Aβ Oligomerization but Not Fibril Formation. *Biochemistry* **2011,** *51*, 108-117.

46. Porat, Y.; Abramowitz, A.; Gazit, E. Inhibition of Amyloid Fibril Formation by Polyphenols: Structural Similarity and Aromatic Interactions as a Common Inhibition Mechanism. *Chem. Biol. Drug Des.* **2006,** *67*, 27-37.

47. Attar, A.; Rahimi, F.; Bitan, G. Modulators of Amyloid Protein Aggregation and Toxicity: EGCG and CLR01. *Transl. Neurosci.* **2013,** *4*, 385-409.

48. Kang, J.; Lemaire, H.-G.; Unterbeck, A.; Salbaum, J. M.; Masters, C. L.; Grzeschik, K.-H.; Multhaup, G.; Beyreuther, K.; Muller-Hill, B. The precursor of Alzheimer's disease amyloid A4 protein resembles a cell-surface receptor. *Nature* **1987,** *325*, 733-736.

49. O'Brien, R. J.; Wong, P. C. Amyloid Precursor Protein Processing and Alzheimer's Disease. *Annu. Rev. Neurosci.* **2011,** *34*, 185-204.

50. Sherrington, R.; Rogaev, E. I.; Liang, Y.; Rogaeva, E. A.; Levesque, G.; Ikeda, M.; Chi, H.; Lin, C.; Li, G.; Holman, K.; Tsuda, T.; Mar, L.; Foncin, J. F.; Bruni, A. C.; Montesi, M. P.; Sorbi, S.; Rainero, I.; Pinessi, L.; Nee, L.; Chumakov, I.; Pollen, D.; Brookes, A.; Sanseau, P.; Polinsky, R. J.; Wasco, W.; Da Silva, H. A. R.; Haines, J. L.; Pericak-Vance, M. A.; Tanzi, R. E.; Roses, A. D.; Fraser, P. E.; Rommens, J. M.; St George-Hyslop, P. H. Cloning of a gene bearing missense mutations in early-onset familial Alzheimer's disease. *Nature* **1995,** *375*, 754-760.

51. Borchelt, D. R.; Thinakaran, G.; Eckman, C. B.; Lee, M. K.; Davenport, F.; Ratovitsky, T.; Prada, C.-M.; Kim, G.; Seekins, S.; Yager, D.; Slunt, H. H.; Wang, R.; Seeger, M.; Levey, A. I.; Gandy, S. E.; Copeland, N. G.; Jenkins, N. A.; Price, D. L.; Younkin, S. G.; Sisodia, S. S. Familial Alzheimer's Disease–Linked Presenilin 1 Variants Elevate Aβ1–42/1–40 Ratio In Vitro and In Vivo. *Neuron* **1996,** *17*, 1005-1013.

52. Levy-Lahad, E.; Wasco, W.; Poorkaj, P.; Romano, D.; Oshima, J.; Pettingell, W.; Yu, C.; Jondro, P.; Schmidt, S.; Wang, K.; al., e. Candidate gene for the chromosome 1 familial Alzheimer's disease locus. *Science* **1995,** *269*, 973-977.

53. Bateman, R.; Aisen, P.; De Strooper, B.; Fox, N.; Lemere, C.; Ringman, J.; Salloway, S.; Sperling, R.; Windisch, M.; Xiong, C. Autosomal-dominant Alzheimer's disease: a review and proposal for the prevention of Alzheimer's disease. *Alzheimer's Res. Ther.* **2011,** *3*, 1.

54. Tanzi, R. E.; Bertram, L. Twenty Years of the Alzheimer's Disease Amyloid Hypothesis: A Genetic Perspective. *Cell* **2005,** *120*, 545-555.

55. Hendriks, L.; van Duijn, C. M.; Cras, P.; Cruts, M.; Van Hul, W.; van Harskamp, F.; Warren, A.; McInnis, M. G.; Antonarakis, S. E.; Martin, J.-J.; Hofman, A.; Van Broeckhoven, C. Presenile dementia and cerebral haemorrhage linked to a mutation at codon 692 of the β-amyloid precursor protein gene. *Nat. Genet.* **1992,** *1*, 218-221.

56. Nilsberth, C.; Westlind-Danielsson, A.; Eckman, C. B.; Condron, M. M.; Axelman, K.; Forsell, C.; Stenh, C.; Luthman, J.; Teplow, D. B.; Younkin, S. G.; Naslund, J.; Lannfelt, L. The 'Arctic' APP mutation (E693G) causes Alzheimer's disease by enhanced Aβ protofibril formation. *Nat. Neurosci.* **2001,** *4*, 887-893.

57. Levy, E.; Carman, M.; Fernandez-Madrid, I.; Power, M.; Lieberburg, I.; van Duinen, S.; Bots, G.; Luyendijk, W.; Frangione, B. Mutation of the Alzheimer's disease amyloid gene in hereditary cerebral hemorrhage, Dutch type. *Science* **1990,** *248*, 1124-1126.

58. Tomiyama, T.; Nagata, T.; Shimada, H.; Teraoka, R.; Fukushima, A.; Kanemitsu, H.; Takuma, H.; Kuwano, R.; Imagawa, M.; Ataka, S.; Wada, Y.; Yoshioka, E.; Nishizaki, T.; Watanabe, Y.; Mori, H. A new amyloid β variant favoring oligomerization in Alzheimer's-type dementia. *Ann. Neurol.* **2008,** *63*, 377-387.

59. Miravalle, L.; Tokuda, T.; Chiarle, R.; Giaccone, G.; Bugiani, O.; Tagliavini, F.; Frangione, B.; Ghiso, J. Substitutions at Codon 22 of Alzheimer's Aβ Peptide Induce Diverse Conformational Changes and Apoptotic Effects in Human Cerebral Endothelial Cells. *J. Biol. Chem.* **2000,** *275*, 27110-27116.

60. Grabowski, T. J.; Cho, H. S.; Vonsattel, J. P. G.; Rebeck, G. W.; Greenberg, S. M. Novel amyloid precursor protein mutation in an Iowa family with dementia and severe cerebral amyloid angiopathy. *Ann. Neurol.* **2001,** *49*, 697-705.

61. Baumketner, A.; Bernstein, S. L.; Wyttenbach, T.; Lazo, N. D.; Teplow, D. B.; Bowers, M. T.; Shea, J.-E. Structure of the 21–30 fragment of amyloid β-protein. *Protein Sci.* **2006,** *15*, 1239-1247.

62. Krone, M. G.; Baumketner, A.; Bernstein, S. L.; Wyttenbach, T.; Lazo, N. D.; Teplow, D. B.; Bowers, M. T.; Shea, J.-E. Effects of Familial Alzheimer's Disease Mutations on the Folding Nucleation of the Amyloid β-Protein. *J. Mol. Biol.* **2008,** *381*, 221-228.

63. Hori, Y.; Hashimoto, T.; Wakutani, Y.; Urakami, K.; Nakashima, K.; Condron, M. M.; Tsubuki, S.; Saido, T. C.; Teplow, D. B.; Iwatsubo, T. The Tottori (D7N) and English (H6R) Familial Alzheimer Disease Mutations Accelerate Aβ Fibril Formation without Increasing Protofibril Formation. *J. Biol. Chem.* **2007,** *282*, 4916-4923.

64. Ono, K.; Condron, M. M.; Teplow, D. B. Effects of the English (H6R) and Tottori (D7N) Familial Alzheimer Disease Mutations on Amyloid β-Protein Assembly and Toxicity. *J. Biol. Chem.* **2010,** *285*, 23186-23197.

65. Wakutani, Y.; Watanabe, K.; Adachi, Y.; Wada-Isoe, K.; Urakami, K.; Ninomiya, H.; Saido, T. C.; Hashimoto, T.; Iwatsubo, T.; Nakashima, K. Novel amyloid precursor protein gene missense mutation (D678N) in probable familial Alzheimer's disease. *J. Neurol., Neurosurg. Psychiatry* **2004,** *75*, 1039-1042.

66. Gessel, M. M.; Bernstein, S.; Kemper, M.; Teplow, D. B.; Bowers, M. T. Familial Alzheimer's Disease Mutations Differentially Alter Amyloid β-Protein Oligomerization. *ACS Chem. Neurosci.* **2012,** *3*, 909-918.

67. Chen, W.-T.; Hong, C.-J.; Lin, Y.-T.; Chang, W.-H.; Huang, H.-T.; Liao, J.-Y.; Chang, Y.-J.; Hsieh, Y.-F.; Cheng, C.-Y.; Liu, H.-C.; Chen, Y.-R.; Cheng, I. H. Amyloid-Beta (Aβ) D7H Mutation Increases Oligomeric Aβ42 and Alters Properties of Aβ-Zinc/Copper Assemblies. *PLoS ONE* **2012,** *7*, e35807.

68. Jonsson, T.; Atwal, J. K.; Steinberg, S.; Snaedal, J.; Jonsson, P. V.; Bjornsson, S.; Stefansson, H.; Sulem, P.; Gudbjartsson, D.; Maloney, J.; Hoyte, K.; Gustafson, A.; Liu, Y.; Lu, Y.; Bhangale, T.; Graham, R. R.; Huttenlocher, J.; Bjornsdottir, G.; Andreassen, O. A.; Jonsson, E. G.; Palotie, A.; Behrens, T. W.; Magnusson, O. T.; Kong, A.; Thorsteinsdottir, U.; Watts, R. J.; Stefansson, K. A mutation in APP protects against Alzheimer's disease and age-related cognitive decline. *Nature* **2012,** *488*, 96-99.

69. Di Fede, G.; Catania, M.; Morbin, M.; Rossi, G.; Suardi, S.; Mazzoleni, G.; Merlin, M.; Giovagnoli, A. R.; Prioni, S.; Erbetta, A.; Falcone, C.; Gobbi, M.; Colombo, L.; Bastone,

A.; Beeg, M.; Manzoni, C.; Francescucci, B.; Spagnoli, A.; Cantù, L.; Del Favero, E.; Levy, E.; Salmona, M.; Tagliavini, F. A Recessive Mutation in the APP Gene with Dominant-Negative Effect on Amyloidogenesis. *Science* **2009,** *323,* 1473-1477.

Chapter 2

Ion Mobility Spectrometry

Due to the aggregation property, the Aβ proteins have been very difficult to be studied by traditional analytical techniques. For example, spectroscopic techniques such as Circular dichroism (CD), IR spectroscopy and NMR can measure only the average properties of all species (form monomer, oligomers, protofibrils to fibrils) in the solution. X-ray crystallography, on the other hand, requires crystal samples which only applied to amyloid fibrils. It is impossible to isolate single oligomer without cross-linking or other chemical methods. Therefore, it is necessary to use non-traditional techniques to investigate amyloid proteins. Here, we use ion mobility spectrometry (IMS) coupled to mass

spectrometry (MS) method to study the structures and assembly of these Aβ proteins, and evaluate the effects of small molecules and familial mutations.

IMS is capable of separating species with different in size or shape, based on their mobility in an inert buffer gas under an electric field. Ion mobility provides insights into the structure. When coupled with mass spectrometry (MS), IMS–MS provides a powerful hybrid analytical tool that can be applied in environmental, biological, structural, pharmaceutical, and other applications. The instrument setup used in this thesis is drift tube ion mobility spectrometry (DTIMS)[1-2] and therefore only this method is described in detail. Other ion mobility instrument setups include Traveling Wave ion mobility spectrometry (TWIMS)[3-4], high filed asymmetric ion mobility spectrometry (FAIMS)[5] and differential mobility spectrometry (DMS)[5], etc.

2.1 Ion Mobility Theory

The ions drift through a buffer gas (used helium in this work) under the influence of a weak uniform electric field, *E*. The ions are accelerated along the field lines, scatter in random directions due to collision with the buffer gas and diffusion. Under the low field condition, the ions are given enough time to reach equilibrium with the gas molecules. As a result, the ions travel with constant velocity parallel to the field lines and their sizes grow due to diffusion. The constant drift velocity, v_d, is determined by the forward accelerating force of the field and the retarding decelerating force of collisions. It is proportional to the electric field:

$$v_d = K \cdot E \qquad (2.1)$$

Using kinetic theory[6], the momentum transfer and energy gained by the ions from the electric field is balanced with the energy lost in buffer gas collisions. The collision cross section σ can be derived,

$$K = \frac{3e}{16N} \left(\frac{2\pi}{\mu k_B T}\right)^{1/2} \frac{1}{\sigma} \qquad (2.2)$$

Here, q is the ion charge, N is the buffer gas number density at STP, μ is the reduced mass of the ion–He collision, and k_B is the Boltzman constant. The mobility (K) and the collision cross section (σ) provide information about the three-dimensional configurations of the ions. This equation demonstrates that the ion mobility depends on the gas pressure, the temperature, the electric field, the size or shape of the analyte ions and the interactions of the ion and the buffer gas. Under the same pressure and temperature, ions with smaller cross section have larger mobility and drift faster. In contrast, ions with large cross section have small ion mobility and drift slower (Figure 2.1).

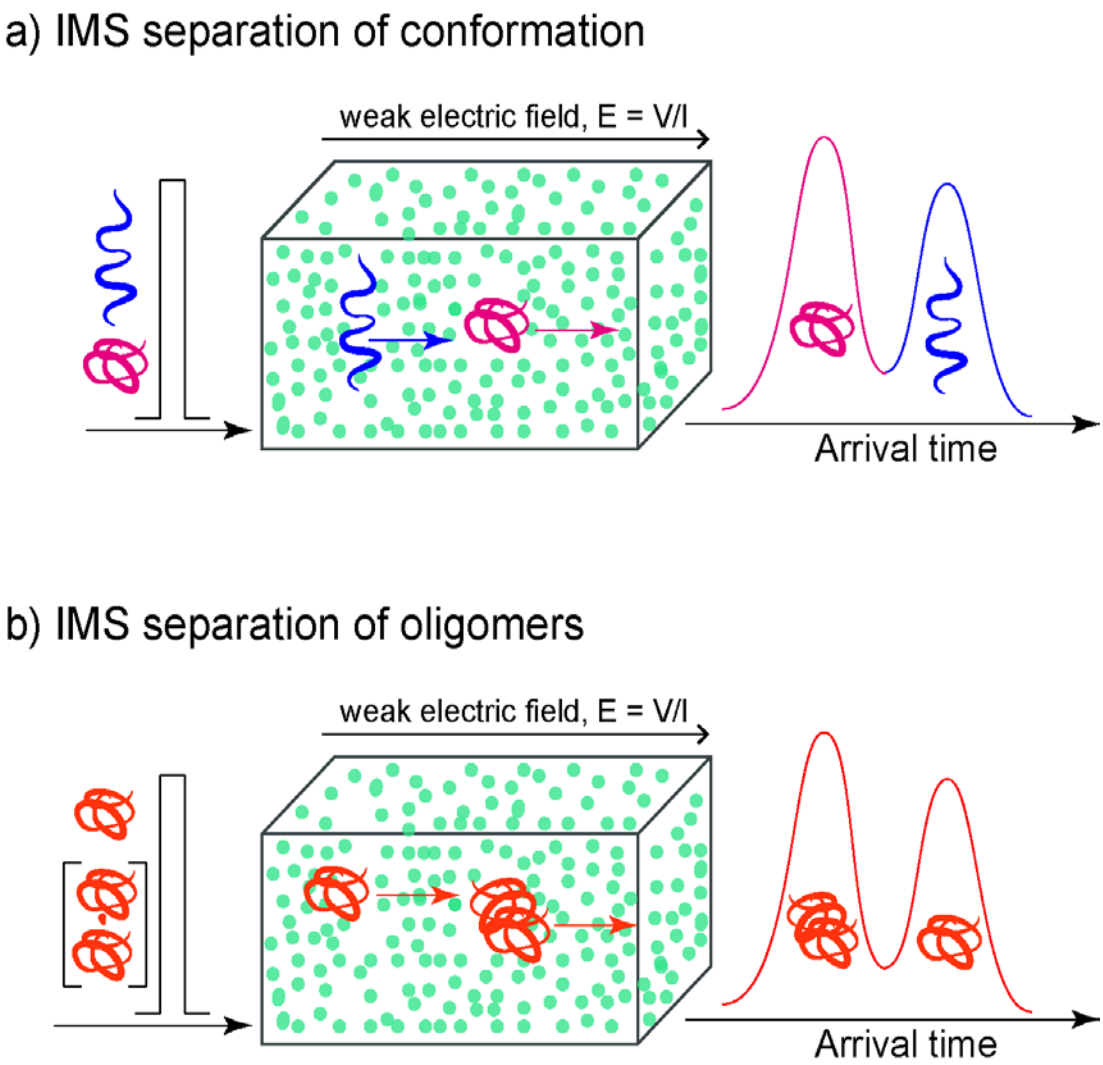

Figure 2.1 Illustration of the ion mobility separation (a) of isomers and (b) oligomers with the same m/z.

2.2 Collision Cross Sections Measurement

During the experiment, the time the analyte ions spending inside and outside the drift cell with length *l*, before reaching the detector is measured directly as arrival time, t_A. It is related to the drift velocity of the ion:

$$v_d = \frac{l}{t_d} = \frac{l}{(t_a - t_0)} \qquad (2.3)$$

The absolute ion mobility is dependent on the temperature (T) and the pressure (P) of the buffer gas, so it is typically converted to K_0, the standard or reduced mobility:

$$K_0 = K \cdot \frac{P}{760} \cdot \frac{273.16}{T} \qquad (2.4)$$

The reduced mobility K_0 can be determined from the instrument parameters by using equation 2 and plotting t_A versus P/V[7]

$$t_A = \frac{l^2}{K_0} \cdot \frac{273.16}{760\,T} \cdot \frac{P}{V} + t_0 \qquad (2.5)$$

In equation 4, *l* is the length of the drift cell, V is the voltage across the drift cell, and t_0 is the time the ions spend outside the drift cell before hitting the detector. Equation 5 gives the arrival time as a function of *P/V*, with a slope that is inversely proportional to K and t_0 as the y-intercept. All of these quantities are either known constants or are measured for each experiment. t_A is measured under different P/V values by keeping constant and changing the drift voltage V. Therefore K_0 can be determined by plotting t_A versus P/V at a given temperature (Figure 2.2). Once the ion mobility is determined for a given species, an experimental collision cross section can be calculated by using Equation 2.

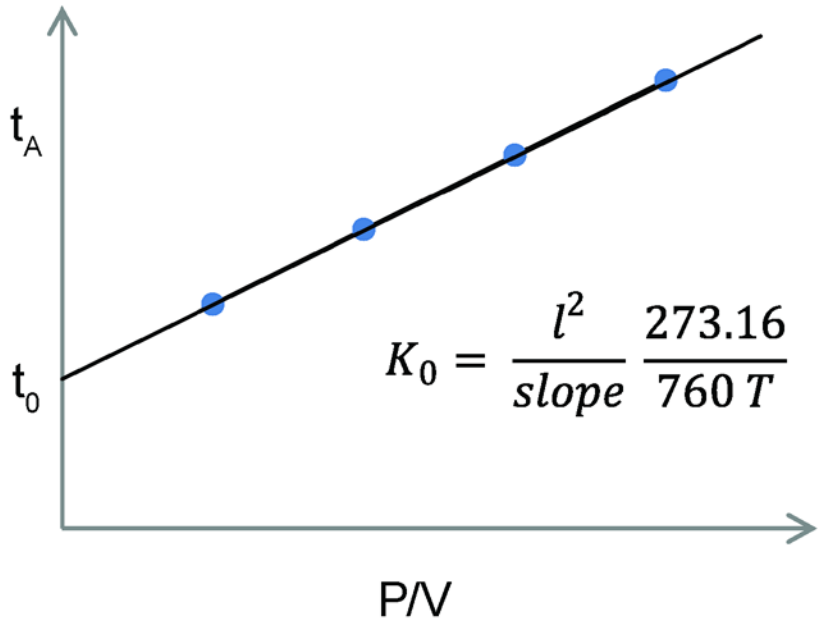

Figure 2.2 Example of an arrival time, t_A, versus P/V plot to determine the mobility of a given species. The slope of the curve is inversely proportional to the mobility and y-intercept is equal to t_0.

2.3 Instrumentation

2.3.1 Ion mobility Instrument

A home-built ion mobility spectrometry-mass spectrometer was used for the majority of the experiments in this thesis. A schematic of this instrument is shown in Figure 2.3. A detailed description of the instrument can be found in literature[8], here only brief introduction is shown below.

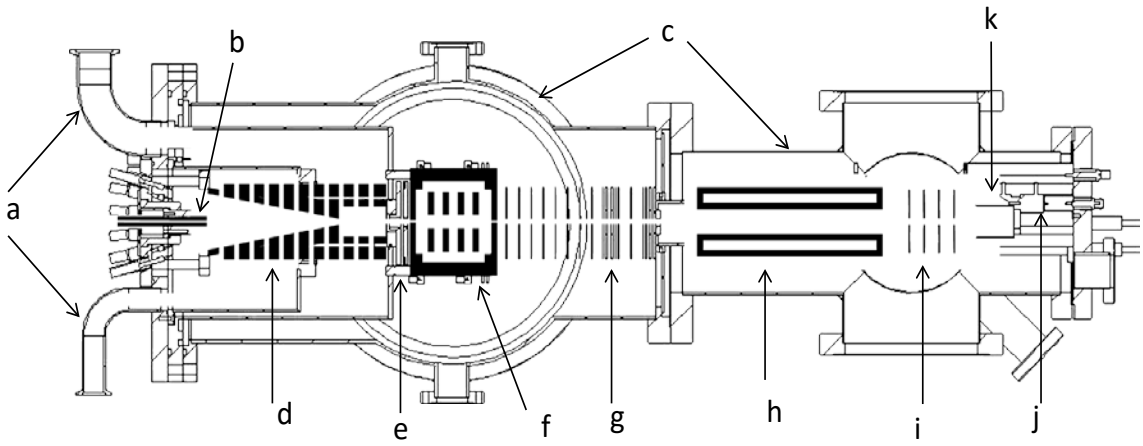

Figure 2.3 Schematic of an ESI-ion mobility mass spectrometer. (a) source roughing, (b) capillary, (c) vacuum chamber, (d) entrance ion funnel, (e) (g) (i) ion optics, (f) temperature-controlled drift cell, (h) quadrupole mass analyzer, (j) detector, (k) conversion dynode.

The ions are generated continuously by a nano-electrospray ionization (ESI) source. ESI is one of the soft ionization methods that cause little or no fragmentation of the analyte compound. The nanospray tips are made in house with borosilicate glass capillary (0.69 mm, o.d 1.2 mm, Sutter Instruments). Briefly, the capillary is heated and pulled by a glass tip puller (Sutter Instruments) and then coated with gold. A few microliters of analyte solution is loaded into the nanospray tip and mounted onto a xyz linear translational stage. A high voltage of ~700-1400 V with respect to the entrance of the instrument is applied to the needle to generate charged ions continuously.

The generated ions travel through the capillary (0.010 in. i.d., 3 in. long) in front of the instrument and enter a high vacuum chamber where they are focused by the ion funnel. The ion funnel is a high transmission RF ion guide device that compresses the divergent ion stream down into a small diameter, and moves the ions from the source region into the drift

cell without the use of high acceleration fields which thus avoids high-energy ion-neutral collisions that may cause fragmentation or conformation changes.

A pulse of ions is injected into a 4.503 cm long drift cell. The drift cell consists of a copper cell body that can be heated by electrical heaters and cooled with a flow of liquid nitrogen, a copper end cap with separate temperature control and a ceramic ring that separates the end cap from the cell body. The cell temperature can be varied from 80 to above 800K. The cell is filled with 3-5 torr helium gas and applied with a weak electric field, ranging from 2 to 20 V/cm to allow experiment conditions within the low field limit that is required for ion mobility measurements.

The ions exiting the drift cell are mass analyzed with a quadrupole mass filter (4000 amu; Extrel; Pittsburgh, PA). The quadrupole can be set to scan over a mass range to generate a mass spectrum or can be set to select only a particular ion of interest to pass through for arrival time recording.

The ions exiting the quadrupole are attracted to a conversion dynode (4 kV) and detected by a channel electron multiplier. The signal output is amplified by a preamp (Ortec), and recorded on a multichannel scalar (MCS plus; EG&G Ortec, Oak Ridge, TN).

2.3.2 Experiments

Mass Spectrum Scan:

The scan mode is used to record a mass spectrum, which allows us to characterize the contents of the analyte sample and identify ions of interest for further analysis. In this

mode, the instrument is run in a continuous mode and the quadrupole is set to scan over a desired mass range and the ion current is recorded.

Arrival time distributions

To record an arrival time distribution (ATD), the ion gate is set on and a pulse of analyte ions are injected into the drift cell. Ion this mode, the quadruple is set to select only the ion of interest to pass through and the ion current is detected as a function of arrival time (started with the pulse injection). This can be repeated at different drift voltages to measure the ion mobility.

Injection energy study

To assign the peaks in the ATDs unambiguously and better understand the distributions for different conformers or oligomers, the ATDs are often measured at different ion injection energies. The voltage between the last lens of ion funnel and the drift cell entrance orifice determines the ion injection energy. The injection energy can be varied from ~20 to ~150 V and is typically 20-60 V. At low injection energy, the ions are rapidly thermalized by cooling collisions with the helium gas in the drift cell. At high injection energy, the ions are given energy that can lead to internal excitation before reaching thermal equilibrium. Such internal excitation can cause isomerization into low energy structure or dissociation of large noncovalent complexes into small species[9]. Usually the injection energy is kept as low as possible to minimize thermal heating of the ions during the injection process.

2.3.3 Resolution

The resolution of an ion mobility drift tube depends on a number of factors, not only the time spread due to ion diffusion in the drift cell, but also the time spread that occurs outside the drift tube (the initial width of injected ion pulse and the time spread created in both the exit funnel and in the quadrupole and detector). The resolution power of an IMS device is a function of drift field and temperature of buffer gas[10]:

$$\frac{t_d}{t_{1/2}} = \frac{1}{4}\left[\frac{q}{k_B ln2}\right]^{1/2}\left[\frac{V_d}{T}\right]^{1/2} \qquad (5)$$

where t_d is the drift time, $t_{1/2}$ is the width of the peak at half-height, q is the ion charge, V_d is the voltage drop across the drift cell, k_B is Boltzmann's constant and T is the temperature of the buffer gas. Following the equation, to increase the resolution, it requires to decrease the temperature of the buffer gas or to increase the electric field. However, increasing E requires increasing in drift length or gas pressure correspondingly to keep E/N constant and to stay in the low-field regime required for ion mobility experiments. With a high pressure of buffer gas, it is difficult to inject the ions into the drift cell. High injection energy is required to inject the ions into the drift cell, which in turn may lead to dissociation or fragmentation of the analyte ions. The length of the drift cell is limited by the diffusion of ions as they travel through the drift cell. The ions will lose to the wall if the drift cell is too long. Therefore, the resolution power is limited by the balance of ion energy, technical feasibility and the quantities determining the resolution.

2.3.4 Calculating the theoretical shape for a single structure in an ATD

The width of a single analyte ion structure in an ATD can be calculated by using kinetic theory[6], which gives information on the structural distribution favored in the ATD. The ion packet is taken as a periodic delta function and the flux is given by equation:

$$\Phi(0,z,t) = \frac{sae^{-\alpha t}}{4(\pi D_L t)^{1/2}} \cdot \left(v_d + \frac{z}{t}\right) \cdot \left[1 - e^{-\frac{{r_o}^2}{4D_T t}}\right] \cdot e^{-\frac{{r_o}^2}{4D_T t}} \qquad (2.6)$$

Here z is the length of the drift cell, r_0 is the radius of the initial ion packet, a is the area of the exit aperture, D_L and D_T are the longitudinal and transverse diffusion coefficients, s is the initial ion density and α is the loss of ions due to reactions in the drift cell. If the width of a feature in the experimental ATD is broader than the calculated one, then the feature possibly represents a family of structures, rather than a single structure.

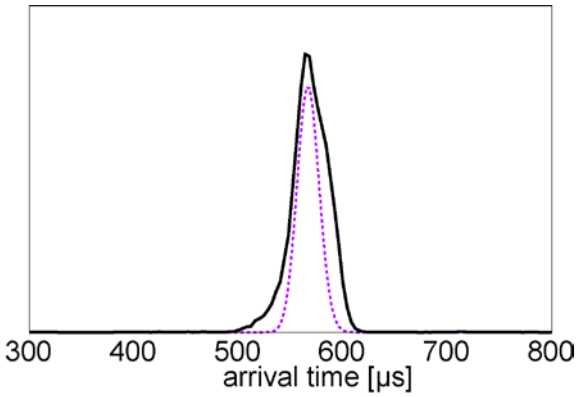

Figure 2.4 Example of an experimental ATD (solid line) in comparison with a calculated theoretical shape for a single structure (dashed line). The experimental ATD is broader than the dashed line, indicating there is a family of conformation instead of a single structure.

2.4 Theoretical calculations for collision cross sections

To obtain structural information from ion mobility experiments, collision cross sections can be calculated for theoretical structures generated by various molecular modeling methods and compared with experimental values. Experimental cross section determined in an ion mobility experiment depends on the shape of the analyte ions and it is an orientation averaged result. The simple way to calculate the collision integral for an ion colliding with buffer gas atoms is projection approximation method (PA). This method essentially calculates the average projection cross section as a model structure is rotated through different orientations using hard spheres with a specific radius for each atom in the system[11-12]. It is fairly quick, however it does not correctly describe the scattering process of buffer gas molecules and often fails for large systems (>200 atoms). A more accurate approach is the trajectory method (TJ)[13]. This TJ method treats the ion itself as a collection of atoms, each of which is represented by a Leonard-Jones (12-6-4) potential, and calculated the sum of these individual potentials to obtain the effective potential of the ion. The orientation averaged collisional cross-section is then determined by integrating over all possible collision geometries. However, the TJ method is computationally expensive, which takes very long time to calculate the cross sections for large systems. Recently, a new method projection superposition approximation method (PSA)[14-17] was developed. It is based on the PA method but corrects both size and shape effects, which gives accurate results for various complex molecular geometries and is low computational cost. In this thesis work, we used PSA method for calculating theoretical cross sections.

References

1. McDaniel, E. W.; Martin, D. W.; Barnes, W. S. Drift Tube - Mass Spectrometer for Studies of Low - Energy Ion - Molecule Reactions. *Review of Scientific Instruments* **1962,** *33*, 2-7.

2. Wyttenbach, T.; Bowers, M. T. Gas-Phase Conformations: The Ion Mobility/Ion Chromatography Method. In *Modern Mass Spectrometry*, Schalley, C., Ed. Springer Berlin Heidelberg: 2003; Vol. 225, pp 207-232.

3. Giles, K.; Pringle, S. D.; Worthington, K. R.; Little, D.; Wildgoose, J. L.; Bateman, R. H. Applications of a travelling wave-based radio-frequency-only stacked ring ion guide. *Rapid Communications in Mass Spectrometry* **2004,** *18*, 2401-2414.

4. Hilton, G.; Thalassinos, K.; Grabenauer, M.; Sanghera, N.; Slade, S.; Wyttenbach, T.; Robinson, P.; Pinheiro, T. T.; Bowers, M.; Scrivens, J. Structural analysis of prion proteins by means of drift cell and traveling wave ion mobility mass spectrometry. *J Am Soc Mass Spectrom* **2010,** *21*, 845-854.

5. Kolakowski, B. M.; Mester, Z. Review of applications of high-field asymmetric waveform ion mobility spectrometry (FAIMS) and differential mobility spectrometry (DMS). *Analyst* **2007,** *132*, 842-864.

6. Mason, E. A.; McDaniel, E. W., Transport Properties of Ions in Gases. In *Wiley: New York*, 1988.

7. Gidden, J.; Baker, E. S.; Ferzoco, A.; Bowers, M. T. Structural motifs of DNA complexes in the gas phase. *Int. J. Mass Spectrom.* **2005,** *240*, 183-193.

8. Wyttenbach, T.; Kemper, P. R.; Bowers, M. T. Design of a new electrospray ion mobility mass spectrometer. *Int. J. Mass Spectrom.* **2001,** *212*, 13-23.

9. Bernstein, S. L.; Wyttenbach, T.; Baumketner, A.; Shea, J.-E.; Bitan, G.; Teplow, D. B.; Bowers, M. T. Amyloid β-Protein: Monomer Structure and Early Aggregation States of Aβ42 and Its Pro19 Alloform. *J. Am. Chem. Soc.* **2005,** *127*, 2075-2084.

10. Revercomb, H. E.; Mason, E. A. Theory of plasma chromatography/gaseous electrophoresis. Review. *Analytical Chemistry* **1975,** *47*, 970-983.

11. Wyttenbach, T.; Helden, G. v.; Batka Jr, J. J.; Carlat, D.; Bowers, M. T. Effect of the long-range potential on ion mobility measurements. *J Am Soc Mass Spectrom* **1997,** *8*, 275-282.

12. von Helden, G.; Hsu, M. T.; Gotts, N.; Bowers, M. T. Carbon cluster cations with up to 84 atoms: structures, formation mechanism, and reactivity. *The Journal of Physical Chemistry* **1993,** *97*, 8182-8192.

13. Mesleh, M. F.; Hunter, J. M.; Shvartsburg, A. A.; Schatz, G. C.; Jarrold, M. F. Structural Information from Ion Mobility Measurements: Effects of the Long-Range Potential. *The Journal of Physical Chemistry* **1996,** *100*, 16082-16086.

14. Bleiholder, C.; Wyttenbach, T.; Bowers, M. T. A novel projection approximation algorithm for the fast and accurate computation of molecular collision cross sections (I). Method. *International Journal of Mass Spectrometry* **2011,** *308*, 1-10.

15. Bleiholder, C.; Contreras, S.; Do, T. D.; Bowers, M. T. A novel projection approximation algorithm for the fast and accurate computation of molecular collision cross sections (II). Model parameterization and definition of empirical shape factors for proteins. *International Journal of Mass Spectrometry* **2013,** *345–347*, 89-96.

16. Anderson, S. E.; Bleiholder, C.; Brocker, E. R.; Stang, P. J.; Bowers, M. T. A novel projection approximation algorithm for the fast and accurate computation of molecular collision cross sections (III): Application to supramolecular coordination-driven assemblies with complex shapes. *International Journal of Mass Spectrometry* **2012,** *330–332*, 78-84.

17. Bleiholder, C.; Contreras, S.; Bowers, M. T. A novel projection approximation algorithm for the fast and accurate computation of molecular collision cross sections (IV). Application to polypeptides. *International Journal of Mass Spectrometry* **2013,** *354–355*, 275-280.

Chapter 3

Z-Phe-Ala-diazomethylketone (PADK) Modulates Aβ42 Early Assembly

This chapter is reproduced partially with permission from:

X. Zheng, M. M. Gessel, M. L. Wisniewski, K. Viswanathan, D. L. Wright, B. A. Bahr and M. T. Bowers, "Z-Phe-Ala-diazomethylketone (PADK) disrupts and remodels early oligomer states of the Alzheimer disease Aβ42 protein", *Journal of Biological Chemistry* **2012**, 287, 6084-6088,

3.1 Introduction

Recently, more and more evidence has shown that the early oligomer states of Aβ42 are important for AD development.[1-3] In solution, Aβ42 forms dimer, tetramer, paranuclei (pentamer and hexamer), decamer and dodecamer before aggregation into fibrils.[4-5] Among them, the 56 kDa-dodecamer has been identified as a proximate toxic agent for AD.[6-7] Therefore, to target the early assembly of Aβ42, especially the dodecamer formation is an important therapeutic strategy for AD treatment.

Small molecules are especially attractive as Aβ42 aggregation inhibitors.[8-9] To date, many small molecules have been discovered and/or designed to have such effect. Natural bioactive molecules, for example, green extract EGCG,[10] turmeric curcumin,[11] and polyphenol compounds[12] have been discovered to be active inhibitors for Aβ42-induced neurotoxicity. Many small molecules are specifically designed and synthesized to target Aβ42 aggregation.

As discussed in Chapter 1, the important aspect of therapeutic strategy for AD is to reduce the level of Aβ proteins by reducing the Aβ production by inhibiting the γ-secretase activity or by facilitating Aβ clearance by enhancing lysosomal proteases. Molecules have been discovered to up-regulate the levels of lysosomal enzymes and thereby result in reduced Aβ level in the brain.[13] For example, a small molecule, Z-Phe-Ala-diazomethylketone(PADK, chemical structure is provided in Figure 3.1), which was used as a lysosomal enzyme up-regulator, has recently been shown to selectively increase the Cathepsin B level in the central nervous system. The increased cathepsin B level has enhanced the clearance of Aβ proteins and thus reduced Aβ levels in the brain, which in turn

offset the defects in synaptic composition and cognitive functions in the transgenic AD mice models.[14]

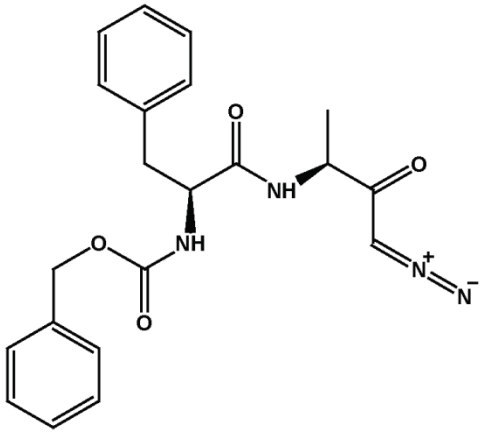

Figure 3.1 Chemical structure of Z-Phe-Ala-diazomethylketone (PADK) molecule. The molecular weight is 394.

As PADK is a small molecule, it is very likely that PADK may interact with Aβ itself directly. Here, we used ion mobility spectrometry-mass spectrometry (IMS-MS) coupled with all atom molecular dynamics (MD) simulation method to probe the interaction of PADK and Aβ42.

Ion mobility spectrometry (IMS)[15] is suitable to separate species with the same mass-to-charge ratio but different structures or oligomer sizes. It has been developed and applied to investigate the structure and the early assembly of amyloid β-proteins and the interactions of small molecules with Aβ.[5,16-19] MD simulations provide an insight into the detail of the interactions of protein and small molecule on the atomic level.[17] Our results provide an example of small molecules directly targeting Aβ42 and inhibiting its aggregation and

toxicity, shedding lights on future small molecule therapeutic development of AD and other diseases.

2.2 Experimental Methods

Peptides and Sample Preparation:

PADK was obtained from Bachem Americas, Inc. (N-1040; Torrance, CA). Full-length Aβ42 protein was synthesized by *N*-9-fluorenylmethoxycarbonyl (FMOC) chemistry.[20] The samples were purified by reverse-phase HPLC and their integrity validated by mass spectrometry and amino acid analysis. Lyophilized Aβ42 protein was dissolved in 10 mM ammonium acetate buffer (pH 7.4) with a final protein concentration of 10 μM. Concentrated PADK molecule was added to the Aβ42 with a final small molecule concentration of 10 or 100 μM.

Ion Mobility Spectrometry-Mass Spectrometry (IMS-MS):

Mass spectrometry analysis and ion mobility studies were performed on a home-built nanoESI instrument described in Chapter 2.3.

Transmission Electron Microscopy (TEM):

Microscopic analysis was performed by using a FEI T-20 transmission electron microscope under 200 kV. The Aβ42 samples were prepared under the same procedure as that for mass spectrometry analysis. The samples were kept in refrigerator (~4 °C) for 2 weeks. For TEM measurements, 10 μL aliquots of samples were spotted on glow-discharged, carbon-coated copper grids (Ted Pella, Inc). The samples on grids were stained with 10 mM

sodium metatungstate aqueous solution for 10 min and gently rinsed twice with DI-water. The sample grids were then dried in room temperature before TEM analysis.

***Molecular Dynamics Simulations*:**

System preparation: Our simulation systems contain one Aβ42 peptide and one PADK molecule, ~5500 water molecules, and three Na^+ ions to neutralize the system. The initial structure of Aβ42 is the most abundant one from the previous study by Garcia and coworkers[21] (Figure 3.9). PADK is initially placed ~15 Å away from the Aβ42 surface. The solute is immersed in a truncated octahedral box ($a = b = c$ = ~69 Å, $\alpha = \beta = \gamma$ = 109.47º) filled with water molecules. The Duan *et al.* all-atom point-charge force field (AMBER ff03)[22] is used to represent the peptides. This force field has been successfully used to model the binding of Aβ(39–42) to Aβ40/ Aβ42 peptides[19,23], the binding between Aβ protofibrils,[24] and the binding of fluorescent dyes to Aβ protofibrils.[25] The water solvent was explicitly represented by the TIP3P[26] model.

Binding Simulations: The AMBER 9 simulation suite[27] is used in molecular dynamics simulations and data analysis. After an initial energy minimization, a total of four simulations were performed with different initial random velocities. The random velocities of atoms are generated according to the Maxwell-Boltzmann distribution at 500 K. A 10 ps run at 500 K is used to further randomize the orientations and positions of the two peptides. The production run (150 ns) is at 310 K, including a short, 1-ns molecular dynamics in the NPT ensemble mode (constant pressure and temperature) to equilibrate the solvent and 149-ns dynamics in the NVT ensemble mode (constant volume and temperature). Periodic boundary conditions are imposed on the system. The particle-mesh Ewald method[28] is used

to treat the long-range electrostatic interactions. SHAKE[29] is applied to constrain all bonds connecting hydrogen atoms, enabling a 2-fs time step used in the dynamics. To reduce computation time, non-bonded forces are calculated using a two-stage RESPA approach[30] where the short-range forces within a 10 Å radius are updated every step and the long range forces beyond 10 Å are updated every two steps. The Langevin dynamics is used to control the temperature (310K) using a collision frequency of 1 ps^{-1}. The center of mass translation and rotation are removed every 500 steps, which removes the "block of ice" problem.[31-32] The trajectories were saved at 10-ps intervals for analysis. In total, 64 Opteron CPU cores (2.3 GHz) were used for ~20 days to complete the 4 binding simulations (a cumulative MD time of 0.6 μs for the system).

Clustering analysis: To gain a better understanding of the binding interactions, the stable complexes (atom contacts >20) are grouped into different structural families based on the Cα Root Mean Square Deviation (RMSD) of the complex (cutoff of 5 Å) using the GROMACS protocol.[33] Representative structures (centroids) of the top abundant clusters from the combined 4 runs of each system are shown Figure 3.11.

Collision Cross Section Calculation: The centroids of the top abundant clusters are also used to calculate their collision cross sections by a projected superposition approximation (PSA) method.[34-37] To correlate better with the solvent-free experiments, these solution-phase structures are converted to 'dehydrated' structures via a 500,000-step energy minimization in vacuum prior to cross-section calculations. This "dehydration" generally reduces the overall size of the structures, while maintaining their solution structural features and in this paper these structures are referred to as "dehydrated solution structures".

3.3 Results

3.3.1 Mass spectrometry: PADK binds directly to Aβ42 monomer and small oligomers

Mass spectra of the pure Aβ42 sample and Aβ42: PADK mixtures (1:1 and 1:10 ratios) were recorded to probe whether PADK interacts with Aβ42 directly besides its positive effects on lysosomal enzyme expression and Aβ42 clearance. As shown in Figure 3.2c, the mass spectrum of the pure Aβ42 sample shows three peaks corresponding to charge states of z/n = -4, -3 and -5/2, where z is the charge and n is the oligomer number. The mass spectrum of the 1:1 mixture of Aβ42 and PADK (Figure 3.2b) shows additional peaks tailing z/n = -3 and -4 Aβ42 species which correspond to Aβ42-PADK monomer complexes. Up to four PADK molecules are observed to bind to Aβ42 monomer. Moreover, there are two additional z/n = -5/2 peaks corresponding to Aβ42-PADK oligomer complexes. These results clearly show that PADK binds directly not only to the Aβ42 monomers but also to the Aβ42 oligomers. The 1:10 mixture shows even more abundant Aβ42-PADK complexes (Figure 3.2a). Note that the relative intensity of the z/n = -5/2 Aβ42 peak (labeled with a triangle) for the 1:10 mixture is significantly decreased compared to that of the pure Aβ42 sample or 1:1 mixture, suggesting there are less z/n = -5/2 oligomers. Taken together, these mass spectrometry results indicate that PADK binds directly to Aβ42 monomer and oligomers, and inhibits the formation of Aβ42 oligomers.

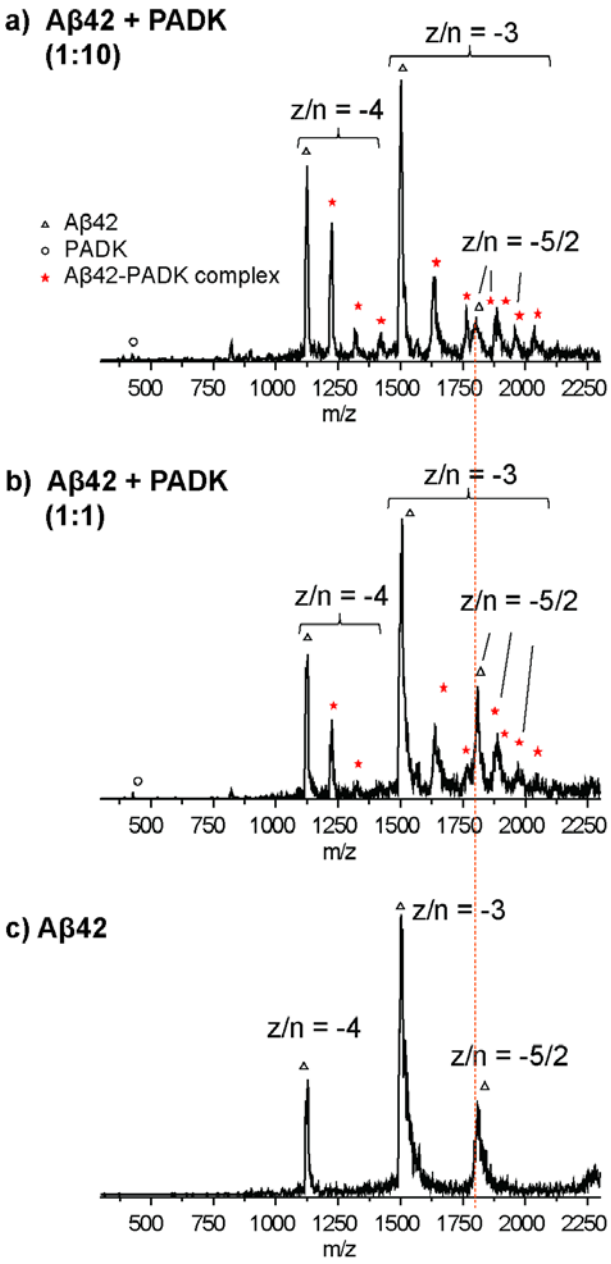

Figure 3.2 Mass spectra of the Aβ42 samples with and without PADK. The charge state of each species is labeled with z/n, where z is the charge and n is the oligomer number. The PADK molecule is noted with circle, the pure Aβ42 peaks are labeled with triangle and the Aβ42-PADK complexes are labeled with stars.

3.3.2 Ion mobility study: PADK modulates Aβ42 oligomer distribution

To examine the effect of PADK on the oligomer distribution of Aβ42, the ATDs of the z/n = -5/2 for the Aβ42 samples with and without PADK are recorded and shown in Figure 3.3. As shown in Figure 3.3c, the ATD of the pure Aβ42 shows four features with arrival times at ~710, 660, 610 and 530 μs, which were previously assigned as Aβ42 dimer, tetramer, hexamer and dodecamer, respectively, based on their cross sections (See ref. 9 for detailed discussion of the z/n = -5/2 peak assignment). The ATDs for the 1:10 mixture and the 1:1 mixture of Aβ42 and PADK (Figure 3.3a and 3.3b) show only three features with arrival times at ~710, 660 and 610 μs, which can be assigned as Aβ42 dimer, tetramer and hexamer, respectively, based on their cross sections. There is no feature with lower arrival time, suggesting the formation of dodecamer is inhibited by PADK. Moreover, the relative intensity of the hexamer feature in the 1:10 mixture is significantly lower than that in the 1:1 mixture or the pure Aβ42 sample, suggesting the formation of hexamer is inhibited by PADK as the PADK concentration increases.

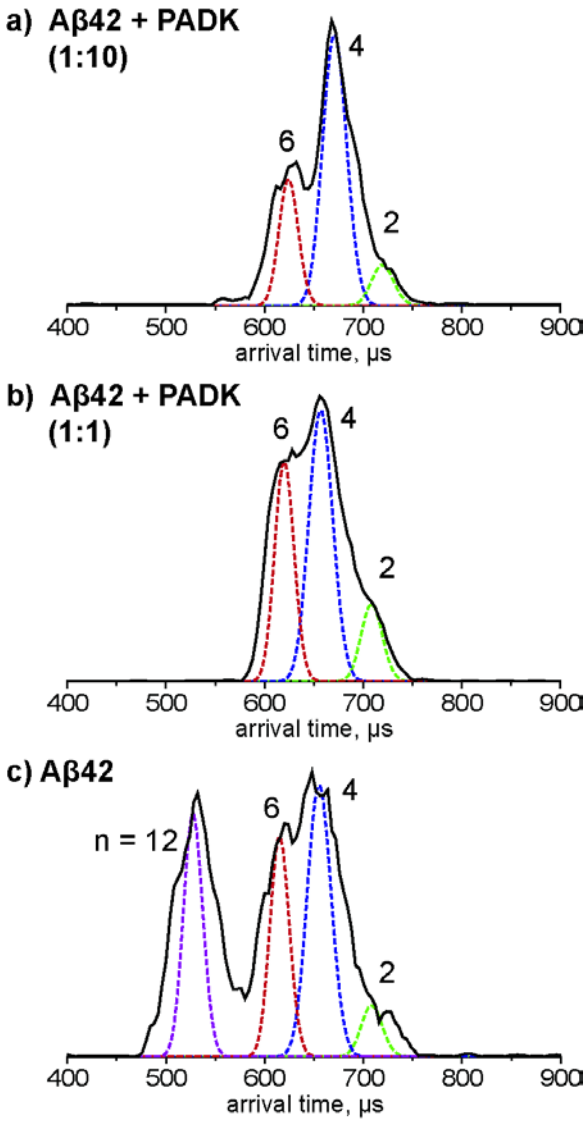

Figure 3.3 ATDs of the z/n = -5/2 peaks for Aβ42 samples with and without PADK. The oligomer number (n) is noted for each feature. The dashed lines represent the shape for a single structure.

The ATD of the z/n = -5/2 peak for the 1:10 mixture was monitored on the second day and still shows only three features of dimer, tetramer and hexamer, while the pure Aβ42 shows very noisy ATD containing dimer, tetramer, hexamer, decamer and dodecamer

(Figure 3.4). These results show that PADK effectively inhibits the formation of Aβ42 oligomers, especially the hexamer and dodecamer formation.

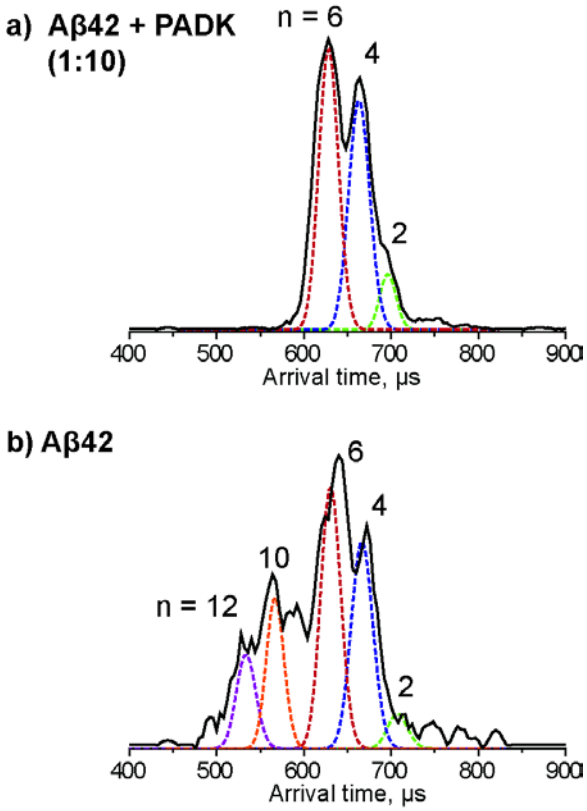

Figure 3.4 ATDs of the z/n = -5/2 peaks for the Aβ42 sample with and without PADK on the second day. The oligomer number (n) of each feature is noted.

To explore the interactions of PADK with Aβ42 oligomers, the ATDs of the z/n = -5/2 Aβ42-PADK oligomer complexes were recorded and shown in Figure 3.5. The [2 + 1] complex (m/z = 1884) shows only three features with arrival times at ~750, 700 and 640 μs, which are assigned as Aβ42 dimer, tetramer and hexamer based on their cross sections, suggesting there is one, two and three PADK molecules complexed with Aβ42 dimer, tetramer and hexamer, respectively. The signal of the [2 + 2] species (m/z = 1963) is relatively lower than that of [2 + 1] species, however, we managed to obtain its ATD (Figure

3.5b). The ATD is slightly noisy but still only shows three features corresponding to Aβ42 dimer, tetramer and hexamer complexed with two, four and six PADK molecules, respectively. The results of these Aβ42 oligomer complexes indicate that PADK not only binds to Aβ42 monomer but also binds to Aβ42 dimer, tetramer and hexamer, and therefore inhibits the formation of dodecamer.

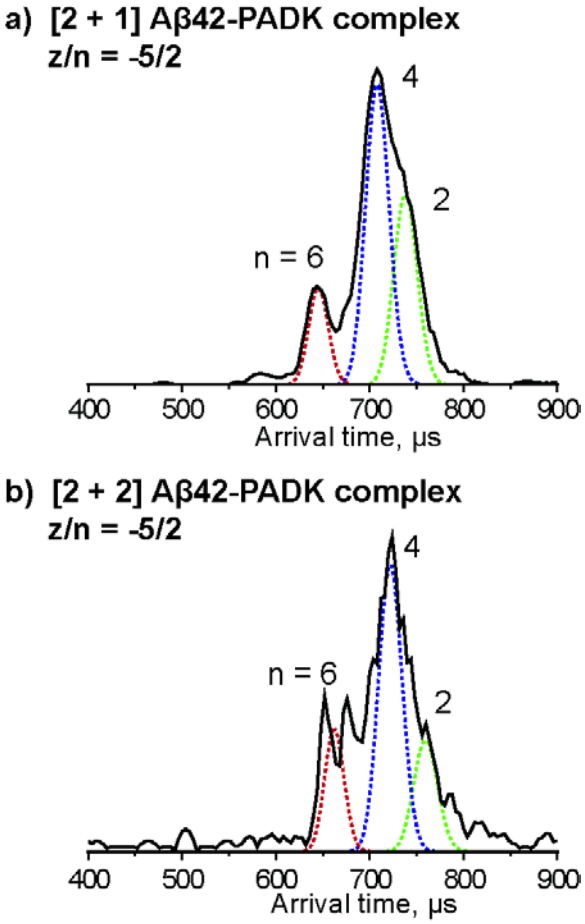

Figure 3.5 The ATDs of the z/n = -5/2 peaks for Aβ42 and Aβ42 oligomer complexes recorded at different injection energies. The oligomer number (n) is noted for each feature.

To assign the peaks in ATDs unambiguously and better understand the Aβ42 oligomer distributions, the ATDs of the z/n = -5/2 peaks for the 1:10 mixtures were recorded

under different injection energies and are shown in Figure 3.6. The injection energy of the ions can be varied from ~20 to ~150 eV. At low injection energy, the ions are rapidly thermalized by cooling collisions with the helium gas in the drift cell and therefore large complexes can be preserved through the process. At high injection energy, the ions are given sufficient energy to lead to internal excitation which can cause isomerization into low energy structure or dissociation of large noncovalent complexes into smaller species. At lower injection energy (Figure 3.6a, top panel, IE = 40 eV), the ATD for the z/n = -5/2 Aβ42 oligomer show a dominant tetramer, a relatively lower hexamer and a minor dimer. At high injection energy (Figure 3.6a, bottom panel, IE = 100 eV), the hexamer feature disappears while the dimer and tetramer features increase and become dominant peaks. This suggests the hexamer species were dissociated into smaller oligomers. Similar trend is observed for ATDs of [2 + 1] and [2 + 2] oligomer complexes. Through such injection energy study, we can unambiguously assign the three features in ATDs of the z/n = -5/2 oligomer and complexes for the Aβ42 and PADK mixture as dimer, tetramer and hexamer and their PADK complexes. Indeed PADK binds to Aβ42 small oligomers and inhibits the formation of dodecamer.

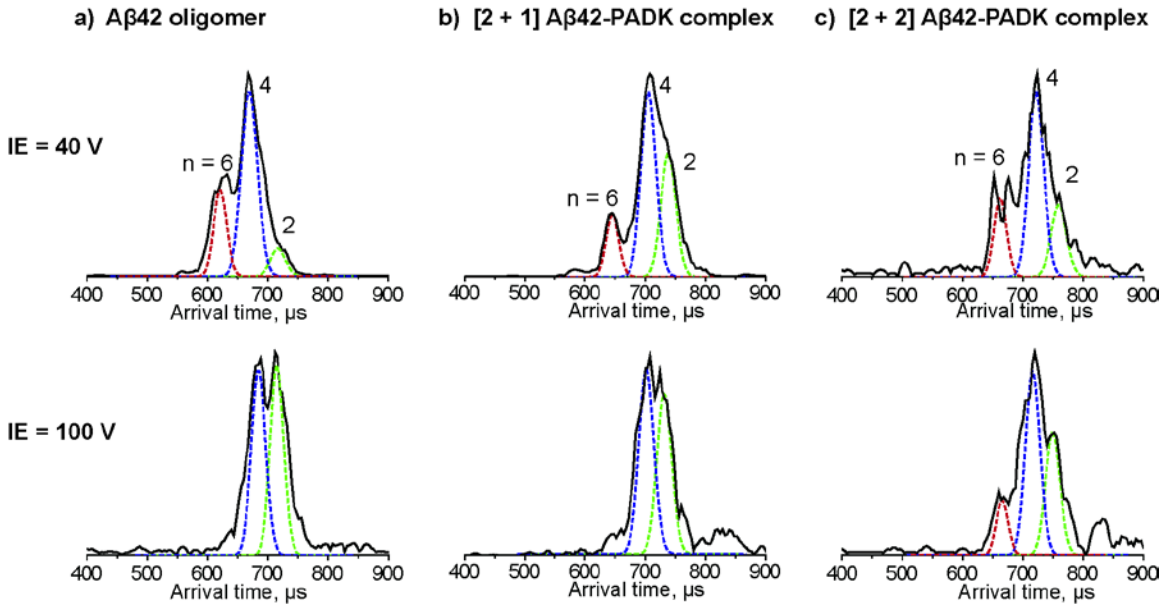

Figure 3.6 ATDs of the z/n = -5/2 Aβ42 oligomer peaks for the 1:10 mixture of Aβ42 and PADK recorded under different injection energies (40 eV and 100 eV). The oligomer number (n) of each feature is noted. With higher injection energy, the intensity of the hexamer feature decreases and the dimer feature increases, suggesting the larger oligomers dissociated into smaller oligomer when given enough energy.

3.3.3 PADK remodels Aβ42 early assembly

To explore whether PADK is able to remodel Aβ42 oligomerization, the pure Aβ42 sample was prepared and incubated to allow the formation of oligomers, and concentrated PADK was added to the sample and ATD of the z/n = -5/2 was monitored over time. As shown in Figure 3.7a, the ATD of the -5/2 peak for the Aβ42 samples after ~5 hours' incubation on ice forms dimer, tetramer, hexamer and dodecamer. Immediately following the addition of 1:10 PADK, the ATD of z/n = -5/2 Aβ42 peak shows only three features of dimer, tetramer and hexamer, with the absence of dodecamer. This is significant and suggests that PADK is able to remove preformed Aβ42 dodecamers. As the incubation time increases, the relative intensity of the hexamer feature decreases, suggesting PADK also

removes preformed hexamers. These results suggest that PADK not only inhibit the formation of dodecamer and hexamer, but also disaggregates preformed dodecamer and hexamer. These results are of significance and consistent with our previously reported results.[38]

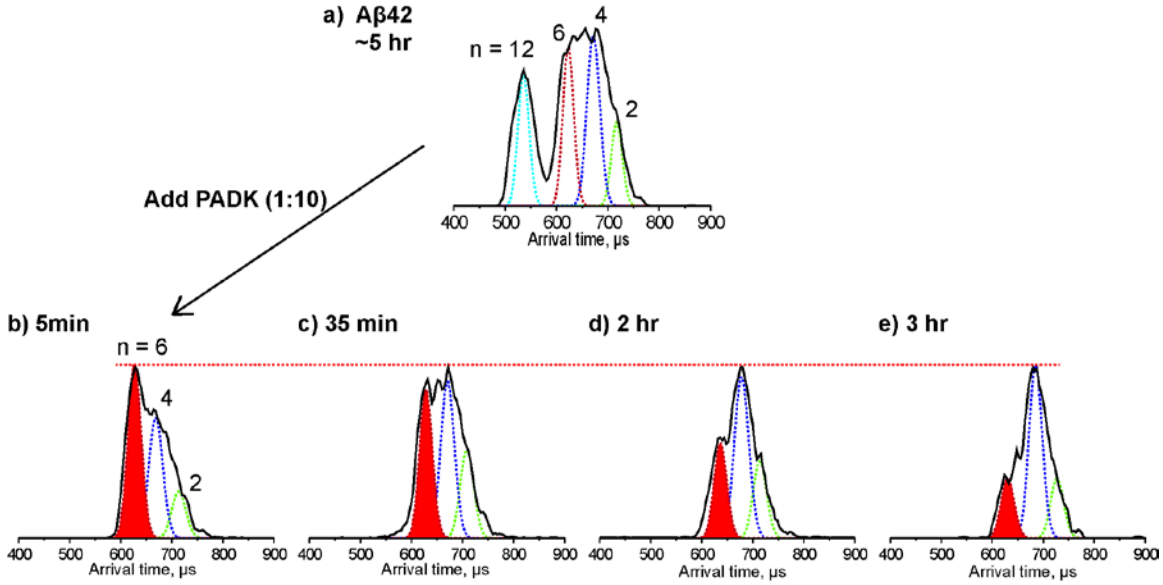

Figure 3.7 A time-dependent study of PADK remodeling preformed Aβ42 oligomers. a-e) ATDs of the z/n = -5/2 peaks of for the Aβ42 sample before and after the addition of PADK. The oligomer number (n) is noted for each feature.

3.3.4 PADK inhibits Aβ42 fibril formation

To explore whether PADK has positive effect on Aβ42 fibril formation, the Aβ42 samples after IMS studies were kept in a 4 °C refrigerator for two weeks and examined by transmission electron microscope (TEM). As shown in Figure 3.8, the Aβ42 sample without PADK shows long fibrils. The Aβ42 sample with 1:10 PADK presents shows almost no fibrils, indicating PADK inhibits fibril formation. However, the sample with 1:1 PADK still

shows some fibrils, indicating a low concentration of PADK does not stop the Aβ42 fibril formation.

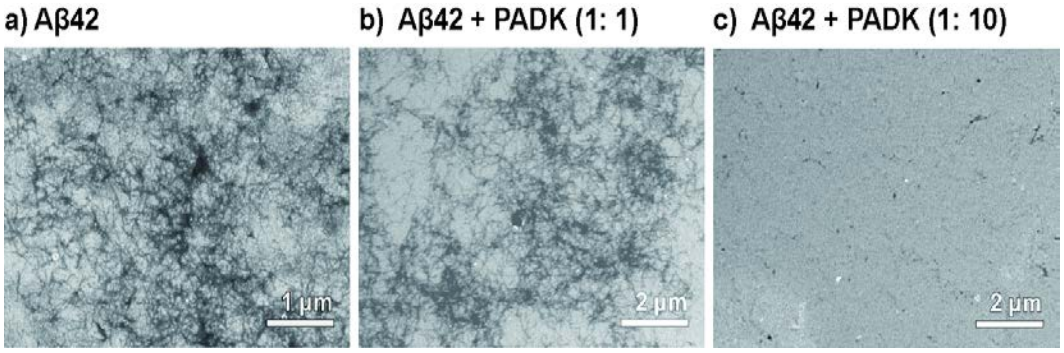

Figure 3.8 TEM images of Aβ42 samples without and with PADK. The scale bar is indicated for each image.

3.3.5 Molecular dynamics simulations: Insight into the detail of PADK-Aβ42 interactions

To understand the binding interactions of PADK molecule with Aβ42 at an atomic level, all-atom molecular dynamics (MD) binding simulations were performed by constructing a system consisting of one PADK and one Aβ42 molecule. The most populated conformation of Aβ42 peptide from previous study (Figure 3.9a) was used as the initial conformation in our simulations to enable efficient sampling of the most important conformations.[39]

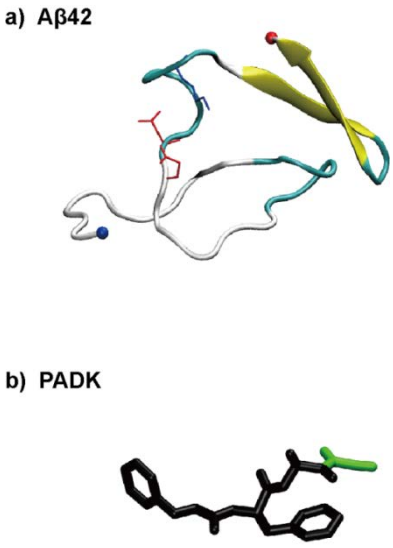

Figure 3.9 The starting structures of Aβ42 (derived from previous study) and PADK. The side-chains of E22, D23 and K28 are shown (blue: positively charged, red: negatively charged). The α-helical, 3-10-helical, β-extended, β-bridged, turn and coiled conformations are colored in purple, blue, yellow, tan, cyan and white. The positively charged N-termini and negatively charged C-termini are indicated by blue and red balls, respectively.

To visualize the overall binding, we superimposed the stable complexes (those with atom contacts > 20) identified from the trajectories in Figure 3.10. The widespread cloud of the overall protein backbones (grey) suggests Aβ42 protein in the complexes has great flexibility, which is expected as the Aβ42 protein is natively disordered. As shown in the overlapped complex structures (Figure 3.10), PADK (cyan balls) binds to multiple sites of Aβ42, including the C-terminal, central hydrophobic core and the N-terminal regions. This suggests PADK interacts with Aβ42 through multiple modes which might contribute to its effective inhibitory activity.

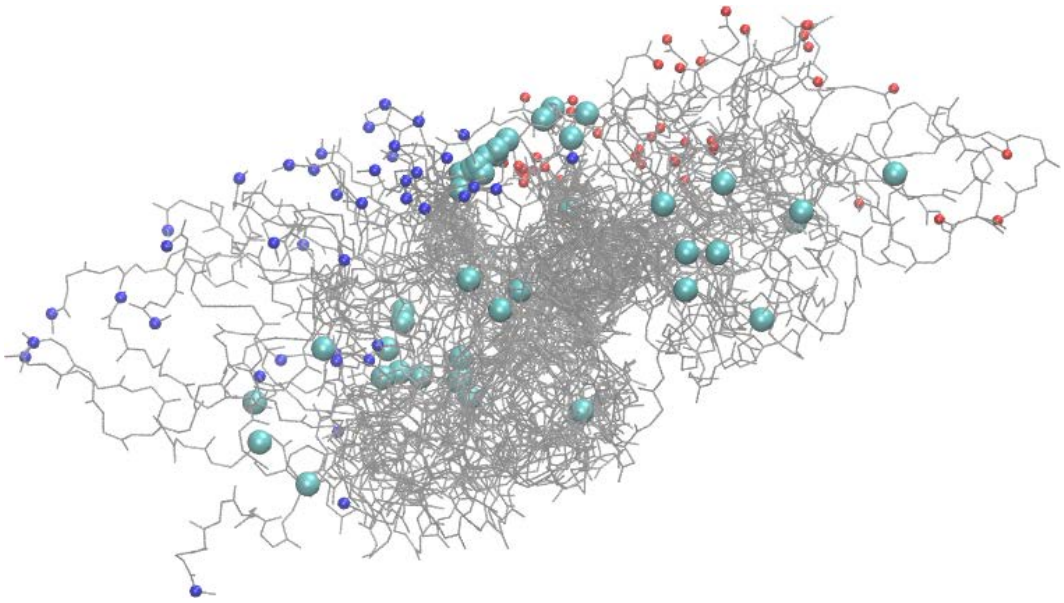

Figure 3.10 Binding interactions of PADK and Aβ42: Superposition of the complexes, where the protein backbones are represented by the grey lines and the PADK are noted with the larger cyan balls. The positively charged N-termini and negatively charged C-termini are noted with small blue and red balls, respectively.

To gain further insight into the different binding modes of PADK to Aβ42, the stable complexes were classified into different structure families. The centroids of the top structural families (>4% of the population) for the Aβ42-PADK complexes are shown in Figure 3.11. The collision cross section of each structure was calculated and listed together with the structures. The top eight structural families (Figure 3.11 A-F) comprise 83% of the total stable complex snapshots.

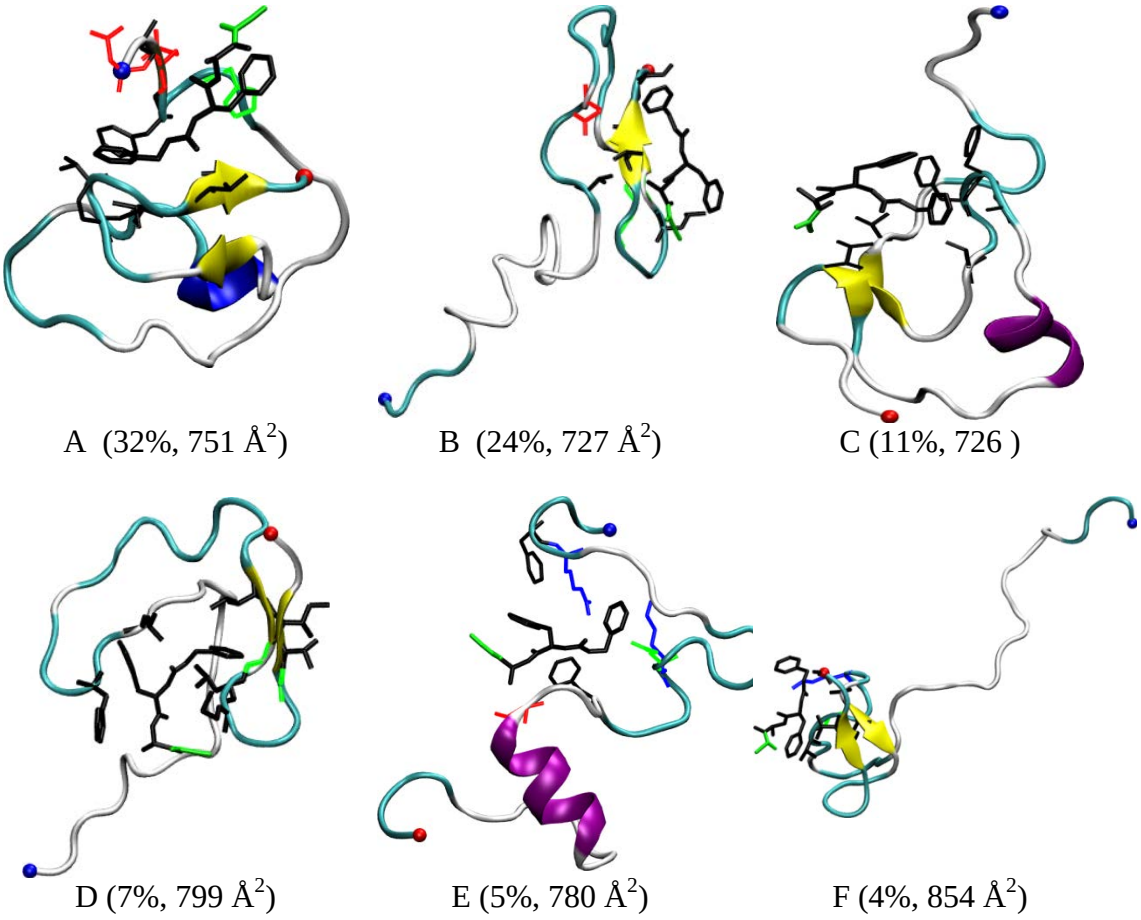

Figure 3.11 Representative structures of the Aβ42-PADK complexes from the most populated structural families (A-F). Only the side-chains in contact with PADK are shown (blue: positively charged, red: negatively charged and black: hydrophobic). The backbone of PADK is also in black. α-helical, 3-10-helical, β-extended, β-bridged, turn and coiled conformations of Aβ42 are colored in purple, blue, yellow, tan, cyan and white. The positively charged N-termini and negatively charged C-termini are indicated by blue and red balls respectively. The abundance is noted below each structure.

To facilitate visualization, the 2D interaction diagrams are plotted in Figure 3.12 for the representative structures of the top three structural families. Several notable features are observed: (1) PADK molecule adopts an extended conformation, interacting fully (B) or partially (A and C) with the C-terminal β-strands of Aβ42. Because the C-terminal β-strands play a critical role in the Aβ42 oligomerization, the interaction with PADK would interrupt

the oligomerization and thus reduces the toxicity. (2) Intermolecular hydrogen bonds are formed between the backbone of PADK and Aβ42 in A and B. As shown in model A, PADK forms three hydrogen bonds with residues Asp2, Glu3 (2 hydrogen bonds formed) in the N-terminal region and one with Val40 on the C-terminal region. In structure B, PADK forms two hydrogen bonds with Leu34 and Val39 on the C-terminal region. These intermolecular interactions suggest that PADK fully interacts with Aβ42, not only with C-terminal but also with N-terminal region. (3) The π-π interactions are also observed in A (PHE 4 and HIE 6) and C (PHEs 4, 19 and 20). (4) Hydrophobic contacts are observed in A-C.

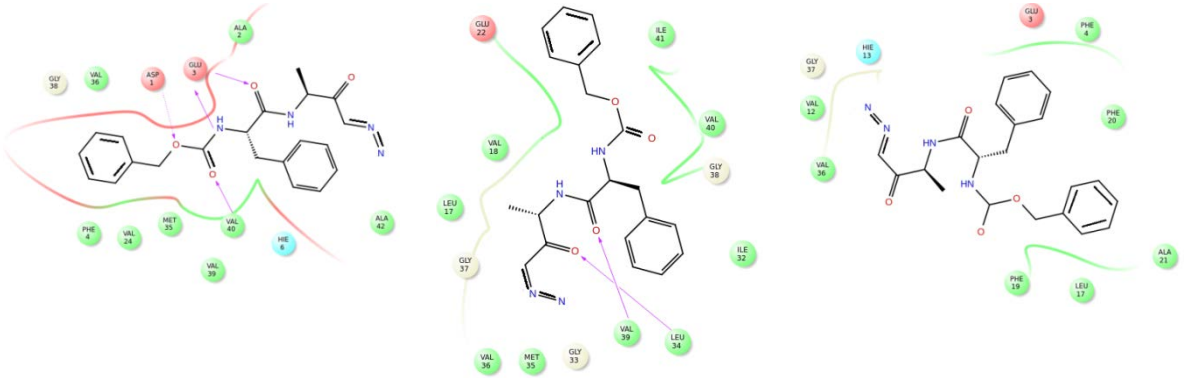

A (32%, 751 Å^2) **B** (24%, 727 Å^2) **C** (11%, 726 Å^2)

Figure 3.12 2D interaction diagrams of the Aβ42-PADK complexes from the top three populated structural families (Figure 3.11A-C). The abundance and the collision cross section are noted. The amino acid residues of Aβ42 are noted with balls that are labeled with three letter and position in Aβ42 sequence, intermolecular H-bonds are indicated by purple arrows. HIE is neutral Histidine with hydrogen on epsilon nitrogen.

3.3.6 The structure of monomer complex

The z/n = -3 Aβ42 monomer and monomer complexes were measured and the results are shown in Figure 3.13. The ATD of Aβ42 monomer shows two features which were previously assigned as a gas-phase compact conformer (M_1) and a solution-like conformer (M_2)[17]. The ATD of Aβ42 monomer with one PADK bound shows two similar features. By analog, they can be assigned as gas-phase conformer and solution-like conformer. The cross sections were measured and show ~7-9% increase in size after the addition of one PADK (Table 3.1), which suggests the binding of PADK to Aβ42 makes it more extended. The experimental cross section for the solution-like structure of [1+1] complex is similar to the theoretical values for the three populated structures from our simulation results, especially the most populated structure (751 $Å^2$, Figure 3.11a). This suggests our simulation results are consistent with our experiment results.

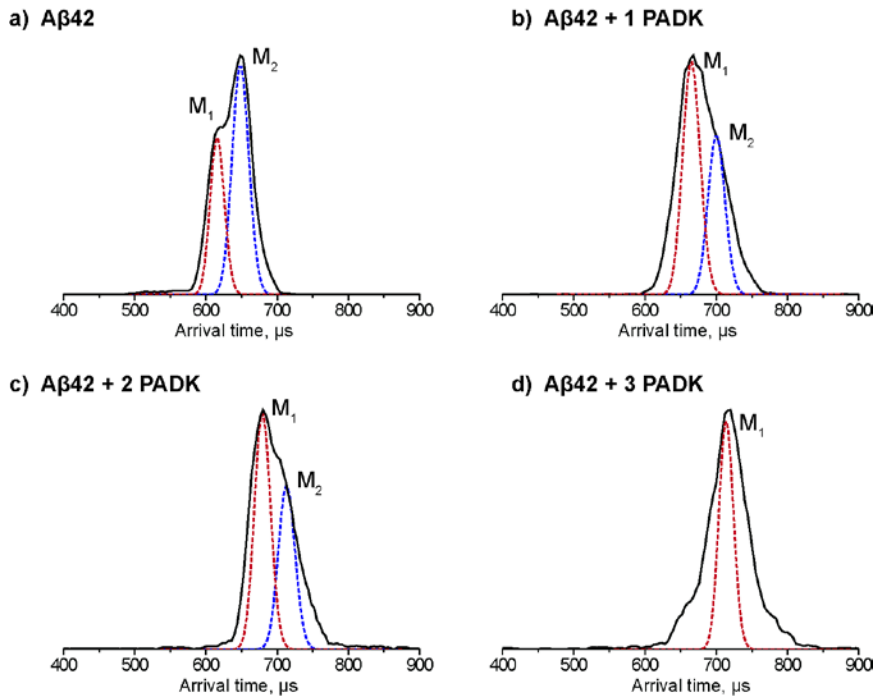

Figure 3.13 The ATDs of z/n = -3 monomer and complex. M_1 and M_2 represent two monomer conformers for Aβ42.

Table 3.1. Cross sections of z/n = -3 Aβ42-PADK complexes. The error of the cross sections is within 1%.

	Charge	Cross sections(σ, Å^2)	
Aβ42	-3	643	702
Aβ42 + 1 PADK	-3	688	765
Aβ42 + 2 PADK	-3	739	835
Aβ42 + 3 PADK	-3	759	879

3.4 Discussion and Conclusions

PADK has been shown to be a potent lysosomal enzyme up-regulator which results in enhanced Aβ clearance and offsets Aβ-induced toxicity.[14] In this work, we investigate the direct effects of PADK on Aβ42 aggregation on molecular level and probe with theoretical study to understand their interactions on atomic level.

Our mass spectrometry analysis shows that PADK binds to Aβ42 monomer and small oligomers (dimer, tetramer and hexamer). Up to four PADK molecules were observed to bind to Aβ42 monomer with relative abundant intensities, suggesting that PADK bind to Aβ42 with relatively high affinity. Moreover, two z/n = -5/2 oligomer complex peaks were observed, indicating PADK not only binds to Aβ42 monomer but also binds to Aβ42 small oligomers. Notably, the relative intensity of the z/n = -5/2 peak is significantly lower in the 1:10 mixture of Aβ42 and PADK than that in the pure Aβ42 sample or the 1:1 mixture, suggesting that the oligomer formation is inhibited by PADK and the inhibitory ability of PADK increases as the concentration increases.

Notably, our ion mobility study of the z/n = -5/2 peak for the Aβ42 samples with PADK presence only shows dimer, tetramer and hexamer, with the absence of dodecamer, indicating that PADK inhibits the formation of dodecamer. In addition, the intensity of the hexamer is lowered in the 1:10 mixture, suggesting that PADK also partially inhibits the formation of hexamer. The ATDs of the z/n = -5/2 oligomer complexes show only dimer, tetramer and hexamer, suggesting PADK also binds to Aβ42 small oligomers and thereby inhibits the dodecamer formation. Our ion mobility studies also show that PADK is able to completely dissociate preformed Aβ42 dodecamers. Moreover, the relative intensity of the hexamer decreases over time of incubation, suggesting PADK is also able to dissociate preformed hexamers slowly over time and reverse the aggregation equilibrium toward smaller oligomers. These results are of significance and consistent with the previous study that showed PADK has positive effect in reducing the Aβ42 level in the brain of the transgenic AD mouse model, which in turn offset the cognitive deficit. Our study suggests that these positive effects of PADK in AD do not only result from the important role of PADK as a lysosomal enzyme up-regulator, but also result from the direct interactions of PADK with Aβ42 molecules modulating its aggregation.

Our all-atom MD simulation study showed that PADK binds to Aβ42 on several regions, including the C-terminal, N-terminal and Central regions. The C-terminal region of Aβ42 has been shown to be critical for Aβ assembly and aggregation. Therefore to disrupt the conformation of the region and alter Aβ42 assembly is a promising strategy. The most populated structure families obtained from MD simulations show that PADK adopts an extended conformation which fully interacts with the C-terminal β-strand of Aβ42. Moreover, PADK also forms intermolecular hydrogen bonds with the residues on the C-

terminal region, suggesting the interactions in the C-terminal regions are of significance for PADK's inhibitory activity. It is very likely that PADK disrupts the structure of the C-terminal region and thereby disrupts Aβ42 assembly and aggregation.

Aromatic interactions have been shown to play an important role in the binding interactions of Aβ protein and its inhibitors[12]. We expected such interactions to be important for PADK's inhibitory activity because it contains two aromatic groups. Our MD simulation results suggest that PADK interacts with the aromatic residues in Aβ42 through π-π interactions. Such interactions are notable in the N-terminal and central regions, PHE 4 and HIE 6 in structure A and PHEs 4, 19 and 20 in structure C (Figure 3.12), which are expected as these regions contain a high content of aromatic residues. Hydrophobic interactions are observed through the most populated structures, suggesting they are important for PADK interacting with Aβ42. Taken together, our MD simulations suggest that PADK interacts with Aβ42 through multiple modes on multiple sites which disrupt Aβ42 folding and assembly and thereby inhibits the formation of toxic oligomers.

Overall, our ion mobility studies reveal the direct positive effects of PADK on Aβ42 oligomerization and MD simulations suggest multiple interaction modes contribute to the structure-function relationship for PADK's inhibitory activity. This study provides an example of PADK as an effective small molecule inhibitor for Aβ42 aggregation and toxicity and sheds lights on the further development of small molecule therapeutic discovery. This study also demonstrated that ion mobility spectrometry combined with theoretical simulations has become a powerful tool in the discovery and understanding of small molecule inhibitors for Aβ and AD treatment.

References

1. Kirkitadze, M. D.; Bitan, G.; Teplow, D. B. (2002) Paradigm shifts in Alzheimer's disease and other neuro degenerative disorders: The emerging role of oligomeric assemblies. *J. Neurosci. Res. 69*, 567-577.

2. Teplow, D. (2013) On the Subject of Rigor in the Study of Amyloid β-Protein Assembly. *Alzheimer's Res. Ther. 5*, 39.

3. Ono, K.; Condron, M. M.; Teplow, D. B. (2009) Structure-neurotoxicity relationships of amyloid beta-protein oligomers. *Proc. Natl. Acad. Sci. U. S. A. 106*, 14745-14750.

4. Bitan, G.; Kirkitadze, M. D.; Lomakin, A.; Vollers, S. S.; Benedek, G. B.; Teplow, D. B. (2003) Amyloid beta-protein (A beta) assembly: A beta 40 and A beta 42 oligomerize through distinct pathways. *Proc. Natl. Acad. Sci. U. S. A. 100*, 330-335.

5. Bernstein, S. L.; Dupuis, N. F.; Lazo, N. D.; Wyttenbach, T.; Condron, M. M.; Bitan, G.; Teplow, D. B.; Shea, J.-E.; Ruotolo, B. T.; Robinson, C. V., et al. (2009) Amyloid-beta protein oligomerization and the importance of tetramers and dodecamers in the aetiology of Alzheimer's disease. *Nat. Chem. 1*, 326-331.

6. Gong, Y.; Chang, L.; Viola, K. L.; Lacor, P. N.; Lambert, M. P.; Finch, C. E.; Krafft, G. A.; Klein, W. L. (2003) Alzheimer's disease-affected brain: presence of oligomeric Aβ ligands (ADDLs) suggests a molecular basis for reversible memory loss. *Proc. Natl. Acad. Sci. U. S. A. 100*, 10417-10422.

7. Lesne, S.; Koh, M. T.; Kotilinek, L.; Kayed, R.; Glabe, C. G.; Yang, A.; Gallagher, M.; Ashe, K. H. (2006) A specific amyloid-beta protein assembly in the brain impairs memory. *Nature 440*, 352-357.

8. Hawkes, C. A.; Ng, V.; McLaurin, J. (2009) Small Molecule Inhibitors of A beta-Aggregation and Neurotoxicity. *Drug Develop. Res. 70*, 111-124.

9. Re, F.; Airoldi, C.; Zona, C.; Masserini, M.; La Ferla, B.; Quattrocchi, N.; Nicotra, F. (2010) Beta Amyloid Aggregation Inhibitors: Small Molecules as Candidate Drugs for Therapy of Alzheimer's Disease. *Curr. Med. Chem. 17*, 2990-3006.

10. Ehrnhoefer, D. E.; Bieschke, J.; Boeddrich, A.; Herbst, M.; Masino, L.; Lurz, R.; Engemann, S.; Pastore, A.; Wanker, E. E. (2008) EGCG redirects amyloidogenic polypeptides into unstructured, off-pathway oligomers. *Nat. Struct. Mol. Biol. 15*, 558-566.

11. Yang, F. S.; Lim, G. P.; Begum, A. N.; Ubeda, O. J.; Simmons, M. R.; Ambegaokar, S. S.; Chen, P. P.; Kayed, R.; Glabe, C. G.; Frautschy, S. A., et al. (2005) Curcumin inhibits formation of amyloid beta oligomers and fibrils, binds plaques, and reduces amyloid in vivo. *J. Biol. Chem. 280*, 5892-5901.

12. Porat, Y.; Abramowitz, A.; Gazit, E. (2006) Inhibition of amyloid fibril formation by polyphenols: Structural similarity and aromatic interactions as a common inhibition mechanism. *Chem. Biol. Drug Design 67*, 27-37.

13. Bahr, B. A.; Wisniewski, M. L.; Butler, D. (2012) Positive Lysosomal Modulation As a Unique Strategy to Treat Age-Related Protein Accumulation Diseases. *Rejuvenation Research 15*, 189-197.

14. Butler, D.; Hwang, J.; Estick, C.; Nishiyama, A.; Kumar, S. S.; Baveghems, C.; Young-Oxendine, H. B.; Wisniewski, M. L.; Charalambides, A.; Bahr, B. A. (2011) Protective Effects of Positive Lysosomal Modulation in Alzheimer's Disease Transgenic Mouse Models. *PLoS ONE 6*, e20501.

15. Wyttenbach, T.; Bowers, M. T. (2003) Gas-Phase Conformations: The Ion Mobility/Ion Chromatography Method. In *Modern Mass Spectrometry* (Schalley, C., Ed.), pp 207-232, Springer Berlin Heidelberg.

16. Bernstein, S. L.; Wyttenbach, T.; Baumketner, A.; Shea, J.-E.; Bitan, G.; Teplow, D. B.; Bowers, M. T. (2005) Amyloid β-Protein: Monomer Structure and Early Aggregation States of Aβ42 and Its Pro19 Alloform. *J. Am. Chem. Soc. 127*, 2075-2084.

17. Baumketner, A.; Bernstein, S. L.; Wyttenbach, T.; Bitan, G.; Teplow, D. B.; Bowers, M. T.; Shea, J.-E. (2006) Amyloid β-protein monomer structure: A computational and experimental study. *Protein Science 15*, 420-428.

18. Bleiholder, C.; Dupuis, N. F.; Wyttenbach, T.; Bowers, M. T. (2011) Ion mobility-mass spectrometry reveals a conformational conversion from random assembly to beta-sheet in amyloid fibril formation. *Nat. Chem. 3*, 172-177.

19. Gessel, M. M.; Wu, C.; Li, H.; Bitan, G.; Shea, J.-E.; Bowers, M. T. (2011) Aβ(39–42) Modulates Aβ Oligomerization but Not Fibril Formation. *Biochemistry 51*, 108-117.

20. Lomakin, A.; Chung, D. S.; Benedek, G. B.; Kirschner, D. A.; Teplow, D. B. (1996) On the nucleation and growth of amyloid beta-protein fibrils: Detection of nuclei and quantitation of rate constants. *Proc. Natl. Acad. Sci. U. S. A. 93*, 1125-1129.

21. Sgourakis, N. G.; Yan, Y. L.; McCallum, S. A.; Wang, C. Y.; Garcia, A. E. (2007) The Alzheimer's peptides Aβ40 and 42 adopt distinct conformations in water: A combined MD/NMR study. *J. Mol. Biol. 368*, 1448-1457.

22. Duan, Y.; Chowdhury, S.; Xiong, G.; Wu, C.; Zhang, W.; Lee, T.; Cieplak, P.; Caldwell, J.; Luo, R.; Wang, J., et al. (2003) A point-charge force field for molecular mechanics simulations of proteins based on condensed-phase QM calculations. *Journal of Computational Chemistry 24*, 1999-2012.

23. Li, H.; Du, Z.; Lopes, D. H. J.; Fradinger, E. A.; Wang, C.; Bitan, G. (2011) C-terminal tetrapeptides inhibit Aβ42-induced neurotoxicity primarily through specific interaction at the n-terminus of Aβ42. *Journal of Medicinal Chemistry 54*, 8451-8460.

24. Wu, C.; Bowers, M. T.; Shea, J. E. (2010) Molecular Structures of Quiescently Grown and Brain-Derived Polymorphic Fibrils of the Alzheimer Amyloid A beta(9-40) Peptide: A Comparison to Agitated Fibrils. *Plos Computational Biology 6*.

25. Wu, C.; Wang, Z. X.; Lei, H. X.; Zhang, W.; Duan, Y. (2007) Dual binding modes of Congo red to amyloid protofibril surface observed in molecular dynamics simulations. *J. Am. Chem. Soc. 129*, 1225-1232.

26. Jorgensen, W. L.; Chandrasekhar, J.; Madura, J. D.; Impey, R. W.; Klein, M. L. (1983) Comparisons of simple potential functions for simulating liquid water. *Journal of Chemical Physics 79*, 926-935.

27. Wang, J. M.; Wolf, R. M.; Caldwell, J. W.; Kollman, P. A.; Case, D. A. (2004) Development and testing of a general amber force field. *Journal of Computational Chemistry 25*, 1157-1174.

28. Essmann, U.; Perera, L.; Berkowitz, M. L.; Darden, T. A.; Lee, H.; Pedersen, L. G. (1995) A smooth particle mesh Ewald method. *Journal of Chemical Physics 103*, 8577-8593.

29. Ryckaert, J.-P.; Ciccotti, G.; Berendsen, H. J. C. (1977) Numerical Integration of the Cartesian Equations of Motion of a System with Constraints: Molecular Dynamics of n-Alkanes. *Journal of Chemical Physics 23*, 327-341.

30. Procacci, P.; Berne, B. J. (1994) Multiple time-scale methods for constant-pressure molecular-dynamics simulations of molecular-systems. *Molec. Phys. 83*, 255-272.

31. Chiu, S. W.; Clark, M.; Subramaniam, S.; Jakobsson, E. (2000) Collective motion artifacts arising in long-duration molecular dynamics simulations. *Journal of Computational Chemistry 21*, 121-131.

32. Harvey, S. C.; Tan, R. K. Z.; Cheatham, T. E. (1998) The flying ice cube: Velocity rescaling in molecular dynamics leads to violation of energy equipartition. *Journal of Computational Chemistry 19*, 726-740.

33. Daura, X.; Gademann, K.; Jaun, B.; Seebach, D.; van Gunsteren, W. F.; Mark, A. E. (1999) Peptide folding: When simulation meets experiment. *Angew. Chem., Int. Ed. 38*, 236-240.

34. Bleiholder, C.; Wyttenbach, T.; Bowers, M. T. (2011) A novel projection approximation algorithm for the fast and accurate computation of molecular collision cross sections (I). Method. *International Journal of Mass Spectrometry 308*, 1-10.

35. Bleiholder, C.; Contreras, S.; Do, T. D.; Bowers, M. T. (2013) A novel projection approximation algorithm for the fast and accurate computation of molecular collision cross sections (II). Model parameterization and definition of empirical shape factors for proteins. *International Journal of Mass Spectrometry 345–347*, 89-96.

36. Anderson, S. E.; Bleiholder, C.; Brocker, E. R.; Stang, P. J.; Bowers, M. T. (2012) A novel projection approximation algorithm for the fast and accurate computation of molecular collision cross sections (III): Application to supramolecular coordination-driven assemblies with complex shapes. *International Journal of Mass Spectrometry 330–332*, 78-84.

37. Bleiholder, C.; Contreras, S.; Bowers, M. T. (2013) A novel projection approximation algorithm for the fast and accurate computation of molecular collision cross sections (IV). Application to polypeptides. *International Journal of Mass Spectrometry 354–355*, 275-280.

38. Zheng, X.; Gessel, M. M.; Wisniewski, M. L.; Viswanathan, K.; Wright, D. L.; Bahr, B. A.; Bowers, M. T. (2012) Z-Phe-Ala-diazomethylketone (PADK) Disrupts and Remodels Early Oligomer States of the Alzheimer Disease Aβ42 Protein. *Journal of Biological Chemistry 287*, 6084-6088.

39. Sgourakis, N. G.; Yan, Y.; McCallum, S. A.; Wang, C.; Garcia, A. E. (2007) The Alzheimer's Peptides Aβ40 and 42 Adopt Distinct Conformations in Water: A Combined MD / NMR Study. *J. Mol. Biol. 368*, 1448-1457.

Chapter 4

Mechanism of C-Terminal Fragments of Amyloid β-Protein as Effective Aβ Inhibitors: Do C-Terminal Interactions Play a Key Role in Their Inhibitory Activity?

4.1 Introduction

Short peptides derived from Aβ sequence itself, and their derivatives have been shown to disrupt Aβ assembly and inhibit its toxicity.[1-2] The C-terminal region of Aβ42, which is highly hydrophobic, has been shown to play an important role in controlling Aβ structure stability and self-assembly.[3-4] Thus researchers hypothesized that peptides derived from the C-terminus of Aβ42 can serve as Aβ inhibitors as they may interact with C-terminal hydrophobic region of Aβ and be coassembled into Aβ42 oligomers, and thereby disrupt their structures and inhibit their toxicity.[5] Indeed this C-terminal interaction hypothesis has leaded to the discovery of several effective C-terminal fragment (CTF) inhibitors for Aβ42 neurotoxicity, including peptides ranging from Aβ(29-42) to Aβ(39-42).[5]

Aβ(39-42), the shortest peptide studied, was shown to modulate Aβ oligomerization and inhibit Aβ neurotoxicity.[6-7] It is particularly interesting because it is a small molecule which can easily penetrate into the membrane barriers. Thus it is very important to understand the mechanism of its inhibitory activity for its future drug development and other peptidomimetics based drug discovery. Previous theoretical study showed that Aβ(39-42) binds to several regions of Aβ42, including the N-terminal, central hydrophobic core and the C-terminal regions.[6] However, interaction with which region is the key for its inhibition activity remains unclear. To better understand the mechanism of action for Aβ(39-42), two terminal modified Aβ(39-42) analogs, N-terminal acetylated Ac-VVIA and C-terminal amidated VVIA-NH_2, were designed to test the charge effect on the interactions of Aβ(39-42) and Aβ42. Previous studies have shown that modifications at the terminus has very

different effects on Aβ toxicity: VVIA-NH_2 inhibits Aβ-induced toxicity while Ac-VVIA does not.[7]

Here, ion mobility spectrometry coupled mass spectrometry (IMS-MS) and all-atom molecular dynamics (MD) simulations were used to investigate the interactions between these two Aβ(39-42) analogs and the full length Aβ42. This study provides an example of ion mobility spectrometry combined with theoretical modeling as a powerful tool to understand the mechanism of Aβ C-terminal fragments as small molecule inhibitors for Aβ assembly and sheds light on the future peptidomimetics based therapeutic strategy for AD and other diseases.

4.2 Experimental Procedures

Peptides and Sample Preparation:

Full-length Aβ42 was synthesized by *N*-9-fluorenylmethoxycarbonyl (FMOC) chemistry.[8] Aβ(39-42) derivatives were prepared using a microwave-assisted peptide synthesizer as described previously[7]. The peptides were purified by reverse-phase HPLC and their integrity validated by mass spectrometry and amino acid analysis.

***Ion Mobility Spectrometry-Mass Spectrometry (IMS-MS)*:**

Lyophilized Aβ42 protein was dissolved in 10 mM ammonium acetate buffer (pH 7.4) with a final protein concentration of 10 μM. Mass spectrometry and ion mobility measurements were performed on a home-built nanoESI instrument, which has been described in Chapter 2.3.

Transmission Electron Microscopy (TEM):

Microscopic analysis was performed by using a FEI T-20 transmission electron microscope under 200 kV. The Aβ42 samples were prepared under the same procedure as that for mass spectrometry analysis. The samples were kept in refrigerator (~4 °C) for 2 weeks. For TEM measurements, 10 μL aliquots of samples were spotted on glow-discharged, carbon-coated copper grids (Ted Pella, Inc). The samples on grids were stained with 10 mM sodium metatungstate aqueous solution for 10 min and gently rinsed twice with DI-water. The sample grids were then dried in room temperature before TEM analysis.

Molecular Dynamics Simulations:

System preparation: Our simulation systems contain one Aβ42 peptide and one Aβ(39-42) derivative (VVIA-NH2 or Ac-VVIA), ~8000 water molecules, and several Na^+ ions to neutralize the system. The initial peptide structures are the most abundant one from the previous study by Garcia and coworkers[3] for Aβ42, and from our own previous study[9] for Aβ(39–42). The Aβ(39-42) derivative is initially placed ~15 Å away from the Aβ42 surface. The solute is immersed in a truncated octahedral box ($a = b = c$ = ~69 Å, $\alpha = \beta = \gamma$ = 109.47º) filled with water molecules. The Duan *et al.* all-atom point-charge force field (AMBER ff03)[10] is used to represent the peptides. This force field has been successfully used to model the binding of Aβ(39–42) to Aβ40/ Aβ42 peptides[6-7], the binding between Aβ protofibrils,[11] and the binding of fluorescent dyes to Aβ protofibrils.[12] The water solvent was explicitly represented by the TIP3P[13] model.

Binding Simulations: The AMBER 9 simulation suite[14] is used in molecular dynamics simulations and data analysis. After an initial energy minimization, a total of eight simulations (four runs for each system) were performed with different initial random velocities. The random velocities of atoms are generated according to the Maxwell-

Boltzmann distribution at 500 K. A 10 ps run at 500 K is used to further randomize the orientations and positions of the two peptides. The production run (150 ns) is at 310 K, including a short, 1-ns molecular dynamics in the NPT ensemble mode (constant pressure and temperature) to equilibrate the solvent and 149-ns dynamics in the NVT ensemble mode (constant volume and temperature). Periodic boundary conditions are imposed on the system. The particle-mesh Ewald method[15] is used to treat the long-range electrostatic interactions. SHAKE[16] is applied to constrain all bonds connecting hydrogen atoms, enabling a 2-fs time step used in the dynamics. To reduce computation time, non-bonded forces are calculated using a two-stage RESPA approach[17] where the short-range forces within a 10 Å radius are updated every step and the long range forces beyond 10 Å are updated every two steps. The Langevin dynamics is used to control the temperature (310K) using a collision frequency of 1 ps^{-1}. The center of mass translation and rotation are removed every 500 steps, which removes the "block of ice" problem.[18-19] The trajectories were saved at 10-ps intervals for analysis. In total, 128 Opteron CPU cores (2.3 GHz) were used for ~50 days to complete the 8 binding simulations (a cumulative MD time of 1.2 μs for the two systems).

Clustering analysis: To gain a better understanding of the binding interactions, the stable complexes (atom contacts >20) are grouped into different structural families based on the Cα Root Mean Square Deviation (RMSD) of the complex (cutoff of 5 Å) using the GROMACS protocol.[20] Representative structures (centroids) of the top abundant clusters from the combined 4 runs of each system are shown in the Figures 4.8-4.9.

Collision Cross Section Calculation: The centroids of the top abundant clusters are also used to calculate their collision cross sections by a projected superposition approximation (PSA) method.[21-24] To correlate better with the solvent-free experiments,

these solution-phase structures are converted to ‘dehydrated’ structures via a 500,000-step energy minimization in vacuum prior to cross-section calculations. This “dehydration” generally reduces the overall size of the structures, while maintaining their solution structural features and in this paper these structures are referred to as “dehydrated solution structures”.

4.3 Results

4.3.1 Mass spectrometry: VVIA-NH_2 binds directly to Aβ42 monomer and oligomers

The mass spectra of Aβ42 samples with and without VVIA analogs were recorded and shown in Figure 4.1a-c. The mass spectrum of Aβ42 sample without VVIA analogs shows three peaks corresponding to the z/n = -4, -3, -5/2 charge states, where z is charge and n is oligomer number. In the mass spectrum of a 1:5 mixture of Aβ42 and VVIA-NH_2 (Figure 4.1a), there are more peaks in addition to the three Aβ42 peaks. These peaks correspond to z/n = -4 and -3 complexes of Aβ42 with one and two VVIA-NH_2 molecules bound (labeled with stars). Moreover, there is a peak tailing the z/n = -5/2 Aβ42 peak which corresponds to -5/2 complex of Aβ42 oligomers with VVIA-NH_2 molecules bound. This indicates VVIA-NH_2 binds directly not only to Aβ42 monomer but also to Aβ42 oligomers. The mass spectrum of a 1:5 mixture of Aβ42 and Ac-VVIA (Figure 4.1b) shows only one additional monomer complex peak, suggesting only one Ac-VVIA binds directly to Aβ42 monomer. These results suggest that VVIA-NH_2 binds directly to Aβ42 with relatively higher affinity than Ac-VVIA to Aβ42.

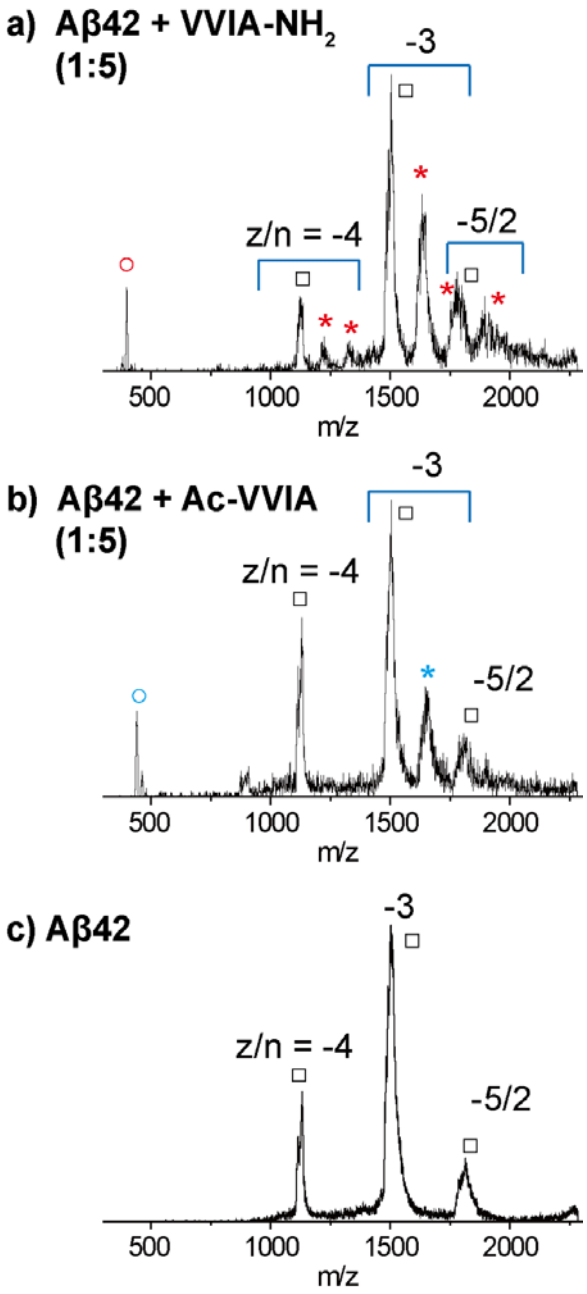

Figure 4.1 a-c) Mass spectra of Aβ42 samples with and without CTF molecules. The charge states of each species are labeled with z/n, where z is charge and n is oligomer number. The Aβ42 peaks are denoted with rectangle, CTF molecules are denoted with circles and the complexes of Aβ42 with CTF molecules are denoted with stars.

4.3.2 Ion mobility studies: VVIA-NH_2 and Ac-VVIA modulate the early assembly of Aβ42

To probe the effects of the two VVIA analogs on the early oligomer formation of Aβ42, an ion mobility study was performed and the results are shown in Figure 4.2. The ATD of the -5/2 peak for Aβ42 alone (Figure 4.2c) shows four features with arrival times at ~710, 680, 610 and 540 μs, which were previously assigned as Aβ42 dimer, tetramer, hexamer and dodecamer, respectively, based on their cross sections (see ref. 8 for a detailed discussion of -5/2 ATD assignment). The dodecamer was previously identified as a proximate toxic agent for AD pathology.[25-26] The ATD of the -5/2 peak for the Aβ42 sample with VVIA-NH_2 (1:5 ratio, Figure 4.2a) shows only three features with arrival times at ~720, 680, and 620 μs, which can be assigned as dimer, tetramer and hexamer, respectively, based on their cross sections. There is no feature with shorter arrival times, indicating there is no dodecamer or other larger oligomer formed with the presence of VVIA-NH_2. The ATD of the -5/2 peak for the Aβ42 and Ac-VVIA mixture (1:5 ratio, Figure 4.2b) shows three similar features corresponding to dimer, tetramer and hexamer, suggesting AC-VVIA also inhibits the formation of Aβ42 dodecamer.

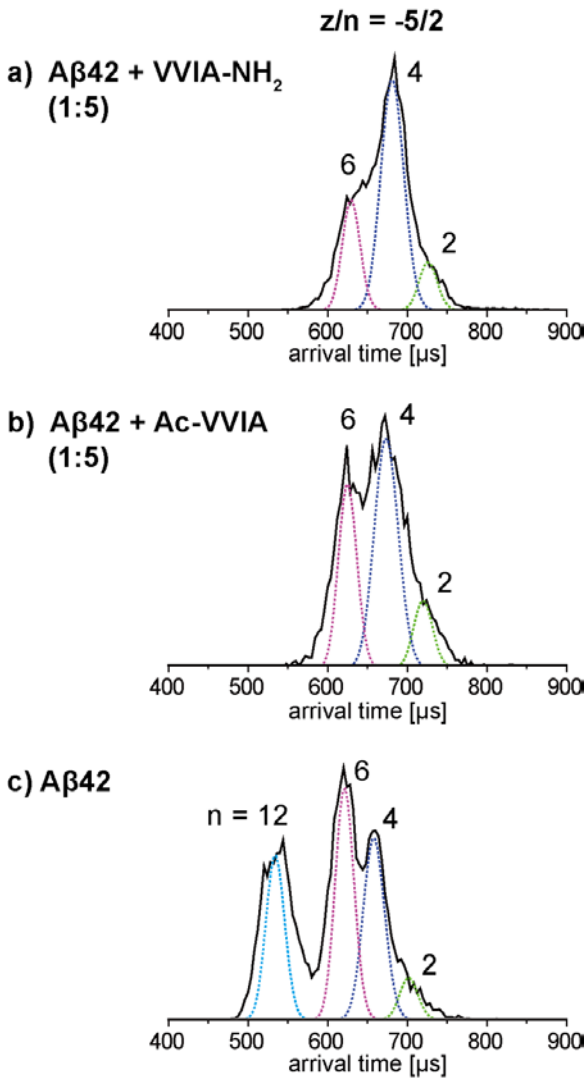

Figure 4.2 a-c) ATDs of the z/n = -5/2 peak for Aβ42 samples with and without CTF molecules. The oligomer number (n) is noted for each feature. The dashed lines represent the shape for a single structure favored in the ATD.

As shown in Figure 4.1a, an additional z/n = -5/2 oligomer complex peak was observed for the mixture of Aβ42 and VVIA-NH_2, therefore its ATD was also recorded to better understand the effect of VVIA-NH_2 on the Aβ42 oligomer distribution and the result is shown in Figure 4.3. The ATD shows three features with arrival times at ~750, 710 and 640 μs, which can be assigned as dimer, tetramer and hexamer complexes, respectively,

based on their cross sections. This is of significance and suggests there are one, two and three VVIA-NH_2 molecules binding to Aβ42 dimer, tetramer and Aβ42 hexamers, respectively, which is not observed for the sample with Ac-VVIA.

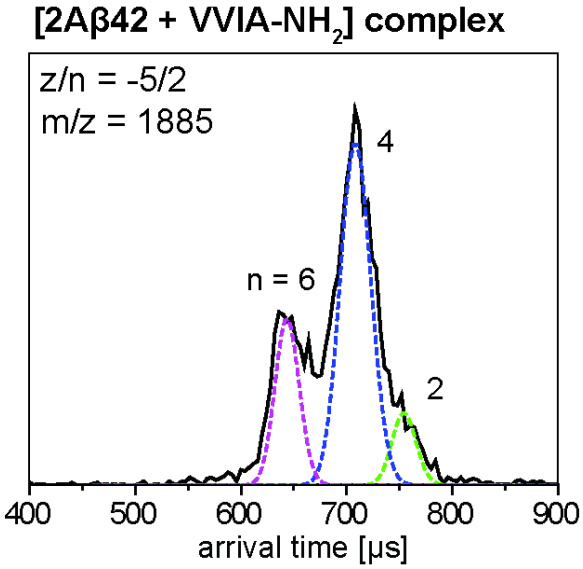

Figure 4.3 ATD of the z/n = -5/2 complex peak for Aβ42 sample with VVIA-NH_2. The oligomer number (n) is noted for each feature.

Taken together, these mass spectrometry and ion mobility results suggest that VVIA-NH_2 and Ac-VVIA both bind directly to Aβ42 directly and modulate the dodecamer formation. However, VVIA-NH_2 binds directly not only to Aβ42 monomer but also to Aβ42 small oligomers (dimers, tetramers and hexamers), while Ac-VVIA only binds to Aβ42 monomer. These results of VVIA-NH2 are similar to previous results of *wild type* VVIA that it bound to Aβ42 monomer and small oligomers and modulated dodecamer formation.[6] This is of significance and supports the fact that both *wild type* VVIA and VVIA-NH_2 inhibit the Aβ42-induced toxicity whereas Ac-VVIA does not inhibit Aβ42 toxicity.[6-7]

4.3.3 Disaggregation of preformed Aβ42 dodecamer by VVIA analogs

To test whether these VVIA analogs can disaggregate preformed Aβ42 oligomers, concentrated VVIA-NH_2 or Ac-VVIA was added to pre-aggregated Aβ42 sample and the ATDs of the z/n = -5/2 Aβ42 were recorded during different time periods. As shown in Figure 4.4a, after ~5 hours' incubation, the wild type Aβ42 forms dimer, tetramer, hexamer and dodecamer. Immediately after the addition of VVIA-NH_2, the ATD of z/n = -5/2 Aβ42 (Figure 4.4b) shows only three features corresponding to dimer, tetramer and hexamer, with the absence of dodecamer feature. The disappearance of dodecamer suggests that VVIA-NH_2 is able to disassociate preformed dodecamer. The ATD of the -5/2 peak for the Aβ42 sample with the addition of Ac-VVIA (Figure 4.4e) also shows only dimer, tetramer and hexamer. However, the Aβ42 sample with Ac-VVIA shows a noisy and broader ATD than that of VVIA-NH_2 sample, which suggests that there may be more families of oligomer structures for the Aβ42 sample with Ac-VVIA. This is important and consistent with observation that the Aβ42 sample with the addition of Ac-VVIA is more difficult to work with. The sample with Ac-VVIA addition becomes difficult to spray and the signal-to-noise of the z/n = -5/2 ATD decreases over time. After three hours, it became impossible to get the sample with Ac-VVIA to spray and no data was able to be collected any more. In contrast, the Aβ42 sample with the addition of VVIA-NH_2 works smoothly during the whole experiment time, even after several days.

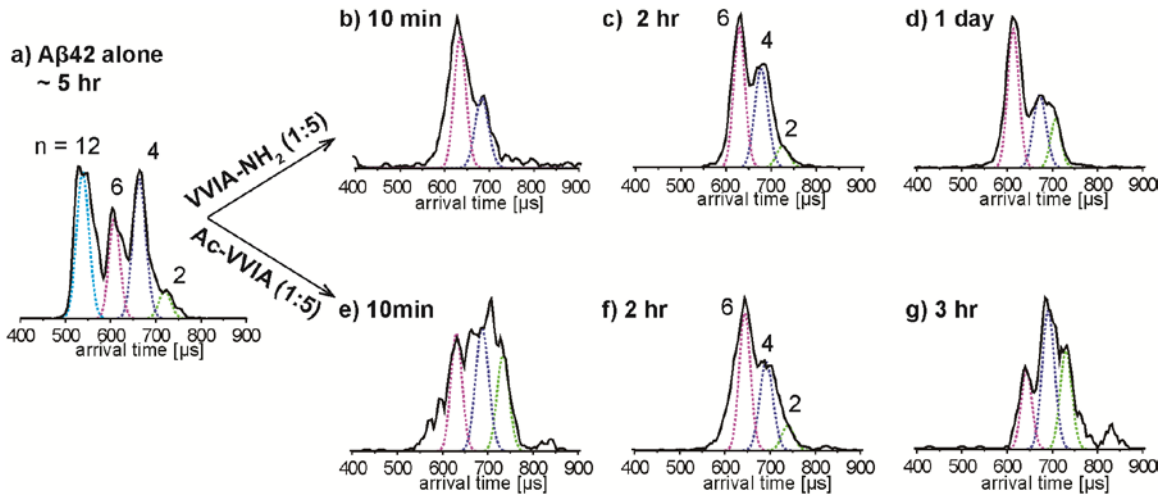

Figure 4.4 A time-dependent study of disaggregation of preformed Aβ42 oligomers by VVIA derivatives. a) ATD of the z/n = -5/2 peak for Aβ42 sample which was preincubated on ice for five hours. b-d) ATDs for the z/n = -5/2 peak for Aβ42 sample after the addition of VVIA-NH_2 and recorded at 10 min, 2 hr and after 1 day. e-g) ATDs of the z/n = -5/2 peak for Aβ42 sample after the addition of Ac-VVIA and recorded at 10 minutes, 2 hours and 3 hours. The oligomer number is noted for each feature in the ATDs.

The ATD of the -5/2 peak recorded on the 2nd day (Figure 4.4d) still shows only dimer, tetramer and hexamer. These results and observation suggest that VVIA-NH_2 can not only inhibit the formation of Aβ42 dodecamer but also remove the pre-formed dodecamer. On the other hand, Ac-VVIA which appears to inhibit dodecamer formation, may actually lead to formation of other larger oligomers or aggregates which clogged the spray tips. These results are consistent with the previous studies showing that VVIA-NH_2 was an effective Aβ42 inhibitor whereas Ac-VVIA was not.[7]

4.3.4 VVIA-NH_2 and Ac-VVIA do not inhibit Aβ42 fibril formation

The *wild type* VVIA was previously shown to modulate the Aβ42 oligomer formation but did not to inhibit the Aβ42 fibril formation. In this work, the effects of VVIA-NH_2 and Ac-VVIA on fibril formation were examined by TEM and the results are shown in

Figure 4.5. After two weeks' incubation at 4 °C, the Aβ42 samples form abundant long fibrils, regardless of the presence of VVIA-NH_2 or Ac-VVIA molecules. This suggests that neither VVIA-NH_2 nor Ac-VVIA inhibits Aβ42 fibril formation, which is similar to that of the *wild type* VVIA.

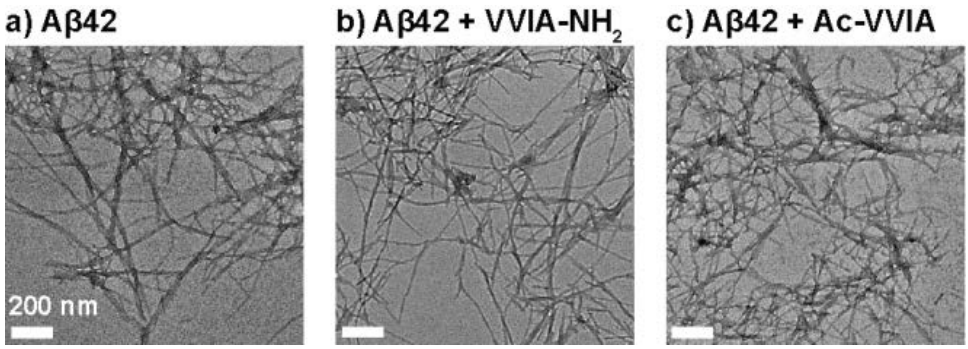

Figure 4.5 a-c) TEM images for Aβ42 samples without and with VVIA derivatives. The scale bar is 200 nm.

4.3.5 Modeling the interactions of Aβ42 with VVIA-NH_2 or Ac-VVIA

To probe the interaction of these two VVIA analogs with the full-length Aβ42 at an atomic level, a system consisting of one Aβ42 and one VVIA-NH_2 or Ac-VVIA molecule was constructed for all-atom molecular dynamics (MD) simulations. The most populated conformation of Aβ42 protein from previous study[3] was used as the initial conformation in our simulations, which enables efficiently sampling of the most important conformations (Figure 4.6).

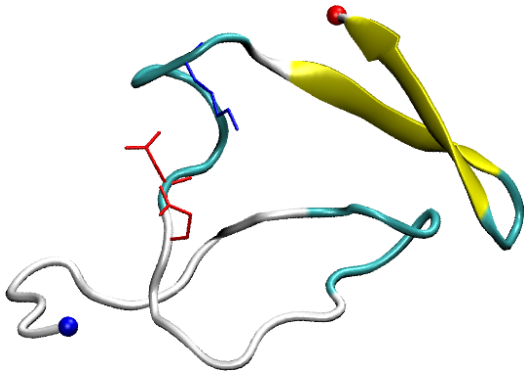

Figure 4.6 The starting structures of Aβ42 and modified Aβ(39-42)s, as derived from previous studies. The side-chains of E22, D23 and K28 are shown (blue: positively charged, red: negatively charged). The α-helical, 3-10-helical, β-extended, β-bridged, turn and coiled conformations are colored in purple, blue, yellow, tan, cyan and white. The N-termini and C-termini of the peptide are indicated by blue and red balls, respectively.

The overall binding was revealed by superimposing the most stable complexes identified from the trajectories and shown in Figure 4.7 (A-B). Aβ42 protein in both complexes shows great flexibility as indicated by the widespread cloud of the overall peptide backbones (grey), which is expected as Aβ42 is a natively disordered peptide. However, the binding of VVIA-NH_2 to Aβ42 is more specific than that of Ac-VVIA. As shown in Figure 4.7A, the VVIA-NH_2 molecules bind exclusively to only one specific region of Aβ42, the hydrophobic C-terminal region. The representative structure of the most populated structural family (57% of total population) from our clustering analysis shows that VVIA-NH_2 binds to the edge of the C-terminal β-hairpin (Figure 4.8A). On the other hand, Ac-VVIA molecules are observed to bind to several regions of Aβ42, including the C-terminal, central hydrophobic core and the N-terminal regions (Figure 4.7B and Figure 4.9). Clearly, the binding of Ac-VVIA to Aβ42 is more disperse and the most populated structural

family only contains 28% of total population (Figure 4.9A). Moreover, the Aβ42-VVIA-NH_2 complexes appear to be more rigid which display a uniform conformation. Whereas the Aβ42-Ac-VVIA complexes show more flexible and extended structures with slightly larger collision cross section.

A) Aβ42 + VVIA-NH_2

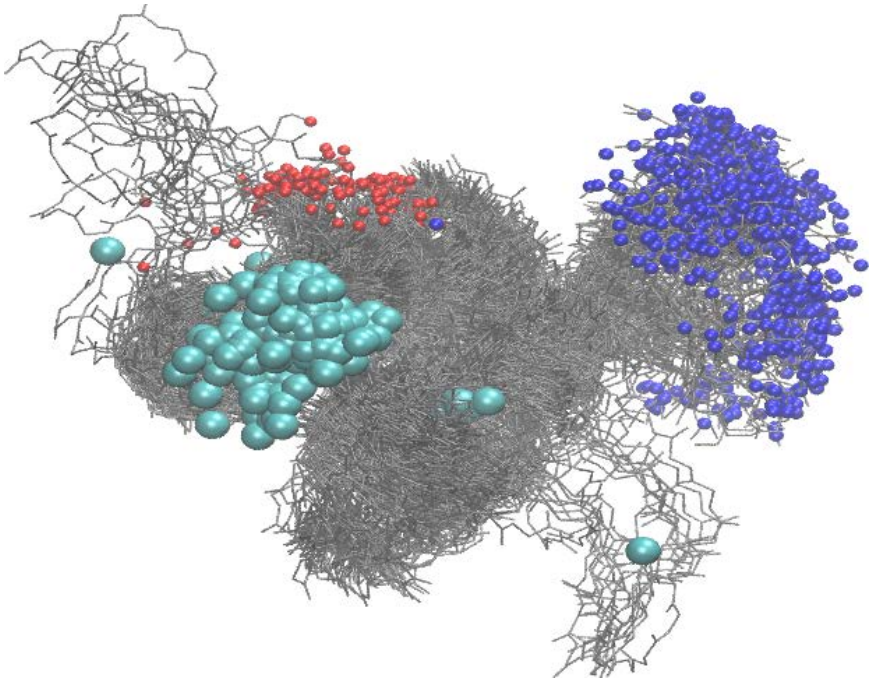

B) Aβ42 + Ac-VVIA

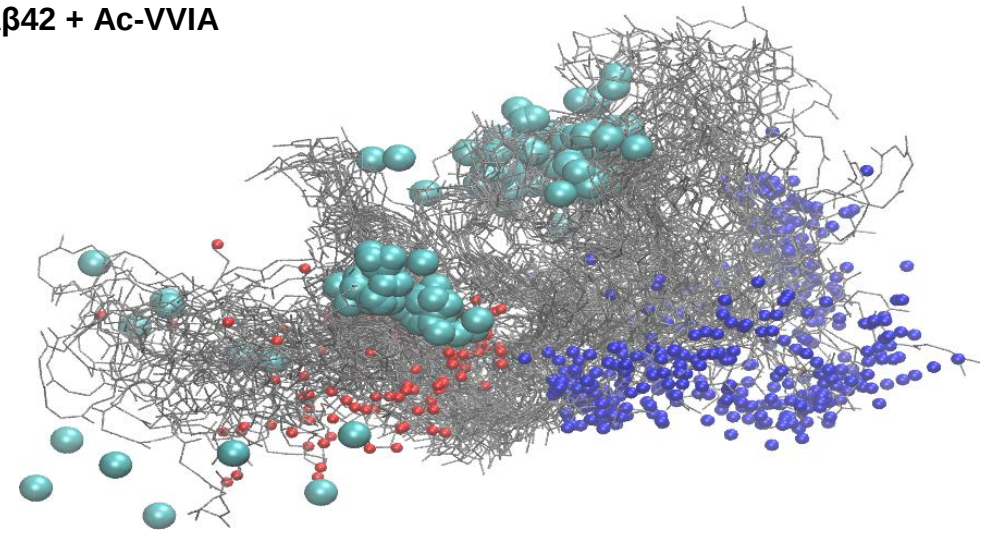

Figure 4.7 Interactions of Aβ42 with VVIA-NH_2 (**A**) or Ac-VVIA (**B**). The N-termini and C-termini are indicated by blue and red balls respectively. **A-B**): Superposition of the complexes where the protein backbones are represented by the grey lines and the VVIA derivatives are noted with the larger cyan balls.

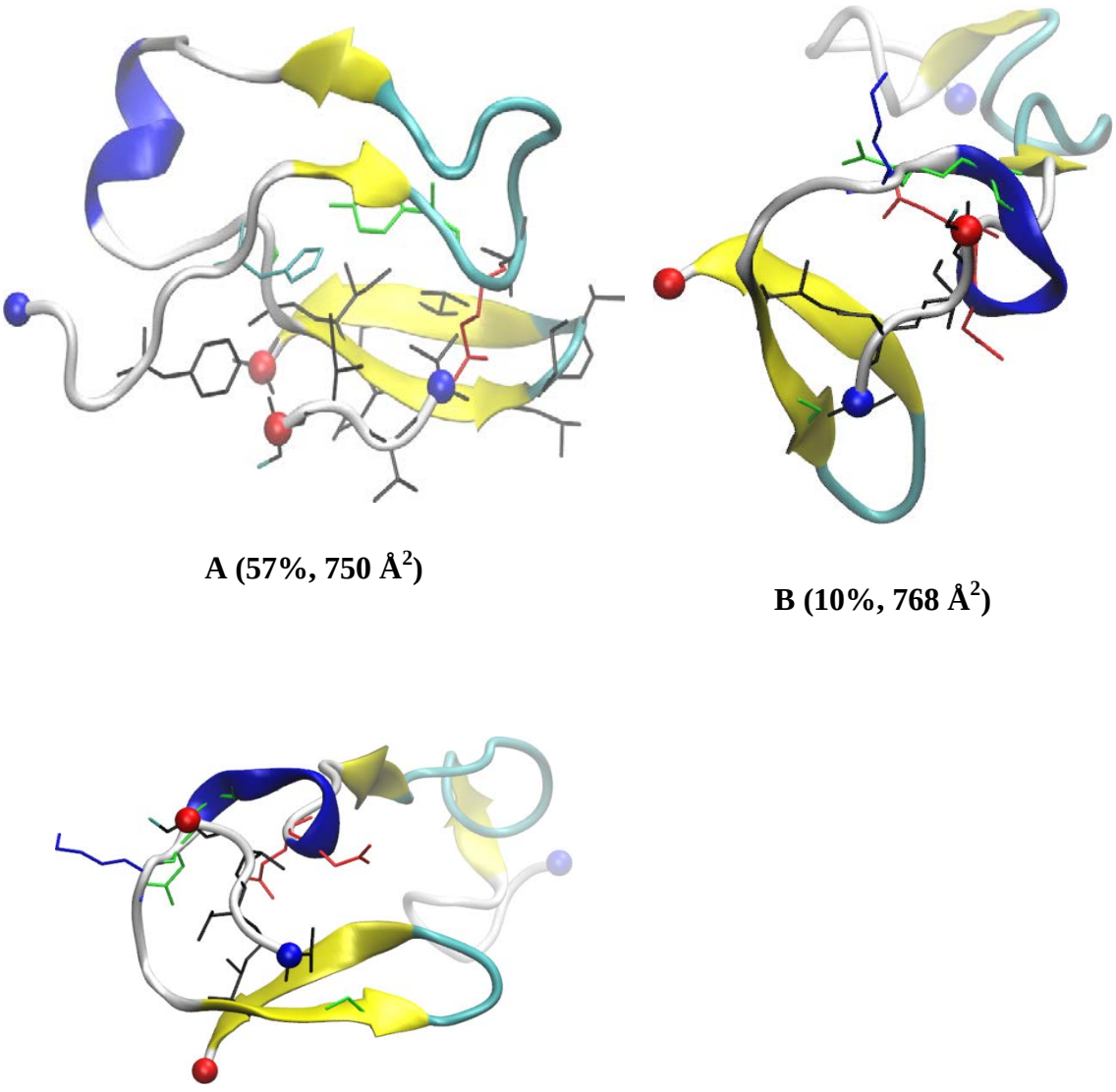

Figure 4.8 Representative structures for complex (Aβ42 + VVIA-NH_2) of the most populated structural families from the clustering analysis. The abundance and collision cross section are noted. Only the side-chains in contact with VVIA-NH_2 are shown (blue: positive charged, red: negative charged, black: hydrophobic and green: hydrophilic). 3-10- helical, β-extended, turn and coiled conformation are colored in blue, yellow, cyan and white. N-termini and C-termini of peptides are indicated by blue and red balls respectively.

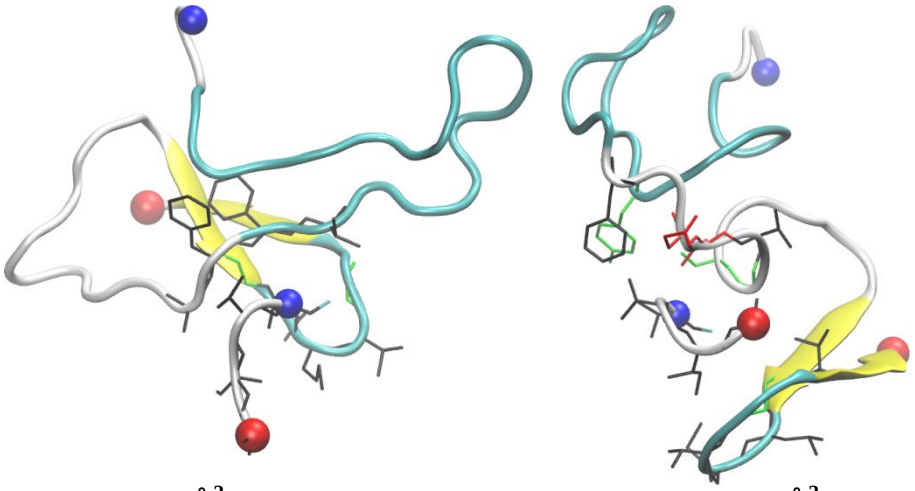

A (28%, 759 Å^2) **B (25%, 774 Å^2)**

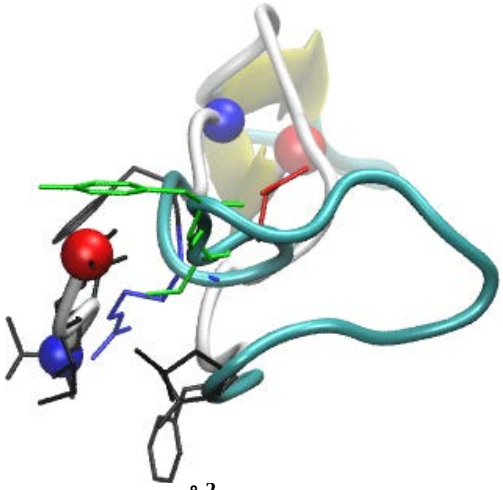

C (15%, 784 Å^2)

Figure 4.9 Representative structures for complex (Aβ42 + Ac-VVIA) of the most populated structural families from the clustering analysis. The abundance and collision cross section are noted. Only the side-chains in contact with Ac-VVIA are shown (blue: positive charged, red: negative charged, black: hydrophobic and green: hydrophilic). 3-10-helical, β-extended, turn and coiled conformation are colored in blue, yellow, cyan and white. N-termini and C-termini are indicated by blue and red balls respectively.

The *wild type* VVIA was previously shown to bind to Aβ42 at several regions, including the C-terminal, central hydrophobic core and the N-terminal regions.[6] Here our binding simulations of VVIA derivatives reveal significant differences in their binding

interactions with Aβ42. While the binding of Ac-VVIA to the C-terminal part of Aβ42 is slightly reduced in comparison to that of the wide type VVIA,[6] the binding of VVIA-NH2 to the C-terminal part of Aβ42 is significantly increased. The electrostatic interaction might contribute to these changes, because while the negatively charged C-terminal of Ac-VVIA is repulsive to the negatively charged C-terminal of Aβ42, the positively charged N-terminal of VV-NH2 is attracted to the negatively charged C-terminal of Aβ42. The correlation of VVIA-NH_2 inhibiting Aβ42 oligomerization and toxicity and VVIA-NH_2 binding specifically to C-terminal hydrophobic region of Aβ42 implies the important role of C-terminal region in Aβ42 structure stability, assembly, toxicity and its inhibition by C-terminal fragments.

4.3.6 Aβ42 monomer complexes

The z/n = -3 Aβ42 monomer and monomer complexes for Aβ42 and VVIA analogs were recorded and the results are shown in Figure 4.10 and Table 4.1. The ATD of Aβ42 monomer shows two features which were previously assigned as a gas-phase compact conformer (M_1) and a solution-like conformer (M_2).[27] The ATD of Aβ42 monomer with one VVIA-NH_2 or Ac-VVIA bound shows two similar features. By analog, they can be assigned as a gas-phase-like conformer and a solution-like conformer. The cross sections were measured and show ~5-6% increase in size after the addition of one VVIA analog (Table 4.1), which suggests the binding of VVIA analogs causes conformation changes in Aβ42. The experimental cross section for the solution-like structure is similar to the theoretical values for the most populated structure (Table 4.1).

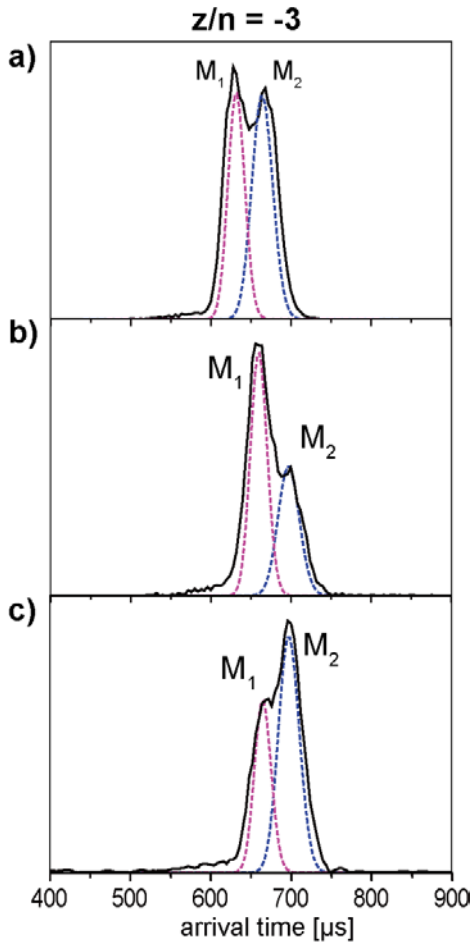

Figure 4.10 The ATDs of z/n = -3 monomer and complex. M_1 and M_2 represent two monomer conformers for Aβ42.

Table 4.1 Experimental and theoretical cross sections of z/n = -3 Aβ42 monomer and complexes. The error of the experimental cross sections is within 1%.

Species	Aβ42		+ 1 VVIA-NH_2		+ 1 Ac-VVIA	
	M_1	**M_2**	**M_1**	**M_2**	**M_1**	**M_2**
Experimental Cross Section ($Å^2$)	631	707	668	748	670	742
PSA cross section ($Å^2$)				750[a]		759[b]

a) from Figure 4.8A; b) from Figure 4.9

4.4 Discussion and conclusions

Several C-terminal fragments of Aβ42, especially Aβ(39-42), have been shown to be effective inhibitors for Aβ early assembly and toxicity.[5-7] It is critical to understand the mechanism of their inhibitory activity for further therapeutic development. Previous study have shown that *wild type* Aβ(39-42) modulates Aβ oligomerization but not fibril formation, and it binds to multiple sites on Aβ42, including the C-terminal, central hydrophobic core and the N-terminal regions.[6] However, it is unclear which region is most important for the Aβ: CTF interaction and the toxicity inhibition. Here, the interactions of two modified Aβ(39-42) molecules, C-amidated VVIA-NH_2 and N-acetylated Ac-VVIA, were investigated to better understand the mechanism of Aβ(39-42) inhibiting Aβ42 aggregation and toxicity. Previous study has shown that VVIA-NH_2 inhibits Aβ toxicity while Ac-VVIA does not.[7] Our mass spectrometry and ion mobility studies reveal that VVIA-NH_2 and Ac-VVIA have different effects on the Aβ42 early assembly. VVIA-NH_2 binds directly not only to Aβ42 monomer (up to two VVIA-NH_2 molecules bound to Aβ42 monomer were observed) but also to Aβ42 small oligomers (dimers, tetramers and hexamers). Consequently VVIA-NH_2 inhibits dodecamer formation and removes preformed dodecamers. On the other hand, only one Ac-VVIA molecule bound directly to Aβ42 monomer was observed. Ac-VVIA appears to modulate the dodecamer formation. However, the Aβ42 sample with addition of Ac-VVIA shows broader ATDs indicating a more complicated structure and oligomer distribution. Moreover the sample with Ac-VVIA clogged the nanospray tip easily and completely stopped working after three hours' incubation, indicating there are large aggregates formed in the solution, which are possibly formed through other pathways that bypass dodecamer formation. These subtle differences reveal the different binding effects of

VVIA-NH_2 and Ac-VVIA to Aβ42 and are consistent with their different effects in inhibiting Aβ42 toxicity (A summary of Aβ42 aggregation without and with VVIA analogs are given in Figure 4.11).

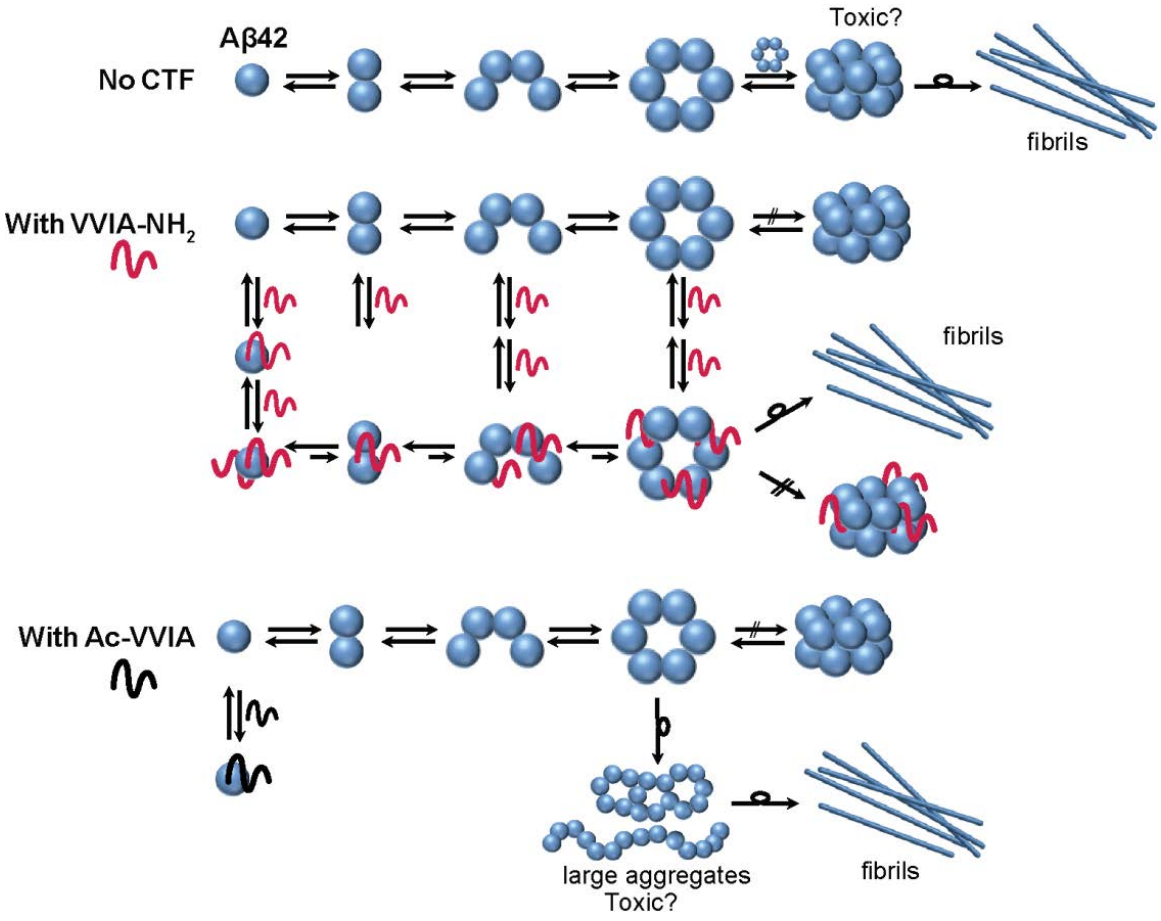

Figure 4.11 Aggregation mechanism of Aβ42 in the absence or presence of VVIA-NH_2 or Ac-VVIA. Wild type Aβ42 usually forms soluble toxic oligomers before self-assembling into large aggregates and fibrils. VVIA-NH_2 binds directly to Aβ42 monomer and small oligomers (dimer, tetramer and hexamer), inhibiting the formation of dodecamer and driving the formation of nontoxic oligomers that eventually form fibrils. Ac-VVIA binds only to Aβ42 monomer, inhibiting the formation of dodecamer, however, Ac-VVIA may lead to other pathway without dodecamer and form other toxic oligomers or aggregates which eventually form fibrils.

Our MD binding simulations show significantly different binding interactions for VVIA-NH_2 and Ac-VVIA with Aβ42. Ac-VVIA binds dispersedly to Aβ42 at multiple sites, including the C-terminal, central region and the N-terminal regions. In contrast, VVIA-NH_2, the effective Aβ42 inhibitor, binds specifically to only the C-terminal β-hairpin region of Aβ42. This is of significance and implies that the interaction at the C-terminal region, rather than at other regions, is the key for the inhibition activity of Aβ(39-42).

The C-terminal hydrophobic region of Aβ42 has been considered to play an important role in the structure stability and oligomerization of Aβ42.[28] Previous studies of prefibrillar Aβ42 showed that Ile41 and Ala42 residues stabilize the C-terminal turn conformation which results in a more rigid C-terminus for Aβ42 than Aβ40.[3] The increased conformation stability of C-terminus is correlated with the formation of more toxic oligomers in Aβ42, which explains how the difference of only two residues between Aβ40 and Aβ42 can significantly change the toxicity and aggregation properties of Aβ proteins.[3] These C-terminal hydrophobic residues in Aβ42 have been considered to be the driving force for protein folding and self-assembly, and stabilize neurotoxic low-order oligomers.[4] Therefore the hypothesis that peptides derived from the C-terminus of Aβ42 may be coassembled into Aβ42 monomer and oligomers, and disrupt their structures and thereby inhibit their toxicity, led to the successful discovery of effective C-terminal fragment inhibitors.[5] However, recent studies using intrinsic tyrosine fluorescence and NMR methods suggested that Aβ(39-42) might primarily interact with the N-terminus of Aβ42.[7] Our earlier simulations on the binding of Aβ(39-42) to Aβ42 corroborated this picture, with Aβ(39-42) observed to bind to multiple sites of Aβ42. These regions included the C-terminal, central hydrophobic core and the N-terminal regions.[6] These studies were intriguing, because they

did not seem in line with the original hypothesis that the C-terminal peptide inhibitors would specifically target the C-terminus of Aβ42. The peptide inhibitor, VVIA-NH_2, binds specifically to the C-terminus of Aβ42 monomers and oligomers resulting in effective inhibition of Aβ42 toxicity. However VVIA is also an effective inhibitor of toxicity and an indiscriminate binder to Aβ42 so C-terminal binding cannot be the exclusive determining factor. What VVIA and VVIA-NH_2 have in common is strong binding to both monomers and oligomers of Aβ42 whereas Ac-VVIA binds more weakly to Aβ42 monomer and not at all to its oligomers. Thus, binding to Aβ42 oligomers appears to be crucial for inhibition of toxicity, but more research is needed to fully understand the mechanism at play.

References

1. Tjernberg, L. O.; Näslund, J.; Lindqvist, F.; Johansson, J.; Karlström, A. R.; Thyberg, J.; Terenius, L.; Nordstedt, C. (1996) Arrest of β-amyloid fibril formation by a pentapeptide ligand. *J. Biol. Chem. 271*, 8545-8548.

2. Arai, T.; Sasaki, D.; Araya, T.; Sato, T.; Sohma, Y.; Kanai, M. (2014) A cyclic KLVFF-derived peptide aggregation inhibitor induces the formation of less-toxic off-pathway amyloid-β oligomers. *ChemBioChem 15*, 2577-2583.

3. Sgourakis, N. G.; Yan, Y.; McCallum, S. A.; Wang, C.; Garcia, A. E. (2007) The Alzheimer's peptides Aβ40 and 42 adopt distinct conformations in water: A combined MD / NMR study. *J. Mol. Biol. 368*, 1448-1457.

4. Ahmed, M.; Davis, J.; Aucoin, D.; Sato, T.; Ahuja, S.; Aimoto, S.; Elliott, J. I.; Van Nostrand, W. E.; Smith, S. O. (2010) Structural conversion of neurotoxic amyloid-β_{1-42} oligomers to fibrils. *Nat. Struct. Mol. Biol. 17*, 561-567.

5. Fradinger, E. A.; Monien, B. H.; Urbanc, B.; Lomakin, A.; Tan, M.; Li, H.; Spring, S. M.; Condron, M. M.; Cruz, L.; Xie, C.-W., et al. (2008) C-terminal peptides coassemble into Aβ42 oligomers and protect neurons against Aβ42-induced neurotoxicity. *Proc. Natl. Acad. Sci. U. S. A. 105*, 14175-14180.

6. Gessel, M. M.; Wu, C.; Li, H.; Bitan, G.; Shea, J.-E.; Bowers, M. T. (2011) Aβ(39–42) modulates Aβ oligomerization but not fibril formation. *Biochemistry 51*, 108-117.

7. Li, H.; Du, Z.; Lopes, D. H. J.; Fradinger, E. A.; Wang, C.; Bitan, G. (2011) C-terminal tetrapeptides inhibit Aβ42-induced neurotoxicity primarily through specific interaction at the n-terminus of Aβ42. *J. Med. Chem. 54*, 8451-8460.

8. Lomakin, A.; Chung, D. S.; Benedek, G. B.; Kirschner, D. A.; Teplow, D. B. (1996) On the nucleation and growth of amyloid β-protein fibrils: Detection of nuclei and quantitation of rate constants. *Proc. Natl. Acad. Sci. U. S. A. 93*, 1125-1129.

9. Wu, C.; Murray, M. M.; Bernstein, S. L.; Condron, M. M.; Bitan, G.; Shea, J. E.; Bowers, M. T. (2009) The structure of Aβ42 C-terminal fragments probed by a combined experimental and theoretical study. *J. Mol. Biol. 387*, 492-501.

10. Duan, Y.; Chowdhury, S.; Xiong, G.; Wu, C.; Zhang, W.; Lee, T.; Cieplak, P.; Caldwell, J.; Luo, R.; Wang, J., et al. (2003) A point-charge force field for molecular mechanics simulations of proteins based on condensed-phase QM calculations. *J. Comput. Chem. 24*, 1999-2012.

11. Wu, C.; Bowers, M. T.; Shea, J. E. (2010) Molecular structures of quiescently grown and brain-derived polymorphic fibrils of the Alzheimer amyloid $A\beta_{9-40}$ peptide: A comparison to agitated fibrils. *PLoS Comput. Biol. 6*.

12. Wu, C.; Wang, Z. X.; Lei, H. X.; Zhang, W.; Duan, Y. (2007) Dual binding modes of Congo red to amyloid protofibril surface observed in molecular dynamics simulations. *J. Am. Chem. Soc. 129*, 1225-1232.

13. Jorgensen, W. L.; Chandrasekhar, J.; Madura, J. D.; Impey, R. W.; Klein, M. L. (1983) Comparisons of simple potential functions for simulating liquid water. *J. Chem. Phys. 79*, 926-935.

14. Wang, J. M.; Wolf, R. M.; Caldwell, J. W.; Kollman, P. A.; Case, D. A. (2004) Development and testing of a general amber force field. *J. Comput. Chem. 25*, 1157-1174.

15. Essmann, U.; Perera, L.; Berkowitz, M. L.; Darden, T. A.; Lee, H.; Pedersen, L. G. (1995) A smooth particle mesh Ewald method. *J. Chem. Phys. 103*, 8577-8593.

16. Ryckaert, J.-P.; Ciccotti, G.; Berendsen, H. J. C. (1977) Numerical integration of the cartesian equations of motion of a system with constraints: Molecular dynamics of n-alkanes. *J. Comput. Phys. 23*, 327-341.

17. Procacci, P.; Berne, B. J. (1994) Multiple time-scale methods for constant-pressure molecular-dynamics simulations of molecular-systems. *Mol. Phys. 83*, 255-272.

18. Chiu, S. W.; Clark, M.; Subramaniam, S.; Jakobsson, E. (2000) Collective motion artifacts arising in long-duration molecular dynamics simulations. *J. Comput. Chem. 21*, 121-131.

19. Harvey, S. C.; Tan, R. K. Z.; Cheatham, T. E. (1998) The flying ice cube: Velocity rescaling in molecular dynamics leads to violation of energy equipartition. *J. Comput. Chem. 19*, 726-740.

20. Daura, X.; Gademann, K.; Jaun, B.; Seebach, D.; van Gunsteren, W. F.; Mark, A. E. (1999) Peptide folding: When simulation meets experiment. *Angew. Chem., Int. Ed. 38*, 236-240.

21. Bleiholder, C.; Wyttenbach, T.; Bowers, M. T. (2011) A novel projection approximation algorithm for the fast and accurate computation of molecular collision cross sections (I). Method. *Int. J. Mass Spectrom. 308*, 1-10.

22. Bleiholder, C.; Contreras, S.; Do, T. D.; Bowers, M. T. (2013) A novel projection approximation algorithm for the fast and accurate computation of molecular collision cross sections (II). Model parameterization and definition of empirical shape factors for proteins. *Int. J. Mass Spectrom. 345–347*, 89-96.

23. Anderson, S. E.; Bleiholder, C.; Brocker, E. R.; Stang, P. J.; Bowers, M. T. (2012) A novel projection approximation algorithm for the fast and accurate computation of molecular collision cross sections (III): Application to supramolecular coordination-driven assemblies with complex shapes. *Int. J. Mass Spectrom. 330–332*, 78-84.

24. Bleiholder, C.; Contreras, S.; Bowers, M. T. (2013) A novel projection approximation algorithm for the fast and accurate computation of molecular collision cross sections (IV). Application to polypeptides. *Int. J. Mass Spectrom. 354–355*, 275-280.

25. Gong, Y.; Chang, L.; Viola, K. L.; Lacor, P. N.; Lambert, M. P.; Finch, C. E.; Krafft, G. A.; Klein, W. L. (2003) Alzheimer's disease-affected brain: Presence of oligomeric Aβ ligands (ADDLs) suggests a molecular basis for reversible memory loss. *Proc. Natl. Acad. Sci. U. S. A. 100*, 10417-10422.

26. Lesné, S.; Koh, M. T.; Kotilinek, L.; Kayed, R.; Glabe, C. G.; Yang, A.; Gallagher, M.; Ashe, K. H. (2006) A specific amyloid-β protein assembly in the brain impairs memory. *Nature 440*, 352-357.

27. Baumketner, A.; Bernstein, S. L.; Wyttenbach, T.; Bitan, G.; Teplow, D. B.; Bowers, M. T.; Shea, J.-E. (2006) Amyloid β-protein monomer structure: A computational and experimental study. *Protein Sci. 15*, 420-428.

28. Lazo, N. D.; Grant, M. A.; Condron, M. C.; Rigby, A. C.; Teplow, D. B. (2005) On the nucleation of amyloid β-protein monomer folding. *Protein Sci. 14*, 1581-1596.

Chapter 5

Amyloid β-protein Assembly: The Effect of Molecular Tweezer CLR01 and CLR03

5.1 Introduction

Molecular tweezers (MTs), which possess a torus-shaped cavity with a surrounding belt of alternating aromatic and aliphatic rings, were designed to serve as host molecules binding specifically to lysine and to a lesser extent to arginine residues.[1-3] MTs were previously shown to be modulators of the aggregation of Aβ and other amyloidogenic proteins and effective inhibitors of the toxicity of these proteins.[4] A lead MT derivative, CLR01 (Figure 5.1a), was shown to inhibit the toxicity of multiple amyloidogenic proteins in cell viability assays using cell lines and primary cell cultures[4-7] and protected synaptic integrity and function of hippocampal and cortical neurons against the synaptotoxicity of Aβ42.[6] In addition, peripheral administration of CLR01 in transgenic mice led to a decrease in amyloid plaques, neurofibrillary tangles, and brain inflammation, suggesting that it is a promising candidate for therapeutic development.[6]

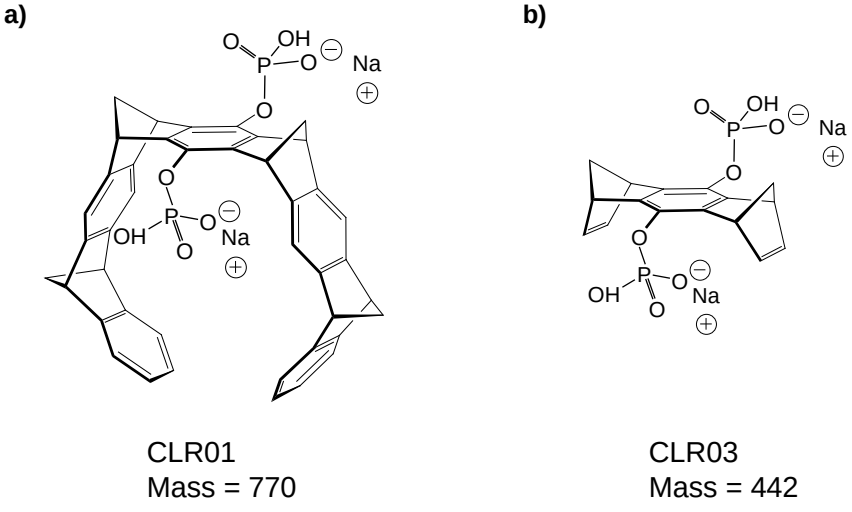

Figure 5.1 Molecular structures of (a) CLR01 and (b) CLR03.

Mechanistic investigation showed that disruption of Aβ self-assembly is mediated by CLR01 binding to the two lysine and the single arginine residues in Aβ.[4] Dynamic light scattering (DLS) and electron microscopy (EM) experiments suggested that CLR01 does not prevent oligomer formation, but rather modulates Aβ self-assembly into formation of structures that are neither amyloidogenic nor toxic.[4] Interestingly, by the relatively low resolution of DLS and EM, these structures were similar in size to the toxic and amyloidogenic oligomers of Aβ alone, suggesting that subtle conformational changes in Aβ might account for the apparent loss of amyloidogenic potential and toxic activity. However, the low-resolution methods could not provide information about what these changes might be. In addition, whether CLR01 binds Aβ monomers, oligomers, and/or larger aggregates has not been demonstrated directly.

In several previous studies, a derivative called CLR03 (Figure 5.1b) was used as a negative control.[4,6] This compound shares the polar bridgehead structure with CLR01 but lacks the hydrophobic arms, and therefore is not expected to bind specifically to lysine or arginine. Consequently, CLR03 indeed acted as a negative control and was not found to inhibit the aggregation and/or toxicity of amyloidogenic proteins. Nonetheless, how CLR03 interacts with Aβ and whether it has any effect on early Aβ oligomerization of Aβ remains to be uncovered.

To address all these questions, here we used ion mobility spectrometry coupled to mass spectrometry (IMS-MS)[8-9] to investigate the effect of CLR01 and CLR03 on Aβ assembly.

5.2 Experimental Methods

Peptide and Sample preparation: Full-length Aβ40 and Aβ42 were synthesized by *N*-9-fluorenylmethoxycarbonyl (FMOC) chemistry. The peptides were purified by reverse-phase HPLC and their integrity validated by mass spectrometry and amino acid analysis as described previously.[10] The samples were prepared in 10 mM ammonium acetate and the pH was adjusted to 7.4. Samples contained 10 μM Aβ42 and molecular tweezers at different concentration ratios. An Aβ42 sample without MTs was prepared under the same procedure as a positive control.

Mass Spectrometry and Ion Mobility spectrometry Analysis: Samples were analyzed on a home-built ion mobility spectrometry-mass spectrometer[8] described in Chapter 2.

5.3 Results

5.3.1 MS reveals different binding effects of CLR01 and CLR03 on Aβ42

Mass spectra of Aβ42 samples in the absence or presence of MTs are shown in Figure 5.2. In the mass spectrum of Aβ42 alone (Figure 5.2c), there are four peaks, which correspond to Aβ42 species with charge states z/n = -4, -3, -5/2 and -2 (where z represents charge and n represents oligomer order), respectively, as described previously.[11-12] In the mass spectrum of a 1:10 mixture of Aβ42 and CLR01 (Figure 5.2a), there are three sets of peaks which correspond to -4, -5 and -6 charge states of the complexes of Aβ42 with one, two, three, or four CLR01 molecules bound. As the mass spectrometry study was conducted

in negative ion mode, the binding form of CLR01 is with loss of sodium ions, which results in producing Aβ42 and CLR01 complexes with higher charge states. Note that no -5/2 Aβ42 peak (m/z = 1805), which represents dimer or higher order oligomers, is observed. This indicates that CLR01 disrupts the formation of Aβ42 dimers and higher order oligomers. No peaks of uncomplexed Aβ42 are observed in the mass spectrum, suggesting that CLR01 binds to Aβ42 directly with high affinity and there are no CLR01-free Aβ42 species present in solution.

In contrast, the spectrum of a 1:10 mixture of Aβ42 and CLR03 (Figure 5.2b) shows four peaks corresponding to the -4, -3, -5/2 and -2 Aβ42 species, similarly to Aβ42 alone (Figure 5.2c). There are two additional small peaks tailing the -3 and -4 Aβ42 peaks corresponding to the -3 and -4 complex species of Aβ42 with one CLR03 bound, respectively. The intensities of these two complex peaks are much lower than those with CLR01 bound suggesting that the affinity of CLR03 binding to Aβ42 is much lower than that of CLR01.

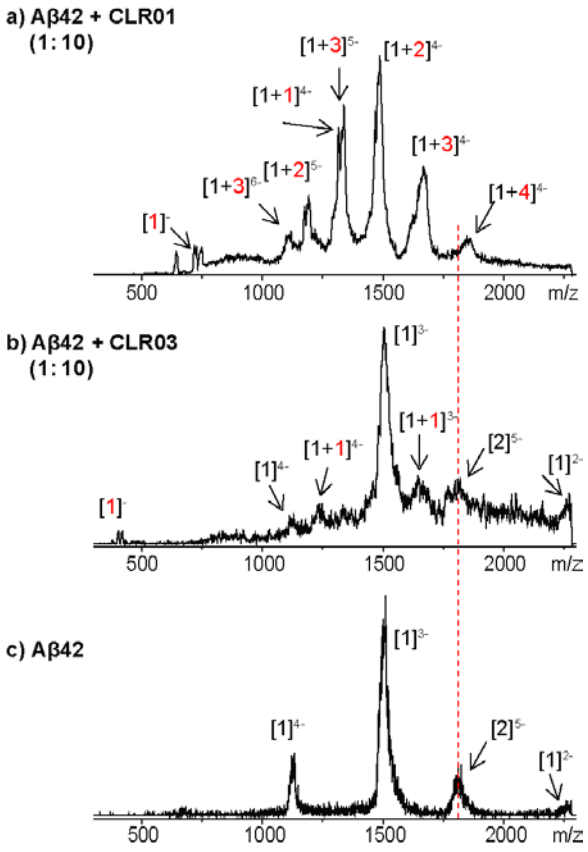

Figure 5.2 Different binding effects of CLR01 and CLR03 on Aβ42. Mass spectra of Aβ42 samples: a) 1:10 mixture of Aβ42 and CLR01; b) 1:10 mixture of Aβ42 and CLR03; c) Aβ42 alone. Each species is noted in the bracket where the first number is the number of Aβ42 molecules and the second number represents the number of bound small molecules. The charge is noted as a superscript.

To better understand the effects of CLR01 on Aβ42, the mass spectra of Aβ42 with different ratios of CLR01 (1:1, 1:2, 1:5 and 1:10) were recorded. The mass spectra of the mixtures are shown in Figure 5.3. The mass spectrum of the 1:5 mixture of Aβ42 and CLR01 is similar to that of the 1:10 mixture (Figure 5.2c) with peaks corresponding to complex species Aβ42 and CLR01 with charge states -4, -5, and -6. As the concentration of CLR01 decreases (1:2 and 1:1 ratios), the complex species of Aβ42 and CLR01 with lower charge states (-4, -3, -5/2) are observed in the mass spectra. One possible explanation is that

CLR01 itself is slightly basic in aqueous solution and the observed binding form of CLR01 is CLR01 with loss of one sodium ion, therefore the complexes tend to carry more charge in the presence of high concentration CLR01. Note that no z/n = -5/2 CLR01-free Aβ42 dimer peak is observed in any of the mixtures. However, in the low-ratio mixtures (1:1 and 1:2, see Figure 5.3a, b), the -5/2 complex peaks of Aβ42 oligomers with CLR01 molecules bound are observed (m/z = 1950, 2096, and 2241 representing [2+**1**], [2+**2**], and [2+**3**] Aβ42-CLR01 complexes, respectively). These results suggest that CLR01 not only binds to Aβ42 monomers, but also to small Aβ42 oligomers with high affinity, thereby disrupting the formation of larger Aβ42 oligomers even at 1:1 ratio. As the concentration of CLR01 increases, the Aβ42 oligomers decrease in abundance or altogether disappear.

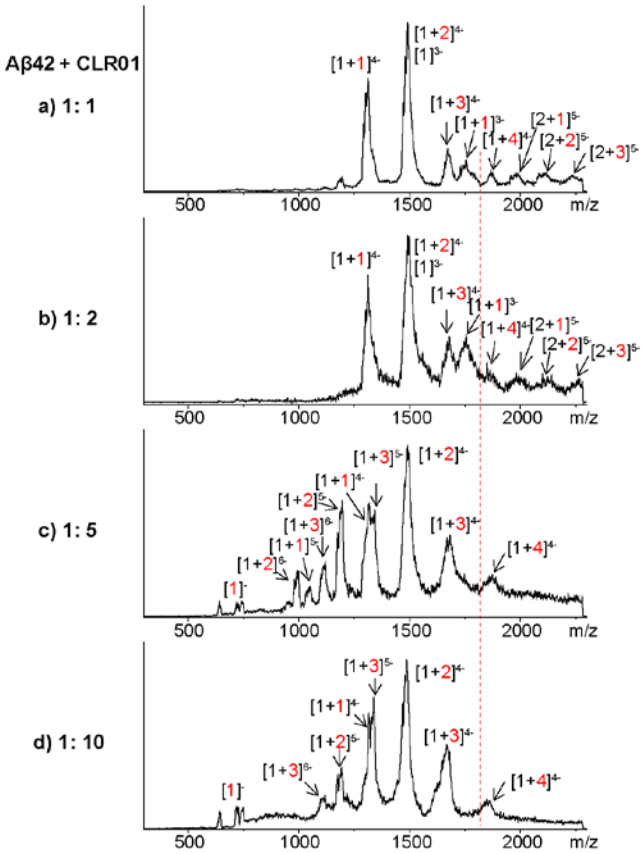

Figure 5.3 Mass spectra of Aβ42 and CLR01 mixtures. a-d) 1:1, 1:2, 1:5, and 1:10 ratio of Aβ42 and CLR01, respectively. Each species is noted in the bracket where the first number is the number of Aβ42 molecules and the second number represents the number of bound CLR01 molecules. The charge is noted as a superscript. The read dash line represents the theoretical position for uncomplexed -5/2 peak.

5.3.2 IMS reveals CLR01 inhibiting early Aβ42 oligomerization

To better understand the effects of CLR01 on Aβ42 oligomerization, an ion mobility study was conducted. No ATDs for the z/n = -5/2 Aβ42 peak (m/z = 1805) could be recorded as it was not observed in any of the mixtures of Aβ42 and CLR01. The ATDs of the [2+**1**] and [2+**2**] complex peaks were recorded and are shown in Figure 5.4b-c (The signal of [2+3] complex species was too weak to obtain a reliable ATD). The ATD of the -5/2 Aβ42 peak of pure Aβ42 (Figure 5.4a) shows four features with arrival times of ~712, 680, 620 and 540 μs, which were previously assigned as Aβ42 dimer, tetramer, hexamer and dodecamer, respectively, based on their cross section values (See references 12 for detailed discussion of the -5/2 peak assignment).

In contrast, in the 1:1 mixture of Aβ42 and CLR01, the ATD of the m/z = 1950 peak (Figure 5.4b, labeled as [2+**1**] species) shows only two features with arrival times of 690 and 640 μs, which are assigned as dimer and tetramer, respectively. This indicates there is one CLR01 molecule bound to the Aβ42 dimer and two CLR01 molecules bound to the Aβ42 tetramer, respectively. No features at lower arrival times are observed, suggesting there are no Aβ42 hexamers, dodecamers or other larger oligomers formed in the presence of CLR01. The ATD of the m/z = 2096 peak (Figure 5.4c, labeled as [2+**2**] species) also shows two dominant features with arrival times of ~700 and 660 μs, which correspond to Aβ42 dimer and tetramer, respectively. This indicates that there are two CLR01 molecules bound to the

Aβ42 dimer and four CLR01 molecules bound to the Aβ42 tetramer. Again, the highest oligomers with CLR01 bound observed are tetramers and absence of features at lower arrival times indicates no hexamer, dodecamer or higher order oligomer formation. These results indicate that CLR01 not only binds to Aβ42 monomers but also to small oligomers and inhibits the formation of hexamer and higher order oligomers.

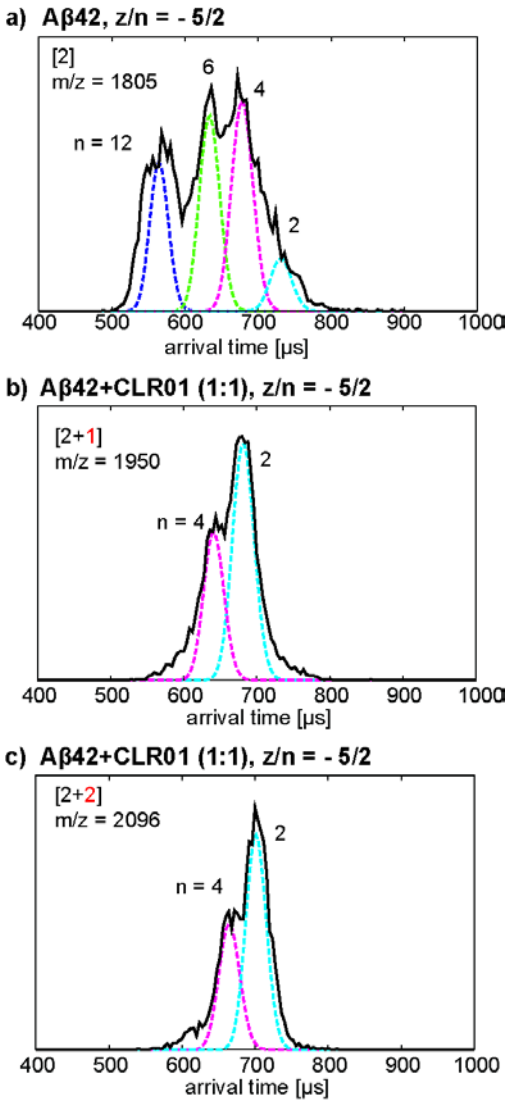

Figure 5.4. Effects of low concentration CLR01 on Aβ42 early oligomerization. ATDs of a) z/n = -5/2 Aβ42 (m/z = 1805) in an Aβ42 sample without CLR01; b) z/n = -5/2 Aβ42 and CLR01 complex (m/z = 1950); and c) z/n = -5/2 Aβ42 and CLR01 complex (m/z = 2096) in a 1:1 mixture of Aβ42 and CLR01.

The cross sections of oligomer complexes are given in Table 5.1. Interestingly, the cross sections of dimers with one or two CLR01 molecules bound are significantly smaller than that of the dimer with no ligands attached, even though their mass has increased. This result suggests CLR01 induces more interaction between the two monomers leading to a compact conformation and overall size reduction. Similarly, the cross sections of tetramers with two or four CLR01 molecules bound are smaller than those of the tetramer with no CLR01 bound. In addition, the tetramer ATD peaks with CLR01 bound (Figure 5.4b, c) are much narrower than in wild type Aβ42. This indicates there is little structure variation in the CLR01 bound tetramer while in wt Aβ42 the tetramer family of structures is both larger and more varied. The unbound Aβ42 tetramer normally adopts a family of structures that have a bent arrangement (~120° angle).[12] It is likely that the tetramers with CLR01 bound adopt either a more closed square ring structure or a pyramidal structure accounting for the fact they are smaller than CLR01-free Aβ42 tetramers and that dimer cannot be added to form hexamer. A similar effect prevents Aβ40 from growing beyond tetramer and explains its greatly reduced toxicity relative to Aβ42.[12]

Table 5.1 Collision Cross sections of dimer and tetramer in the uncomplexed or CLR01-complexed -5/2 Aβ42. The error for the cross sections reported here is between 0-1%.

Oligomer	Charge State	σ(Å²)		
		[2]	[2+1]	[2+2]
Dimer	-5	1243	1072	1124
Tetramer	-10	2173	1934	2084

5.3.3 CLR01 remodels pre-formed Aβ42 oligomers

To explore whether CLR01 can remodel the early oligomerization of Aβ42 not only immediately upon dissolution but also after the oligomers have already formed, Aβ42 was incubated for 4 hours on ice, following which CLR01 was added to the samples. The samples were incubated at a low temperature to allow quasi-equilibrium of small oligomers to be reached, but avoid extensive aggregation, which happens at higher temperatures and leads to clogging of the nano-ESI capillaries, preventing further analysis. The results are shown in Figure 5.5.

Following incubation, the mass spectrum of Aβ42 (Figure 5.5a) shows four peaks with charge states of z/n = -4, -3, -5/2 and -2. Upon addition of CLR01 at 1:1 concentration ratio, new peaks appeared corresponding to z/n = -4, -3 monomer complexes and z/n = -5/2 oligomer complexes (Figure 5.5b). Overall, the spectrum was similar to the one obtained in the inhibition study, with the exception that no peaks were observed with 3 or 4 CLR01 molecules bound. The data indicate that CLR01 binds to Aβ42 monomers and preformed Aβ42 oligomers directly, mostly with 1:1 or 1:2 stroichiometry, whereas binding of additional CLR01 molecules is less likely after incubation. This suggests the existence of two main binding sites for CLR01 on Aβ, Lys16 and Lys28.[4]

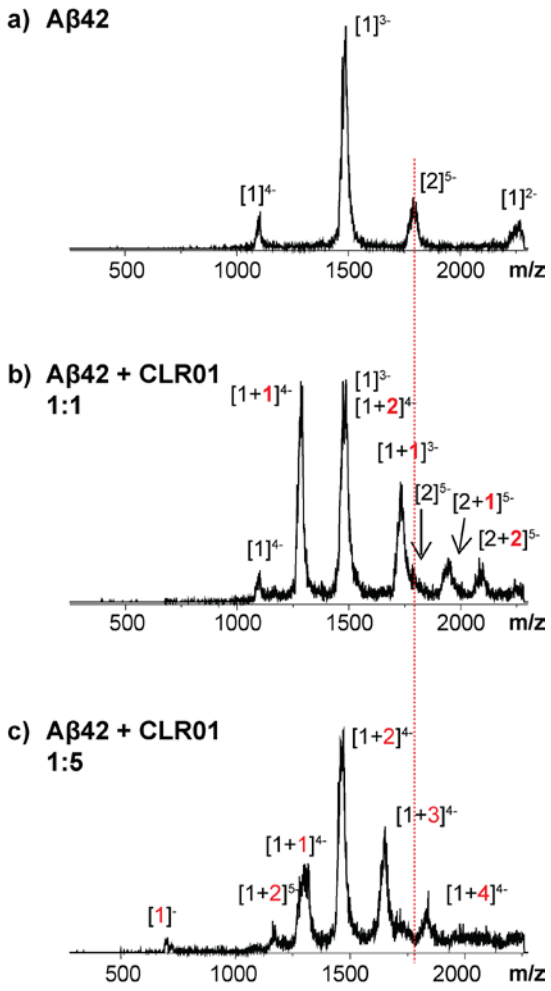

Figure 5.5 CLR01 remodels the early oligomerization of Aβ42. a) Mass spectrum of Aβ42 alone with ~4 hours' incubation on ice; b) and c) mass spectra of Aβ42 sample immediately after the addition of 1:1 and 1:5 CLR01. Each species is noted in the bracket where the first number is the number of Aβ42 and the second number represents the number of bound CLR01 molecules. The charge is noted as a superscript.

To test the effect of the Aβ42:CLR01 concentration ratio on the remodeling of Aβ42 oligomerization, higher ratios of CLR01 (1:5 and 1:10, respectively) were added to 4-hour incubated Aβ42. The mass spectrum of the 1:5 mixture, is shown in Figure 5.5c (the result of the 1:10 ratio was similar to that of the 1:5 mixture and therefore is not shown). The mass spectrum of the 1:5 mixture showed mostly complexes of Aβ42 monomer with CLR01

molecules. No z/n = -5/2 peak of CLR01-free or CLR01-complexed Aβ42 was observed. These results suggest that high concentrations of CLR01 dissociate pre-formed Aβ42 oligomers. Taken together, these results indicate that CLR01 remodels Aβ42 oligomerization both at low and high concentration ratios.

The ATD of -5/2 peak for Aβ42 alone after 4 hours' incubation, shows four features corresponding to dimer, tetramer, hexamer and dodecamer (Figure 5.6a). Interestingly, the ATD of the z/n = -5/2 unbound Aβ42 peak (Figure 5.6b) showed only three features representing dimer, tetramer and a small amount of hexamer after the addition of equimolar CLR01. The feature representing Aβ42 dodecamer was eliminated after the addition of CLR01, suggesting that the binding of CLR01 dissociated the pre-formed Aβ42 dodecamer. Moreover, the relative intensity of the hexamer decreased significantly compared to that before CLR01 addition (Figure 5.6a), suggesting CLR01 began to also dissociate hexamers. The ATDs of the z/n = -5/2 Aβ42:CLR01 oligomer complex peaks (Figure 5.6c, d) showed only the two features corresponding to dimer and tetramer with CLR01 molecules bound, as observed immediately upon mixing of Aβ42 and CLR01 (Figure 5.4b and c), suggesting that binding of CLR01 to Aβ42 dimers or tetramers changes their structure so that additional dimers cannot be added to form hexamers.

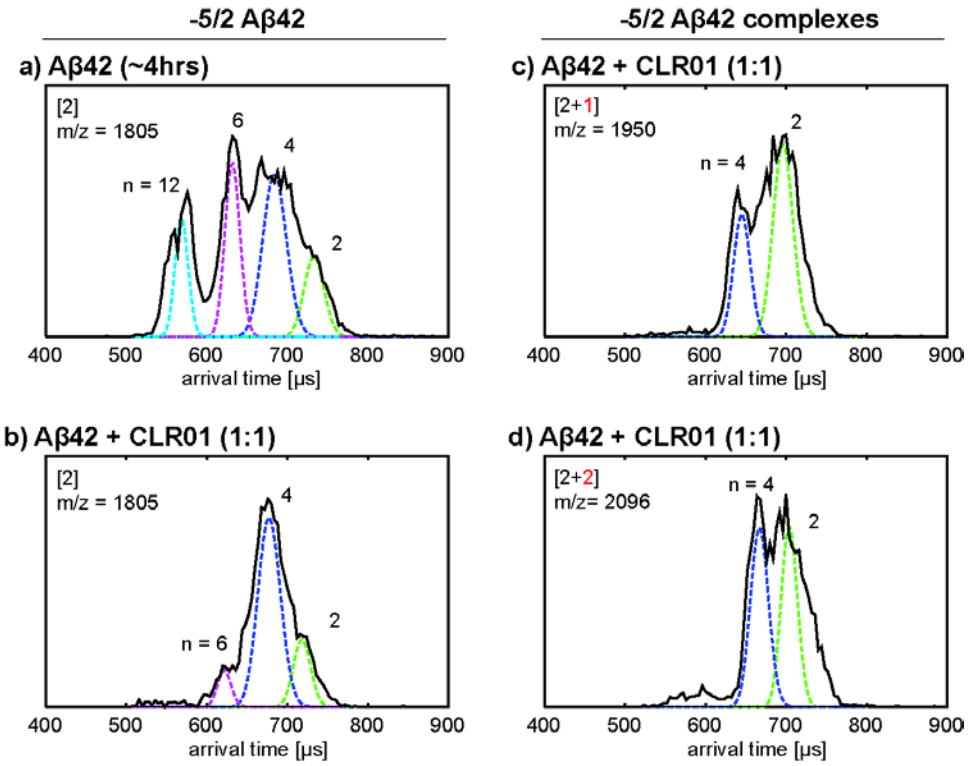

Figure 5.6 CLR01 remodels the early oligomerization of Aβ42. a) ATD of z/n = -5/2 Aβ42 peak for the Aβ42 in the absence of CLR01 after ~4 hours' incubation on ice. b) ATD of z/n = -5/2 Aβ42 peak after addition of 1:1 CLR01. c) and d) the ATDs of -5/2 Aβ42 oligomer complexes after addition of 1:1 CLR01 to the pre-aggregated Aβ42 sample. The oligomer order (n) is noted for each feature.

The ATDs of the z/n = -5/2 peaks were monitored again after one day of incubation at 4°C and the results (see Figure 5.7) were similar to those obtained following 4 hours of incubation, suggesting that CLR01 maintained the distribution of Aβ42 oligomers, in which dodecamers were excluded and hexamers were a minor species.

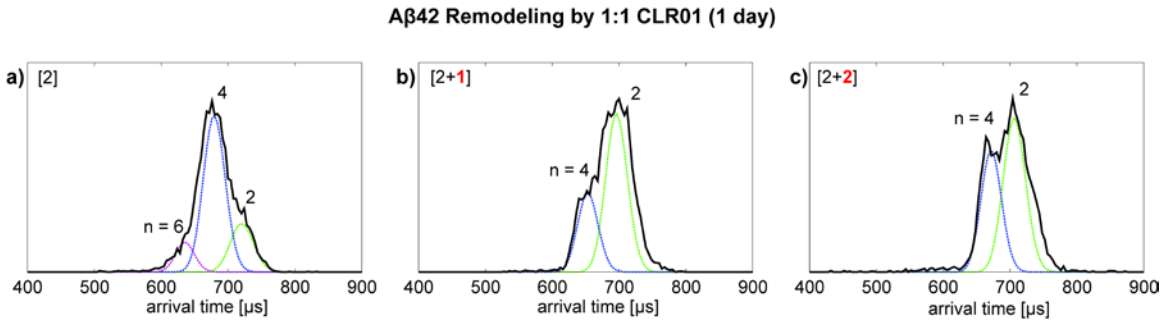

Figure 5.7 ATDs of CLR01 remodeling the early oligomerization of Aβ42 after one day. a-c) ATDs of z/n = -5/2 Aβ42 peaks without and with CLR01 molecules bound. Each ATD is fitted with multiple features using the procedure described in the experimental section. The oligomer order (n) is noted for each feature.

5.3.4 Ion mobility spectrometry of Aβ42 monomer complexes

The ATDs of z/n = -3 of Aβ42 monomer in the absence or presence of CLR01 (1:1) are shown in Figure 5.8. In the ATD of the -3 monomer peak of Aβ42 alone there are two dominant peaks with arrival times of ~640 and ~680 μs, previously identified as a solvent-free conformer and a solution-like conformer, respectively.[13] The ATD for the -3 peak of Aβ42 complexed with one CLR01 molecule shows two similar features with arrival times of ~668 and ~712 μs. By analogy, these are assigned as the solvent-free and solution-like conformers of Aβ42 monomer with one CLR01 bound, respectively.

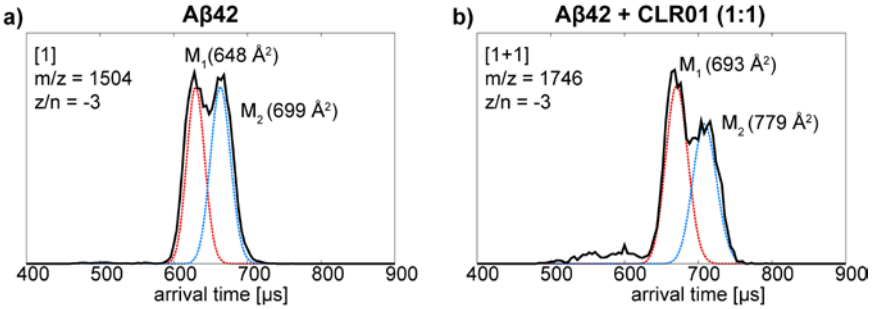

Figure 5.8 ATDs of z/n = -3 Aβ42 monomers in the absence (a) or presence (b) of CLR01. Each ATD is fitted with multiple features using the procedure described in the experimental section. M_1 and M_2 represent the compact and extended conformers of Aβ42 monomers.

The ATDs of z/n = -4 and -5 complexes of Aβ42 with one, two, three, or four CLR01 molecules bound in a 1:5 mixture, respectively, are shown in Figure 5.9. Those for z/n = -4 have two features in their ATDs and as the number of bound CLR01 molecules increases, the intensity of the compact, shorter-time feature increases, relative to the more extended, longer-time feature. Overall, there are no features with shorter arrival times detected which indicates that only monomer with CLR01 complexed is present in solution. The cross sections of the Aβ42:CLR01 monomer complexes are shown in Figure 5.9c. Addition of each CLR01 ligand increases the size of the complex by an amount comparable to the size of CLR01 suggesting that no major structural transitions occur in the monomers upon CLR01 binding.

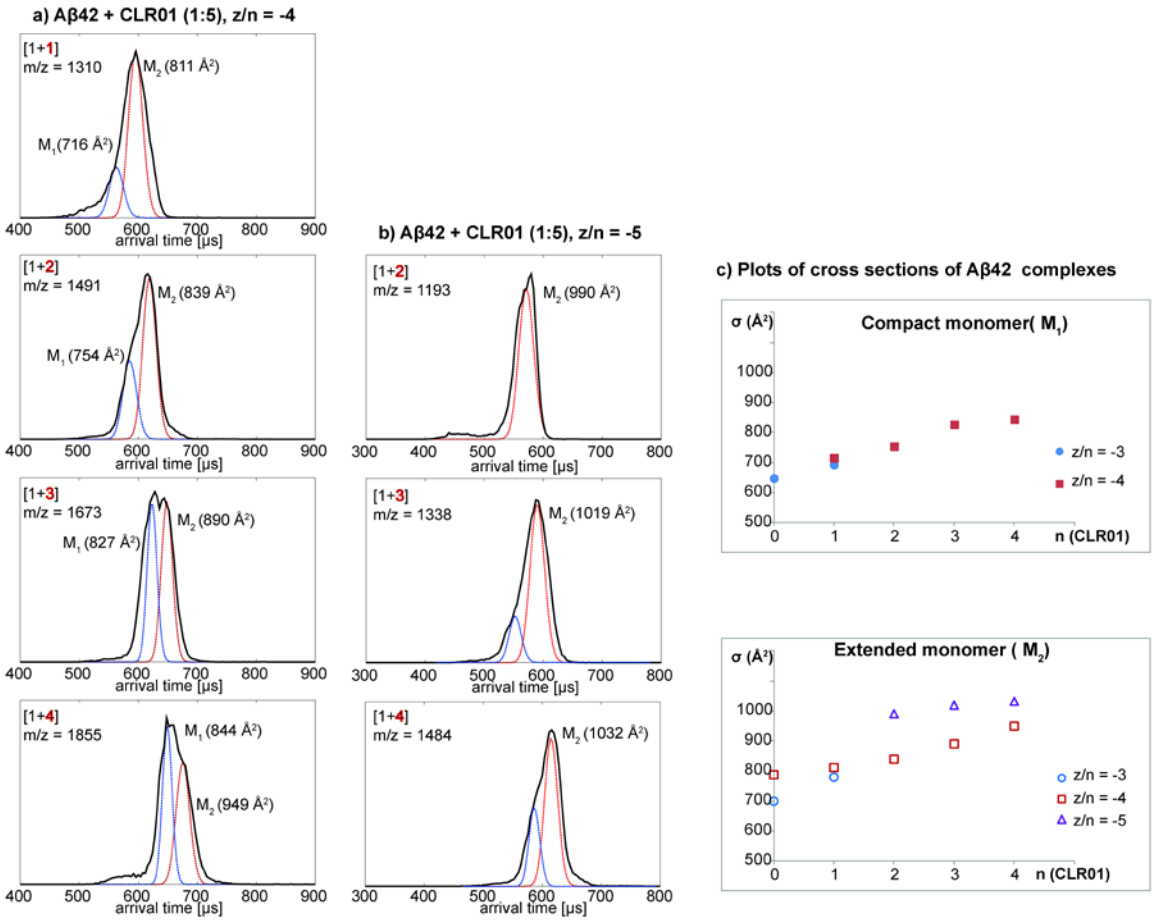

Figure 5.9 ATDs of a) z/n = -4 and b) z/n = -5 complexes of Aβ42 with one, two, three, or four CLR01 molecules bound in a 1:5 mixture of Aβ42 and CLR01. Each ATD is fitted with multiple features using the procedure described in the experimental section. c) Plots of cross sections of Aβ42 monomer complexes versus number of bound CLR01 molecules.

5.3.5 Effects of CLR01 on Aβ40 assembly

Aβ40 has an identical sequence to that of Aβ42 except for absence of Ile41 and Ala42 residues at the C-terminus, but has very different assembly and pathological properties. Thus, it is interesting to examine how CLR01 affects its early oligomerization in comparison to Aβ42. The mass spectra of Aβ40 alone and Aβ40 mixed with CLR01 at different ratios are provided in Figure 5.10 The mass spectrum of Aβ40 alone shows three peaks which correspond to z/n = -4, -3 and -5/2, similar to the spectrum of the Aβ42. The

mass spectra of mixtures of Aβ40 and CLR01 at different ratios show sets of peaks at charge states -3, -4, -5 and -6 corresponding to Aβ40:CLR01 complexes. Up to four CLR01 molecules are observed bound to Aβ40. At lower CLR01 concentration (1:1 ratio, Figure 5.10b), there are three z/n = -5/2 peaks at m/z = 1876, 2021, and 2167, corresponding to [2+**1**], [2+**2**] and [2+**3**] oligomer complexes of Aβ40 and CLR01. At higher concentrations of CLR01 (1:5 and 1:10 ratios), no -5/2 oligomer complexes were detected, suggesting that no dimer or higher-order oligomers formed.

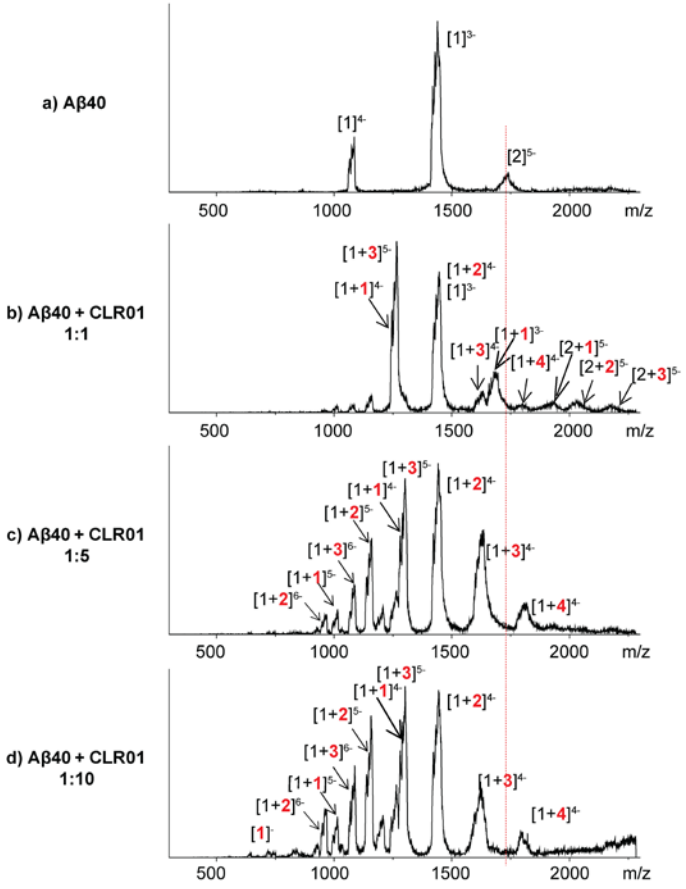

Figure 5.10 Mass spectra of Aβ40 and CLR01 mixtures. a) Aβ40 alone and b-d) mixtures of Aβ40 and CLR01 at 1:1, 1:5 and 1:10 ratio, respectively. Each species is noted in the bracket where the first number is the number of Aβ40 molecules and the second number, in red, represents the number of bound CLR01 molecules. The charge is noted as a superscript.

The ATDs of these -5/2 oligomer peaks are shown in Figure 5.11 (the signal of the [2+3] complex was too weak to obtain a reliable ATD and therefore is not shown). The -5/2 peak of Aβ40 (m/z = 1731, Figure 5.11a) shows two features with arrival times of ~690 and ~620 μs which previously were assigned as Aβ40 dimer and tetramer (see reference 12 for a detailed discussion of the -5/2 peak assignment). For the 1:1 mixture of Aβ40 and CLR01, the ATDs of -5/2 [2+**1**] and [2+**2**] oligomer complexes (Figure 5.11b and c) show two primary features, which can be assigned as dimer and tetramer based on their cross sections. These results indicate that there are one or two CLR01 molecules bound to Aβ40 dimers and two or four CLR01 molecules bound to Aβ40 tetramers. No features at shorter arrival times were observed, indicating that there are no hexamer or larger oligomers formed. Interestingly, the intensities of the tetramer feature for [2+**1**] and [2+**2**] complex species (Figure 5.11b and c) are lower than that of the -5/2, CLR01-free Aβ40 tetramer feature, which indicates that the formation of tetramer is slower in the presence of CLR01 in the Aβ40 sample than in its absence.

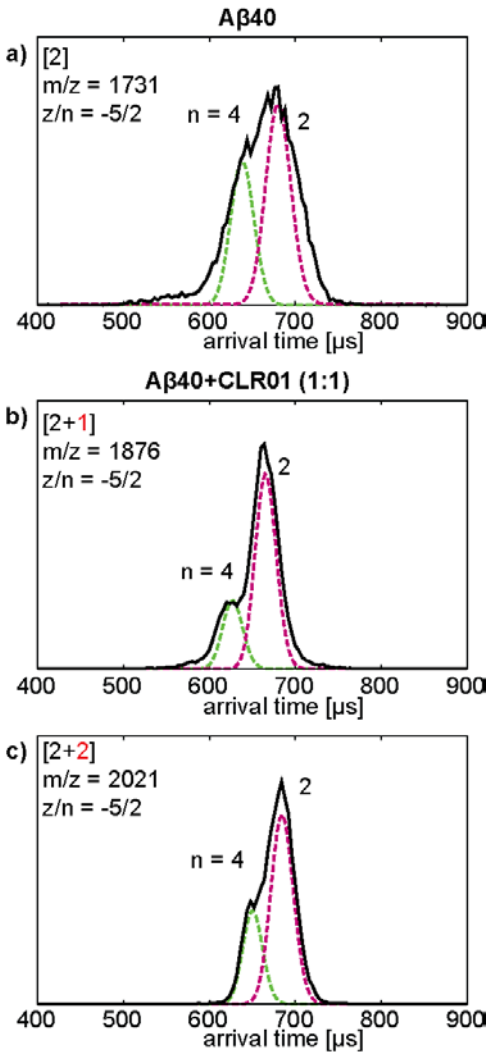

Figure 5.11 Effects of low concentration CLR01 on Aβ40 oligomerization. a) ATD of z/n = -5/2 Aβ40 (m/z = 1731) for Aβ40 alone; b) and c), ATDs of z/n = -5/2 Aβ40 and CLR01 complexes (m/z = 1876 and 2021) in the 1:1 mixture of Aβ40 and CLR01. Each ATD is fit with multiple features using the procedure described in the experimental section and the oligomer order (n) is noted for each feature. Note the ATDs with CLR01 bound, panels b and c, are significantly narrower than wild type, panel a.

The ATDs of monomer complexes with charge states z/n = -3, -4, -5, or -6 are shown in Figures 5.12 and 5.13. The z/n = -4 species (Figure 5.13a) show two features in their ATDs corresponding to the solvent-free conformer and the solution-like conformer of Aβ40 complexed with CLR01. Taken together, these results indicate that CLR01 binds to Aβ40

with relatively high affinity and inhibits its early oligomerization. The cross sections of Aβ40 monomer complexes are shown in Figure 5.13b. Similarly to the Aβ42 case, addition of each CLR01 ligand increases the size of the monomer complex by an amount comparable to the size of CLR01 suggesting that no major structural transitions occur in the monomers upon CLR01 binding.

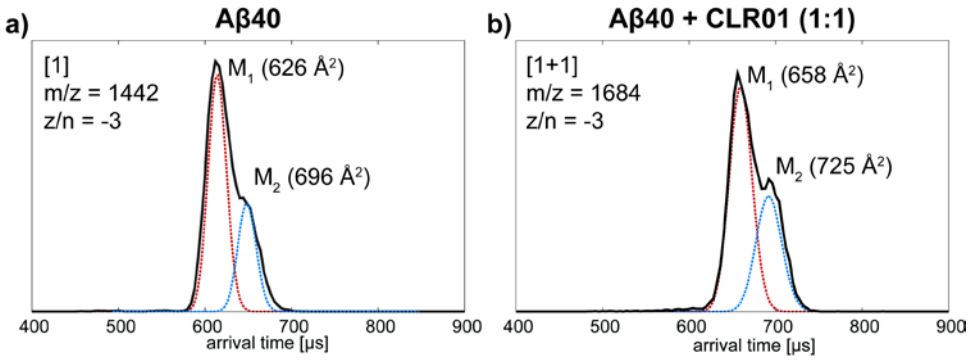

Figure 5.12 ATDs of z/n = -3 Aβ40 monomers in the absence (a) or presence (b) of CLR01. Each ATD is fitted with multiple features using the procedure described in the experimental section. M_1 and M_2 represent the compact and extended conformers of Aβ42 monomers.

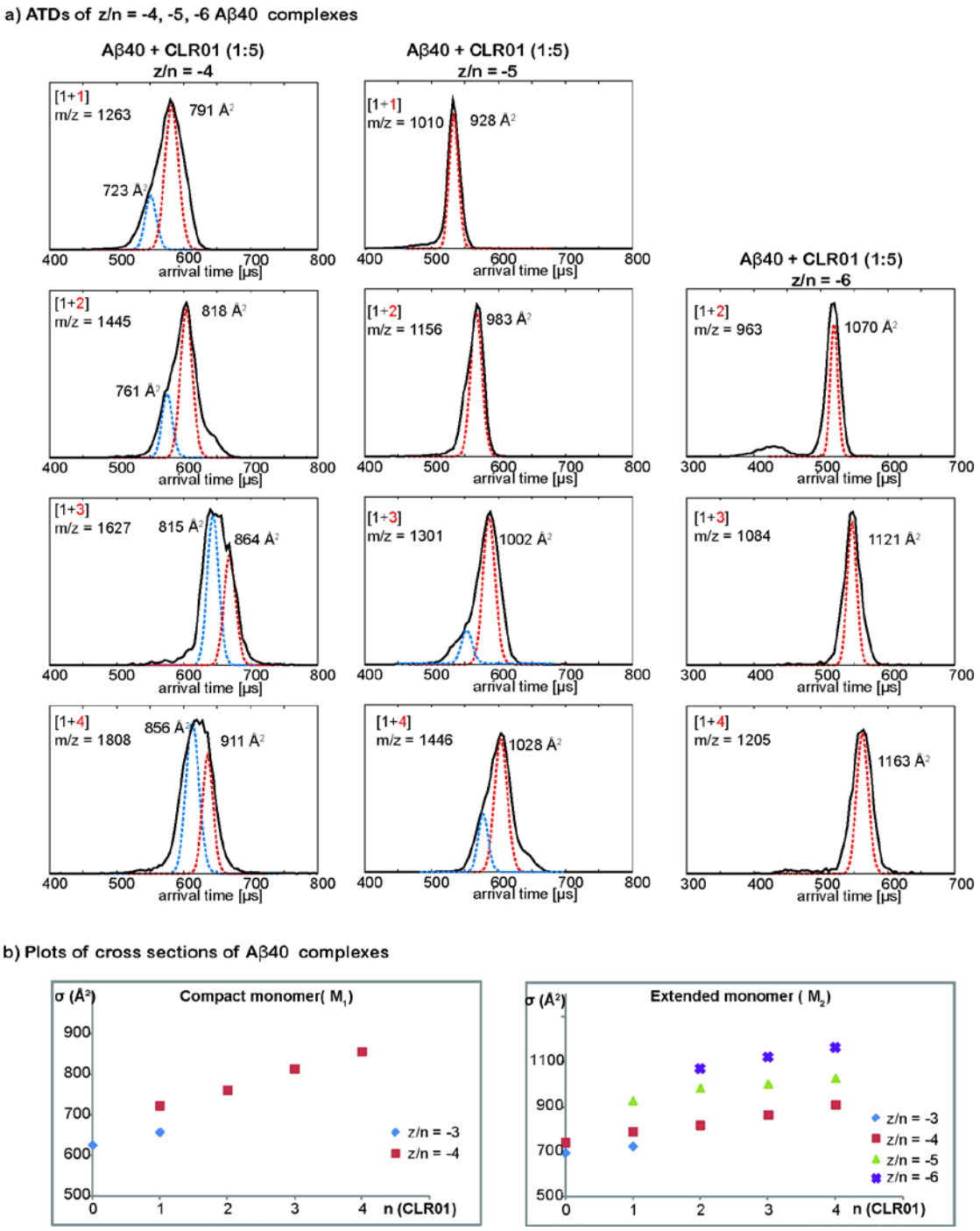

Figure 5.13 a) ATDs of z/n = -4, -5, and -6 Aβ40 and CLR01 complexes, respectively, in their 1:5 mixture. Each ATD is fitted with multiple features using the procedure described in the experimental section. b) The cross section for each feature is plotted versus the number of CLR01 molecules bound.

5.3.6 IMS reveals that CLR03 facilitates early Aβ42 oligomerization

As noted above, CLR03 has been used as a negative-control compound, which was not expected to inhibit Aβ oligomerization or aggregation. Hence, we felt it important to do similar experiments that are reported here.

A time dependent study of the ATDs of the -5/2 Aβ42 peak (m/z = 1805) of Aβ42 alone and the 1:10 mixture of Aβ42 and CLR03 are shown in Figure 5.14. The ATD of the -5/2 Aβ42 peak for the 1:10 mixture of Aβ42 and CLR03, respectively, at 30 minutes (Figure 5.14a) shows four features that can be assigned as Aβ42 dimer, tetramer, hexamer and dodecamer based on their cross sections, which is similar to the results of Aβ42 alone at 30 minutes (Figure 5.14d). Interestingly, the intensity of the dodecamer feature of the -5/2 peak for the mixture of Aβ42 and CLR03 is relatively higher than other features, whereas the intensity of the dodecamer feature of Aβ42 alone at 30 minutes is relatively lower than other features, suggesting that the growth of dodecamer in the presence of CLR03 is faster than in its absence. After up to 24 hours of incubation, the dodecamer in the Aβ42 and CLR03 mixture becomes an even more dominant feature in the ATDs (Figure 5.14b and c), whereas the CLR01-free Aβ42 sample does not change substantially and appears to be in a state of quasi-equilibrium (Figure 5.14e and f). The observation of dodecamer and the significant rapid growth of dodecamer in the Aβ42 sample in the presence of CLR03 suggest that CLR03 not only does not inhibit the formation of Aβ42 dodecamer, but actually facilitates the dodecamer formation.

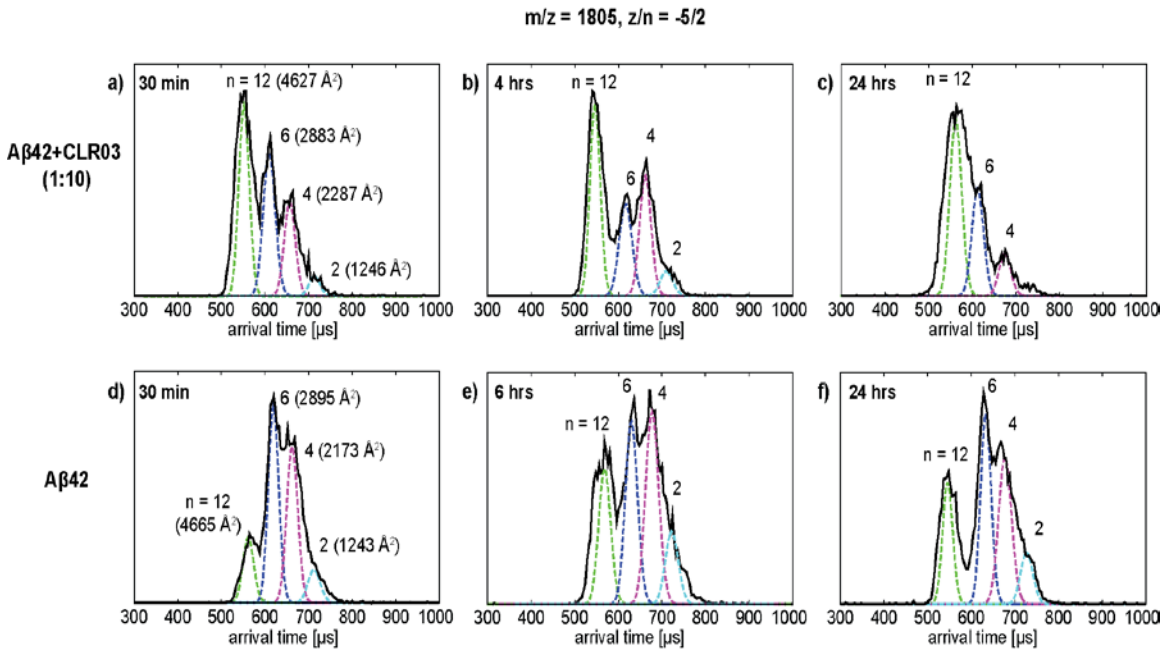

Figure 5.14 Time-dependent ion mobility study of the effects of CLR03 on Aβ42 early oligomerization. a-c) ATDs of -5/2 Aβ42 peak (m/z = 1805) for the 1:10 mixture of Aβ42 and CLR03 at different time points; d-f) ATDs of -5/2 Aβ42 peak (m/z = 1805) for Aβ42 alone at different time points. Each ATD is fit with multiple features using the procedure described in the experimental section. The oligomer order (n) and cross section are noted for each feature.

ATDs of z/n = -3 and -4 peaks for Aβ42 alone and a 1:1 mixture of Aβ42 and CLR03 are shown in Figure 5.15. The ATD of the z/n = -3 Aβ42 peak for the mixture of Aβ42 and CLR03 (Figure 5.15b) shows two features at ~640 and ~680 μs corresponding to the compact and extended conformers, respectively, which is similar to those of Aβ42 alone (Figure 5.15a). Remarkably, there is another feature at a substantially shorter arrival time (~500 μs) as noted by the arrow in addition to the two monomer features, which is not observed for Aβ42 alone. This indicates the presence of relatively large oligomers (n ≥2) formed in the presence of CLR03. A similar feature is observed in the ATD of the z/n = -3 peak of Aβ42 with one CLR03 bound, which corresponds to large oligomers (n ≥2). In

Figure 5.15e and f, dominant features with shorter arrival times are observed in the ATDs for z/n = -4 peaks of Aβ42 with and without CLR03 bound, in addition to the monomer feature, indicating the presence of large oligomers (n≥2). These results are consistent with the results of the ATDs of z/n = -5/2 Aβ42 peak (m/z = 1805, Figure 5.14) and further support the fact that CLR03 facilitates self-assembly of Aβ42.

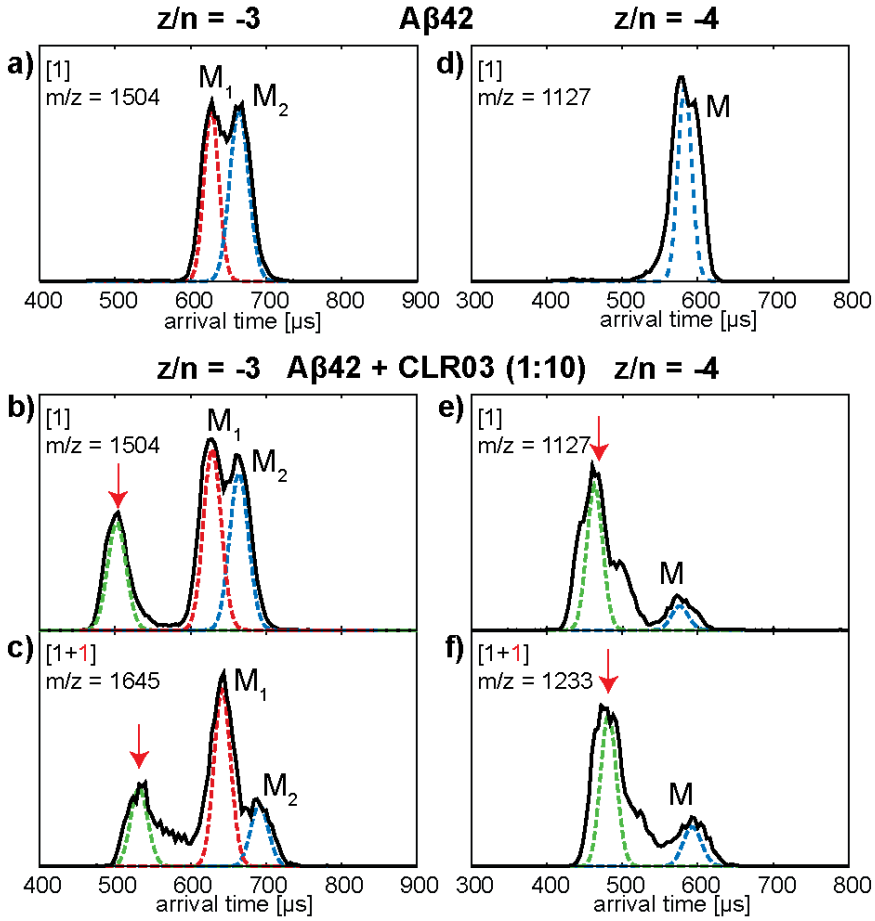

Figure 5.15 CLR03 facilitates Aβ42 oligomer formation a) ATD of z/n = -3 peak for Aβ42 alone, b) and c) ATDs of z/n = -3 Aβ42 without and with CLR03 bound for a 1:10 mixture of Aβ42 and CLR03, d) ATD of z/n = -4 peak for Aβ42 alone, e) and f) z/n = -4 Aβ42 without and with CLR03 bound for a 1:10 mixture of Aβ42 and CLR03. Each ATD is fit with multiple features using the procedure described in the experimental section. M_1 and M_2 represent two conformations of Aβ42 monomer. The arrows indicate the formation of oligomers (n ≥ 2) in the mixture of Aβ42 and CLR03.

5.3.7 CLR03 facilitates Aβ40 assembly

The effect of CLR03 on Aβ40 oligomerization is shown in Figure 5.16. The mass spectrum of a 1:10 mixture of Aβ40 and CLR03 shows peaks corresponding to z/n = -3 and z/n = -4 monomer with one CLR03 bound but no CLR03 attachment to the z/n = -5/2 peak (Figure 5.16b). However, the ATD of the -5/2 Aβ40 peak (m/z = 1731) in the presence of CLR03 (Figure 5.16d) shows formation of both Aβ40 hexamer and dodecamer based on the cross section calculations. In Figure 16e the cross sections for the dimers and tetramers of Aβ40 are given for Aβ40 alone and for Aβ40 mixed with CLR01 and CLR03. Note that CLR03 significantly increases both cross sections whereas CLR01 significantly decreases both cross sections. Further aggregation is enhanced by CLR03 and inhibited by CLR01.

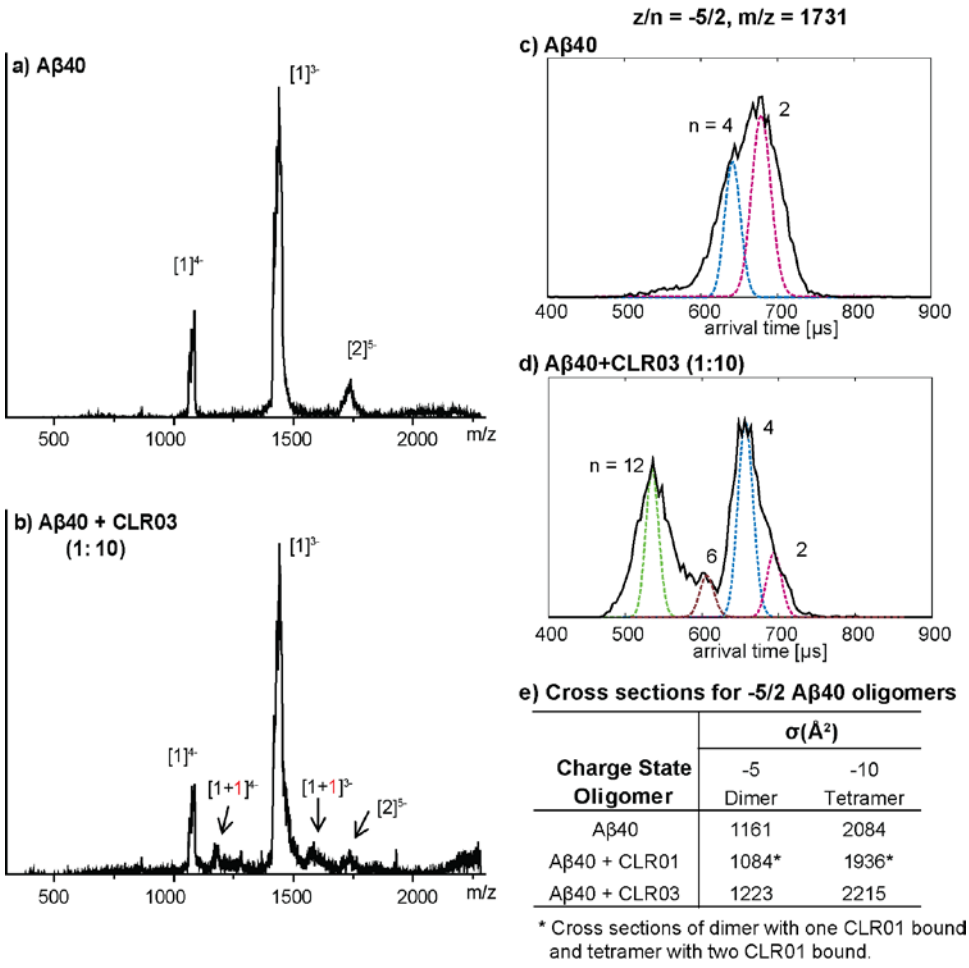

e) Cross sections for -5/2 Aβ40 oligomers

Charge State Oligomer	σ(Å²) -5 Dimer	σ(Å²) -10 Tetramer
Aβ40	1161	2084
Aβ40 + CLR01	1084*	1936*
Aβ40 + CLR03	1223	2215

* Cross sections of dimer with one CLR01 bound and tetramer with two CLR01 bound.

Figure 5.16 CLR03 facilitates Aβ40 assembly. a-b) Mass spectra of Aβ40 samples: a) Aβ40 alone; b) 1:10 mixture of Aβ40 and CLR03. Each species is noted in the bracket where the first number is the number of Aβ40 molecules and the second number, in red, represents the number of bound CLR03 molecules. The charge is noted as a superscript. c-d) ATDs of -5/2 Aβ40 peak (m/z = 1731) for the Aβ40 samples in the absence or presence of CLR03. Each ATD is fit with multiple features using the procedure described in the experimental section and the oligomer order (n) is noted for each feature. e) Cross sections of -5/2 Aβ40 oligomers for samples of Aβ40 in the absence or presence of CLR01 or CLR03. The error for the cross sections reported here is between 0-1%.

The ATDs of z/n = -3 and -4 peaks of the 1:10 Aβ40:CLR03 mixture (Figure 5.17) show features at arrival times shorter than those of monomers, suggesting formation of large

oligomers (n ≥2) in the presence of CLR03. Overall, these results reveal that CLR03 facilitates early oligomerization of Aβ40.

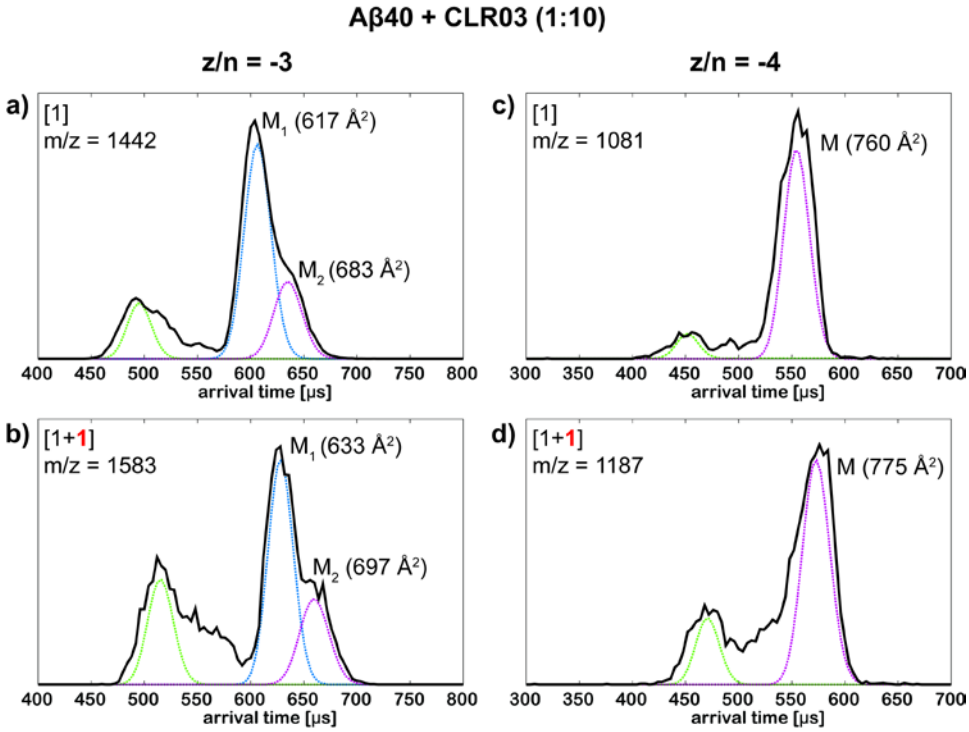

Figure 5.17 CLR03 facilitates Aβ40 assembly. a-b) ATDs of z/n = -3 Aβ40 without and with CLR03 bound (m/z = 1442 and 1583, respectively). c-d) z/n = -4 Aβ40 without and with CLR03 bound (m/z = 1081 and 1187, respectively) in the 1:10 mixture of Aβ40 and CLR03. Each ATD is fitted with multiple features using the procedure described in the experimental section. The oligomer order (n) and cross section are noted for each feature.

5.4 Discussion and Conclusions

Our mass spectrometry study of the lead molecular tweezer, CLR01, and the related derivative, CLR03, provides novel observations that could not have been obtained previously due to the low resolution of the methods used. Our investigation reveals that CLR01 and CLR03 bind to Aβ with very different affinities. Three CLR01 molecules bind

with relatively higher affinity and a fourth weakly, but only one CLR03 molecule binds weakly to Aβ.

The Aβ:CLR01 stoichiometry found in our study is consistent with previous data suggesting that there are three possible binding sites for molecular tweezers on Aβ at Arg5, Lys16, and Lys 28.[4] Possible explanations for our observation of a fourth CLR01 molecule weakly binding to Aβ40 and Aβ42 could simply stem from differences in instrumentation, or might reflect non-discriminating electrostatic and/or aromatic interactions between Aβ and CLR01 molecules, which might have been broken under harsher ionization conditions in the study by Sinha et al.[4] These nonspecific dispersive interactions could also explain the weak binding of one CLR03 molecule to Aβ, which was not observed within the limits of NMR detection in the previous study.[4]

The observation of three z/n = -5/2 oligomer complexes in the 1:1 and 1:2 mixtures of Aβ42 and CLR01, respectively, suggests that CLR01 not only binds to Aβ42 monomers but also to small Aβ42 oligomers (dimers and tetramers). Moreover, IMS reveals that CLR01 inhibits the formation of hexamers and dodecamers. This is important as dodecamers have been identified as probable toxic agents in AD.[12,14-15] Understanding the mechanism of how CLR01 blocks dodecamer formation is crucial for developing a therapeutic strategy for AD. Remarkably, the cross sections of the dimer and tetramer decreased substantially upon binding of CLR01 (See Table 5.1). These results suggest that CLR01 interacts with Aβ42 to change the folding of the monomer, which in turn changes the binding interface in dimer and tetramer formation resulting in compact structures that resist further aggregation. Once multiple CLR01 ligands bind to the monomer even dimer formation is prevented.

The ability of CLR01 to remodel early Aβ42 oligomerization after the oligomers had an opportunity to form and reach a quasi-equilibrium state for 4 hours was assessed by IMS as well. Interestingly, even at low concentration (1:1 ratio), CLR01 was capable of removing pre-formed Aβ42 dodecamers and hexamers. At high concentrations (1:5 and 1:10 ratios), CLR01 removes essentially all preformed Aβ42 oligomers. These data are consistent with the inhibition results immediately upon mixing Aβ42 and CLR01. It is possible that CLR01 binds to Aβ42 monomers and oligomers and redirects them into either a slower aggregation process or an off-pathway set of structures. In either case, the resulting structures are non-amyloidogenic and non-toxic.[4-6] Our data reveal for the first time that the loss of amyloid-formation propensity and toxicity correlate with disruption of the oligomerization process and compaction of oligomers formed in the presence of CLR01.

Surprisingly, the related derivative, CLR03, was found to facilitate the early aggregation of Aβ42, especially promoting the formation of hexamers and dodecamers. Perhaps even more surprisingly, CLR03 also facilitated the formation of hexamers and dodecamers in Aβ40, which does not form these oligomers on its own. Previous studies showed that CLR03 did not inhibit Aβ42- or Aβ40-induced neurotoxicity.[4] However, how CLR03 interacts with Aβ has been unclear. Given the fact that CLR03 is an organic phosphate, we wondered whether it is possible the addition of CLR03 has a simple "salting out"-like effect, which would thereby promote Aβ aggregation. To address this possibility, an organic phosphate, *p*-nitrophenylphosphate (PNPP) was added to Aβ samples and was found not to induce significant changes in Aβ oligomerization (see Figure 5.18). This result implies a simple "salting out"-like effect is not occurring for CLR03 and that CLR03 interacts with Aβ in a specific manner.

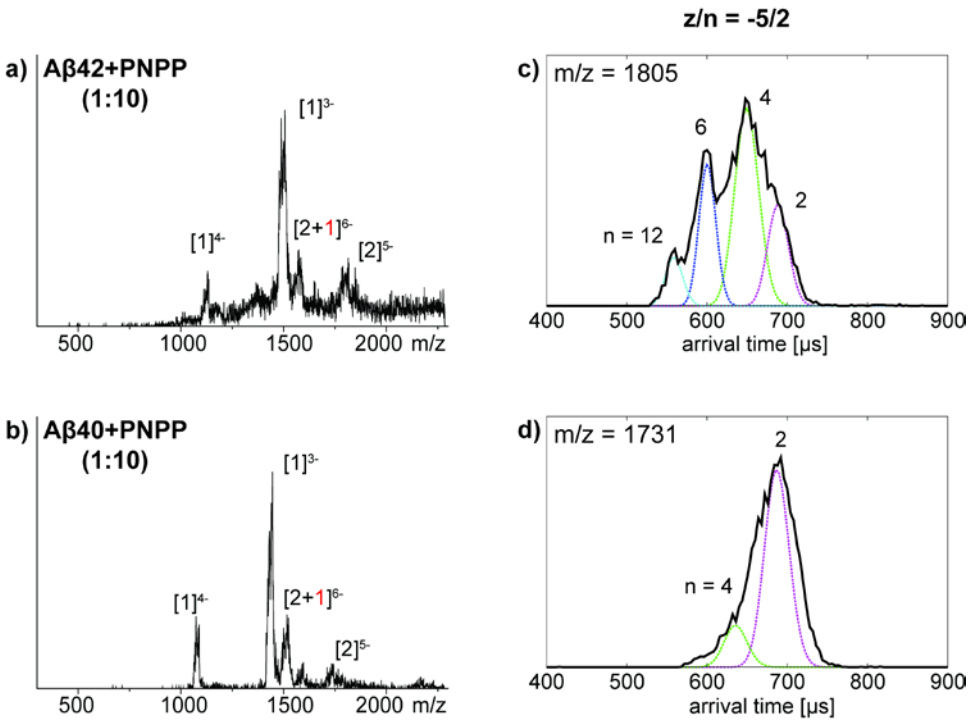

Figure 5.18 Evaluation of a putative "salting-out"-like effect of CLR03 by examining a simple organic phosphate, p-nitrophenylphosphate (PNPP) on Aβ42 oligomerization. a) and b) Mass spectra of 1:10 mixtures of Aβ42 or Aβ40 with PNPP. Each species is noted in the bracket where the first number is the number of Aβ40 molecules and the second number represents the number of bound CLR01 molecules. The charge is noted as a superscript. c) and d) ATDs of z/n = -5/2 peaks for 1:10 mixtures of Aβ42 /Aβ40 and PNPP. Each ATD is fitted with multiple features using the procedure described in the experimental section. The oligomer order (n) is noted for each feature.

A major difference between the structures of CLR01 and CLR03 is that CLR01 has a torus-shaped cavity whereas CLR03 does not have a cavity structure. CLR03 carries a bridge-like structure with negatively charged phosphate groups on each side. It is possible that one of the phosphate groups on CLR03 interacts with positively charged residues (Lys, Arg, N-terminus) of Aβ through Coulombic interactions. The other phosphate group on the other side of CLR03 could then attract a positively charged residue of another Aβ or Aβ

oligomer. Thus, by attracting positively charged residues in Aβ, CLR03 could facilitate Aβ oligomerization and aggregation.

Alternatively, CLR03 may interact weakly with two positively charged groups in a single Aβ, resulting in no observation of peaks for single Aβ with multiple CLR03 in the mass spectra (Figure 5.2b). As a consequence conformation change may occur that promotes Aβ assembly. This is a form of salting out and it may be more effective than PNPP. However, the fact that assembly is promoted to structures similar to wt Aβ42, speaks against salting out as a dominant assembly mechanism.

CLR01, which also carries two phosphate groups, however, does not catalyze Aβ oligomerization. This suggests that inclusion of lysine or arginine inside the cavity of CLR01 is of paramount importance for CLR01's mode of action. The central hydrophobic region of Aβ is regarded to be important for the hydrophobic clustering of Aβ. Recently a macrocyclic inhibitor cucurbit[7]uril has been shown to inhibit amyloid fibrillation by hydrophobic interactions with nonpolar phenylalanine residues of Aβ.[16] CLR01, which has hydrophobic arms, is likely to have additional hydrophobic interactions with lysine residues. The binding of CLR01 to lysine residues, especially Lys16 which is close to the central hydrophobic region of Aβ, may result in conformation change of Aβ and compaction of Aβ oligomers. Our data suggest that binding of CLR01 causes Aβ monomers to either resist oligomer formation altogether or to redirect them to non-toxic oligomer assembly.

Previous detailed analysis showed that Aβ40 formed a nearly closed planar tetramer that resisted further dimer addition.[12] Here, we found that adding CLR01 to Aβ40 significantly reduced the cross sections of both the dimer and tetramer leading to nearly

isotropic assembly and reducing the likelihood of even forming the tetramer, much less higher-order oligomers. On the other hand, the presence of CLR03 in the solution significantly extended both the dimer and tetramer yielding cross sections similar to those of the corresponding Aβ42 oligomers and leading to hexamer and dodecamer formation.

The essential features of these results are given in cartoon style in Figure 5.19. Aβ42 wt rapidly forms dodecamer but addition of the molecular tweezer CLR01 eliminates dodecamer formation by inducing the dimer and tetramer to form compact species that cannot add additional Aβ42. The opposite effect is obtained by CLR03. Aβ40 wt forms terminal compact tetramers but addition of CLR03 leads to open tetramer formation and eventual dodecamer formation. These contrary effects are potentially of great importance in Aβ assembly and require further study to reveal the details involved. These studies, which will include both high level molecular dynamics modeling and additional direct sampling of structures of Aβ oligomers are underway.

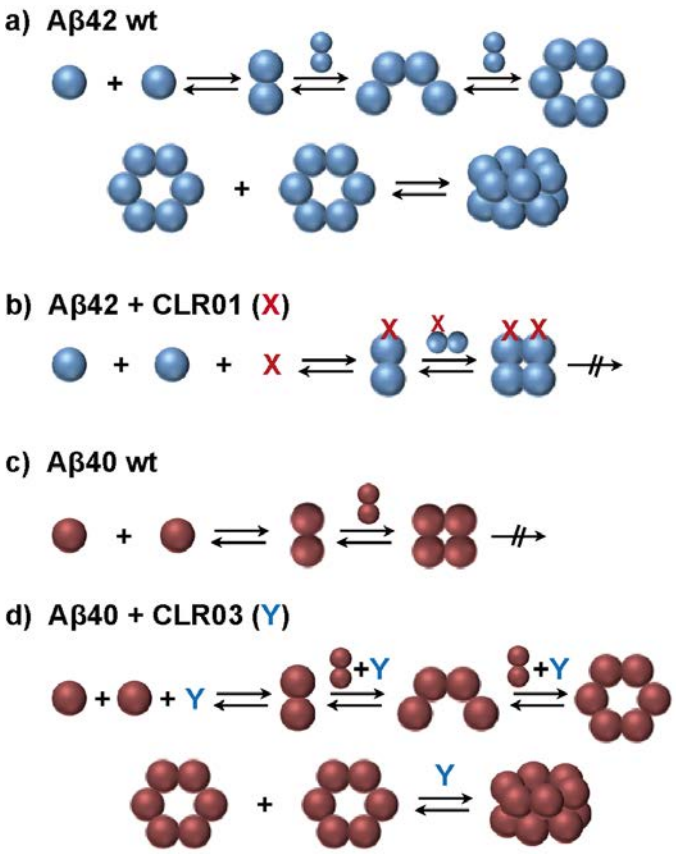

Figure 5.19 Different effects of CLR01 and CLR03 on Aβ early oligomerization. Oligomerization of a) Aβ42 wild type; b) Aβ42 with the presence of CLR01; c) Aβ40 wild type; d) Aβ40 with the presence of CLR03. Aβ42 and Aβ40 are represented with blue and red balls, respectively. CLR01 and CLR03 molecules are noted as X and Y.

References

1. Fokkens, M.; Schrader, T.; Klärner, F.-G. A Molecular Tweezer for Lysine and Arginine. *J. Am. Chem. Soc.* **2005,** *127*, 14415-14421.

2. Klärner, F.-G.; Schrader, T. Aromatic Interactions by Molecular Tweezers and Clips in Chemical and Biological Systems. *Accounts Chem. Res.* **2012,** *46*, 967-978.

3. Dutt, S.; Wilch, C.; Gersthagen, T.; Talbiersky, P.; Bravo-Rodriguez, K.; Hanni, M.; Sánchez-García, E.; Ochsenfeld, C.; Klärner, F.-G.; Schrader, T. Molecular Tweezers with Varying Anions: A Comparative Study. *J. Org. Chem.* **2013,** *78*, 6721-6734.

4. Sinha, S.; Lopes, D. H.; Du, Z.; Pang, E. S.; Shanmugam, A.; Lomakin, A.; Talbiersky, P.; Tennstaedt, A.; McDaniel, K.; Bakshi, R., et al. Lysine-Specific Molecular Tweezers are Broad-Spectrum Inhibitors of Assembly and Toxicity of Amyloid Proteins. *J. Am. Chem. Soc.* **2011,** *133*, 16958-16969.

5. Sinha, S.; Du, Z.; Maiti, P.; Klärner, F. G.; Schrader, T.; Wang, C.; Bitan, G. Comparison of Three Amyloid Assembly Inhibitors: the Sugar Scyllo-Inositol, the Polyphenol Epigallocatechin Gallate, and the Molecular Tweezer CLR01. *ACS Chem. Neurosci.* **2012,** *3*, 451-458.

6. Prabhudesai, S.; Sinha, S.; Attar, A.; Kotagiri, A.; Fitzmaurice, A. G.; Lakshmanan, R.; Ivanova, M. I.; Loo, J. A.; Klärner, F. G.; Schrader, T., et al. A Novel "Molecular Tweezer" Inhibitor of α-Synuclein Neurotoxicity In Vitro and In Vivo. *Neurotherapeutics* **2012,** *9*, 464-476.

7. Attar, A.; Ripoli, C.; Riccardi, E.; Maiti, P.; Li Puma, D. D.; Liu, T.; Hayes, J.; Jones, M. R.; Lichti-Kaiser, K.; Yang, F., et al. Protection of Primary Neurons and Mouse Brain From Alzheimer's Pathology by Molecular Tweezers. *Brain* **2012,** *135*, 3735-3748.

8. Wyttenbach, T.; Kemper, P. R.; Bowers, M. T. Design of a New Electrospray Ion Mobility Mass Spectrometer. *Int. J. Mass Spectrom.* **2001,** *212*, 13-23.

9. Wyttenbach, T.; Bowers, M. Gas-Phase Conformations: The Ion Mobility/Ion Chromatography Method. In *Modern Mass Spectrometry*, Schalley, C., Ed. Springer Berlin Heidelberg: 2003; Vol. 225, pp 207-232.

10. Lomakin, A.; Chung, D. S.; Benedek, G. B.; Kirschner, D. A.; Teplow, D. B. On the Nucleation and Growth of Amyloid β-Protein Fibrils: Detection of Nuclei and Quantitation of Rate Constants. *Proc. Natl. Acad. Sci. U. S. A.* **1996,** *93*, 1125-1129.

11. Bernstein, S. L.; Wyttenbach, T.; Baumketner, A.; Shea, J.-E.; Bitan, G.; Teplow, D. B.; Bowers, M. T. Amyloid β-Protein: Monomer Structure and Early Aggregation States of Aβ42 and Its Pro19 Alloform. *J. Am. Chem. Soc.* **2005,** *127*, 2075-2084.

12. Bernstein, S. L.; Dupuis, N. F.; Lazo, N. D.; Wyttenbach, T.; Condron, M. M.; Bitan, G.; Teplow, D. B.; Shea, J.-E.; Ruotolo, B. T.; Robinson, C. V., et al. Amyloid-β Protein Oligomerization and the Importance of Tetramers and Dodecamers in the Aetiology of Alzheimer's Disease. *Nat. Chem.* **2009,** *1*, 326-331.

13. Baumketner, A.; Bernstein, S. L.; Wyttenbach, T.; Bitan, G.; Teplow, D. B.; Bowers, M. T.; Shea, J.-E. Amyloid β-protein monomer structure: A computational and experimental study. *Protein Science* **2006,** *15*, 420-428.

14. Lesné, S.; Koh, M. T.; Kotilinek, L.; Kayed, R.; Glabe, C. G.; Yang, A.; Gallagher, M.; Ashe, K. H. A specific amyloid-β protein assembly in the brain impairs memory. *Nature* **2006,** *440*, 352-357.

15. Gong, Y.; Chang, L.; Viola, K. L.; Lacor, P. N.; Lambert, M. P.; Finch, C. E.; Krafft, G. A.; Klein, W. L. Alzheimer's disease-affected brain: presence of oligomeric Aβ ligands (ADDLs) suggests a molecular basis for reversible memory loss. *Proc. Natl. Acad. Sci. U. S. A.* **2003,** *100*, 10417-10422.

16. Lee, H. H.; Choi, T. S.; Lee, S. J. C.; Lee, J. W.; Park, J.; Ko, Y. H.; Kim, W. J.; Kim, K.; Kim, H. I. Supramolecular Inhibition of Amyloid Fibrillation by Cucurbit[7]uril. *Angew. Chem., Int. Ed.* **2014,** *53*, 7461-7465.

Chapter 6

Rational design of a novel molecule that targets and modulates Amyloid β and Metal-Aβ Species

This chapter is reproduced in part with permission from:

S. Lee, **X. Zheng**, J. Krishnamoorthy, M. G. Savelieff, H. M. Park, J. R. Brender, J. H. Kim, J. S. Derrick, A. Kochi, H. J. Lee, C. Kim, A. Ramamoorthy, M. T. Bowers, and M. H. Lim, "Rational design of a structural framework with potential use to develop chemical reagents that target and modulate multiple facets of Alzheimer's disease", *Journal of the American Chemical Society* **2014**, 136, 299–310.

6.1 Introduction

Development of a cure for Alzheimer's disease (AD) has been hindered by a lack of understanding of both the causes and mechanisms of disease onset and progression[1-5]. The AD brain exhibits several characteristic pathological features, such as accumulation of misfolded amyloid-β (Aβ), metal ion dyshomeostasis and miscompartmentalization, and elevated oxidative stress[1-10]. In addition to Aβ imbalance, high levels of metal ions (Cu, *ca*. 0.4 mM; Zn, *ca*. 1 mM; Fe, *ca*. 0.9 mM) have been found in Aβ plaques of AD brains[2,4-5,7-8,10-13]. These metals, particularly Cu and Zn, bind to Aβ peptides facilitating their aggregation. Moreover, dysregulated, redox-active metal ions, Cu(I/II) and Fe(II/III), both unbound and bound to Aβ peptides, are observed to promote overproduction of reactive oxygen species (ROS) that damage biological targets such as proteins, DNA, and lipids[2-3,7-10]. Overall, due to the involvement of numerous factors (*e.g.*, metal-free/-associated Aβ species, metals, free radicals) and their potential inter-connections in AD pathogenesis, the causative agents in this multifaceted disease remain unidentified.

Chemical reagents to target and modulate these multiple factors in AD are desirable to advance our understanding of AD complexity and offer possible answers for remediation. Toward this effort, small molecules have been developed via a rational structure-based approach by incorporating an Aβ-interacting framework with a metal chelation moiety into a single molecule designed to target metal–Aβ species[5,7,12,14-19]. These molecules were shown to control metal-induced Aβ aggregation, and attenuate ROS formation by metal–Aβ, and/or metal–Aβ toxicity in vitro and in living cells[14-19]. To the best of our knowledge, however, a single compound, targeting all these factors (*i.e.*, Aβ species, metal–Aβ species, metal ions, and free radicals, Figure 6.1a) and regulating their reactivities, has not been reported to date.

Herein we present a novel ligand (**ML**) as the first example of a rationally designed molecule to afford multifunctionality within a single entity (Figure 6.1a). Our investigations on **ML**'s activity toward Aβ, metal–Aβ, metal ions, and free radicals, as well as its potential blood-brain barrier (BBB) permeability confirm that careful selection and consideration of molecular properties can result in the design of a molecule to target multiple pathological features of AD.

6.2 Materials and methods

Materials. All reagents were purchased from commercial suppliers and used as received unless otherwise noted. Aβ40 and Aβ42 were purchased from Anaspec (Fremont, CA, USA) or synthesized by N-9-fluorenylmethoxycarbonyl (FMOC) chemistry. The compounds, (8-aminoquinolin-2-yl)methanol (**1**)[20-21] and 5-(dimethylamino)-2-hydroxybenzaldehyde[22], were prepared following previously reported procedures. NMR and mass spectrometric analyses of small molecules were conducted on a 400 MHz Varian NMR spectrometer and a Micromass LCT Electrospray Time-of-Flight (TOF) mass spectrometer, respectively. Trace metal contamination was removed from buffers and solutions used for metal binding and Aβ experiments by treating with Chelex overnight (Sigma-Aldrich, St. Louis, MO, USA). Optical spectra were recorded on an Agilent 8453 UV-Visible (UV-Vis) spectrophotometer. Transmission electron microscopic (TEM) images were taken using a Philips CM-100 transmission electron microscope (Microscopy and Image Analysis Laboratory, University of Michigan, Ann Arbor, MI, USA). Absorbance values for biological assays, including cell viability assay, parallel artificial membrane permeability assay adapted for blood-brain barrier (PAMPA-BBB), 2-deoxyribose assay, and Trolox

equivalent antioxidant capacity (TEAC) assay, were measured on a SpectraMax M5 microplate reader (Molecular Devices, Sunnyvale, CA, USA). Mass spectra for investigating the interaction of Aβ with **ML** in the absence and presence of Cu(II) and Zn(II) were acquired on a traveling-wave Quadrupole TOF (Q-TOF) mass spectrometer (Waters Synapt Prototype; Milford, MA, USA)[23] and a home-built electrospray ionization (ESI) ion mobility-mass spectrometer[24]. NMR studies of Aβ with **ML** and/or Zn(II) were conducted on a 900 MHz Bruker spectrometer equipped with a cryogenic probe at Michigan State University in Lansing, MI USA.

Synthesis of 4-(dimethylamino)-2-(((2-(hydroxymethyl)quinolin-8-yl)amino)methyl)phenol (ML). A solution (dry ethyl acetate (EtOAc), 8.0 mL) of **1**[20-21] (174 mg, 0.99 mmol) and 5-(dimethylamino)-2-hydroxybenzaldehyde[22] (164 mg, 0.99 mmol) was stirred overnight at room temperature. After removing the solvent, the resulting solid material was dissolved in dichloroethane (DCE, 8.0 mL) followed by addition of sodium triacetoxyborohydride ($NaB(OAc)_3H$, 420 mg, 2.0 mmol). After stirring for 24 h at room temperature, the crude product was purified by column chromatography (SiO_2, 1:5 hexanes/EtOAc, R_f = 0.47). The final product (orange powder, HCl salt form) was obtained by recrystallization (upon addition of 1:1 HCl/H_2O to a MeOH solution of crude products) (198 mg, 0.50 mmol, 51%).

Ion mobility-mass spectrometry (IM-MS). Lyophilized Aβ40 and Aβ42 were dissolved in 10 mM ammonium acetate buffer (pH 7.4) to generate a final peptide concentration of 10 μM for all mass spectrometry experiments. Mass spectra were recorded on a prototype of the commercial Waters Synapt instrument (Milford, MA, USA)[23] and a home-built ESI ion mobility-mass spectrometer[24] which is described in Chapter 2.

Transmission electron microscopy (TEM). Samples for TEM were prepared according to previously reported methods[14-18,25]. Glow-discharged grids (Formar/Carbon 300-mesh, Electron Microscopy Sciences, Hatfield, PA, USA) were treated with Aβ samples from the inhibition and disaggregation experiments (5 μL) for 2 min at room temperature. Excess sample was removed using filter paper followed by washing twice with ddH_2O. Each grid was incubated with uranyl acetate (1% w/v ddH_2O, 5 μL, 1 min). Upon removal of excess uranyl acetate, the grids were dried for 15 min at room temperature. Images from each sample were taken on a Philips CM-100 transmission electron microscope (80 kV, 25,000x magnification).

Cell viability measurements. The murine neuroblastoma Neuro-2a (N2a) cell line was purchased from the American Type Cell Collection (ATCC, Manassas, VA, USA). N2a cells stably overexpressing the Swedish mutant (K670N and M671L) human amyloid precursor proteins (APP) (N2aAPPswe)[26] were the generous gift of Professor Gopal Thinakaran (University of Chicago). Both cell lines ware maintained in media containing 45% DMEM, 50% OPTI-MEM, 5% fetal bovine serum (FBS, Atlanta Biologicals, Lawrenceville, GA, USA), 100 U/mL penicillin (Gibco, Grand Island, NY, USA), and 100 mg/mL streptomycin (Gibco). For the N2aAPPswe cell line, 0.2 mg/mL G418 (geneticin, Gibco) was added to the culture medium. The cells were grown in a humidified atmosphere with 5% CO_2 at 37 °C. For the MTT assay (MTT = 3-(4,5-dimethyl-2-thiazolyl)-2,5-diphenyl-2H-tetrazolium bromide)**,** cells were seeded in a 96 well plate (15,000 cells/100 μL). The cells were then treated with Aβ (10 μM) with or without $CuCl_2$ or $ZnCl_2$ (10 μM) followed by the addition of **ML** or **1** (final concentration 10 μM, 1% v/v final DMSO concentration). After 24 h incubation, 25 μL MTT (5 mg/mL in phosphate buffered saline (PBS, pH 7.4, Gibco

(Grand Island, NY, USA)) was added to each well and the plate was incubated for 4 h at 37 °C. Formazan produced by the cells was solubilized by addition of an acidic solution of *N*,*N*-dimethylformamide (50%, v/v, aq) and sodium dodecyl sulfate (SDS, 20%, w/v) overnight at room temperature in the dark. The absorbance was measured at 600 nm using a microplate reader.

2-Deoxyribose assay. The ability of **ML** to suppress free radical Fenton chemistry was determined by the 2-deoxyribose assay. The assay was performed based on previously established methods with some modifications[36]. Chelexed solutions were used and reactions (total volume, 200 μL) were setup by mixing, in the following order, buffer (50 mM NaH_2PO_4, pH 7.4), ligand (50-200 μM), $CuCl_2$ (10 μM), 2-deoxy-D-ribose (15 mM), H_2O_2 (200 μM), and sodium ascorbate (2 mM), and allowed to react for 1 h at 37 °C with constant agitation. The reactions were quenched upon addition of trichloroacetic acid (200 μL of 2.8% w/v) and 2-thiobarbituric acid (200 μL of 1% w/v) and heated at 100 °C for 20 min, cooled for 5 min, and their absorbance values at 532 nm measured immediately afterwards. In addition, samples without ligand were prepared as a control. Experiments were performed in two sets of triplicates (6 data points) and absorbance data was averaged over all six measurements for each ligand at each concentration. Normalized absorbance values (A/A_0) were calculated by taking the absorbance (A) and dividing by the absorbance of the control (A_0).

Trolox equivalent antioxidant capacity (TEAC) assay. The antioxidant activity of **ML** and **1** was determined by the TEAC assay. The assay was performed according to the previously reported method with slight modifications[27-28]. To generate blue ABTS cation radicals ($ABTS^{+\bullet}$; ABTS = 2,2'-azino-bis(3-ethylbenzothiazoline-6-sulfonic acid)

diammonium salt), a solution of ABTS (7.0 mM) and potassium persulfate (2.5 mM) was prepared in 5 mL water and incubated for 16 h at room temperature in the dark. The resulting solution was diluted with EtOH to an absorbance of *ca.* 0.7 at 734 nm. $ABTS^{+\bullet}$ solution (200 μL) was added to the wells of a clear 96 well plate and incubated for 5 min at 30 °C. Various concentration (0, 1, 2.5, 5, 7.5, 10, and 15 μM) of **ML**, **1** (1% v/v final DMSO concentration), or Trolox (Trolox = 6-hydroxy-2,5,7,8-tetramethylchroman-2-carboxylic acid; dissolved in EtOH) were added and incubated with the $ABTS^{+\bullet}$ solution at 30 °C for different time periods (1, 3, 6, and 10 min). The percent inhibition was calculated according to the measured absorbance at 734 nm (% inhibition = $100 \times (A_0 - A)/A_0$) and was plotted as a function of ligand concentration. The TEAC value of compounds for each time point was calculated as a ratio of the slope of the standard curve of the compound to that of Trolox. The measurements were carried out in triplicate.

Parallel artificial membrane permeability adapted for blood-brain barrier (PAMPA-BBB) assay. PAMPA-BBB experiments were carried out using the PAMPA Explorer kit (*p*ION Inc., Billerica, MA, USA) with modification to previously reported protocols[14,18-19,25,29-30]. Each stock solution was diluted with Prisma HT buffer (pH 7.4, *p*ION) to a final concentration of 25 μM (1 % v/v final DMSO concentration). The resulting solution was added to wells of the donor plate (200 μL, number of replicates = 12 (for **ML**) and 11 (for **1**)). BBB-1 lipid formulation (5 μL, *p*ION) was used to coat the polyvinylidene fluoride (PVDF, 0.45 μM) filter membrane on the acceptor plate. This acceptor plate was placed on top of the donor plate forming a sandwich. Brain sink buffer (BSB, 200 μL, *p*ION) was added to each well of the acceptor plate. The sandwich was incubated for 4 hours at ambient temperature without stirring. UV-Vis spectra of the solutions in the reference,

acceptor, and donor plates were measured using a microplate reader. The PAMPA Explorer software v. 3.5 (*p*ION) was used to calculate logP_e for each compound. CNS/designations were assigned by comparison to compounds that were identified in previous reports[14,18-19,25,29-30].

6.3 Results and discussion

6.3.1 Design consideration for a multifunctional molecule (ML)

To develop a chemical tool capable of both targeting and modulating the reactivity of multiple AD pathological factors in biological systems, we designed a novel molecule (**ML**) with the potential for Aβ and metal-Aβ interaction, metal chelation, control of ROS generation, antioxidant activity, water solubility, and blood-brain barrier (BBB) permeability (Figure 6.1a). For Aβ/metal-Aβ interactions and metal chelation, **ML** was constructed by combining *p*-I-stilbene, a known Aβ imaging agent[14,31-33], L2-b, a molecule previously reported to target metal–Aβ[15], and **1**, a metal chelator[20] (Figure 6.1). For enhanced metal binding properties, an additional hydroxyl group, along with nitrogen and oxygen donor atoms from **1**, was incorporated into **ML** affording a tetradentate ligand for Cu(II) with 1:1 metal-to-ligand stoichiometry[20]. **ML** was designed to accommodate a slightly distorted square planar geometry for Cu(II) similar to 2-[(8-quinolinylamino)methyl]phenol[20]. In this conformation, the ligand cannot easily accommodate the preferred tetrahedral geometry of Cu(I) for redox cycles of Cu(I/II) and thus inhibits ROS generation. For antioxidant activity, substituents known to have antioxidant capability (*i.e.*, quinoline and phenolic groups, Figure 6.1)[28–30] were integrated

into **ML**. Lastly, polar functionalities (*e.g.*, hydroxyl and amino groups) were introduced into the backbone for water solubility. All structural elements were selected to adhere to values of Lipinski's rules and logBB for possible drug-likeness and BBB penetration (Table 6.1)[15,19,25,29-30].

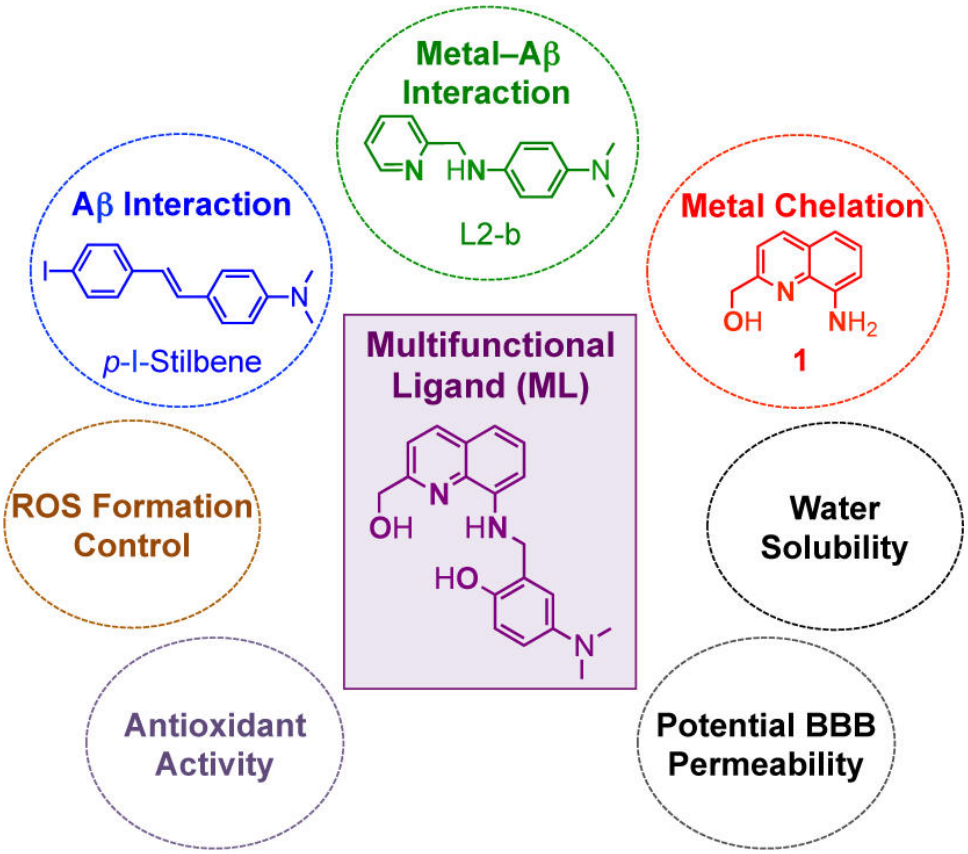

Figure 6.1 Rational structure-based design principle (incorporation approach) of a multifuncitonal ligand (ML). Atoms responsible for metal binding are in bold. Chemical structures: ML = 4-(dimethylamino)-2-(((2-(hydroxymethyl)quinolin-8-yl)-amino)-methyl)phenol; p-I-stilbene = (E)-4-(4-iodostyryl)-N,N-dimethylaniline); L2-b = N1,N1-dimethyl-N4-(pyridin-2-ylmeth-yl)benzene-1,4-diamine; **1** = (8-aminoquinolin-2-yl)methanol.

ML was synthesized by modifications of previously reported procedures (Schiff base condensation followed by reduction of imine to amine, *ca.* 50% yield) as shown in Figure 6.2[20].

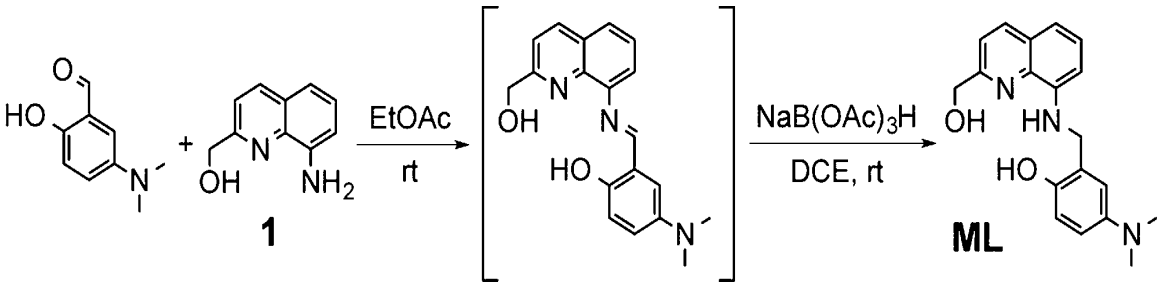

Figure 6.2 Synthesis scheme of ML compound.

6.3.2 Mass Spectrometry: ML interacts with Aβ42 directly

To determine whether **ML** binds to Aβ42, the mass spectra of Aβ42 samples with and without **ML** were recorded and are shown in Figure 6.3. In the mass spectrum of a 1:5 mixture of Aβ42 and **ML** (Figure 6.3a), there were three peaks corresponding to Aβ42 with charge (z) to oligomer number (n) ratio z/n = -4, -3, and -5/2, similar to the mass spectrum of pure Aβ42 without **ML** (Figure 6.3b). Moreover, there were two tailing peaks (m/z = 1611 and 1719, respectively) corresponding to z/n = -3 complexes of Aβ42 with one and two **ML** molecules bound, respectively. These results show that ML binds to Aβ42 directly.

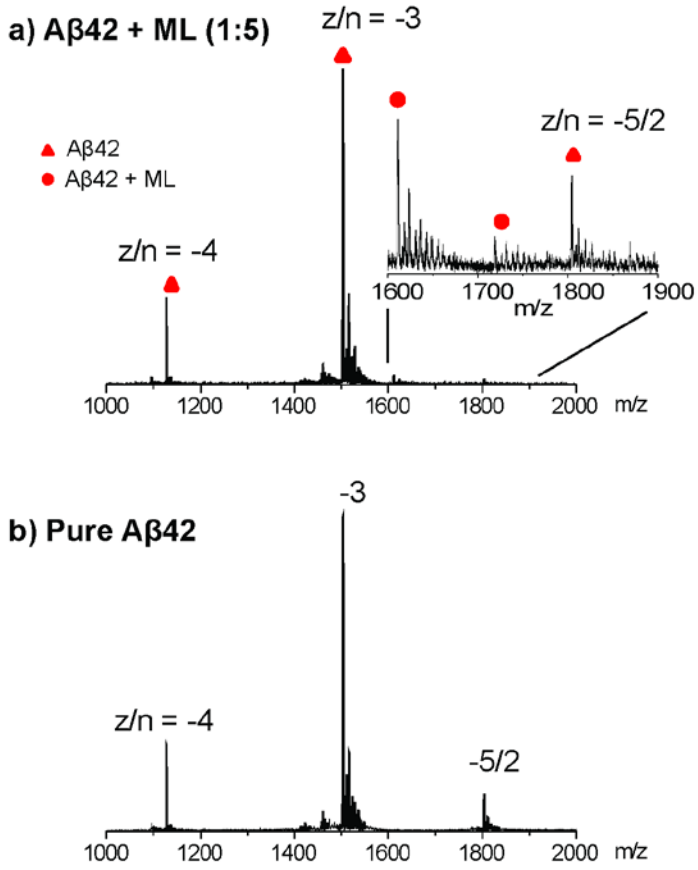

Figure 6.3 ML interacts with Aβ42 directly. Mass spectra of **(a)** 1: 5 mixture of Aβ42 and **ML** and **(b)** pure Aβ42. The charge state z/n is noted for each species, where z is the charge and n is the oligomer number.

6.3.3 Ion mobility spectrometry: ML modulates Aβ42 early assembly

To test the effects of **ML** on Aβ42 assembly, the arrival time distributions (ATDs) of the z/n = -5/2 peaks for Aβ42 samples with and without **ML** were recorded and are shown in Figure 6.4. The ATD of the –5/2 peak of Aβ42 without **ML** (Figure 6.4b) shows four features with arrival times at ~ 720, 680, 620, and 540 μs, previously assigned[34] as the -5 dimer, -10 tetramer, -15 hexamer, and -30 dodecamer, respectively (see ref. 32 for detailed discussion of -5/2 peak assignments). The dodecamers, potentially associated with memory impairment in mice[35], is of particular interest to AD pathology. ATD of -5/2 peak for **ML**

treated Aβ42 exhibited only three features which are assigned to the -5 dimer, -10 tetramer, and -15 hexamer based on their cross sections (Figure 6.4a). Notably, the feature representing Aβ42 dodecamer is not observed in the presence of **ML**. In addition, the intensity of hexamer feature is lower compared to that of the Aβ42 sample without **ML** (Figure 6.4b). These results indicate that dodecamer formation is completely inhibited and hexamer formation is partially inhibited by **ML**.

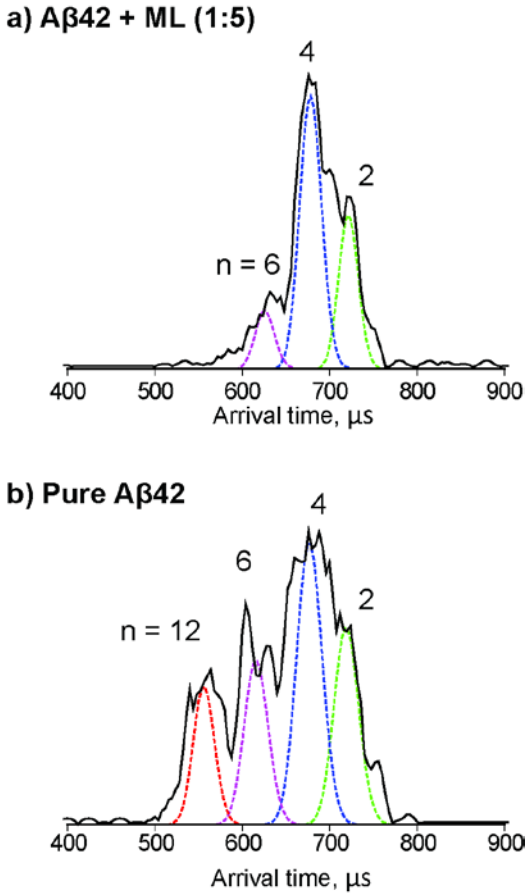

Figure 6.4 ML inhibits Aβ42 oligomerization. ATDs of the z/n = -5/2 for (a) 1: 5 mixture of Aβ42 and **ML**, and (b) pure Aβ42. The oligomer number (n) is noted for each species. The dashed lines represent the peak shape for a single conformation.

6.3.4 ML remodeling Aβ42 oligomerization

The ability of **ML** to disaggregate preformed Aβ aggregates was also explored. The

ATD for pure Aβ42 incubated on ice for ~4 hours shows four features corresponding to Aβ42 dimers, tetramers, hexamers, and dodecamers (Figure 6.5a). Concentrated **ML** was added to the pre-incubated Aβ42 sample to make a 1:5 mixture of Aβ42 and **ML**. The -5/2 ATD of the mixture (Figure 6.5b) shows only three features corresponding to Aβ42 dimers, tetramers, hexamers. Note that the dodecamers disappears after the addition of **ML**, implying **ML** disaggregates pre-formed dodecamers. Taken together, these ion mobility studies indicate that **ML** not only inhibits dodecamer formation but also removes preformed dodecamers in the early oligomerization of Aβ42.

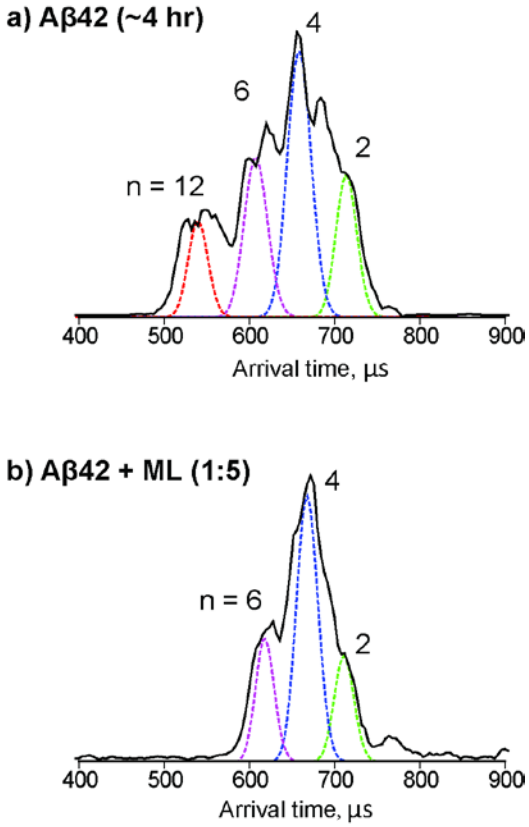

Figure 6.5 ML remodels Aβ42 oligomerization. ATDs of the z/n = -5/2 for (a) pure Aβ42 after 4 hours' incubation on ice, and (b) after addition of 1:5 ML to the pre-incubated sample. The oligomer number (n) is noted for each species. The dashed lines represent the peak shape for a single conformation.

6.3.5 Effects of ML on Aβ40 oligomerization

The effects of **ML** on Aβ40 system were investigated and the results are shown in Figure 6.6. In the mass spectrum of the mixture of Aβ40 and **ML**, a tailing peak corresponding to the z/n = −3 complex of Aβ40 and **ML** was also observed. These results suggest **ML** can directly bind to both Aβ40 and Aβ42 with either a 1:1 or 1:2 Aβ: **ML** stoichiometry. However, **ML** does not affect the early oligomerization of Aβ40 significantly, Aβ40 forming dimers and tetramers with or without ML.

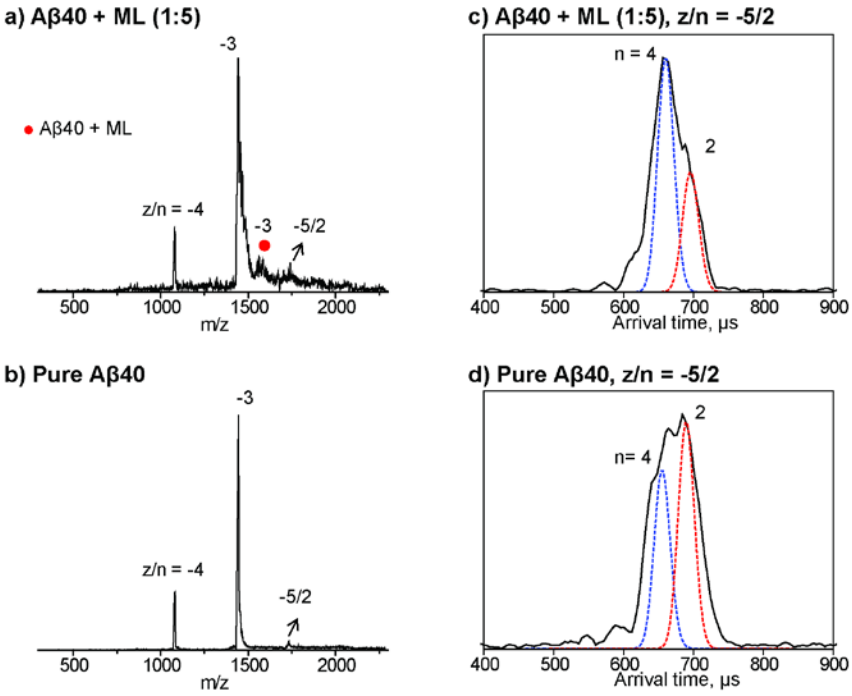

Figure 6.6 Effects of **ML** on Aβ40. Mass spectra of (a) 1: 5 mixture of Aβ40 and **ML** and (b) pure Aβ40. The charge state z/n is noted for each species, where z is the charge and n is the oligomer number. (c) and (d) ATDs of the z/n = -5/2 peak for 1: 5 mixture of Aβ42 and ML, and pure Aβ42, respectively. The oligomer number (n) is noted for each species. The dashed lines represent the peak shape for a single conformation.

6.3.6 Effects of ML on Metal-associated Aβ42 species

To further explore the effects of ML on metal-associated Aβ species, we performed

MS analysis to examine the interactions of **ML** and Cu(II)- or Zn(II)-associated Aβ samples. The results of Cu(II)-associated Aβ42 samples are shown in Figure 6.7. The mass spectrum of a 1:1 mixture of Aβ42 and Cu(II) without **ML** shows two sets of peaks for each charge state z/n = -4, -3, and -5/2, corresponding to Aβ42 with one and two Cu(II) binding, respectively (Figure 6.7b). Metal-free Aβ42 species are not observed under these conditions. When **ML** was added to preincubated Cu(II)-Aβ42, a mixture of species was perceived (Figure 6.7a). In addition to the peaks observed in **ML**-free samples corresponding to Aβ42 with one or two Cu(II), three additional peaks representing metal-free Aβ42 with z/n = -4, -3, and -5/2 were also detected, indicating **ML** can competitively chelate Cu(II) from Aβ42. Note that peak intensities of Aβ42 with two Cu(II) bound decreased dramatically upon **ML** addition. A tailing peak corresponding to a complex of Aβ42 with one **ML** bound was observed. Moreover, peaks corresponding to complexes of Aβ42 and **ML** and one or two Cu(II) (m/z = 1633 and 1653, respectively) were present, indicating **ML** bound to Aβ42 and metal-Aβ42.

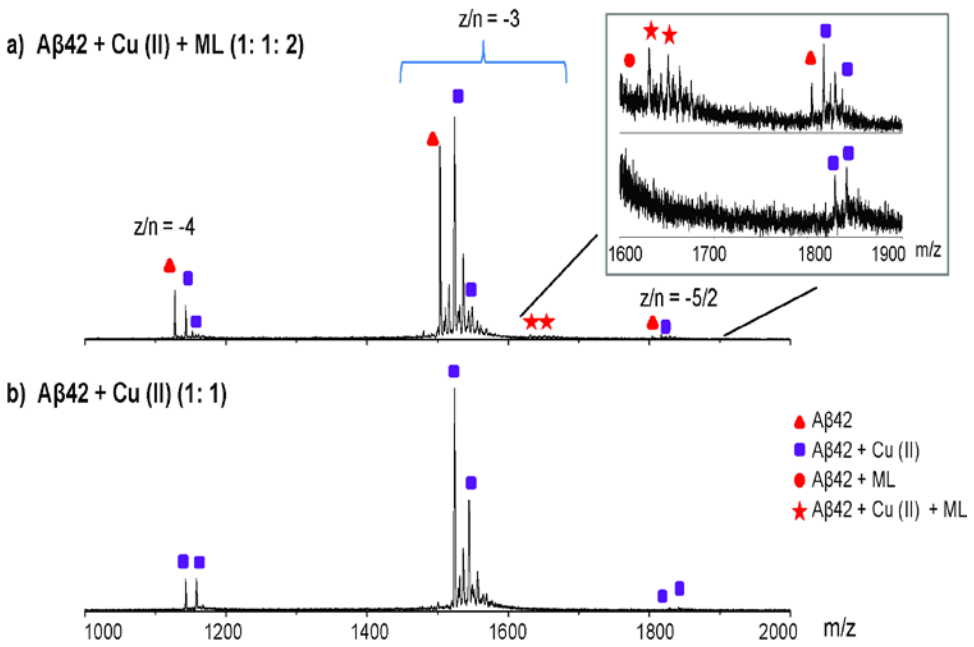

Figure 6.7 ML interacts with Cu-associated Aβ42 species. Mass spectra of (**a**) an 1: 1: 2 mixture of Aβ42, Cu(II), and **ML**; (**b**) an 1:1 mixture of Aβ42 and Cu(II). Peaks for pure Aβ42, Cu(II)-bound Aβ42, **ML**-bound Aβ42, and Aβ42-Cu(II)-**ML** complexes are noted with triangles, rectangles, circles, and stars, respectively.

Zn(II)-associated Aβ40/42 were also investigated with **ML**. The mass spectrum of a 1: 1: 2 mixture of Aβ42: Zn(II): **ML** showed peaks corresponding to Aβ42-Zn(II)-**ML** complexes (z/n= -3 and -5/2) as well as slight increased intensity of peaks corresponding metal-free Aβ compared to those without **ML** (Figure 6.8). Overall, these results indicate that **ML** not only forms complexes with both Cu(II)–Aβ and Zn(II)–Aβ but also competitively chelates metal ions from metal–Aβ generating metal-free Aβ species.

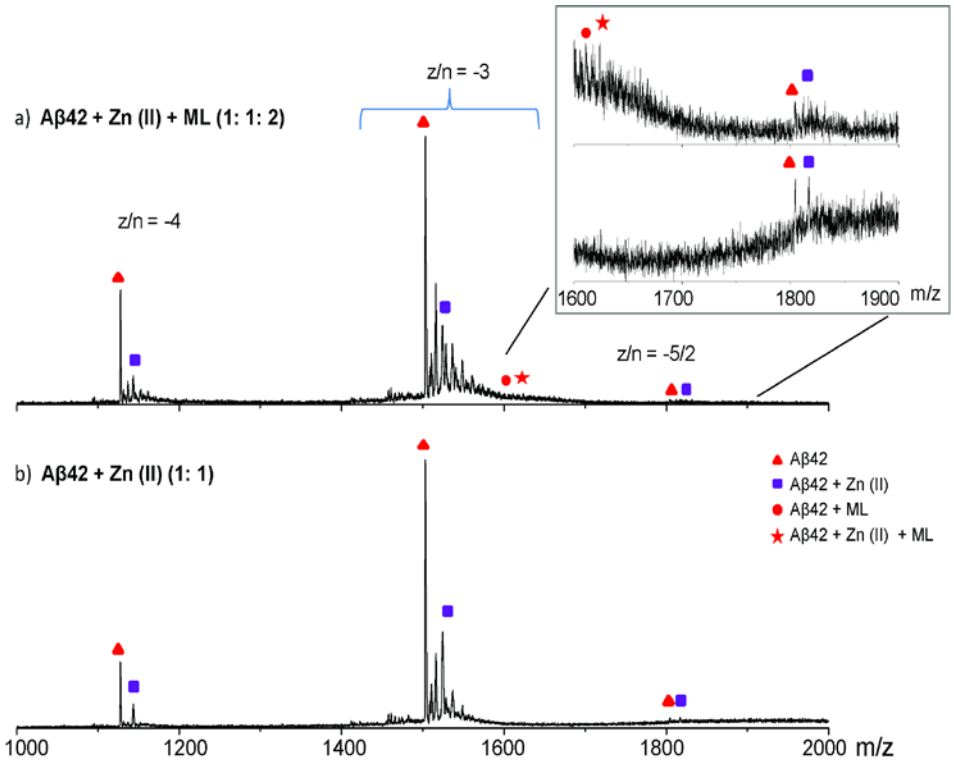

Figure 6.8 ML interacts with Zn-associated Aβ42 species. Mass spectra of (a) an 1: 1: 2 mixture of Aβ42, Zn(II), and **ML**; (b) an 1:1 mixture of Aβ42 and Zn(II). Peaks for pure Aβ42, Zn(II)-bound Aβ42, **ML**-bound Aβ42, and Aβ42-Zn(II)-**ML** complexes are noted with triangles, rectangles, circles, and stars, respectively.

As for Aβ40, the mass spectrum of pre-incubated metal-Aβ40 treated with **ML** displayed peaks indicative of both Aβ40-metal-**ML** complexes and metal-Aβ40 complexes (Figure 6.9).

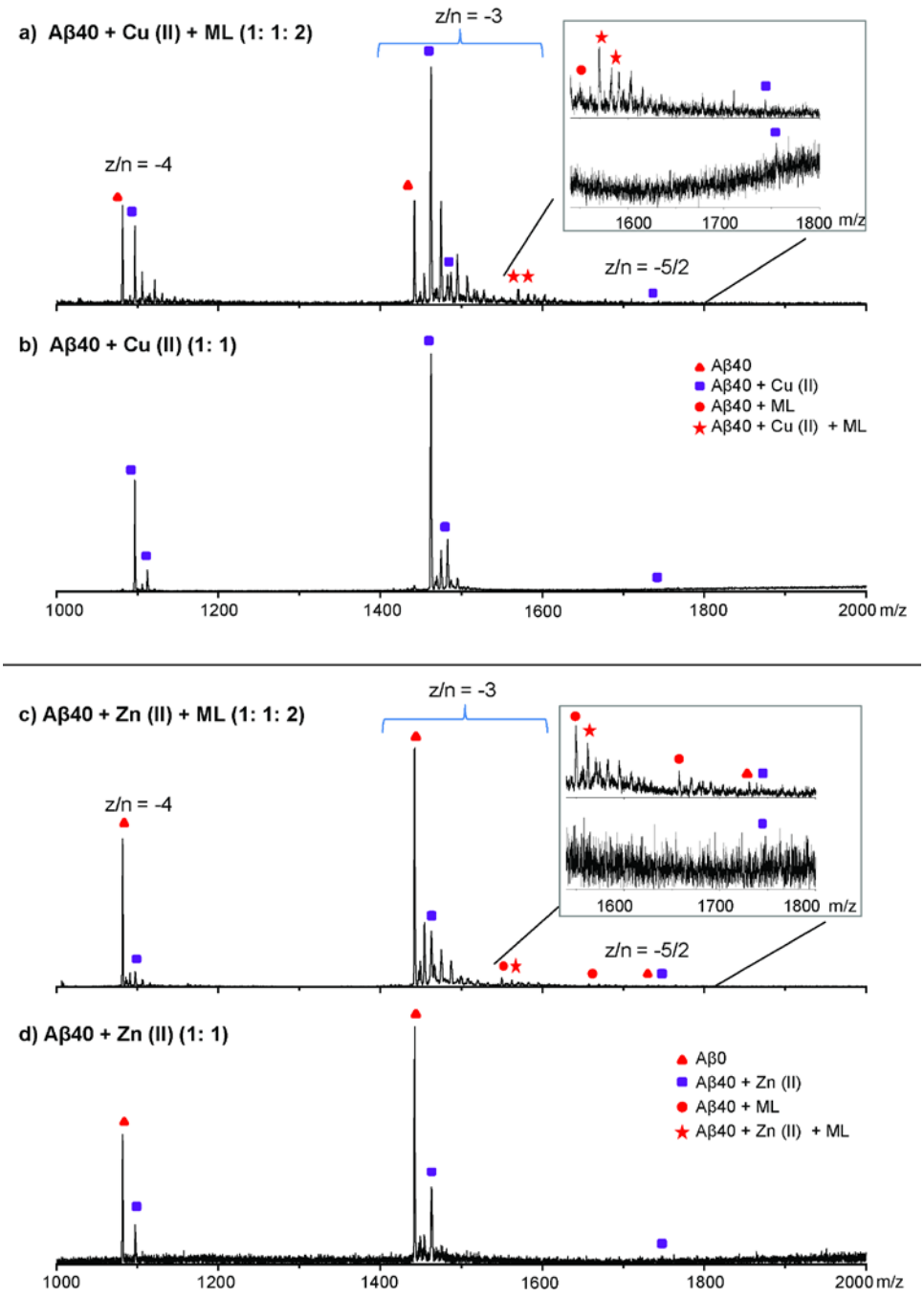

Figure 6.9 ML interacts with metal-associated Aβ40 species. Mass spectra of (a) an 1: 1: 2 mixture of Aβ40, Cu(II), and **ML**; (b) an 1:1 mixture of Aβ40 and Cu(II); (**c**) an 1: 1: 2 mixture of Aβ40, Zn(II), and **ML**; (d) an 1:1 mixture of Aβ40 and Zn(II). Peaks for pure Aβ40, Metal-bound Aβ40, **ML**-bound Aβ40, and Aβ40-Metal-**ML** complexes are noted with triangles, rectangles, circles, and stars, respectively.

6.3.7 Effects of ML on the fibril formation of Aβ and metal-Aβ species

Morphological alterations of Aβ species were examined by TEM and the results are shown in Figure 6.10. Upon incubation of both Aβ40 and Aβ42 without metal ions for 24 h at 37 °C, well-ordered, fibril structures were observed. Even more aggregated forms were observed in the presence of Cu(II) or Zn(II). Addition of **ML** to both Aβ40 and Aβ42 aggregates resulted in aggregates which were much smaller and less ordered than in the controls in the absence of **ML**. These results clearly show that compound **ML** is able to inhibit metal-induced Aβ fibril formation.

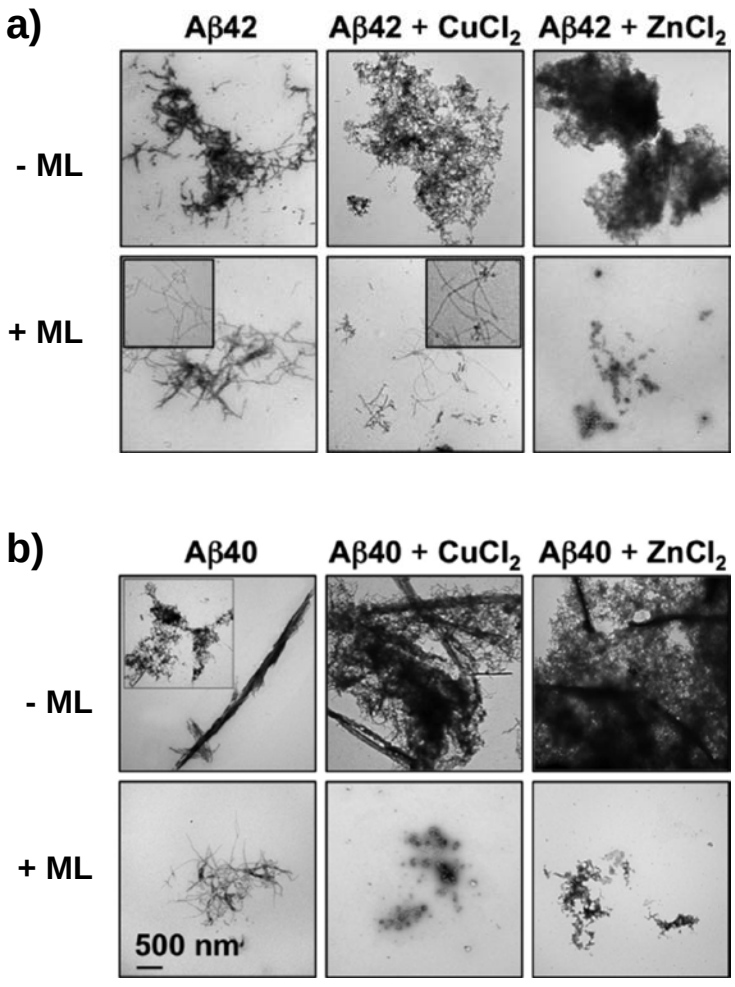

Figure 10. The Effects of ML on the fibril formation of Aβ and Metal-associated Aβ. TEM images of (a) Aβ42 and (b) Aβ40 samples with 24 hours' incubation at 37 °C.

6.3.8 ML rescues Aβ and metal-associated Aβ induced cell toxicity

We examined the neuroprotective properties of **ML** toward Aβ- or metal–Aβ-induced toxicity in murine Neuro-2a neuroblastoma cells with and without overexpression of the Swedish mutant human APP (N2aAPPswe AD cell line[42]; both Aβ40 and Aβ42 were examined). Cells incubated with Aβ (10 μM) for 24 h with/without metal (Cu(II) or Zn(II), 10 μM) showed viability of *ca*. 70% (Aβ), *ca*. 60–70% (Aβ with Cu(II)), or *ca*. 70% (Aβ with Zn(II)) (Figure 6.11a). Upon addition of **ML** (10 μM) to Aβ-treated N2aAPPswe or N2a cells, *ca*. 100% cell survival was observed with and without metal ions (Figure 6.11a). Overall, our cell studies suggest **ML** may regulate metal-free and metal-associated Aβ-induced toxicity in living cells.

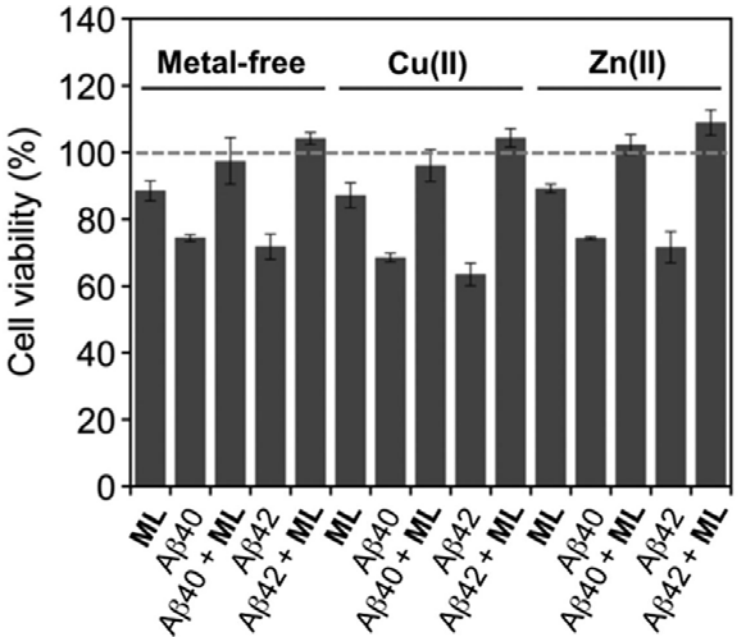

Figure 6.11 Effect of ML on toxicity triggered by metal-free Aβ and metal-Aβ species in N2aAPPswe cells. Cells treated with Aβ (10 μM), a metal chloride salt ($CuCl_2$ or $ZnCl_2$; 10 μM), or ML (10 μM) were incubated for 24 h at 37 °C. Cell viability (%) was determined by the MTT assay compared to cells treated with DMSO only (0−1%, v/v) (MTT = 3-(4,5-dimethyl-2-thiazolyl)-2,5-diphenyl-2H-tetrazolium bromide). Data are mean ± SEM, $P < 0.05$, $n = 3$.

6.3.9 ROS formation control, antioxidant activity, and BBB permeability of ML

From a biological perspective, inhibiting ROS formation by binding and constraining Cu(II) from redox cycling is an attractive feature. Accordingly, we explored the inhibitory ability of **ML** toward ROS production by 2-deoxyribose assay. As shown in Figure 6.12, copper-mediated generation of hydroxyl radicals is significantly reduced upon treatment with **ML**.

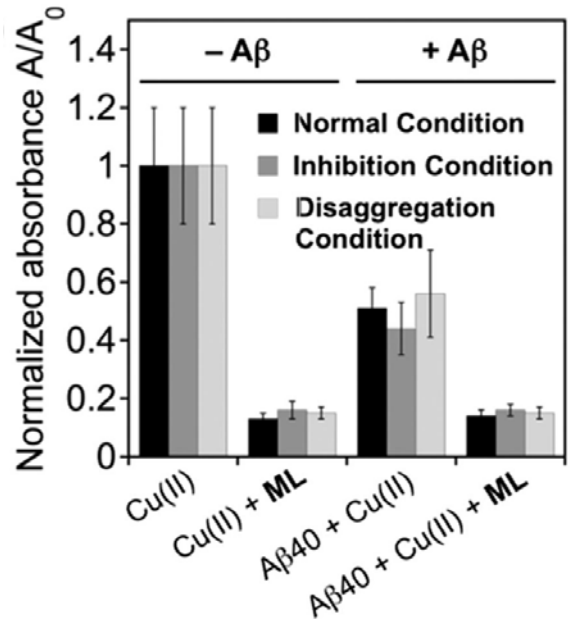

Figure 6.12 Inhibitory activity toward ROS formation in the absence and presence of freshly prepared Aβ40 (normal condition) and Aβ40 aggregates (inhibition and disaggregation conditions), determined by the 2-deoxyribose assay. The absorbance values are normalized compared to ligand-free condition (Aβ/$CuCl_2$/ML = 25/10/125 μM).

The antioxidant activity of **ML** was evaluated by the Trolox equivalent antioxidant capacity (TEAC) assay which measures a compound's ability to quench ABTS cation radicals ($ABTS^{+\bullet}$; ABTS = 2,2'-azino-bis(3-ethylbenzothiazoline-6-sulfonic acid))[27-28,36]. **ML** scavenges free radicals more effectively than **1** and Trolox (vitamin E analogue) by a

factor of 2.6 (Figure 6.13), suggesting the presence of both quinoline and phenolic groups within one framework could enhance antioxidant capability.

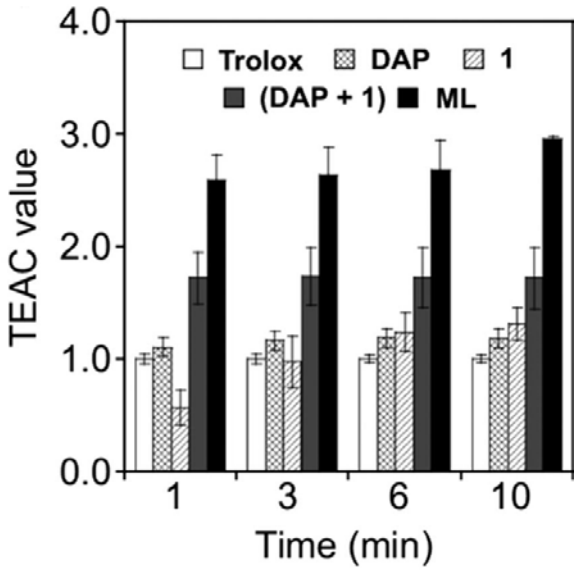

Figure 6.13 Antioxidant activity of ML, DAP, 1, and a mixture of DAP and 1 (DAP + 1) identified by the TEAC assay. The TEAC values are relative to a vitamin E analogue, Trolox (6-hydroxy-2,5,7,8-tetramethylchroman-2-carboxylic acid).

Lastly, for potential brain applications, the BBB permeability of **ML**, predicted from Lipinski's rules and logBB (Table 6.1), was examined by the parallel artificial membrane permeability assay adapted for BBB (PAMPA-BBB)[15,19,25,29-30]. These values (Table 6.1), when compared to previously reported BBB permeable molecules[25,29-30], indicate that **ML** may cross the BBB, making this molecule valuable for potential brain applications.

Compound	MW	*c*logP	HBA	HBD	PSA (Å)	logBB	$-\log P_e$	CNS+/− prediction[b]
ML	323	2.57	5	3	68.1	−0.478	4.49 ± 0.01	CNS+
1	174	0.889	3	3	58.6	−0.593	4.70 ± 0.01	CNS+
Lipinski's rules and others	≤ 450	≤ 5.0	≤ 10	≤ 5	≤ 90	> 3.0 (readily) < −1.0 (poorly)	< 5.4 > 5.7	CNS+ CNS−

Table 6.1 | Values (MW, *c*logP, HBA, HBD, PSA, logBB, and $-\log P_e$)[a] of **ML** and **1**.
[a] MW, molecular weight; *c*logP, calculated logarithm of the octanol-water partition coefficient; HBA, hydrogen bond acceptor atoms; HBD, hydrogen bond donor atoms; PSA, polar surface area; logBB = −0.0148 × PSA + 0.152 × *c*logP + 0.139 (logBB > 3.0, readily crosses BBB; logBB < −1.0, poorly distributed to the brain); $-\log P_e$ values were determined using the Parallel Artificial Membrane Permeability assay (PAMPA) and average $-\log P_e$ values were then calculated by the PAMPA9 Explorer software v. 3.5. [b] Prediction of a compound's ability to penetrate the central nervous system (CNS) based on suggested values. Compounds categorized as CNS+ possess the ability to penetrate the BBB and are available in the CNS. Compounds assigned as CNS−, have poor permeability through the BBB and therefore their bioavailability into the CNS is considered to be minimal.

6.4 Conclusions

The complexity of AD is suggested to arise from multiple pathological factors such as Aβ/metal-Aβ species, metal ions, and free radicals; however, the roles of individual elements and, more importantly, their inter-connections in disease development remain unclear. To advance our understanding of this aspect and target/control all these features, we have rationally designed a novel molecule, **ML**, by incorporating structural moieties for Aβ/metal-Aβ interactions, metal chelation, ROS generation control, and antioxidant activity into a single framework. Water solubility and BBB permeability were considered for potential biological applications, particularly in the brain, as part of our design approach. To the best of our knowledge, **ML** is the first example of a single molecule that can control multiple reactivities, *i.e.*, metal-free and metal-induced Aβ aggregation, toxicity induced by Aβ and metal-Aβ, ROS generation, and free radical reactions. **ML**'s multifunctionality validates our rational structure-based design strategy, and substantiates that a molecule can be tailored to a specific purpose despite the challenges and complexity of the pathological features of the disease it is intended to examine. Our efforts presented herein build a foundation toward the development of chemical tools for uncovering complex AD

pathogenesis and serve as a step for the discovery of effective therapeutics for this disease.

References

1. Hardy, J. A.; Higgins, G. A. Alzheimer's disease: the amyloid cascade hypothesis. *Science* **1992,** *256*, 184-185.

2. Jakob-Roetne, R.; Jacobsen, H. Alzheimer's Disease: From Pathology to Therapeutic Approaches. *Angew. Chem., Int. Ed.* **2009,** *48*, 3030-3059.

3. Rauk, A. The chemistry of Alzheimer's disease. *Chemical Society Reviews* **2009,** *38*, 2698-2715.

4. Kepp, K. P. Bioinorganic chemistry of Alzheimer's disease. *Chem Rev* **2012,** *112*.

5. Jones, M. R.; Service, E. L.; Thompson, J. R.; Wang, M. C. P.; Kimsey, I. J.; DeToma, A. S.; Ramamoorthy, A.; Lim, M. H.; Storr, T. Dual-function triazole-pyridine derivatives as inhibitors of metal-induced amyloid-β aggregation. *Metallomics* **2012,** *4*, 910-920.

6. Jarrett, J. T.; Berger, E. P.; Lansbury, P. T., Jr. The carboxy terminus of the beta amyloid protein is critical for the seeding of amyloid formation: implications for the pathogenesis of Alzheimer's disease. *Biochemistry* **1993,** *32*, 4693-4697.

7. Scott, L. E.; Orvig, C. Medicinal inorganic chemistry approaches to passivation and removal of aberrant metal ions in disease. *Chem Rev* **2009,** *109*, 4885-4910.

8. Faller, P.; Hureau, C. Bioinorganic chemistry of copper and zinc ions coordinated to amyloid-β peptide. *Dalton Transactions* **2009**, 1080-1094.

9. Faller, P. Copper and zinc binding to amyloid-β: coordination, dynamics, aggregation, reactivity and metal-ion transfer. *ChemBioChem* **2009,** *10*, 2837-2845.

10. Zatta, P.; Drago, D.; Bolognin, S.; Sensi, S. L. Alzheimer's disease, metal ions and metal homeostatic therapy. *Trends in Pharmacological Sciences* **2009,** *30*, 346-355.

11. Rodríguez-Rodríguez, C.; Telpoukhovskaia, M.; Orvig, C. The art of building multifunctional metal-binding agents from basic molecular scaffolds for the potential application in neurodegenerative diseases. *Coordination Chemistry Reviews* **2012,** *256*, 2308-2332.

12. Pithadia, A. S.; Lim, M. H. Metal-associated amyloid-β species in Alzheimer's disease. *Current Opinion in Chemical Biology* **2012,** *16*, 67-73.

13. Duce, J. A.; Bush, A. I. Biological metals and Alzheimer's disease: implications for therapeutics and diagnostics. *Progress in Neurobiology* **2010,** *92*, 1-18.

14. Hindo, S. S.; Mancino, A. M.; Braymer, J. J.; Liu, Y.; Vivekanandan, S.; Ramamoorthy, A.; Lim, M. H. Small molecule modulators of copper-induced Aβ aggregation. *Journal of the American Chemical Society* **2009,** *131*, 16663-16665.

15. Choi, J.-S.; Braymer, J. J.; Nanga, R. P. R.; Ramamoorthy, A.; Lim, M. H. Design of small molecules that target metal-Aβ species and regulate metal-induced Aβ aggregation and neurotoxicity *Proceedings of the National Academy of Sciences of the United States of America* **2010,** *107*, 21990-21995.

16. Braymer, J. J.; Choi, J.-S.; DeToma, A. S.; Wang, C.; Nam, K.; Kampf, J. W.; Ramamoorthy, A.; Lim, M. H. Development of bifunctional stilbene derivatives for targeting and modulating metal-amyloid-β species. *Inorganic Chemistry* **2011,** *50*, 10724-10734.

17. Choi, J.-S.; Braymer, J. J.; Park, S. K.; Mustafa, S.; Chae, J.; Lim, M. H. Synthesis and characterization of IMPY derivatives that regulate metal-induced amyloid-β aggregation. *Metallomics* **2011,** *3*, 284-291.

18. DeToma, A. S.; Choi, J.-S.; Braymer, J. J.; Lim, M. H. Myricetin: a naturally occurring regulator of metal-induced amyloid-β aggregation and neurotoxicity. *ChemBioChem* **2011,** *12*, 1198-1201.

19. Pithadia, A. S.; Kochi, A.; Soper, M. T.; Beck, M. W.; Liu, Y.; Lee, S.; DeToma, A. S.; Ruotolo, B. T.; Lim, M. H. Reactivity of diphenylpropynone derivatives toward metal-associated amyloid-β species. *Inorganic Chemistry* **2012,** *51*, 12959-12967.

20. Lim, M. H.; Wong, B. A.; Pitcock, W. H.; Mokshagundam, D.; Baik, M.-H.; Lippard, S. J. Direct nitric oxide detection in aqueous solution by copper(II) fluorescein complexes. *Journal of the American Chemical Society* **2006,** *128*, 14364-14373.

21. Roth, R.; Erlenmeyer, H. Über einige derivate der 8-aminochinaldinsäure. metallionen und biologische wirkung, 25. mitteilung. *Helvetica Chimica Acta* **1954,** *37*, 1064-1068.

22. Waibel, M.; Hasserodt, J. Efficient synthesis and fluorescence properties of highly functionalized 2-aryl-quinazolin-4(3H)-ones. *Tetrahedron Letters* **2009,** *50*, 2767-2769.

23. Pringle, S. D.; Giles, K.; Wildgoose, J. L.; Williams, J. P.; Slade, S. E.; Thalassinos, K.; Bateman, R. H.; Bowers, M. T.; Scrivens, J. H. An investigation of the mobility separation of some peptide and protein ions using a new hybrid quadrupole/travelling wave IMS/oa-ToF instrument. *International Journal of Mass Spectrometry* **2007,** *261*, 1-12.

24. Wyttenbach, T.; Kemper, P. R.; Bowers, M. T. Design of a new electrospray ion mobility mass spectrometer. *International Journal of Mass Spectrometry* **2001,** *212*, 13-23.

25. Mancino, A. M.; Hindo, S. S.; Kochi, A.; Lim, M. H. Effects of clioquinol on metal-triggered amyloid-β aggregation revisited. *Inorganic Chemistry* **2009,** *48*, 9596-9598.

26. Thinakaran, G.; Teplow, D. B.; Siman, R.; Greenberg, B.; Sisodia, S. S. Metabolism of the Swedish amyloid precursor protein variant in neuro2a (N2a) cells: evidence that cleavage at the "β-secretase" site occurs in the golgi apparatus. *Journal of Biological Chemistry* **1996,** *271*, 9390-9397.

27. Re, R.; Pellegrini, N.; Proteggente, A.; Pannala, A.; Yang, M.; Rice-Evans, C. Antioxidant activity applying an improved ABTS radical cation decolorization assay. *Free Radical Biology and Medicine* **1999,** *26*, 1231-1237.

28. Schugar, H.; Green, D. E.; Bowen, M. L.; Scott, L. E.; Storr, T.; Böhmerle, K.; Thomas, F.; Allen, D. D.; Lockman, P. R.; Merkel, M.; Thompson, K. H.; Orvig, C. Combating Alzheimer's disease with multifunctional molecules designed for metal passivation. *Angew. Chem., Int. Ed.* **2007,** *46*, 1716-1718.

29. Avdeef, A.; Bendels, S.; Di, L.; Faller, B.; Kansy, M.; Sugano, K.; Yamauchi, Y. PAMPA-critical factors for better predictions of absorption. *Journal of Pharmaceutical Sciences* **2007,** *96*, 2893-2909.

30. Di, L.; Kerns, E. H.; Fan, K.; McConnell, O. J.; Carter, G. T. High throughput artificial membrane permeability assay for blood-brain barrier. *Eur. J. Med. Chem.* **2003,** *38*, 223-232.

31. Kung, H. F.; Lee, C.-W.; Zhuang, Z.-P.; Kung, M.-P.; Hou, C.; Plössl, K. Novel stilbenes as probes for amyloid plaques. *Journal of the American Chemical Society* **2001,** *123*, 12740-12741.

32. Ono, M. Development of positron-emission tomography/single-photon emission computed tomography imaging probes for in vivo detection of beta-amyloid plaques in Alzheimer's brains. *Chem Pharm Bull* **2009,** *57*, 1029-1039.

33. Hong, M. C.; Kim, Y. K.; Choi, J. Y.; Yang, S. Q.; Rhee, H.; Ryu, Y. H.; Choi, T. H.; Cheon, G. J.; An, G. I.; Kim, H. Y.; Kim, Y.; Kim, D. J.; Lee, J.-S.; Chang, Y.-T.; Lee, K. C. Synthesis and evaluation of stilbene derivatives as a potential imaging agent of amyloid plaques. *Bioorgan Med Chem* **2010,** *18*, 7724-7730.

34. Bernstein, S. L.; Dupuis, N. F.; Lazo, N. D.; Wyttenbach, T.; Condron, M. M.; Bitan, G.; Teplow, D. B.; Shea, J.-E.; Ruotolo, B. T.; Robinson, C. V.; Bowers, M. T. Amyloid-β protein oligomerization and the importance of tetramers and dodecamers in the aetiology of Alzheimer's disease. *Nature Chemistry* **2009,** *1*, 326-331.

35. Lesné, S.; Koh, M. T.; Kotilinek, L.; Kayed, R.; Glabe, C. G.; Yang, A.; Gallagher, M.; Ashe, K. H. A specific amyloid-β protein assembly in the brain impairs memory. *Nature* **2006,** *440*, 352-357.

36. He, X.; Park, H. M.; Hyung, S.-J.; DeToma, A. S.; Kim, C.; Ruotolo, B. T.; Lim, M. H. Exploring the reactivity of flavonoid compounds with metal-assosicated amyloid-β species. *Dalton Transactions* **2012,** *41*, 6558-6566.

Chapter 7

Amyloid β-Protein Assembly: Differential Effects of the Protective A2TMutation and the Recessive A2V Familial Alzheimer's Disease Mutation

This chapter is reproduced with the permission from:

X. Zheng, D. Liu, R. Roychaudhuri, D. B. Teplow and M. T. Bowers, "Amyloid β-Protein Assembly: Differential Effects of the Protective A2T Mutation and the Recessive A2V Familial Alzheimer's Disease Mutation", *ACS Chemical Neuroscience,* Article ASAP

DOI: 10.1021/acschemneuro.5b00171, Copyright © 2015, American Chemical Society

7.1 Introduction

Although most AD cases occur sporadically, ~5% of AD cases are caused by mutations in the APP[1-2], presenilin 1 (PS1)[3-4], or presenilin 2 (PS2)[5] genes. These familial AD (FAD) cases, often lead to early onset of disease (<60 years of age). Numerous FAD-related mutations in the APP gene have been identified and many of them are near β- or γ-secretase cleavage sites. This results most commonly in overproduction of Aβ or relative increases in the amount of Aβ42 that is produced relative to Aβ40[6]. However, as many mutations occur within the Aβ region, it is very likely that these substitutions would alter the structural and aggregation properties of the resultant Aβ42 and Aβ40 peptides. Notably, many mutations in the APP gene result in amino acid substitutions within the central region of Aβ, as, for example, Flemish (A21G)[7], Arctic (E22G)[8], Dutch (E22Q)[9], Osaka (E22Δ)[10], Italian (E22K)[11] and D23N (Iowa)[12] mutations. The resulting peptides exhibit distinct aggregation propensity and toxicity. The central region of Aβ has been shown to be crucial for the initial nucleation of Aβ folding and assembly[13]. Mutations near this region may disrupt the Aβ conformation, resulting in increased aggregation propensity and formation of toxic oligomers[14].

On the other hand, the role of the N-terminus in aggregation, toxicity and pathology has been less thoroughly studied due to the fact that this region appears disordered in the fibril state[15-16]. However, as with the central region of Aβ, a number of APP mutations result in amino acid substitutions at the N-terminus, and these substitutions alter Aβ assembly. These include the English (H6R)[17-18], Tottori (D7N)[17-20], and Taiwanese (D7H)[21] mutations. The importance of the Aβ N-terminus in disease causation thus is clear. Most recently, two new APP mutations have been described that result in the substitutions A2T and A2V can be

important in Aβ structure and assembly[22-23]. In the work presented here, we elucidate the effects on early Aβ assembly of these two recently discovered mutations.

The A2T substitution substantially decreases AD risk, as well as protecting against age-related cognitive decline in the elderly without AD[22]. It is thought to be the first example of a sequence variant that protects against AD. The A2T substitution occurs immediately adjacent to the β-secretase site, and indeed, the mutation has been found to reduce Aβ production ~20% in heterozygous carriers. Such a reduction may be responsible for its protective function in AD pathology[22]. However, as the mutation is within the Aβ sequence, it is possible that the A2T mutation also changes the aggregation properties of Aβ proteins, thus contributing to its protective effect, a possibility we investigate here.

The mutation causing the A2V substitution results in early onset AD in the homozygotes, whereas some protection against AD is observed in heterozygotes[23]. In contrast to the A2T substitution, A2V increases Aβ production. Interestingly, co-incubation of A2V Aβ42 and *wt* Aβ42 produced slower aggregation rates than exhibited by either peptide alone, as well as decreased toxicity[23]. The A2V substitution accelerates Aβ42 oligomerization and also leads to the production of annular structures with a higher hydrophobicity than *wt* Aβ42[24].

A consensus regarding the effects of the A2T and A2V substitutions on Aβ assembly has not been reached. Two recent studies of A2T and A2V peptides reported different aggregation kinetics by thioflavin T (ThT) fluorescence studies. Benilova *et al.* showed that the A2T substitution has little effect on Aβ42 aggregation, but did affect its solubility[25]. Maloney *et al.*, in contrast, showed that the A2T mutant had a lower aggregation propensity compared to the A2V mutant or to *wt* Aβ42[26]. For Aβ40, the A2T mutant was shown to

aggregate similarly to *wt*, whereas the A2V mutant exhibited faster aggregation and a shorter lag phase, making this peptide behave more Aβ42-like[25-26].

To improve our understanding of the A2T and A2V substitutions, we used ion mobility coupled to mass spectrometry (IM-MS) to examine the early assembly and subsequent aggregation of these mutant peptides. We examine here the early oligomer distributions of A2T- and A2V-containing Aβ40 and Aβ42 to understand how each assembles and whether the early assembly pathways are identical or different. We also examine the early oligomer distributions of mixtures of *wt* and mutant peptides to understand how each affects the other's assembly. This provides the means to model *in vitro* the homozygous and heterozygous states that exist in humans. These studies provide mechanistic insights into the aetiology of FAD, mechanisms of protection from FAD, and potential targets for therapeutic agents.

7.2 Methods

Peptide and Sample preparation: Full-length Aβ and mutants were synthesized by *N*-9-fluorenylmethoxycarbonyl (FMOC) chemistry[27]. The peptides were purified by reverse-phase HPLC and their quality validated by mass spectrometry and amino acid analysis. Samples were prepared in 10 mM ammonium acetate buffer, pH 7.4, at a final peptide concentration of 10 μM. Equimolar mixtures of *wt* and mutant Aβ were prepared at a total peptide concentration of 10 μM (5 μM of each peptide).

Mass Spectrometry and Ion Mobility spectrometry Analysis: Most data were recorded on a home-built ion mobility spectrometry-mass spectrometer[28] described in Chapter 2 or a Micromass QTOF2 quadrupole/time-of-flight tandem mass spectrometer.

7.3 Results

7.3.1 Different oligomer distributions of wt and mutant Aβ42.

Mass spectra of *wt* Aβ42, A2T, and A2V were recorded individually and are shown in Figure 7.1. Four common peaks were observed for each peptide, corresponding to z/n ratios of -4, -3, -5/2 and -2, where z is charge and n is oligomer size. The mass spectrum of A2V Aβ42 was interesting because in addition to the four peaks, another peak was observed between z/n = -3 and -5/2 in the spectrum, corresponding to z/n = -8/3. This indicates the A2V mutant forms a trimer, which is not observed for *wt* or A2T Aβ42. Moreover, there is another peak between z/n = -4 and -3 for A2V, denoted by *, which is assigned as fragment peak or impurity.

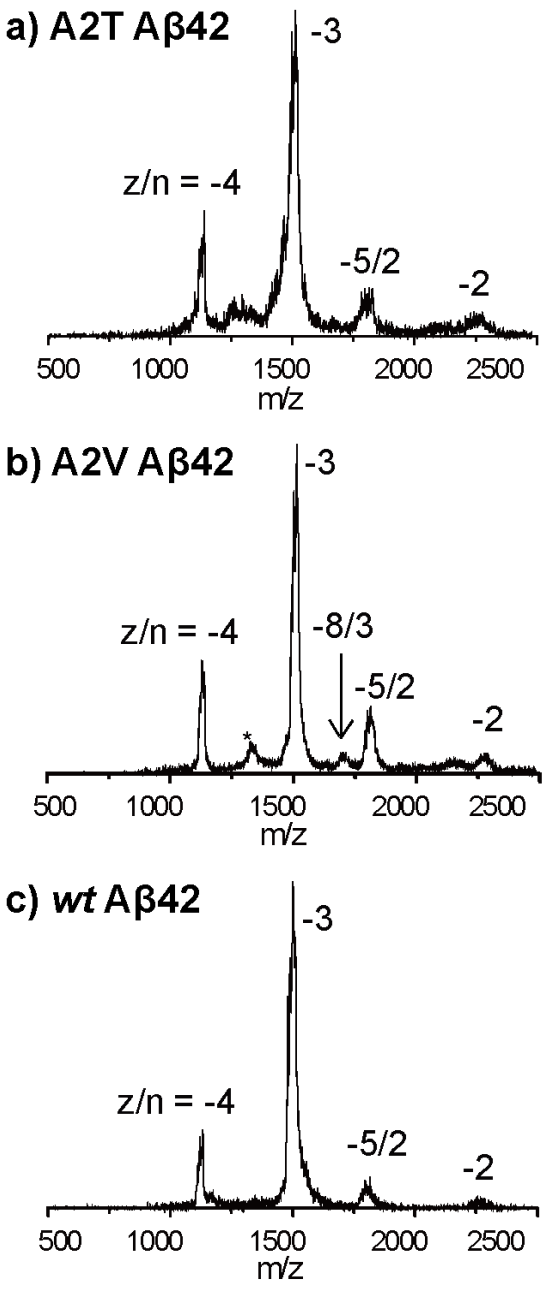

Figure 7.1. a-c) Mass spectra of A2T, A2V and *wt* Aβ42. The charge state of each species is noted with z/n, where z is the charge and n is oligomer number. The peak marked with * in panel b is assigned as a fragment peak or impurity.

The arrival time distributions (ATDs) of the z/n = -5/2 peaks for all three Aβ42 alloforms are shown in Figure 7.2. The ATD of *wt* Aβ42 shows four features, with arrival times at ~710, 670, 610 and 540 μs, which were previously assigned as Aβ42 dimer,

tetramer, hexamer, and dodecamer, respectively, based on their calculated collision cross sections (See reference 7 for detailed discussion of these assignments). However, the ATD of A2T or A2V Aβ42 (Figure 7.2a or b) shows only three features, with arrival times at ~710, 670, 610 μs which were assigned as dimer, tetramer, and hexamer, respectively, based on their calculated cross sections. There is no feature at lower arrival time observed in either of the ATD for mutants, indicating no other oligomers larger than hexamers are formed. These results suggest the formation of Aβ42 dodecamer is inhibited by both A2T and A2V mutations.

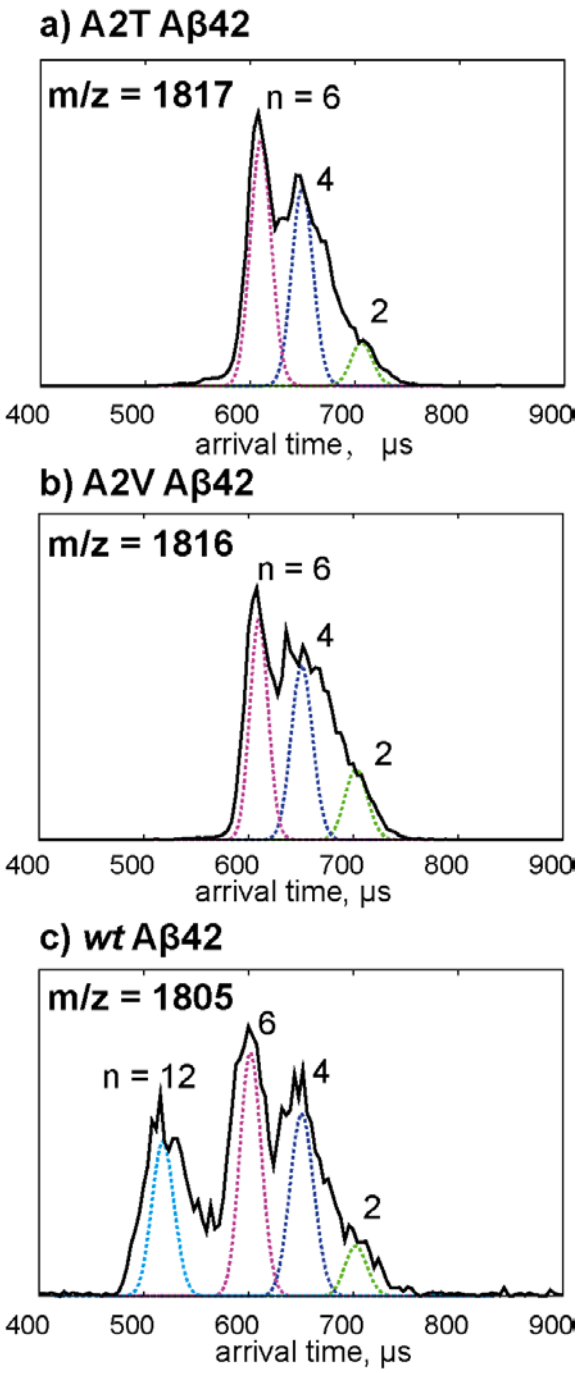

Figure 7.2 a-c) ATDs of z/n = -5/2 peaks for A2T, A2V and *wt* Aβ42. The oligomer order (n) is noted for each feature. The dashed lines represent the peak shape for a single conformation. The injection energy in panels d, e, and f is 40 eV.

To assign the peaks in the ATDs unambiguously, and to better understand the oligomer distributions of the Aβ42 mutants, the -5/2 ATDs for Aβ42 mutants were measured

at different injection energies. At low injection energy, the ions are rapidly thermalized by cooling collisions with the helium gas in the drift cell and therefore large complexes can be preserved through the process. At high injection energy, the ions are given sufficient energy to lead to internal excitation which can cause isomerization into low energy structure or dissociation of large noncovalent complexes into smaller species.

As shown in Figure 7.3, the ATDs measured at intermediate injection energy (40 eV) are the same ones shown in Figure 7.2b and c. When the injection energy is lowered to 25 eV (Figure 7.3 top panel), the hexamer peak becomes especially prominent, whereas the tetramer and dimer features decrease. However, there are still no peaks with lower arrival times observed, suggesting that oligomers of size dodecamer or larger are not formed in solution. At high injection energy (100 eV, Figure 7.3 bottom panel), the hexamer peak disappears whereas the tetramer and dimer peaks dominate the spectrum. This suggests hexamer dissociation into smaller oligomers. These injection energy studies are fully consistent with the assignment of the three peaks in the ATDs as dimer, tetramer, and hexamer.

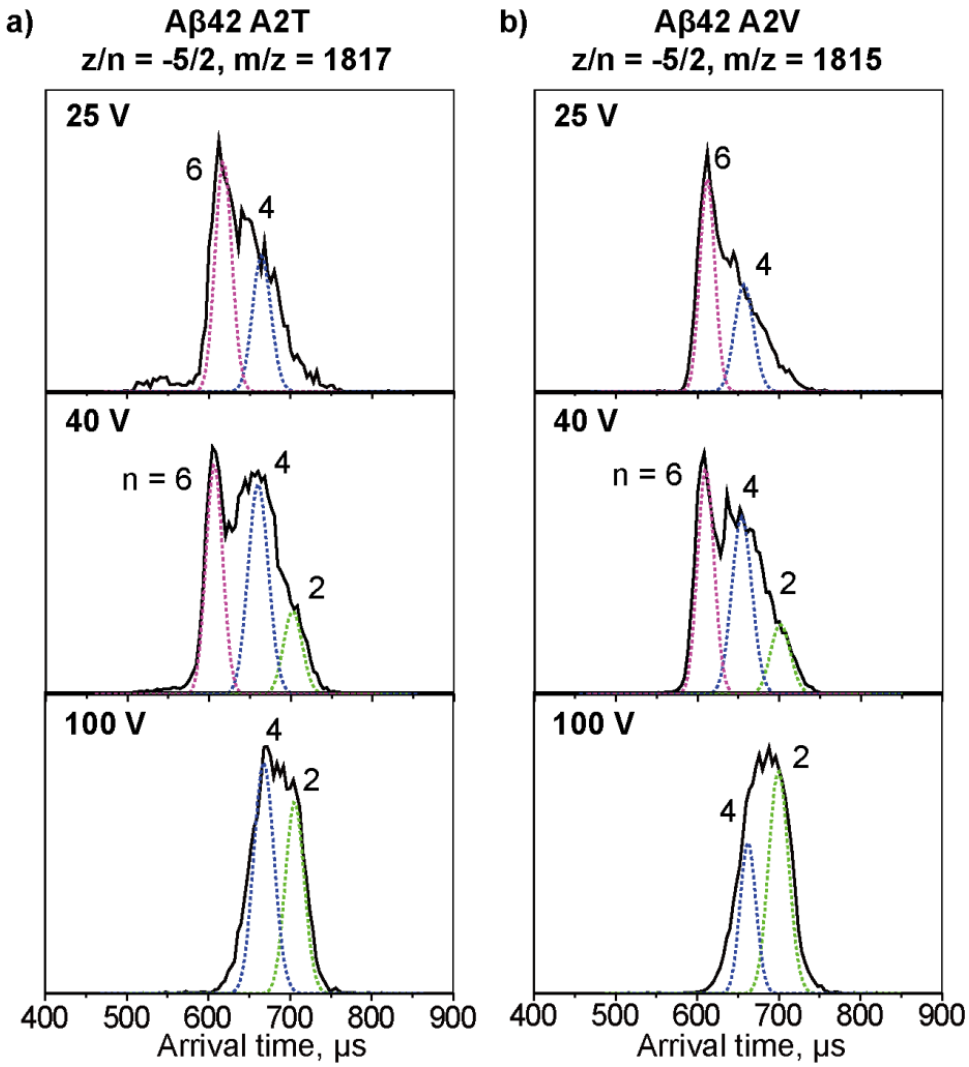

Figure 7.3 ATDs for z/n = -5/2 peaks for a) Aβ42 A2T and b) Aβ42 A2V under different injection energies. The oligomer order (n) is noted for each feature. The dashed lines represent the peak shape for a single conformation.

7.3.2 Ion mobility study of z/n = -2 and -8/3 peaks: A2V Aβ42 forms trimers.

The z/n = -2 Aβ42 is a relative low charge state of the Aβ42 alloforms and possibly consists of high order oligomers, making its ATD of interest. The signal of the z/n = -2 peak for *wt* Aβ42 is too low to obtain a reliable ATD, therefore no data is shown. However, we were able to record ATDs for the -2 peaks of A2T and A2V Aβ42 (Figure 7.4).

The ATD of -2 A2T Aβ42 shows three features, with arrival times at ~820, 720, 670 μs, which can be assigned as monomer, dimer, and trimer, respectively. Similarly, the ATD of the z/n = -2 A2V Aβ42 shows three features, corresponding to monomer, dimer and trimer. However, the relative intensity of the A2T trimer is much lower than that of its dimer while the relative intensity of the A2V trimer is comparable to that of its dimer, indicating the formation of trimer is more favored for A2V Aβ42.

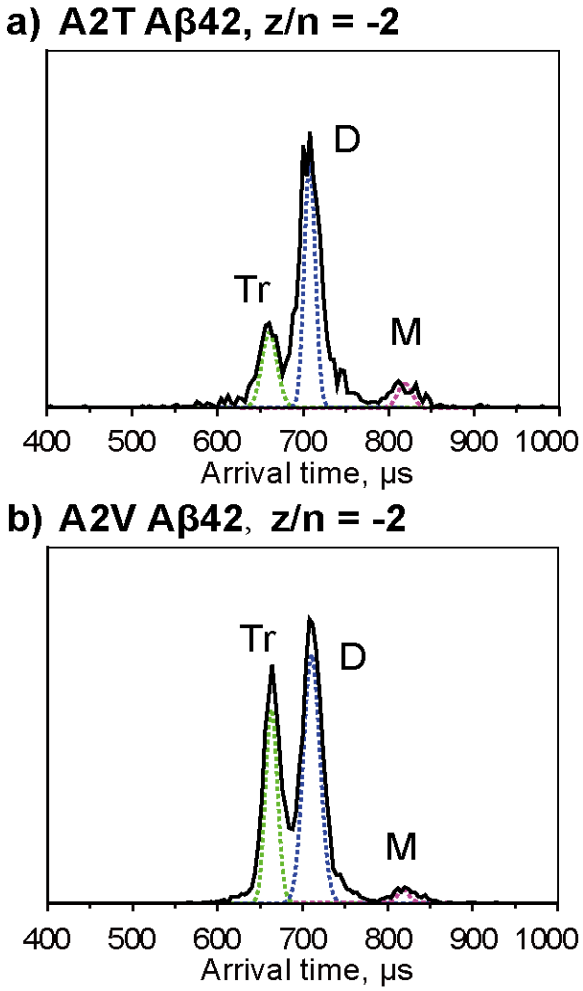

Figure 7.4 a) and b), ATDs of the z/n = -2 peaks for A2T and A2V Aβ42, respectively. c) ATD of the z/n = -8/3 peak for A2V. The dashed lines represent the peak shape for a single conformation. The oligomer order is noted for each feature where M represents monomer, D represents dimer, Tr represents trimer and H represents hexamer. The injection energy is 40 eV.

Injection energy studies of z/n = -2 peaks (Figure 7.5) show that at low injection energies the trimer of A2V Aβ42 is dominant while the trimer of A2T Aβ42 remains minor, indicating trimer in the A2V mutant is significant in solution. This supports that the formation of trimer is more favored for A2V Aβ42 than for A2T Aβ42.

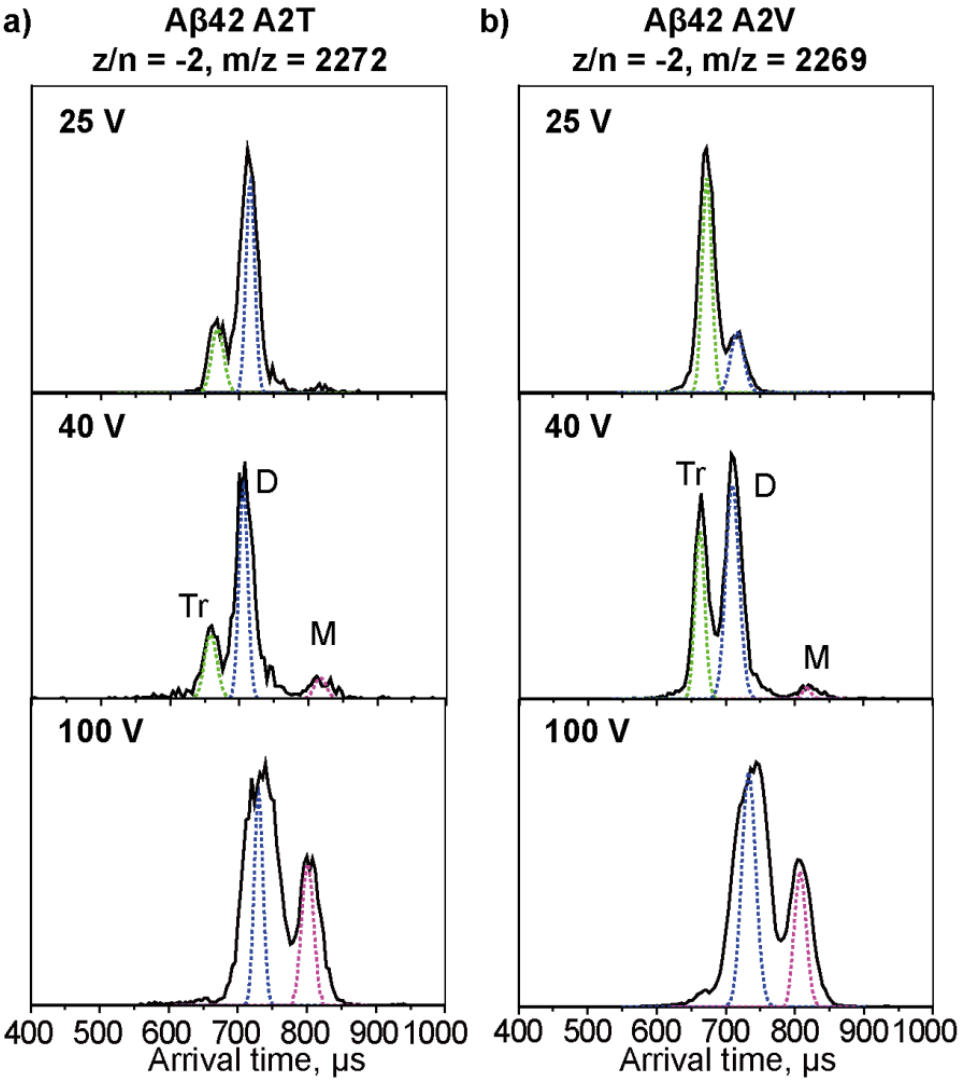

Figure 7.5 ATDs for z/n = -2 peaks for a) A2T Aβ42, b) A2V Aβ42 under different injection energies. The oligomer order is noted for each feature where M represents monomers, D represents dimer and Tr represents trimers, H represents hexamer. The dashed lines represent the peak shape for a single conformation.

The ATD of z/n = -8/3 A2V Aβ42 (Figure 7.6 middle panel, 40 eV) shows two features, with arrival times at ~660 and 590 μs observed, which correspond to an A2V trimer and hexamer, respectively. The breadth of the trimer feature indicates there is a family of trimer structures existing in the solution. The injection energy study shows that the hexamer feature increases at lowest energies and the trimer peak gets sharper (Figure 7.6 top panel, 25 eV). At high energy (Figure 7.6 bottom panel, 100 eV), the hexamer feature disappears and the broad trimer feature becomes the dominant peak.

Taken together, these ion mobility results reveal that the oligomerization pattern is different for each of the alloforms. *wt* Aβ42 forms dimer, tetramer, hexamer, and dodecamer. A2T and A2V Aβ42 form dimer, tetramer, and hexamer, without the formation of dodecamer, but A2V forms a significant trimer which is only very minor in A2T and may not be present in *wt* Aβ42 at all.

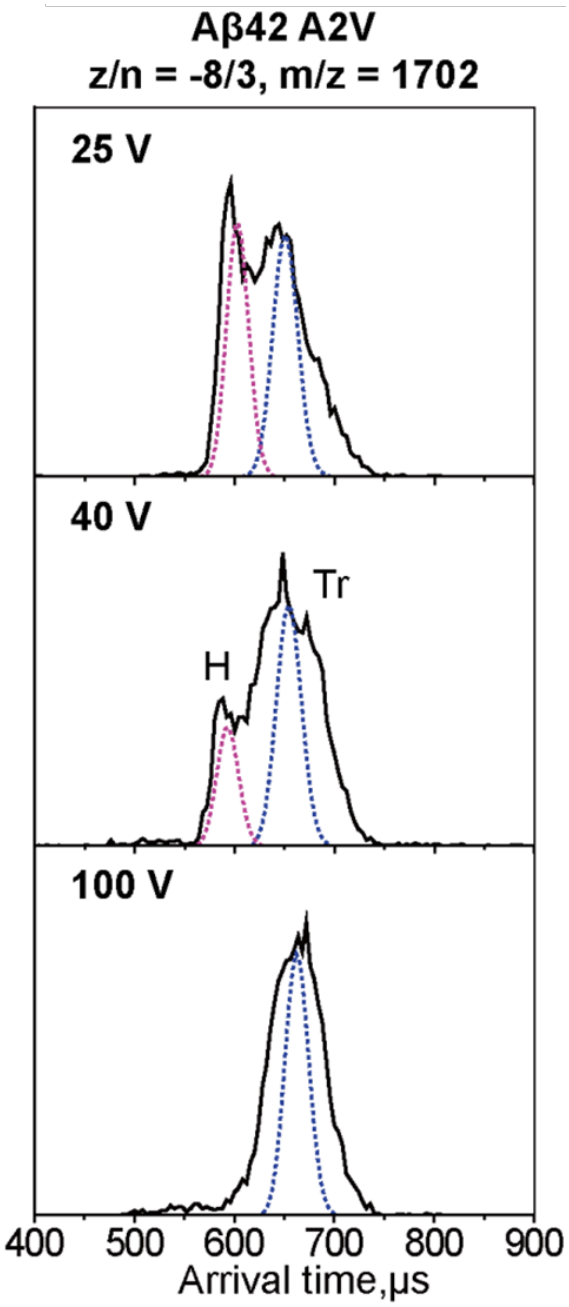

Figure 7.6 ATDs for z/n = -8/3 peak for A2V Aβ42 under different injection energies. The oligomer order is noted for each feature where Tr represents trimers, H represents hexamer. The dashed lines represent the peak shape for a single conformation.

7.3.3 Mixtures of *wt* and mutant Aβ42: The effects on *wt* Aβ42 oligomerization

The A2T mutation has been shown to protect carriers from AD or normal age-related cognitive decline[22]. To model the effects of this peptide in heterozygotes, we created an equimolar mixture of A2T and *wt* Aβ42 and then performed MS (Figure 7.7). Four sets of peaks were observed, corresponding to z/n = -4, -3, -5/2 and -2 charge states. A zoom-in spectrum of the -5/2 region using the QTOF-MS was obtained and shows that there are three peaks with charge state of -5/2, which correspond to -5/2 *wt* Aβ42 homo-oligomers, *wt*/A2T hetero-oligomers (1:1 ratio), and A2T homo-oligomers. The ATDs of these three peaks (Figure 7.7b, c, d) display a similar oligomer distribution with three features with arrival times of ~710, 670 and 600 μs. We assign these features as dimers, tetramers, and hexamers, respectively. Note that no feature at shorter arrival time was observed, indicating there is no homo-/hetero-dodecamer or higher oligomer formation. These results indicate that the A2T mutant forms small hetero-oligomers (up to hetero-hexamers) with *wt* Aβ42 and inhibits the formation of *wt* Aβ42 dodecamer or higher oligomers.

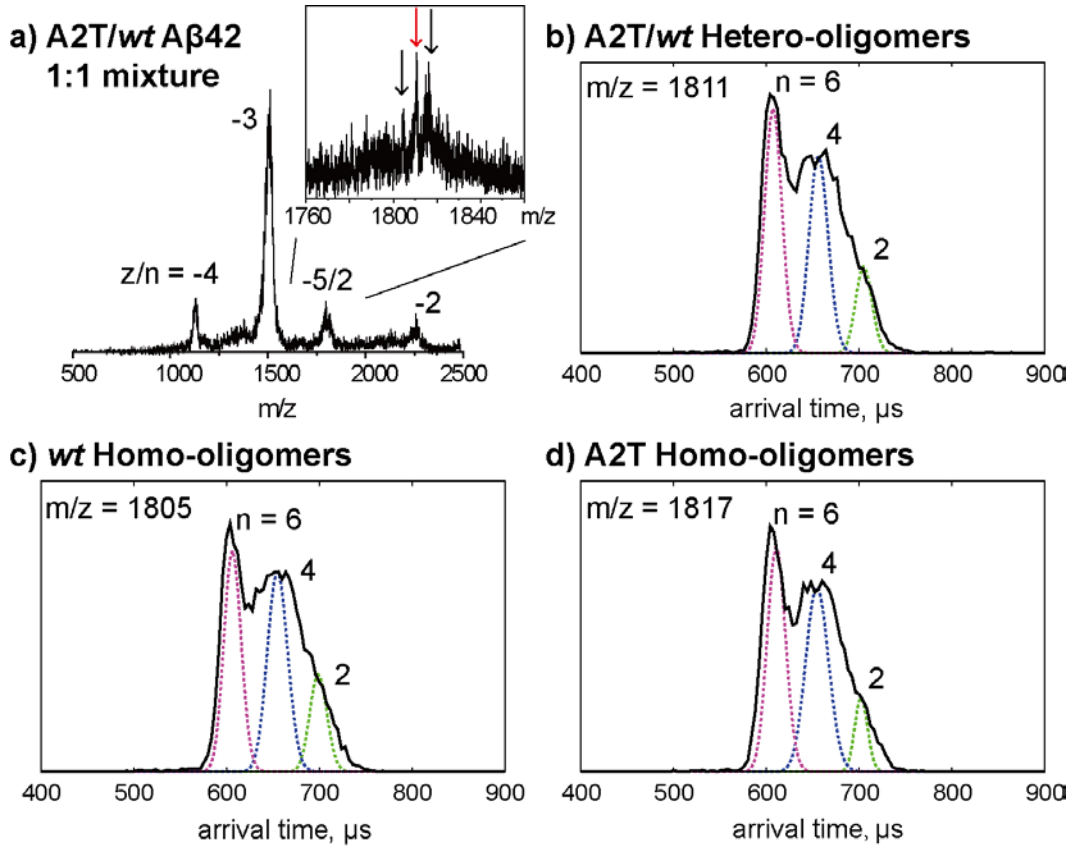

Figure 7.7 Ion mobility study of an equimolar mixture of *wt* and A2T Aβ42. a) A full mass spectrum of *wt*/A2T Aβ42 mixture and a zoom-in spectrum of z/n = -5/2 peaks which contains three species which correspond to *wt* Aβ42 homo-oligomers, *wt*/A2T Aβ42 hetero-oligomers and A2T Aβ42 homo-oligomers. b-d) ATDs of the three -5/2 oligomer peaks. The oligomer order (n) is noted for each feature. The dashed lines represent the peak shape for a single conformation. The injection energy in panels b, c, and d is 40 eV.

Previous studies showed that A2V is a recessive mutation that causes early-onset of AD in homozygotes but appears protective in heterozygotes[23]. To provide insight into this these observations, we performed ion mobility studies on an equimolar mixture of *wt* and A2V Aβ42 (Figure 7.8). Similar to the A2T/*wt* mixture, the A2V/*wt* mixture shows three -5/2 peaks, corresponding to *wt* Aβ42 homo-oligomers, *wt*/A2V hetero-oligomers (1:1 ratio) and A2V homo-oligomers. The ATDs of these -5/2 peaks all show three features that can be assigned as dimer, tetramer, and hexamer, respectively. The data show that A2V Aβ42

forms small hetero-oligomers (only up to hexamers) with *wt* Aβ42 and prevents the formation of larger oligomers.

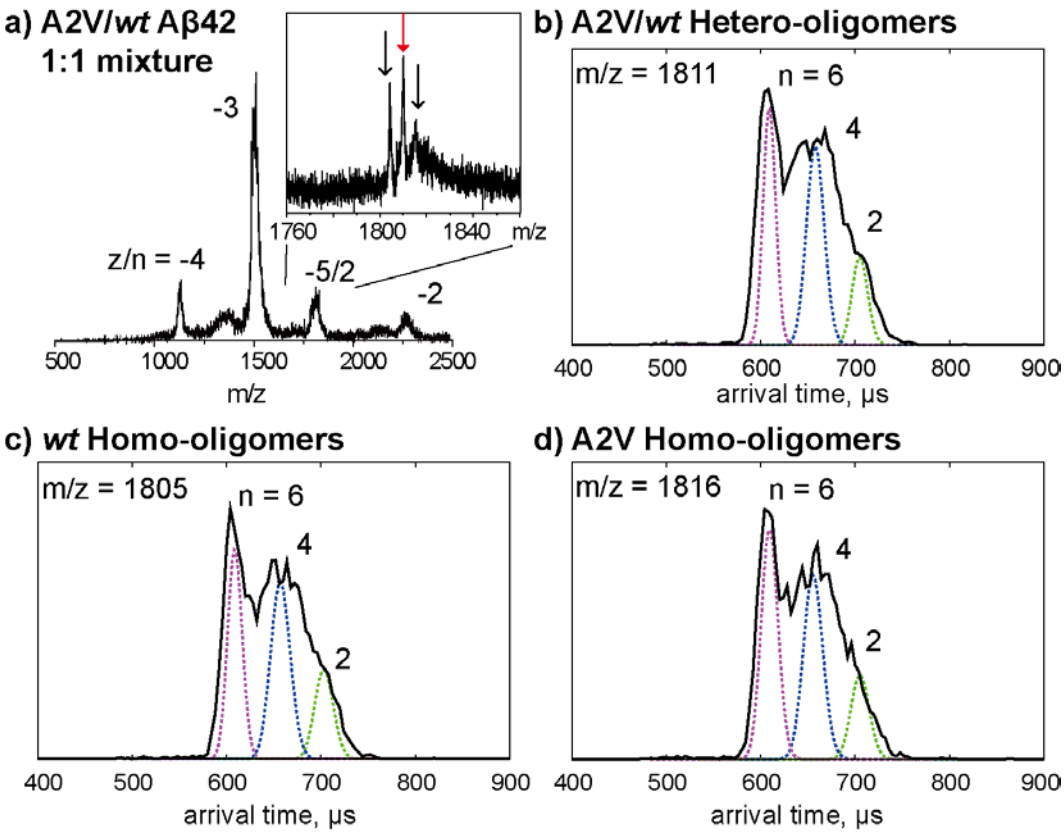

Figure 7.8 Ion mobility study of an equimolar mixture of *wt* Aβ42 and A2V mutant. a) A full mass spectrum of A2V/*wt* Aβ42 mixture and a zoom-in spectrum of z/n = -5/2 peaks which contains three species which correspond to *wt* Aβ42 homo-oligomers, *wt* /A2V Aβ42 hetero-oligomers and A2V Aβ42 homo-oligomers. b-d) ATDs of the three -5/2 oligomer peaks. Each ATD is fitted with multiple features using the procedure described in the experimental section and the oligomer order (n) is noted for each feature. The injection energy in panels b, c, and d is 40 eV.

There is no -8/3 trimer peak observed in the equimolar mixture of *wt* and A2V Aβ42. Moreover, the ATD of the z/n = -2 peak for the *wt*/A2V mixture (Figure 7.9b shows a dominant dimer peak and only a minor trimer peak, unlike A2V alone (Figure 7.4b). These results indicate that A2V trimer formation is inhibited by *wt* Aβ42.

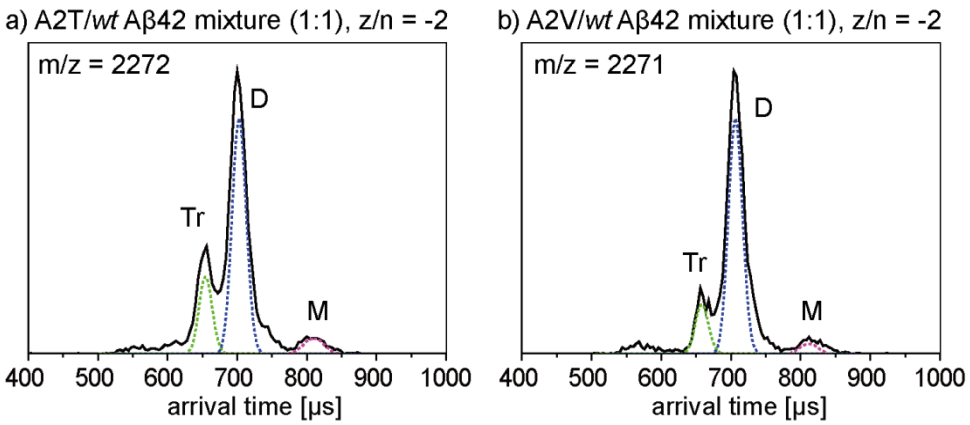

Figure 7.9 ATDs of z/n = -2 for the A2T/*wt* and A2V/*wt* Aβ42 mixtures. The oligomer order is noted for each feature where M represents monomers, D represents dimer and Tr represents trimers. The dashed lines represent the peak shape for a single conformation. The injection energy in panels a, and b is 40 eV.

7.3.4 Ion mobility study of Aβ40 mutants: A2V Aβ40 forms hexamer and dodecamer

We next examined the effects of the A2T and A2V substitutions on Aβ40 assembly (see Figure 7.10). The mass spectra for the A2T and A2V mutants (Figure 7.10b and c) showed four peaks, corresponding to z/n = -4, -3, -5/2 and -2, which is similar to that of the *wt* Aβ40 (Figure 7.10a).

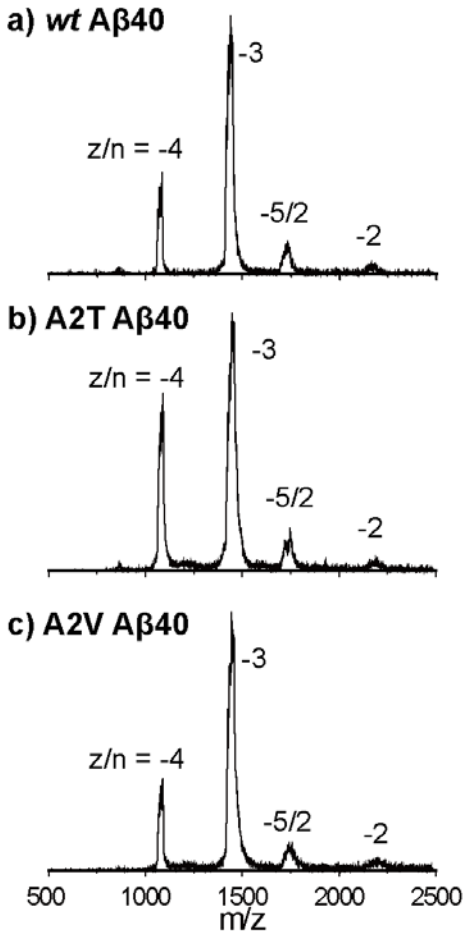

Figure 7.10 a-c) Mass spectra of Aβ40 *wt* , A2T and A2V. The charge state of each species is noted with z/n, where z is the charge and n is oligomer number. d-f) ATDs of z/n = -5/2 peaks for Aβ40 *wt*, A2T and A2V. g-i) ATDs of z/n = -2 peaks for Aβ40 *wt*, A2T and A2V. Each ATD is fitted with multiple features using the procedure described in the experimental section and the oligomer order (n) is noted for each feature. The injection energy in panels d, e, f, g, h, and i is 40 eV.

The ATD of z/n = -5/2 *wt* Aβ40 (Figure 7.11a) displays two features, with arrival times at ~710 and 670 μs, which were previously assigned as Aβ40 dimer and tetramer, respectively[29]. The ATD of the z/n = -5/2 A2T Aβ40 (Figure 7.11b) again shows two features, with arrival times at ~710 and 670 μs, corresponding to dimer and tetramer, respectively. This ATD was similar to that of *wt* Aβ40. However, the ATD of z/n = -5/2

A2V Aβ40 (Figure 7.11c) shows four features with arrival times of ~710, 670, 620 and 550 μs, which can be assigned as dimer, tetramer, hexamer and dodecamer, respectively. Hence, A2V Aβ40 forms hexamers and dodecamers, something not observed for *wt* or A2T Aβ40. This is consistent with previous ThT studies showing A2V Aβ40 displays a shorter lag phase during aggregation, which is similar to that of *wt* Aβ42[25-26].

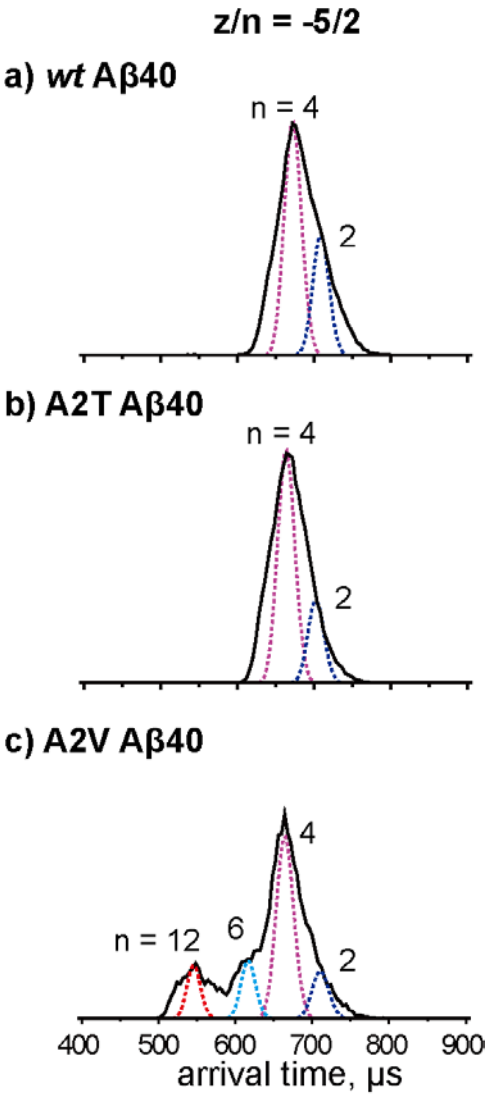

Figure 7.11 a-c) ATDs of z/n = -5/2 peaks for Aβ40 *wt*, A2T and A2V. Each ATD is fitted with multiple features using the procedure described in the experimental section and the oligomer order (n) is noted for each feature. The injection energy is 40 eV.

The ATDs of z/n = -2 Aβ40 alloforms were recorded and are shown in Figure 7.12. The ATD of *wt* Aβ40 shows a dominant dimer peak at ~720 μs and a small monomer peak at ~840 μs. The dimer peak is slightly broad at the bottom, which indicates there might be a small amount of trimer formed. The ATDs of A2T and A2V Aβ40 (Figure 7.12b and c) show one additional peak, with a shorter arrival time at ~680 μs, which is assigned as trimer. The relative intensity of the A2V trimer is greater than that of the A2T trimer or *wt* Aβ40 trimer. This is consistent with the results of z/n = -5/2 peaks, which suggests that A2V Aβ40 is aggregating into larger oligomers than is A2T and *wt* Aβ40.

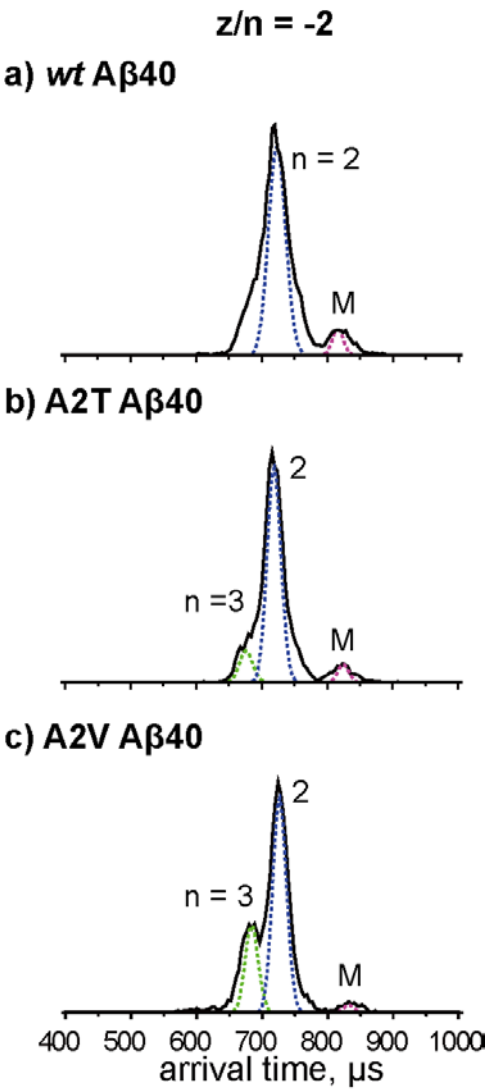

Figure 7.12 a-c) ATDs of z/n = -2 peaks for Aβ40 *wt*, A2T and A2V. The dashed lines represent the peak shape for a single conformation. The oligomer order (n) is noted for each feature. The injection energy is 40 eV.

In summary, the A2T mutation does not significantly change Aβ40 oligomerization. The A2V mutation, in contrast, promotes Aβ40 oligomerization and causes it to undergo a more "Aβ42-like" aggregation process. Although the relative intensity of the A2V dodecamer is smaller than observed for *wt* Aβ42 (Figure 7.2c), the Aβ40 isoform is ten

times more abundant than Aβ42 *in vivo*. Hence this is a significant result and is fully consistent with the fact homozygous carriers of the A2V mutation develop early-onset of AD.

The results of co-incubation experiments using *wt* and mutant Aβ40 are shown in the Figure 7.13 and 14. The mass spectrum of *wt*/A2T Aβ40 mixture (Figure 7.13a) shows four sets of peaks corresponding to z/n = -4, -3, -5/2 and -2 charge states. The ATDs of the -5/2 oligomer peaks (Figure 7.13b, c and d) show two features with arrival times at ~710 and 670 μs, which can be assigned as *wt*/A2T homo- or hetero-dimers, tetramers, based on their cross sections. This result is consistent with the results of the *wt*/A2T Aβ42 mixture that A2T inhibits the formation of *wt* Aβ42 dodecamer and that A2T mutation protects against AD and protects against the cognitive decline in the elderly without AD.

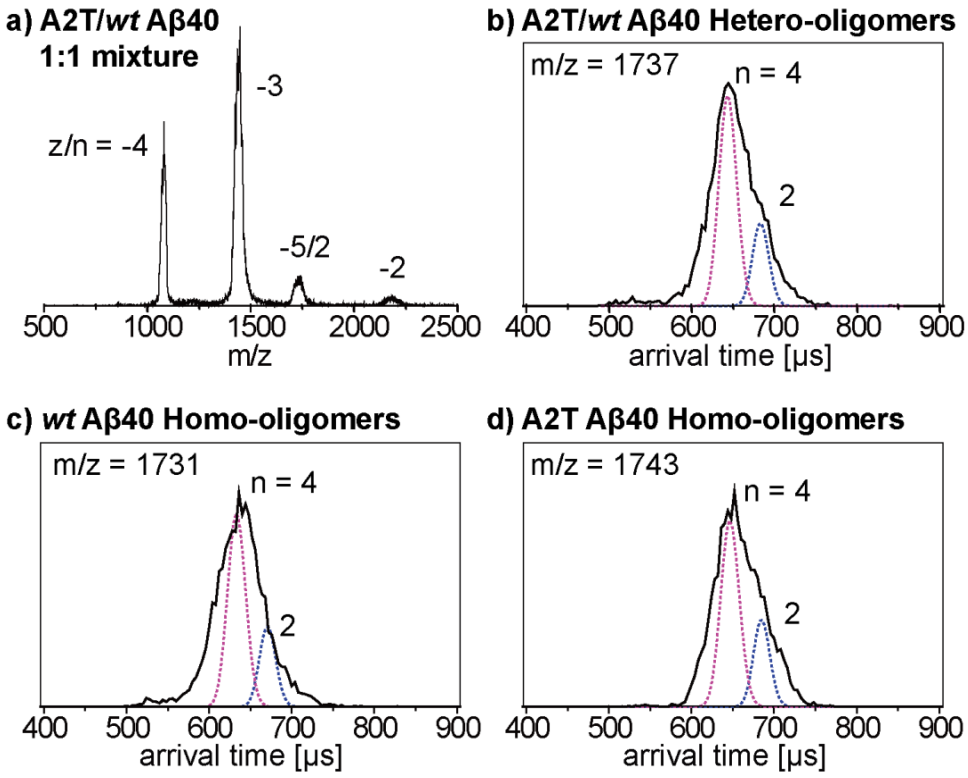

Figure 7.13 Ion mobility study of an equimolar mixture of Aβ40 *wt* and A2T mutant. a) Mass spectrum of Aβ40 A2T/*wt* mixture. b-d) ATDs of three -5/2 oligomer peaks. The oligomer order (n) is noted for each feature. The injection energy in panels b, c, and d is 40 eV.

Ion mobility studies of an equimolar mixture of A2V and *wt* Aβ40 were performed and the results are shown in Figure 7.14. The mass spectrum of Aβ40 *wt*/A2V mixture (Figure 7.14a) shows four sets of peaks corresponding to z/n = -4, -3, -5/2 and -2 charge states. The ATDs of the -5/2 oligomer peaks all display two features with arrival times at ~710 and 670 μs, which can be assigned as *wt*/A2V Aβ40 homo- or hetero-dimers, tetramers and no larger oligomers especially hexamers and dodecamers are observed. These results indicate that A2V mutant forms small hetero-oligomers (hetero-dimer and tetramers) with *wt* Aβ40 and inhibits the formation of A2V Aβ40 hexamer or dodecamer. This is important because it indicates *wt* Aβ40 inhibits formation of A2V hexamer or dodecamer. Hence, heterozygous A2V carriers are protected from dodecamer formation while homozygous A2V carriers are not.

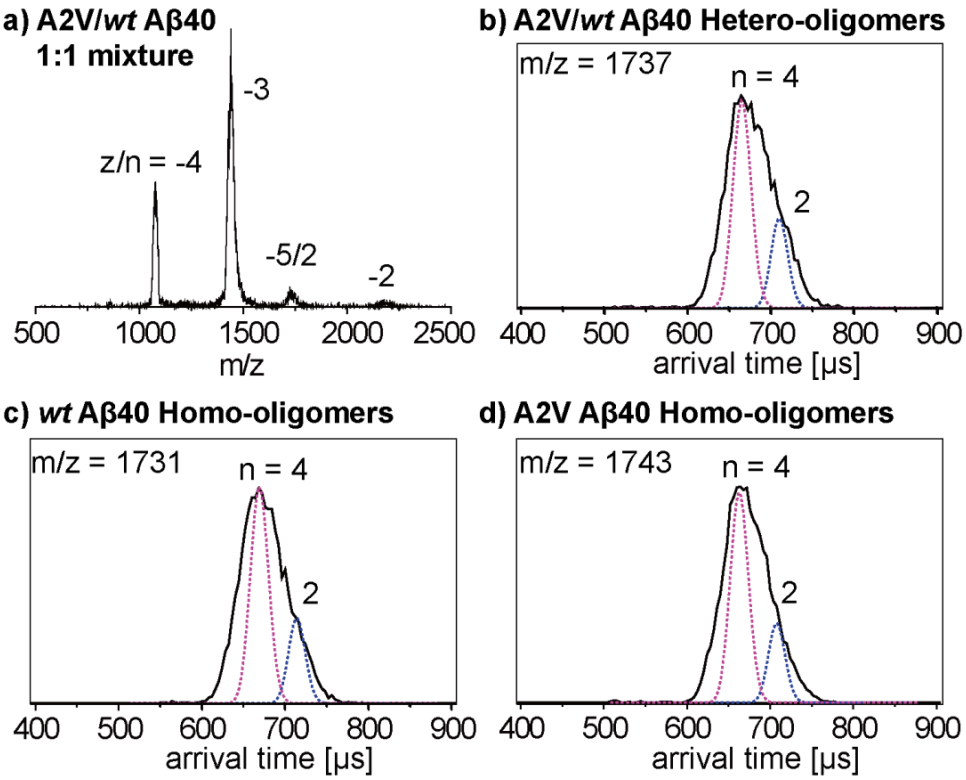

Figure 7.14 Ion mobility study of an equimolar mixture of *wt* and A2V Aβ40. a) mass spectrum of the A2V/*wt* Aβ40 mixture. b-d) ATDs of three -5/2 oligomer peaks. The oligomer order (n) is noted for each feature. The injection energy in panels b, c, and d is 40 eV.

7.4 Discussion

Our results show that amino acid substitutions at Ala2 of Aβ affect Aβ42 oligomerization (summarized in Figure 7.15). The Iceland mutation A2T was observed to prevent the formation of Aβ42 dodecamer, which was previously identified as an important neurotoxin in AD[30-31]. These results are consistent with previous studies demonstrating that A2T is a protective mutation[22]. However, our ion mobility studies show that the A2T mutation does not have a significant effect on oligomerization of the less toxic Aβ40 isoform.

The A2V mutation was observed to inhibit the formation of Aβ42 dodecamer as well. However, the A2V mutation leads to a much greater fraction of Aβ42 trimer formation and observation of a unique z/n = -8/3 trimer peak that contains a significant fraction of hexamer not formed in A2T or *wt* Aβ42. This result implies A2V Aβ42 may adopt another early assembly pathway through trimer that leads to toxic oligomers before going on to form fibrils. Even more interestingly, the A2V mutation shows significant effects on Aβ40 assembly, resulting in the formation of Aβ40 hexamer and dodecamer, which are not observed for A2T or *wt* Aβ40. Hence, the A2V mutation changes the Aβ40 aggregation pathway into a Aβ42-like pathway, which is consistent with a previous ThT fluorescence study showing A2V has a shorter aggregation lag phase than *wt* Aβ40[25]. Although the relative intensity of dodecamer in A2V Aβ40 is smaller than for *wt* Aβ42 (Figure 7.1f), this peptide is ten times more abundant than Aβ42 *in vivo* and hence the fact it produces potentially toxic oligomer states will be strongly amplified *in vivo*. This result, while not proof, is entirely consistent with the fact the A2V mutant results in early onset AD in homozygous carriers[23].

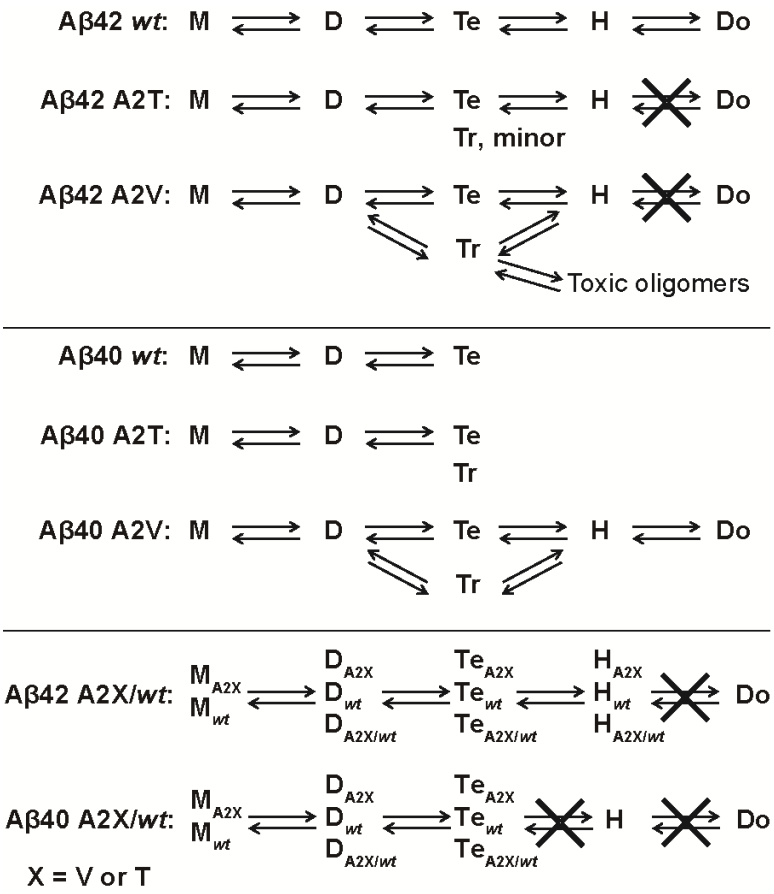

Figure 7.15 Different oligomerization patterns for *wt* Aβ, A2T, A2V alloforms and mixtures. M, D, Tr, Te, H, Do represent monomer, dimer, trimer, tetramer, hexamer and dodecamer, respectively.

The effects of the A2T and A2V substitutions on *wt* Aβ42 oligomerization were evaluated by co-incubating equimolar mixtures of the mutant and *wt* Aβ42 proteins. Both mutants formed small hetero-oligomers with *wt* Aβ42, including dimers, tetramers, and hexamers. However, no hetero- or homo-dodecamers were observed, indicating the formation of Aβ42 dodecamer is inhibited by the mutants. Co-incubation of A2T and *wt* Aβ40 shows formation of dimers and tetramers, which is similar to that of *wt* Aβ40, indicating no enhancement of aggregation by A2T (Figure 7.13). However, co-incubation of A2V and *wt* Aβ40 shows only homo- and hetero-dimer and tetramer formation, indicating

thathexamer and dodecamer formation is inhibited (Figure 7.14). This indicates that rapid A2V aggregation is inhibited by *wt* Aβ40. These results are consistent with previous studies suggesting that A2T protects against AD and A2V heterozygous carriers are not affected by this mutation[22-23].

The N-terminus of Aβ is relatively hydrophilic and appears to exist in a disordered state. It thus has been argued that it plays only a modest (or no) role in controlling Aβ assembly compared to the central hydrophobic cluster region or the C-terminus [15]. However, we find here that single A2T and A2V amino acid substitutions *do* affect Aβ oligomerization quite significantly, offering a mechanistic explanation for the phenotypes of humans expressing the cognate genes.

Threonine (T) and valine (V) have similar sizes but different hydrophobicity. The substitution of the neutral alanine (A) with a nucleophilic threonine or a hydrophobic valine will change the hydrophobicity of the N-terminus region and perhaps change the conformation of Aβ. A recent simulation study of A2T and A2V Aβ42 showed significantly different conformational landscapes of the Aβ42 monomer[32]. The A2T Aβ42 mutant makes the N-terminus more polar, which displays unusual long-range electrostatic interactions with residues such as Lys16 and Glu22[32]. Through such electrostatic interactions, the hairpin structure in the central hydrophobic region is disrupted, resulting in a population of unique conformations with only a C-terminal hairpin. In contrast, the A2V Aβ42 shows an enhanced double-hairpin population due to hydrophobic interactions between the N-terminus and distant hydrophobic regions (Central hydrophobic core and C-terminus hydrophobic region)[32]. A previous simulation showed that the A2V mutation reduced the intrinsic disorder and increased the hairpin population in the Aβ(1-28) monomer[33]. In

addition, a previous MD simulation study showed that the N-terminus of Aβ40 displayed a β-strand structure at Ala-2-Phe-4 which was not present in Aβ42[34]. The hydrophilic N-termini of Aβ proteins are on the surface of the oligomers, thus the presence of an N-terminal β-strand in Aβ40 might prevent the hydrophobic core of the oligomers from adding additional Aβ40 molecules to form larger oligomers, which explains why Aβ40 aggregates slower and forms smaller oligomers than Aβ42. Therefore the substitution of Ala with a hydrophobic Val may disrupt the formation of a hydrophilic N-terminal β-strand and make the hydrophobic core accessible for other Aβ40 molecules, shifting the A2V Aβ40 oligomerization toward those of Aβ42. Our ion mobility studies reveal different oligomerization for Aβ proteins with a single mutation in the N-terminus region and imply the importance of the N-terminus region for Aβ assembly, results consistent with these previous studies[32-34].

In this work, we have demonstrated that IMS-MS is becoming a powerful tool to carry out studies that lead to understanding of AD familial mutations. This is of significance as single mutations have been implied to be important in disease aetiology. For instance, recently the G127V mutation in a prion variant has been shown to completely protect transgenic mice from prion disease[35]. Hence understanding the mechanism of these positive substitutions becomes important for future therapeutic development. Thus IMS-MS can be used as a new tool to study other systems of this kind and provide an insight into their structure-disease relationship.

7.5 Conclusions

1. The A2T mutation prevents formation of Aβ42 dodecamer both in homo- and heterozygotes. The dodecamer has been implicated as a proximate toxic agent in AD.
2. The A2V mutation in homozygotes also prevents dodecamer formation in Aβ42 but promotes trimer formation which may initiate a new pathway for early oligomer formation in Aβ42.
3. The A2V mutation in homozygotes promotes hexamer and dodecamer formation in Aβ40, whereas *wt* Aβ40 assembly terminates at the tetramer. Since Aβ40 is 10 times more prevalent than Aβ42 *in vivo*, facilitation of Aβ40 hexamer and dodecamer formation may well explain why the A2V mutation causes early onset of AD in homozygotes.
4. Both the A2T and A2V mutations eliminate dodecamer formation in heterotypic mixtures with *wt* Aβ40 and Aβ42, consistent with the protective effects of these substitutions in heterozygotes.
5. Ion mobility methods are emerging as an important new tool in developing an understanding of the effect of familial mutations on Aβ assembly in AD and the assembly of other mutated protein systems.

References

1. Kang, J.; Lemaire, H.-G.; Unterbeck, A.; Salbaum, J. M.; Masters, C. L.; Grzeschik, K.-H.; Multhaup, G.; Beyreuther, K.; Muller-Hill, B. (1987) The precursor of Alzheimer's disease amyloid A4 protein resembles a cell-surface receptor. *Nature 325*, 733-736.

2. O'Brien, R. J.; Wong, P. C. (2011) Amyloid Precursor Protein Processing and Alzheimer's Disease. *Annu. Rev. Neurosci. 34*, 185-204.

3. Sherrington, R.; Rogaev, E. I.; Liang, Y.; Rogaeva, E. A.; Levesque, G.; Ikeda, M.; Chi, H.; Lin, C.; Li, G.; Holman, K., et al. (1995) Cloning of a gene bearing missense mutations in early-onset familial Alzheimer's disease. *Nature 375*, 754-760.

4. Borchelt, D. R.; Thinakaran, G.; Eckman, C. B.; Lee, M. K.; Davenport, F.; Ratovitsky, T.; Prada, C.-M.; Kim, G.; Seekins, S.; Yager, D., et al. (1996) Familial Alzheimer's Disease–Linked Presenilin 1 Variants Elevate Aβ1–42/1–40 Ratio In Vitro and In Vivo. *Neuron 17*, 1005-1013.

5. Levy-Lahad, E.; Wasco, W.; Poorkaj, P.; Romano, D.; Oshima, J.; Pettingell, W.; Yu, C.; Jondro, P.; Schmidt, S.; Wang, K., et al. (1995) Candidate gene for the chromosome 1 familial Alzheimer's disease locus. *Science 269*, 973-977.

6. Tanzi, R. E.; Bertram, L. (2005) Twenty Years of the Alzheimer's Disease Amyloid Hypothesis: A Genetic Perspective. *Cell 120*, 545-555.

7. Hendriks, L.; van Duijn, C. M.; Cras, P.; Cruts, M.; Van Hul, W.; van Harskamp, F.; Warren, A.; McInnis, M. G.; Antonarakis, S. E.; Martin, J.-J., et al. (1992) Presenile dementia and cerebral haemorrhage linked to a mutation at codon 692 of the β-amyloid precursor protein gene. *Nat. Genet. 1*, 218-221.

8. Nilsberth, C.; Westlind-Danielsson, A.; Eckman, C. B.; Condron, M. M.; Axelman, K.; Forsell, C.; Stenh, C.; Luthman, J.; Teplow, D. B.; Younkin, S. G., et al. (2001) The 'Arctic' APP mutation (E693G) causes Alzheimer's disease by enhanced Aβ protofibril formation. *Nat. Neurosci. 4*, 887-893.

9. Levy, E.; Carman, M.; Fernandez-Madrid, I.; Power, M.; Lieberburg, I.; van Duinen, S.; Bots, G.; Luyendijk, W.; Frangione, B. (1990) Mutation of the Alzheimer's disease amyloid gene in hereditary cerebral hemorrhage, Dutch type. *Science 248*, 1124-1126.

10. Tomiyama, T.; Nagata, T.; Shimada, H.; Teraoka, R.; Fukushima, A.; Kanemitsu, H.; Takuma, H.; Kuwano, R.; Imagawa, M.; Ataka, S., et al. (2008) A new amyloid β variant favoring oligomerization in Alzheimer's-type dementia. *Ann. Neurol. 63*, 377-387.

11. Miravalle, L.; Tokuda, T.; Chiarle, R.; Giaccone, G.; Bugiani, O.; Tagliavini, F.; Frangione, B.; Ghiso, J. (2000) Substitutions at Codon 22 of Alzheimer's Aβ Peptide Induce Diverse Conformational Changes and Apoptotic Effects in Human Cerebral Endothelial Cells. *J. Biol. Chem. 275*, 27110-27116.

12. Grabowski, T. J.; Cho, H. S.; Vonsattel, J. P. G.; Rebeck, G. W.; Greenberg, S. M. (2001) Novel amyloid precursor protein mutation in an Iowa family with dementia and severe cerebral amyloid angiopathy. *Ann. Neurol. 49*, 697-705.

13. Baumketner, A.; Bernstein, S. L.; Wyttenbach, T.; Lazo, N. D.; Teplow, D. B.; Bowers, M. T.; Shea, J.-E. (2006) Structure of the 21–30 fragment of amyloid β-protein. *Protein Sci. 15*, 1239-1247.

14. Krone, M. G.; Baumketner, A.; Bernstein, S. L.; Wyttenbach, T.; Lazo, N. D.; Teplow, D. B.; Bowers, M. T.; Shea, J.-E. (2008) Effects of Familial Alzheimer's Disease Mutations on the Folding Nucleation of the Amyloid β-Protein. *J. Mol. Biol. 381*, 221-228.

15. Sgourakis, N. G.; Yan, Y.; McCallum, S. A.; Wang, C.; Garcia, A. E. (2007) The Alzheimer's Peptides Aβ40 and 42 Adopt Distinct Conformations in Water: A Combined MD / NMR Study. *J. Mol. Biol. 368*, 1448-1457.

16. Takeda, T.; Klimov, D. K. (2009) Probing the Effect of Amino-Terminal Truncation for Aβ1−40 Peptides. *J. Phys. Chem. B. 113*, 6692-6702.

17. Hori, Y.; Hashimoto, T.; Wakutani, Y.; Urakami, K.; Nakashima, K.; Condron, M. M.; Tsubuki, S.; Saido, T. C.; Teplow, D. B.; Iwatsubo, T. (2007) The Tottori (D7N) and English (H6R) Familial Alzheimer Disease Mutations Accelerate Aβ Fibril Formation without Increasing Protofibril Formation. *J. Biol. Chem. 282*, 4916-4923.

18. Ono, K.; Condron, M. M.; Teplow, D. B. (2010) Effects of the English (H6R) and Tottori (D7N) Familial Alzheimer Disease Mutations on Amyloid β-Protein Assembly and Toxicity. *J. Biol. Chem. 285*, 23186-23197.

19. Wakutani, Y.; Watanabe, K.; Adachi, Y.; Wada-Isoe, K.; Urakami, K.; Ninomiya, H.; Saido, T. C.; Hashimoto, T.; Iwatsubo, T.; Nakashima, K. (2004) Novel amyloid precursor protein gene missense mutation (D678N) in probable familial Alzheimer's disease. *J. Neurol., Neurosurg. Psychiatry 75*, 1039-1042.

20. Gessel, M. M.; Bernstein, S.; Kemper, M.; Teplow, D. B.; Bowers, M. T. (2012) Familial Alzheimer's Disease Mutations Differentially Alter Amyloid β-Protein Oligomerization. *ACS Chem. Neurosci. 3*, 909-918.

21. Chen, W.-T.; Hong, C.-J.; Lin, Y.-T.; Chang, W.-H.; Huang, H.-T.; Liao, J.-Y.; Chang, Y.-J.; Hsieh, Y.-F.; Cheng, C.-Y.; Liu, H.-C., et al. (2012) Amyloid-Beta (Aβ) D7H Mutation Increases Oligomeric Aβ42 and Alters Properties of Aβ-Zinc/Copper Assemblies. *PLoS ONE 7*, e35807.

22. Jonsson, T.; Atwal, J. K.; Steinberg, S.; Snaedal, J.; Jonsson, P. V.; Bjornsson, S.; Stefansson, H.; Sulem, P.; Gudbjartsson, D.; Maloney, J., et al. (2012) A mutation in APP protects against Alzheimer's disease and age-related cognitive decline. *Nature 488*, 96-99.

23. Di Fede, G.; Catania, M.; Morbin, M.; Rossi, G.; Suardi, S.; Mazzoleni, G.; Merlin, M.; Giovagnoli, A. R.; Prioni, S.; Erbetta, A., et al. (2009) A Recessive Mutation in the APP Gene with Dominant-Negative Effect on Amyloidogenesis. *Science 323*, 1473-1477.

24. Messa, M.; Colombo, L.; del Favero, E.; Cantù, L.; Stoilova, T.; Cagnotto, A.; Rossi, A.; Morbin, M.; Di Fede, G.; Tagliavini, F., et al. (2014) The Peculiar Role of the A2V Mutation in Amyloid-β (Aβ) 1–42 Molecular Assembly. *J. Biol. Chem. 289*, 24143-24152.

25. Benilova, I.; Gallardo, R.; Ungureanu, A.-A.; Castillo Cano, V.; Snellinx, A.; Ramakers, M.; Bartic, C.; Rousseau, F.; Schymkowitz, J.; De Strooper, B. (2014) The Alzheimer Disease Protective Mutation A2T Modulates Kinetic and Thermodynamic Properties of Amyloid-β (Aβ) Aggregation. *J. Biol. Chem. 289*, 30977-30989.

26. Maloney, J. A.; Bainbridge, T.; Gustafson, A.; Zhang, S.; Kyauk, R.; Steiner, P.; van der Brug, M.; Liu, Y.; Ernst, J. A.; Watts, R. J., et al. (2014) Molecular Mechanisms of Alzheimer Disease Protection by the A673T Allele of Amyloid Precursor Protein. *J. Biol. Chem. 289*, 30990-31000.

27. Lomakin, A.; Chung, D. S.; Benedek, G. B.; Kirschner, D. A.; Teplow, D. B. (1996) On the Nucleation and Growth of Amyloid β-Protein Fibrils: Detection of Nuclei and Quantitation of Rate Constants. *Proc. Natl. Acad. Sci. U. S. A. 93*, 1125-1129.

28. Wyttenbach, T.; Kemper, P. R.; Bowers, M. T. (2001) Design of a new electrospray ion mobility mass spectrometer. *Int. J. Mass Spectrom. 212*, 13-23.

29. Bernstein, S. L.; Dupuis, N. F.; Lazo, N. D.; Wyttenbach, T.; Condron, M. M.; Bitan, G.; Teplow, D. B.; Shea, J.-E.; Ruotolo, B. T.; Robinson, C. V., et al. (2009) Amyloid-β protein oligomerization and the importance of tetramers and dodecamers in the aetiology of Alzheimer's disease. *Nat. Chem. 1*, 326-331.

30. Lesné, S.; Koh, M. T.; Kotilinek, L.; Kayed, R.; Glabe, C. G.; Yang, A.; Gallagher, M.; Ashe, K. H. (2006) A specific amyloid-β protein assembly in the brain impairs memory. *Nature 440*, 352-357.

31. Gong, Y.; Chang, L.; Viola, K. L.; Lacor, P. N.; Lambert, M. P.; Finch, C. E.; Krafft, G. A.; Klein, W. L. (2003) Alzheimer's disease-affected brain: presence of oligomeric Aβ ligands (ADDLs) suggests a molecular basis for reversible memory loss. *Proc. Natl. Acad. Sci. U. S. A. 100*, 10417-10422.

32. Das, P.; Murray, B.; Belfort, G. (2015) Alzheimer's Protective A2T Mutation Changes the Conformational Landscape of the Aβ1–42 Monomer Differently Than Does the A2V Mutation. *Biophys. J. 108*, 738-747.

33. Nguyen, P. H.; Tarus, B.; Derreumaux, P. (2014) Familial Alzheimer A2V Mutation Reduces the Intrinsic Disorder and Completely Changes the Free Energy Landscape of the Aβ1–28 Monomer. *J. Phys. Chem. B. 118*, 501-510.

34. Urbanc, B.; Cruz, L.; Yun, S.; Buldyrev, S. V.; Bitan, G.; Teplow, D. B.; Stanley, H. E. (2004) In silico study of amyloid β-protein folding and oligomerization. *Proc. Natl. Acad. Sci. U. S. A. 101*, 17345-17350.

35. Asante, E. A.; Smidak, M.; Grimshaw, A.; Houghton, R.; Tomlinson, A.; Jeelani, A.; Jakubcova, T.; Hamdan, S.; Richard-Londt, A.; Linehan, J. M., et al. (2015) A naturally occurring variant of the human prion protein completely prevents prion disease. *Nature 522*, 478-481.

Chapter 8

Role of Species-Specific Primary Structure Differences in Aβ42 Assembly and Neurotoxicity

8.1 Introduction

Alzheimer's disease (AD) is the most common form of late-life dementia[1]. An important working hypothesis of disease causation is aberrant folding and assembly of AB42[2]. This assembly leads to the production of extracellular amyloid plaques by the amyloid β-protein (Aβ) and of intracellular neurofibrillary tangles by tau. Such histopathologic findings are pathognomonic for AD and accompany progressive declines in cognitive ability and executive function[1,3-5]. AD pathology also has been observed in dogs, polar bears, rabbits, cows, sheep, pigs, guinea pigs, orangutans, and rhesus monkeys, but until recently, it has not been found in mice or rats[6-8]. In 2005, Inestrosa *et al.*[9-10] reported that the brush-tailed rat, *Octodon degus* (a rodent indigenous to Chile), normally expresses neuronal APP695 and displays both intra- and extra-cellular deposits of Aβ, intracellular accumulation of phosphorylated tau, strong astrocytic responses, and pyramidal neurons rich in acetylcholinesterase. *O. degus* naturally develop these neuropathological signs of AD between 12-36 months of age. This pathology has been correlated with decreases in spatial and object recognition memory, postsynaptic function, and synaptic plasticity[11-12]. Interestingly, the brains from another rodent, the naked mole rat (the longest lived rodent, with a life span ≈32 years) showed levels of Aβ42 similar to a 3X-Tg-AD mouse model of AD[13].

```
                          1         10        20        30        42
          Human (Aβ42): DAEFRHDSGYEVHHQKLVFFAEDVGSNKGAIIGLMVGGVVIA
   Mus musculus (Mm): DAEFGHDSGFEVRHQKLVFFAEDVGSNKGAIIGLMVGGVVIA
Octodon degus (Od): DAEFRHDSGYEVRHQKLVFFAEDVGSNKGAIIGLMVGGVVIA
```

Figure 8.1 Primary structures of human, *Mm*, and *Od* Aβ42. One-letter amino acid code is used to present the sequences of each Aβ42 peptide. Underlined, italicized letters indicate amino acid differences or substitutions among the peptides.

Examination of the primary structure of Aβ42 in *O. degus* and in the naked mole rat reveals 100% identity[13-14], and this amino acid sequence is identical to that of human Aβ42, *except* for a His13Arg substitution (Figure 8.1). In contrast, mouse (*Mus musculus*; *Mm*) Aβ42 differs from human Aβ42 in having three amino acid substitutions, Arg5Gly, His13Arg, and Tyr10Phe[6,15-17]. Mutations in the amyloid β-protein precursor (APP) that result in amino acid substitutions at other sites in Aβ cause familial AD and cerebral amyloid angiopathy (CAA) [1]. It is particularly interesting that an identical amino acid substitution in humans, His→Arg (the English mutation), but at His6 rather than His13, may be associated with AD[18]. Whether this mutation is causative or simply a polymorphism remains unclear, but incorporation of this substitution into Aβ has been found to substantially increase β-sheet formation, fibril seeding ability, and formation of toxic oligomers[19]. It thus is reasonable to hypothesize that the presence of the two additional amino acid substitutions in *Mm* Aβ42 explains why wild type mice do not show AD-like pathology.

It has been suggested that species-specific differences in Aβ42 primary structure are key factors controlling the development of AD-like pathology[15,20]. However, some of the work in this area is contradictory[16-17,21]. Fraser *et al.* [22] and Hilbich *et al.* [16] argue that differences in primary structure do not account for the lack of amyloid deposits in the brains of aged rats and mice, and have no effect on the morphology and organization of fibrils. In contrast, Ötvös *et al.*[15] and Dyrks *et al.*[21] suggest that subtle interspecies differences in amino acid residues may account for the inability of the rodent peptide to form amyloid

fibrils *in situ*. The reductionist approach of arguing that amino acid sequence differences in Aβ are the *sole* explanation for species-specific development, or lack of development, of AD-like pathology, ignores the fact that mice aren't human. Other explanations for the species-specific differences in neuropathology may exist. Here, we investigate how the natural differences in APP gene sequence among humans, *Mm*, and *O. degus* affect the biophysical, biochemical, and biological properties of the respective Aβ peptides.

8.2 Materials and Methods

Chemicals and Reagents. All chemicals were purchased from Sigma Chemical Co. (Saint Louis, MO) and were of the highest purity available. Water was de-ionized and filtered using a Milli-Q system (Millipore Corp., Bedford, MA). Xpress™ silver-staining kits were from Invitrogen (Carlsbad, CA). Buffers were prepared with sterile, autoclaved water containing 0.002% (w/v) sodium azide. SYPRO Orange dye was purchased from Invitrogen Corp. Annexin-V staining kits were purchased from BioVision, Inc, Milpitas, CA.

Peptide synthesis and preparation. Aβ42 peptides were synthesized using 9-fluorenylmethoxycarbonyl (Fmoc) chemistry and purified by reverse phase high performance liquid chromatography (RP-HPLC), essentially as described[23]. The identity and purity (usually >97%) of the peptides were confirmed by amino acid analysis, mass spectrometry, and reverse phase high performance liquid chromatography (RP-HPLC). Peptides were solvated with 1,1,1,3,3,3-hexafluoroisopropanol (HFIP) as described [24]. Briefly, 100-300 μg of peptide lyophilizate were dissolved in 200 μl of 100% HFIP in a 1.5 ml V-bottom polypropylene microcentrifuge tube (Eppendorf, Fisher Scientific). Each tube was covered with a Kimwipe® (Fisher Scientific) tissue and placed in a chemical fume hood overnight to allow evaporation of the HFIP. Tubes then were placed in a SpeedVac rotary

evaporator (Savant SPD121P, ThermoScientific) for 2 h to ensure complete HFIP removal. The resulting peptide films were dissolved in 10% (v/v) 60 mM NaOH, 45% (v/v) Milli Q water, followed by 45% (v/v) 20 mM sodium phosphate, pH 7.5, containing 0.002% (w/v) sodium azide ("phosphate buffer"). The solutions then were thoroughly mixed and sonicated for 1 min in a Branson 1200 bath sonicator (Branson Ultrasonics Corp., Danbury, CT). The resulting peptide solution either was used immediately or stored at -20°C for future use. When used immediately, the sample was placed on ice and the peptide concentrations were estimated by UV absorbance (ε_{280}=1280 $cm^{-1}M^{-1}$ for human and *Od*; and ε_{257}=200 $cm^{-1}M^{-1}$ for *Mm*). The final concentration of Aβ42, as necessary for each experiment, was achieved by dilution with phosphate buffer. Equimolar amounts of Aβ42 were used in each experiment and a minimum of three independent experiments were performed.

Ion mobility-mass spectrometry (IM-MS). The Aβ42 samples were prepared in 10 mM ammonium acetate buffer (pH = 7.4) with a final peptide concentration of 10 μM. The samples were analyzed on a home-built ion mobility spectrometry-mass spectrometer[25], which has been described in Chapter 2.

Quasielastic light scattering spectroscopy (QLS). *Mm*, *Od*, and human Aβ42 were dissolved at a concentration of 0.5 mg/ml in phosphate buffer, briefly vortexed, sonicated for 20 s, and filtered using a 20 nm Anotop filter (Whatman, Maidstone, England). Samples were monitored at ≈22°C for 7–10 days. Measurements were done using a custom optical setup comprising a 40 mW He-Ne laser (λ=633nm) (Coherent, Santa Clara, CA) and PD2000DLS detector/correlator unit (Precision Detectors, Bellingham, MA). Light scattering was measured at a 90° angle. The intensity correlation function and the diffusion coefficient (*D*) frequency distribution were determined using Precision Deconvolve software

(Precision Detectors, Bellingham, MA). Hydrodynamic radius R_H was calculated from D according to the Stokes-Einstein equation $R_H = k_B T / 6\pi\eta D$; where k_B is Boltzmann's constant, T is Kelvin, and η is the solvent viscosity [26].

To determine the instrument-independent rate of change in relative intensity, we calculate the normalized quantity $(dI/dt)/I_0$ (units of h^{-1}). The rate of change in scattering intensity, dI/dt, was determined by fitting to a linear function spanning the first hour of incubation. I_0 was determined from the derived line $I_t=(dI/dt)t + I_0$ by substitution of $t=0$. Both dI/dt and I_0 depend on the aperture in which light is collected, which in turn is a function of the instrument used. We note that these quantities are precise, but likely not absolutely accurate, because the intensity versus time dependency over this time interval is significantly non-linear.

Thioflavin T (ThT) binding. HFIP-treated Aβ42 peptide films were prepared in phosphate buffer at a nominal concentration of 1 mg/ml on ice and added to 96-well optical-bottom microtiter plates (Thermo Fisher Scientific, Rochester NY), followed by 1.6 µl of ThT at a concentration of 5 mM in phosphate buffer. Phosphate buffer was added to the wells to produce a final volume of 200 µl and final Aβ and ThT concentrations of 20 and 40 µM, respectively. The solutions were mixed gently by pipetting solution into and out of the pipette tip. The plates were sealed using an adhesive plate sealer and incubated at 37°C with gentle shaking (160 rpm) (Innova 4080 incubator shaker, New Brunswick Scientific, NJ). Fluorescence was determined using λ_{ex}=450 nm and λ_{em}=482 nm. Readings were taken immediately (0 h), every hour for 6 h, and subsequently at 24 h intervals. Buffer alone, instead of peptide, constituted the ThT blank. A minimum of 5 replicates of each sample was measured. The mean of the blank readings were subtracted from the mean of the sample

readings at each time point and the corrected values, along with mean and SD, were plotted using KaleidaGraph (v 4.1, Synergy Software, Reading, PA). Statistical analyses (*t*-test and Mann-Whitney Rank test) were performed using SigmaStat (Jandel Scientific, San Jose, CA).

Bis-ANS fluorescence. Bis-ANS (1,1′-Bis(4-anilino, 5-naphthalene sulfonic acid)) fluorescence was monitored periodically in 20 μM Aβ42 samples incubating at 37°C with shaking (160 rpm). Fifty μl of the sample (5 μM final concentration in the cuvette) was removed at regular intervals and added to 150 μl of 133.3 μM Bis-ANS solution in a 1.5 ml semi-micro disposable fluorescence cuvette (Brand, Germany). The cuvette was placed in the dark at room temperature (RT; 22.5 °C) for 5 min without shaking and then fluorescence (λ_{ex}=400 nm and λ_{em}=495 nm) was determined using a Hitachi model F-4500 Fluorescence Spectrophotometer (Hitachi America, NJ). The excitation and emission slit widths were both 5 nm. Each sample was read in triplicate, averaged, and corrected using a buffer blank incubated for the same amount of time. The samples were read at 2 h intervals for the first 12 h and subsequently at 24 h intervals. The data were plotted in KaleidaGraph (v 4.1, Synergy Software, Reading, PA). Statistical analyses on the data (*t*-test and Mann-Whitney Rank test) were performed using SigmaStat (Jandel Scientific, San Jose, CA).

Circular Dichroism Spectroscopy. *Mm*, *Od*, and human Aβ42 peptides were prepared from HFIP dried films at final concentrations of 20 μM. For the mixture Aβ42 samples, the final concentration of each peptide in the mixture was 10 μM. The peptides were incubated in 1 mm path length cuvettes, without shaking, at 37 ºC. Spectra were acquired using a JASCO J-810 spectropolarimeter (Tokyo, Japan) every 15 min for the first 3 h and subsequently every 30-60 min. CD measurement parameters were: wavelength range,

190–260 nm; data pitch, 0.2 nm; continuous scan mode; scan speed, 100 nm/min; response time, 1 s; band width, 2 nm; scan number per sample, 7. The raw spectra were smoothed using the means movement smoothing parameters within the data acquisition software (Spectra Manager 2). The data were subsequently plotted in KaleidaGraph (v 4.1, Synergy Software, Reading, PA).

Electron microscopy (EM). Formvar 400 mesh grids were glow discharged on a Med010 mini-deposition system EM glow discharge attachment model BU007284-T (Balzers Union Ltd, Hudson, NH) containing a cylindrical discharge compartment and an adjacent discharge control and timer unit. Aβ42 was incubated at 37°C with continuous shaking (160 rpm). Eight µl aliquots were mixed thoroughly and then they were applied to the grid at days 0 and 7. The grid was covered and incubated for 20 min at RT. Liquid was wicked off carefully using a filter paper wick by gently touching the tip of the filter paper to the edge of the grid. Five µl of 2.5% (v/v) glutaraldehyde in water were added to the grid, which then was incubated for 3 min in the dark. The glutaraldehyde solution was wicked off and replaced with 5 µl of 1% (w/v) uranyl acetate in water, which then was incubated for 3 minutes in the dark. The grids then were wicked off and air-dried. A JEOL 1200 EX (JEOL Ltd., Tokyo, Japan; 40-120 kV) transmission electron microscope used to visualize the samples on the grid[27].

Neuronal Cell Cultures. Primary cortical or hippocampal neurons were prepared as described previously [28]. Briefly, pregnant E18 rats were euthanized with CO_2 and the pups were removed immediately. Brains were dissected in chilled Leibovitz's L-15 medium, pH 7.5, (ATCC, Manassas, VA) in the presence of 1 µg/ml penicillin/streptomycin (Invitrogen, Carlsbad, CA). The tissue was incubated with 0.25% (w/v) trypsin in phosphate-buffered

saline, pH 7.5 (PBS), containing 0.02% (w/v) EDTA for 30 min and then mechanically dissociated in a small volume of Leibovitz's L-15 medium using a fire-polished Pasteur pipette. The neurons were suspended in Dulbecco's modified Eagle's medium, pH 7.5, (DMEM; ATCC) containing 10% (v/v) heat-inactivated fetal bovine serum (FBS) (ATCC) and penicillin/streptomycin (1 μg/ml) and plated on poly-D-lysine (0.1 mg/ml, Sigma)-coated 96-well COSTAR plates (Corning, Lowell, MA) at a density of 3×10^5 cells/ml. Twenty-four hours after the cells had been plated, the medium was replaced with fresh medium supplemented with 5 μM cytosine β-d-arabinofuranoside (Sigma Chemical Co, St Louis, MO) to inhibit the proliferation of glial cells. The cultures were maintained for 6 d before being treated with Aβ42. PC-12 cells were cultured and differentiated with 50 ng/ml nerve growth factor (NGF) 24 h prior to treatment with peptides, as described previously[29]. Human SHSY-5Y cells were grown in DMEM/F12K (1:1) media, pH 7.5, containing 10% (v/v) heat-inactivated FBS and penicillin/streptomycin (1μg/ml), 2 mM glutamine, and 1.5 g/L sodium bicarbonate. The cultures were maintained at 37°C in a humidified atmosphere of 5% (v/v) CO_2.

MTT (3-(4,5-Dimethylthiazol-2-yl)-2,5-diphenyltetrazolium bromide) Assay. Cell metabolism was evaluated using the MTT assay, as described previously [30]. Briefly, rat primary cortical neurons or NGF-differentiated PC12 cells were treated with 10 μM freshly prepared Aβ42 for 24 h at 37 °C. Following treatment, 15 μl of MTT, prepared by dissolution in 10% (*v/v*) Triton-X 100 in 2-propanol containing 0.1N HCl, according to the manufacturer's instructions (Promega, Madison, WI), was added to each well and the samples were incubated for 4 h at 37°C. "Stop solution" (Promega, Madison, WI) then was added and the samples were incubated overnight at RT. $OD_{570\text{-}630}$ was measured using a

Synergy plate reader (Bio-TEK Instruments, Winooski, VT). A minimum of three independent experiments (six wells per data point) were performed. Data were normalized to the medium control group and expressed as the mean ± the standard error of the mean (SEM).

LDH (Lactate Dehydrogenase) Assay. Rat primary cortical neurons and NGF-differentiated PC12 cells were incubated with 10 μM Aβ42 peptide for 48 h at 37°C in Eagle's minimal essential medium (MEM, Earle's salts, supplied glutamine-free) supplemented with 5% (*v/v*) heat-inactivated horse serum, 5% (*v/v*) fetal bovine serum, 2 mM glutamine, and 25 mM glucose. Cell death was assayed by measuring released LDH activity, as described previously[27]. Data from a minimum of three independent experiments (six wells per data point) were normalized to media control and expressed as mean ± SEM.

Apoptosis Assay: Apoptosis was estimated using Annexin V-FITC fluorescence. Briefly, SH-SY5Y neuroblastoma cells (ATCC® CRL-2266) were grown on cover slips coated with poly D-lysine (0.1 mg/ml) in DMEM/F12K (1:1) medium containing 10% (*v/v*) heat-inactivated fetal bovine serum (FBS), penicillin/streptomycin (1 μg/ml), 2 mM glutamine, and 1.5 g/L sodium bicarbonate. The cells were maintained at 37°C in a humidified atmosphere of 5% (*v/v*) CO_2 in air until a cell density of 1-5 × 10^5 cells per well was obtained, at which point the cells were exposed to peptide (10 μM final concentration) for 24 h. The peptides were prepared by dissolution of HFIP films in cell culture medium. Staurosporine (1 μM final concentration) was added to cells as a positive control for apoptosis. The negative control was cells treated with medium containing no Aβ42. After the incubation period, the coverslip was washed in PBS and fixed with 4% (v/v) paraformaldehyde in PBS. The cells were stained with an Annexin V-FITC apoptosis

detection kit (Bio Vision Incorporate, Milpitas, CA) according to the manufacturer's instructions. Images were recorded using a confocal laser scanning microscope (Zeiss, Model: LSM 700; λ_{ex}=488 nm and λ_{em}=535 nm). The numbers of apoptotic cells were counted in a 100 μm^2 area using Image-J software (Image-J, NIH). A minimum of 30 microscopic fields was used for morphometric analysis from two independent experiments.

8.3 Results and Discussion

8.3.1 Ion mobility-mass spectrometry (IM-MS) and Aβ42 monomer structure

To probe the effects of primary sequence difference (Figure 8.1) on the peptide structure and oligomer distributions of all Aβ42 alloforms, we performed an ion mobility coupled with mass spectrometry (IM-MS) analysis. The mass spectra of all three Aβ42 alloforms immediately after preparation were recorded and shown in Figure 8.2. All alloforms show three peaks corresponding to the z/n = -4, -3, and -5/2 charge states, where z is the charge and n is the oligomer number. It is notable that the relative intensity of the z/n = -5/2 peak for *Mm* is relatively higher than that of the Aβ42 or *Od*, suggesting the oligomer formation for *Mm* is more abundant. In addition, there is a z/n = -2 peak which might contain oligomer species observed for *Mm*. These mass spectrometry results suggest that *Mm* oligomerizes more readily than do Aβ42 or *Od.* Interestingly, this suggestion is consistent with the observation that the *Mm* sample clogged the nano-electrospray tips more easily during the experiment than either Aβ42 or *Od*.

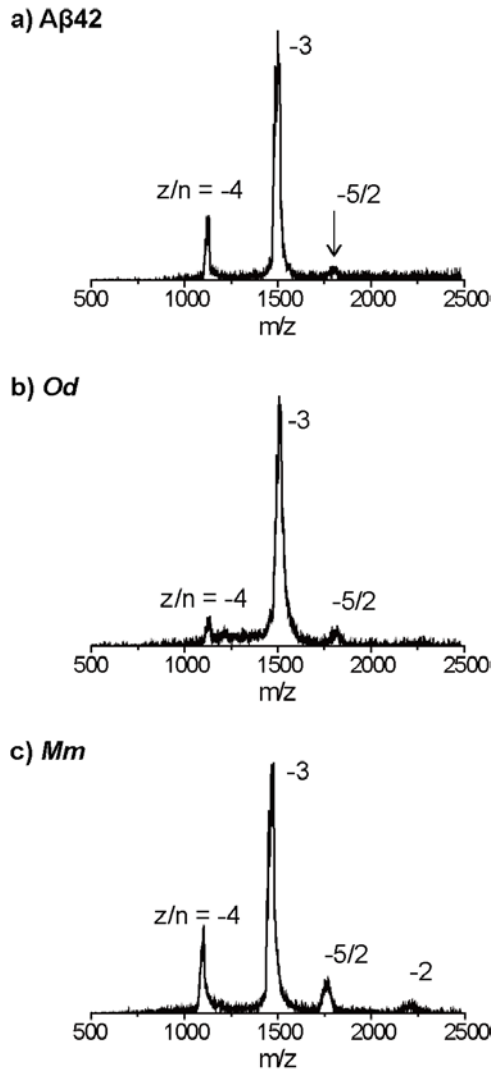

Figure 8.2 Mass spectra of all Aβ42 alloforms. The charge state z/n is noted for each species where z is the charge and n is the oligomer number.

To probe whether these Aβ42 alloform have different monomer structures, the ATDs for the z/n = -3 species were recorded and shown in Figure 8.3. The ATD of the z/n = -3 Aβ42 (Figure 8.3a) has been studied in previous studies [31-32] showing two major features with arrival times at ~620 and 670 μs which were assigned as a compact solvent free-like conformer and an extended solution-like conformer, respectively. Similarly, the ATD of the z/n = -3 *Od* shows two features which can be assigned as compact solvent free and extended

solution-like conformers, based on their cross sections. Interestingly, the ATD of the z/n = -3 *Mm* displays three features, two with similar arrival times as Aβ42 or *Od* and one with a longer arrival time, which is not observed for Aβ42 or *Od* species. This indicates there is an additional monomer conformer with more extended structure for *Mm*. As shown in Table 8.1, the collision cross sections of M_1 and M_2 monomers for each peptide are very similar, suggesting that all three Aβ42 alloforms have similar monomer conformations (M_1 and M_2). *Mm* forms one additional extended conformer (M_3), which may be of relevant to its aggregation kinetics.

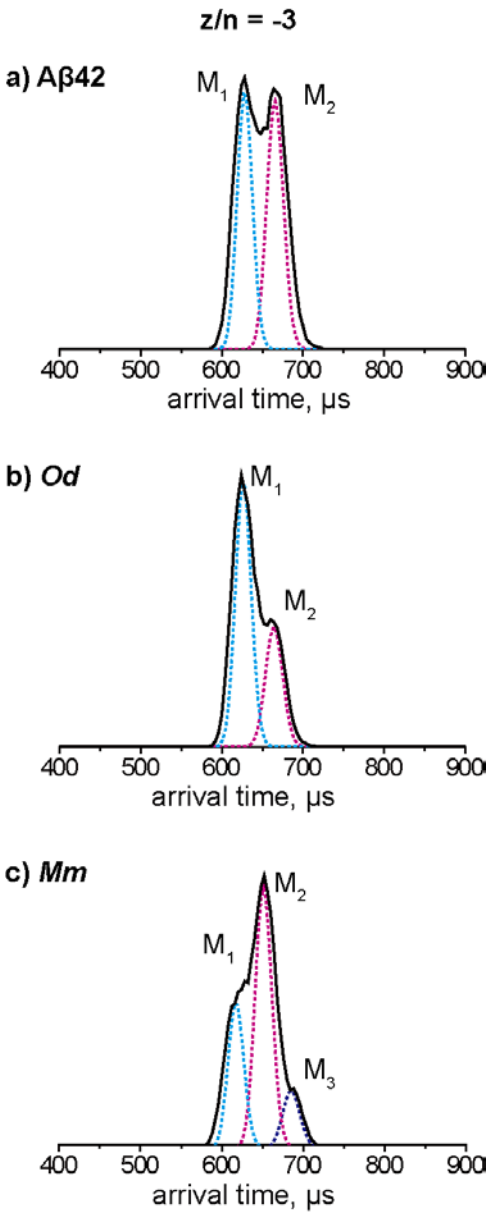

Figure 8.3 The ATDs of the z/n = -3 for all Aβ42 alloforms. M_1, M_2 and M_3 represent three monomer conformers with different sizes.

Table 8.1 Cross sections of the monomers and oligomers for all Aβ42 alloforms in $Å^2$. σ is the cross section and σ/n represents the cross section for the monomer in the oligomer.

Oligomer	Charge state	Aβ42		*Od*		*Mm*	
		σ	σ/n	σ	σ/n	σ	σ/n
Monomer	-2	-	-	-	-	618	618
	-3 (M_1)	643	643	630	630	635	635
	-3 (M_2)	702	702	692	692	698	698
	-3 (M_3)	-	-	-	-	757	757
	-4	792	792	790	790	807	807
Dimer	-4	-	-	-	-	968	484
	-5	1246	623	1218	609	1234	617
Trimer	-6	-	-	-	-	1275	425
Tetramer	-10	2172	543	2156	539	2204	551
Hexamer	-15	2838	473	2928	488	2910	485
Dodecamer	-30	4560	380	4512	376	-	-

8.3.2 Ion mobility spectrometry and Aβ42 oligomer distributions

To understand the early oligomer distributions of the Aβ42 species, the ATDs of the z/n = -5/2 peaks were recorded and are shown in Figure 8.4. The ATD of Aβ42 shows four features with arrival times at ~710, 680, 620 and 540 μs, which have previously [31,33] been assigned as dimer, tetramer, hexamer and dodecamer based on their cross section values (Table 8.1, also see reference 25 for a detailed discussion of the Aβ42 oligomer assignments). Similarly, the ATD of *Od* shows four features corresponding to dimer, tetramer, hexamer and dodecamer. However, the ATD of *Mm* shows only three features corresponding to dimer, tetramer and hexamer. Finally, the ATD of the z/n = -2 *Mm* was

recorded and shows two primary features corresponding to dimer and trimer (Figure 8.4d), indicating that *Mm* forms trimer, which is not observed for Aβ42 or *Od* under these experimental conditions. The lack of dodecamer in mouse is interesting as it may correlates with the fact *Mm* does not naturally display AD-like neuropathology, in contrast to mice expressing the human form of Aβ[34], which express substantial levels of Aβ*56, a dodecamer linked to memory deficits.

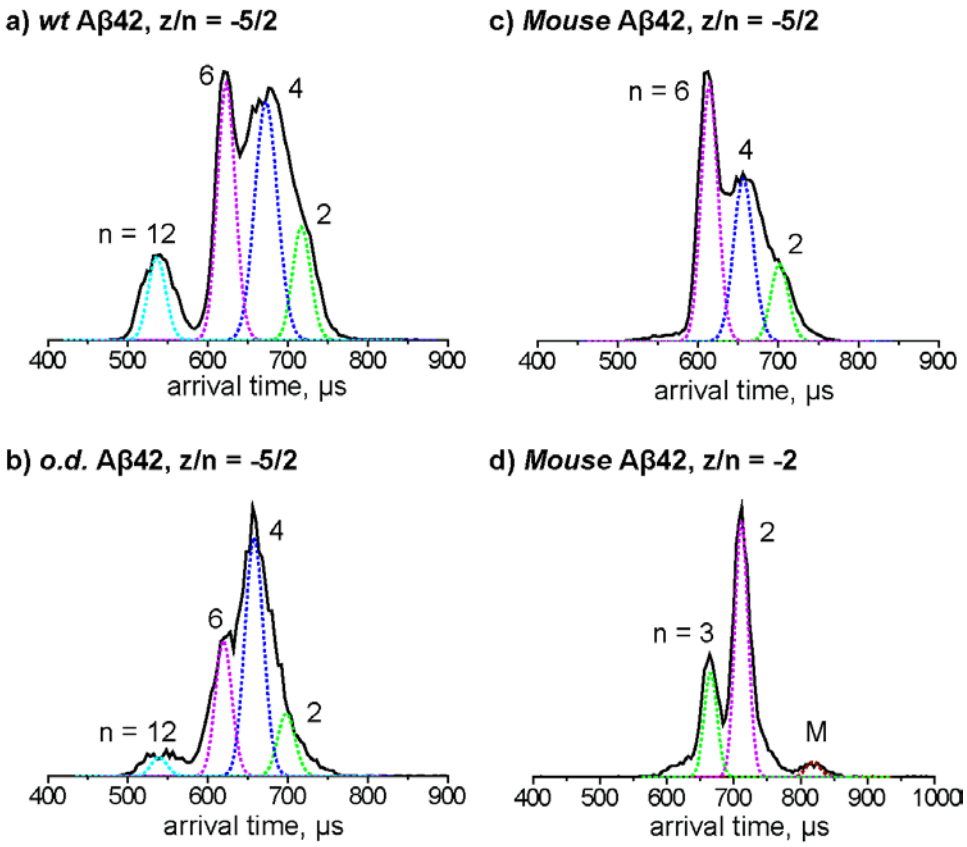

Figure 8.4 Ion mobility spectrometry and Aβ42 oligomer distributions. a-c) The ATDs of the z/n = -5/2 peaks for all Aβ42 alloforms. d) The ATD of the z/n = -2 peak for mouse Aβ42. The oligomer number (n) is noted for each feature.

8.3.3 Monitoring Aβ assembly by quasielastic light scattering spectroscopy (QLS)

QLS is a method for the non-invasive monitoring of the diffusion coefficients (*D)* of particles in solution[35]. We used QLS, and the Stokes-Einstein equation (see Methods), to derive R_H distributions of each peptide after 0.5 h and 24 h of incubation (Figure 8.5). Aβ42 initially produced a distribution composed primarily of small particles of $R_H \approx$ 8-10 nm (darkened area). Particles of $R_H \sim$ 100–1000 nm also were observed, but because scattering intensity is proportional to the square of molecular weight, these peaks must have been produced by relatively few particles. After 24 h, the contributions to the scattered light intensity of larger particles had increased substantially, consistent with a process of Aβ assembly. However, oligomers of $R_H \approx$ 8-10 nm remained[1]. Such oligomers have been reported previously[29]. In contrast, the other peptides did not form oligomers of this size. After 24 h of incubation, the distribution of *Mm* changed little, showing only a slightly increased average R_H of its predominant peak. Deconvolution of R_H distributions depends on the specific parameterizations used, especially that for data smoothing[35]. Although deconvolution yielded two peaks for *Mm*, it is possible that only one heterodisperse population of scatterers was present. For this reason, the average R_H was calculated across the entire distribution. *Od* showed substantial increases in R_H over 24 h, yielding three nodes of R_H intensity, at ≈90 nm, ≈500 nm, and ≈4000 nm. The average R_H was 1740 nm. Interestingly, the time-dependence of the distributions of R_H showed that those of Aβ42 and *Od* primarily comprised relatively small scatterers initially ($\overline{R_H} \approx 10\ nm$ and $\overline{R_H} \approx 62\ nm$, respectively) but that after 24 h the distribution range expanded to larger sizes with maximal

[a] The scattering intensity varies as the square of the molecular weight of the scatterer. The maximum intensity of small scatterers (shaded bars) was equivalent to those for larger scatterers (unshaded bars), which means that a disproportionate percentage of scatterers in this mixture were small. For the purpose of comparison between the two time points, we focused on these small scatterers when we calculated scatterer R_H.

$R_H > 1000\,nm$. *Mm* was unique in initially displaying larger scatterers ($\overline{R_H} \approx 233\,nm$) whose size remained relatively constant over 24 h.

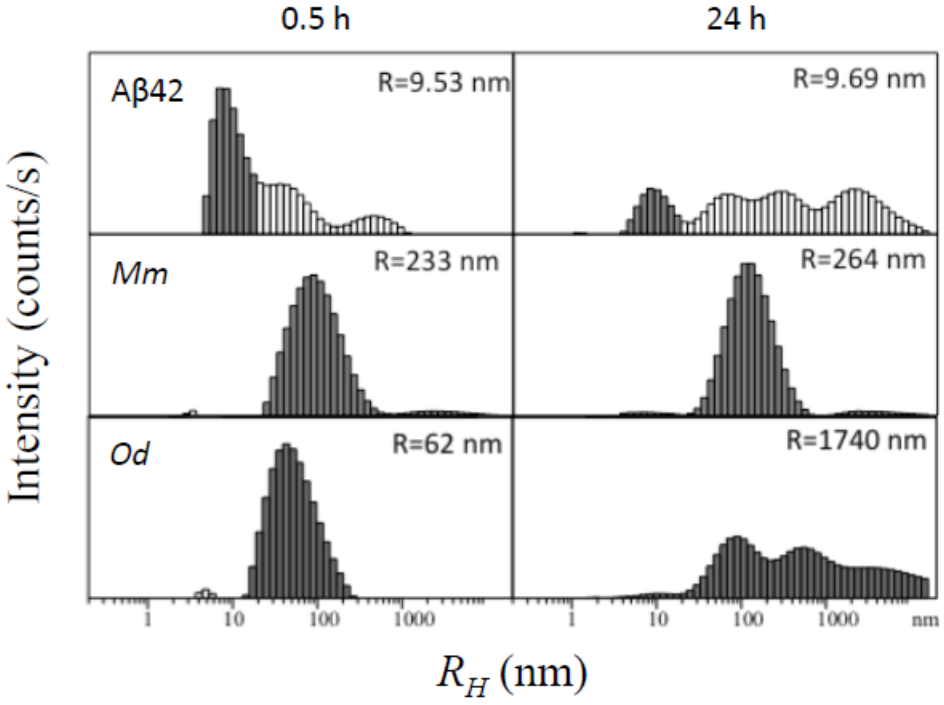

Figure 8.5 Quasielastic light scattering spectroscopy (QLS). Intensity (counts/sec) is plotted versus hydrodynamic radius (R_H in nm). The data are from samples monitored ≈. The number in the top right corner of the panel represents the average R_H for the shaded regions of the distributions. Buffer spectra produce no scattering and thus are not shown.

It should be noted that all samples were filtered through a 20 nm porosity filter immediately after preparation. During the first 30 min of monitoring, for all peptides except Aβ42, we observed a rapid increase in scatterer size, reflecting a rapid assembly process. The particle size distributions then were relatively stable while overall scattering intensity continued to rise due to increasing contribution to scattering from large particles. We calculated the rate of growth in the scattering intensity during the first hour of incubation

(Table 8.2). Rates for Aβ42 and *Mm* were moderate, consistent with relative constancy of their particle size distributions.

Taken together, the data on the time-dependent evolution of R_H and scattering intensity suggest that *Mm* rapidly forms small aggregates that are relatively stable, whereas both Aβ and *Od* display a lag time before fibril assembly is observed.

Table 8.2 Rate of change in scattering intensity. The rate of change in scattering intensity, *dI/dt*, determined by fitting I_t to a linear function spanning the first hour of incubation. I_0 was determined from the derived line $I_t = dI/dt \times t + I_0$ by substitution of $t=0$. Both *dI/dt* and I_0 depend on the aperture in which light is collected, which in turn is a function of the instrument used. To determine the instrument-independent rate of change in relative intensity, we report the normalized quantity $(dI/dt)/I_0$. We note that these quantities are precise, but likely not absolutely accurate, because the intensity versus time dependency over this time interval is significantly non-linear.

Peptide	$(dI/dt)/I_0$
Aβ42	0.05
Mm	0.09
Od	1.43

8.3.4 Monitoring Aβ42 assembly kinetics by ThT fluorescence.

ThT binding was performed to monitor the assembly of β-sheet-rich structures [36-38] (Figure 8.6A). Aβ42 displayed a classical ThT fluorescence curve starting at a low fluorescence level (~25 FU), remaining constant for ≈1 h, and then monotonically increasing during the next 5 h. In contrast, *Mm* fluorescence tripled within the first hour. *Od* displayed a somewhat higher initial level of ThT fluorescence than did Aβ42 but only a gradual increase during the initial 6 h. We continued monitoring for 21 d, during which time all three peptides displayed increasing rates of increase of ThT fluorescence (dFU/dt), until a plateau level was reached. The final fluorescence level of Aβ42 was substantially lower than

that of *Mm* (≈425 versus ≈800 FU) and somewhat lower than that of *Od* (≈425 versus ≈500 FU). It was interesting that the maximal value of dFU/dt for each peptide was similar. A similar behavior as in QLS was observed in the ThT experiments in that *Mm* quickly displayed substantial fluorescence that remained relatively constant for the first day, before increasing substantially over the next three weeks. The ThT fluorescence of Aβ42, as with its R_H, was the lowest among the four peptides after the first day of incubation.

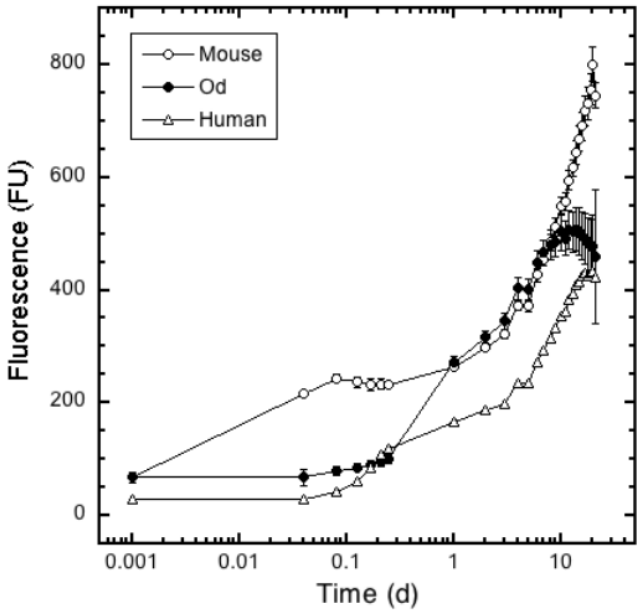

Figure 8.6 Aβ assembly kinetics. ThT fluorescence. Peptides (20 μM) were incubated with 40 μM ThT at pH 7.5 and 37°C with shaking. Data are present on a semi-log plot to allow visualization of data in a single figure for the entire time range (t=0 d, 0.04 d (1h), up to 21 d).

These data are consistent with a reaction coordinate model (Figure 8.7) in which *Mm* has a relatively low activation energy for formation of relatively stable oligomers. This produces the rapid kinetics for oligomer formation and the relatively long lifetimes of the oligomers thus formed. However, thermodynamically, the ΔG for fibril formation is similar to those of Aβ and *Od* (Table 8.3), thus eventually *Mm* does from fibrils.

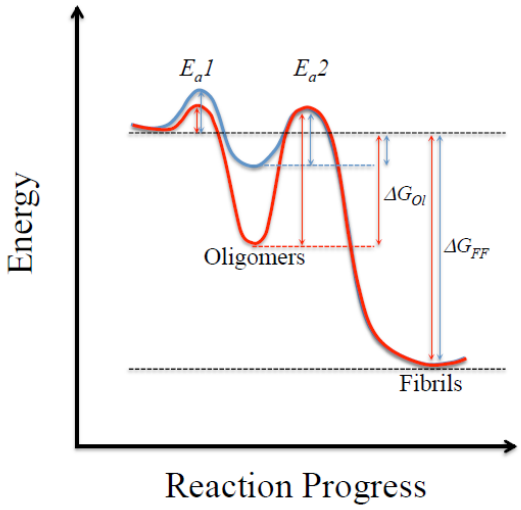

Figure 8.7 Reaction coordinate for peptide assembly. The graph illustrates one reaction coordinate that is consistent with the results of our experiments. The assembly of monomeric peptides into oligomers, and then into fibrils, is illustrated for the *Mm* and Aβ42 peptides. For clarity, *Od*, which behaves similarly to Aβ42, is not illustrated. The assembly of peptide monomers into oligomers is accompanied by an activation energy (E_a1), illustrated pictorially by red *(Mm)* and blue (Aβ42) arrows. E_a1 for *Mm* is lower than for Aβ42, explaining the more rapid oligomerization of the former peptide. In addition, the *Mm* oligomers appear to be more stable, suggesting a lower free energy of formation compared to Aβ42 oligomers (note the larger oligomerization free energy (ΔG_{Ol}) of *Mm* oligomerization). In contrast, the experimentally determined free energies of fibril formation (ΔG_{FF}) are similar (Table 8.2). This explains why the end-state assembly for all three peptides is fibrils, and why although the *Mm* oligomers are most stable, their conversion into fibrils is thermodynamically favored.

Table 8.3 Determination of critical concentration and free energy of fibril formation. Peptides were incubated at a concentration of 20 μM in 20 mM phosphate buffer, pH 7.5, at 37°C for 21 days without shaking. The samples then were centrifuged at 436,000 × ***g*** for 1 h (TLA 120.2 rotor; 120,000 rpm; Beckman Optima TLX Ultracentrifuge). The concentration of Aβ monomer1 present in the supernate was quantified by amino acid analysis (AAA). This concentration is equal to the critical concentration, *Cr*, which is the inverse of the amyloid fibril equilibrium constant, i.e., $k=1/Cr$ (1, 2). The Gibb's free energy change for monomer binding to fibrils then was determined according to the formula $\Delta G_0 = -RT \ln k$. Statistical analysis was performed using *t*-test (paired) and Mann Whitney Rank (MWR) test in SigmaStat (Jandel Scientific Corp, San Jose, CA). The values shown are averages ± S.D. (in parentheses) derived from four independent experiments. *p*-values are relative to Aβ42. The range of *Cr* values varied over an order of magnitude, from ≈0.5-5 μM, displaying a

rank order of concentration of *Mm* < Aβ42 << *Od*. The ΔG_0 values varied proportionately, from -9.20 to -7.64 kcal/mole, respectively. Mm fibrils were the most stable. Aβ42 fibrils displayed a similar but lesser stability. In contrast, *Od* fibrils were significantly less stable than were Aβ42 fibrils.

Peptide	C_r (μM)	*p*-value	ΔG^0 (kcal/mole)	*p*-value
Aβ42	1.10 (0.20)		-8.45 (0.12)	
Mm	0.45 (0.40)	0.065	-9.20 (0.65)	0.123
Od	4.04 (0.99)	0.016	-7.64 (0.14)	<0.001

8.3.5 Exposure of hydrophobic surfaces during Aβ42 assembly by Bis-ANS Fluorescence.

We monitored exposure of hydrophobic surfaces during peptide assembly using Bis-ANS fluorescence (Figure 8.8). Bis-ANS is a hydrophobic molecular probe that is essentially non-fluorescent in water but fluorescent in nonpolar or hydrophobic environments. This property makes it a sensitive indicator of protein conformation (e.g., molten globules, exposed hydrophobic surfaces, or native folds)[39-43].

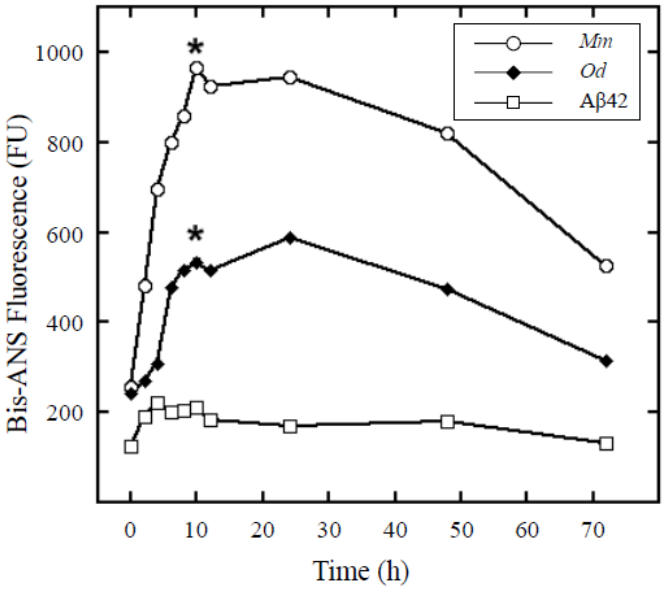

Figure 8.8 Bis-ANS fluorescence. Aliquots from Aβ assembly reactions were removed at regular intervals, mixed with Bis-ANS, and then monitored for fluorescence (as arbitrary fluorescence units (FU)).

Aβ42 showed a rapid but modest increase in fluorescence during the first 4 h of incubation (to ≈200 AU), after which a slow monotonic decrease in fluorescence was observed. *Mm* displayed the highest initial fluorescence level among these peptides, the most rapid increase in fluorescence, and the highest plateau value (≈950 AU). Fluorescence then decreased monotonically with time. *Od* displayed the second highest rate of increase, and plateau level, of fluorescence. Peak fluorescence occurred at ≈24 h, later than for Aβ42 or *Mm*. Experiments also were done with SYPRO Orange (data not shown), a dye with properties similar to that of Bis-ANS. The rates of fluorescence increase and the plateau levels of fluorescence produced by SYPRO Orange exhibited the same rank order as with Bis-ANS, namely *Mm* > *Od* > Aβ42.

The rapid increase in fluorescence in the *Mm* sample suggests early exposure of hydrophobic surfaces. The formation of such surfaces has been postulated to occur as the intrinsically disordered Aβ monomer begins folding[44-45]. This phenomenon would produce rapid aggregation, as seen by ThT (Figure 8.6). The different initial fluorescence levels observed between *Od* and Aβ42 also is consistent with the ThT fluorescence data, which showed higher initial levels of β-sheet in *Od* compared to Aβ42.

8.3.6 Determining secondary structure dynamics by CD spectroscopy

We used circular dichroism spectroscopy (CD) to determine the time-dependence of the distribution of secondary structures for each peptide (Figure 8.9)[46-47]. Aβ42 displayed statistical coil structure initially, but then exhibited a progressive increase in β-sheet content that was clear within hours and produced a classical β-sheet spectrum at 24 h. The spectra appeared to display an isodichroic point at ≈208 nm. This isodichroic point was observed with all these peptides, suggesting the existence of a two-state transition (likely statistical coil→α-helix)[48]. *Mm* exhibited *some* β-sheet content immediately after preparation. Progressive increases in β-sheet were observed throughout the 24 h monitoring period, as with Aβ42. However, the level of β-sheet was higher than in Aβ42, as indicated by the relative increase in absolute values of the molar ellipticities at ≈195 and ≈215 nm. *Od* had the least statistical coil content of any of the peptides when its CD spectrum was first acquired, and the highest β-sheet content. Progressive increases in β-sheet structure then were observed.

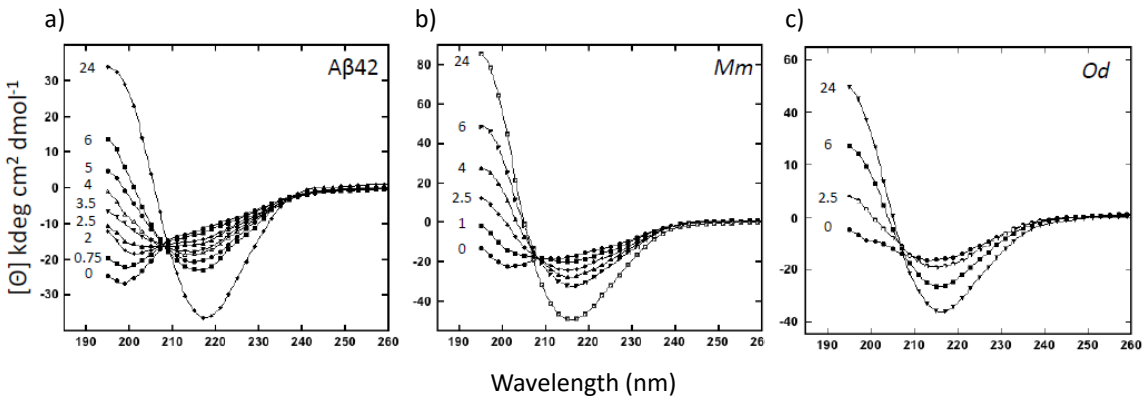

Figure 8.9 Secondary structure dynamics. CD spectroscopy was used to monitor temporal changes in secondary structure. Numbers shown vertically at the 190 nm tick marks are the times (h) at which the respective spectra were collected.

To visualize the relative rates of change in β-sheet content, we plotted $[\Theta]_{215}$ versus time (Figure 8.10). *Mm* showed the highest initial β-sheet content, the fastest increase in the level of this secondary structure element, and the highest overall β-sheet content at the end of the experiment. *Od* also displayed relatively high initial β-sheet content, but the evolution of β-sheet occurred at a slower rate. Aβ42 had the lowest initial β-sheet level, but this level eventually reached that of *Od*. The high initial β-sheet in the *Mm* peptide is consistent with its rapid oligomerization. The monotonic increase in β-sheet for all three peptides suggests a progressive assembly phenomenon that was confirmed in subsequent EM experiments.

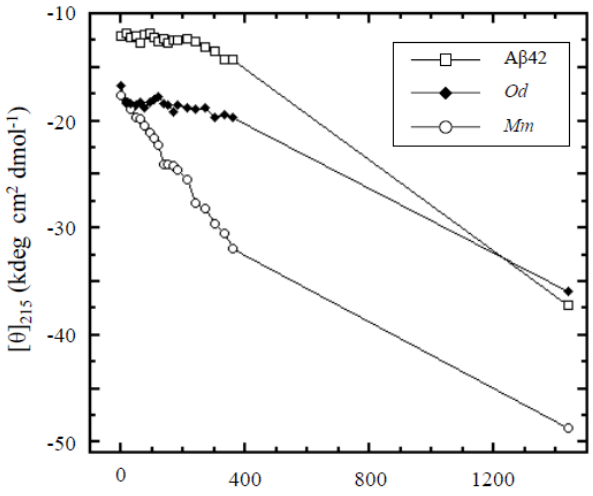

Figure 8.10 Time-dependence of $[\Theta]_{215}$. Molar ellipticity at 215 nm is plotted versus time as a measure of time-dependent changes in β-sheet secondary structure.

8.3.7 Assembly Morphology of Aβ42 alloforms

We used electron microscopy to determine the morphologies of assemblies present at the initiation of peptide incubation and after the assembly process was complete (day 7) (Figure 8.11A, B). Small structures ("globules") were observed initially in the Aβ42 sample. These globules ranged in diameter from 11-23 nm (white arrows, Figure 8.11A), often displaying pore-like central cavities filled with uranyl acetate stain. These annuli had outside diameters ranging from ≈13-25 nm and inside diameters ranging from ≈4-11 nm. *Mm*, in contrast, formed aggregates comprising short beaded chains of different diameters (black arrows) and irregular structures (open arrows). These irregular assemblies ranged in diameter from 11-21 nm and had lengths from 16-75 nm. *Od* displayed filamentous aggregates (open arrows), as well as occasional long filaments to which smaller assemblies appeared to be associated (curved arrow). Small globules (black arrows) were interspersed

among these other structures. The globules range in diameter from 11-54 nm. The diameters of the long fibrils ranged from ≈7-19 nm.

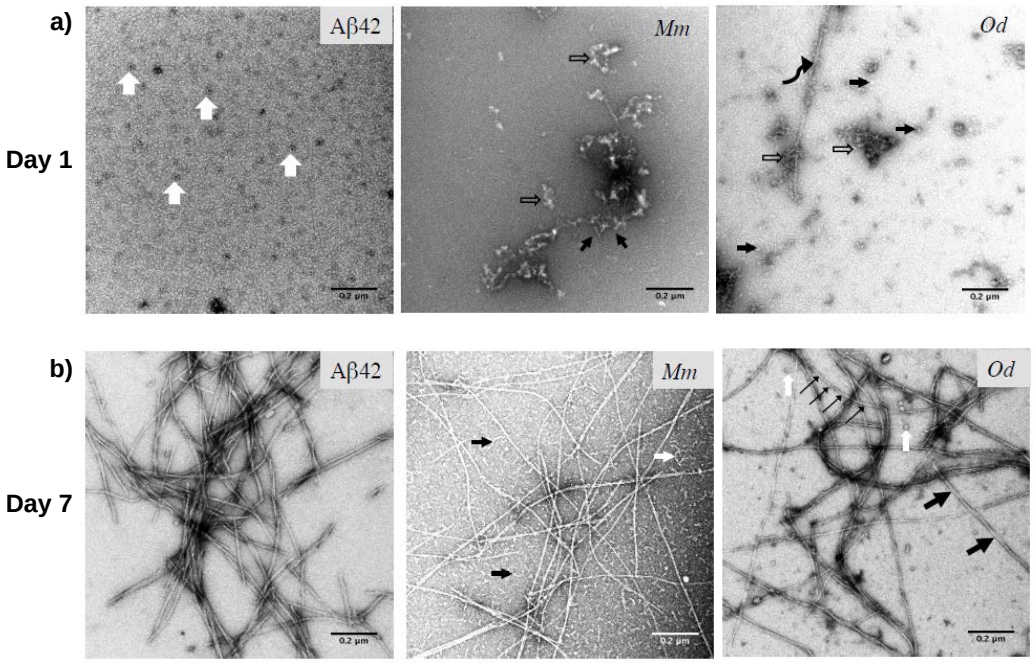

Figure 8.11 Assembly morphology. EM was used to determine assembly morphology. Aliquots of assembly reactions were removed at days 0 (panel A) and 7 (panel B). Determination of geometric parameters (lengths, diameters) was done using Image J software. Scale bars are 200 nm.

Considering the heterogeneity of assembly morphologies observed immediately after sample preparation, it was interesting that by 7 days all samples formed long straight or curved fibrils (Figure 8.11B). Aβ42 predominately formed fibrils of quite different lengths (56-303 nm) and with diameters of ≈7-12 nm (Table 8.3). Long fibrils had a diameter of 9-21 nm. The *Mm* sample contained numerous fibrils that were thinner than those of Aβ42 (Table 8.4), but also abundant smaller curved "protofibril-like" structures (black and white arrows) [23]. *Od* formed long and short fibrils interspersed with numerous globules. Bifilar structures with helical twist were observed (thick black arrow) along with thinner fibrils,

often with helical twists (thin black arrows). A number of annuli also were observed (white arrows).

The results of electron microscopic examination of assembly morphology correlated with the results from the prior experiments. For example, the initial rank order of average assembly size was *Mm* > *Od* > Aβ42, and as would be predicted from the QLS, ThT, and CD experiments, large (fibrillar) assemblies were observed after 7 d. *Mm* continued to behave somewhat uniquely in that the distribution of assemblies at day 7 included abundant protofibrillar species (not seen with the other peptides) and narrower fibrils. The continued presence of the small protofibrils is consistent with the relatively constant distribution of scatter sizes seen during the first 24 h by QLS.

Table 8.4 Dimensions of assemblies observed by EM. Peptides were incubated at 37°C with shaking. Aliquots of assemblies were removed at day 0 and day 7. Following incubation, different classes of assemblies were observed, including globules, short fibrils, and long fibrils. If present, the numbers represent the size range, in units of nm, of each assembly type. Assembly lengths are reported in nm within parentheses.

Peptide	**Day 0**			**Day 7**		
	globules	*short fibrils*	*long fibrils*	*globules*	*short fibrils*	*long fibrils*
Aβ42	11-23	-	-	-	7-12 (56-303)	9-21
Mm	11-21 (16-75)	-	-	-	-	4-19
Od	11-54	-	7-19	7-17	7-17 (37-182)	7-17

8.3.8 Neurotoxic activities of Aβ assemblies.

MTT assays were performed to evaluate the effects of freshly prepared peptides on MTT metabolism[49]. The assay was performed both on PC12 cells (Figure 8.12A) and rat primary cortical neurons (Figure 8.12B). AB42 caused an ≈23% decrease in MTT metabolism in PC12 cells, whereas *Mm* and *Od* were non-toxic. The differences in toxicity between Aβ42 and each of the other peptides was highly significant ($p<0.001$). The data from primary cortical neurons were similar to the same as those from PC12 cells Quantitatively, the levels of toxicity of all peptides assayed with primary cortical neurons was greater than with PC12 cells. LDH assays were performed to measure cell death. The results of these assays were consistent with those of the MTT assays (Figure 8.12C, D). Aβ42 was most toxic while *Mm* and *Od* were least toxic.

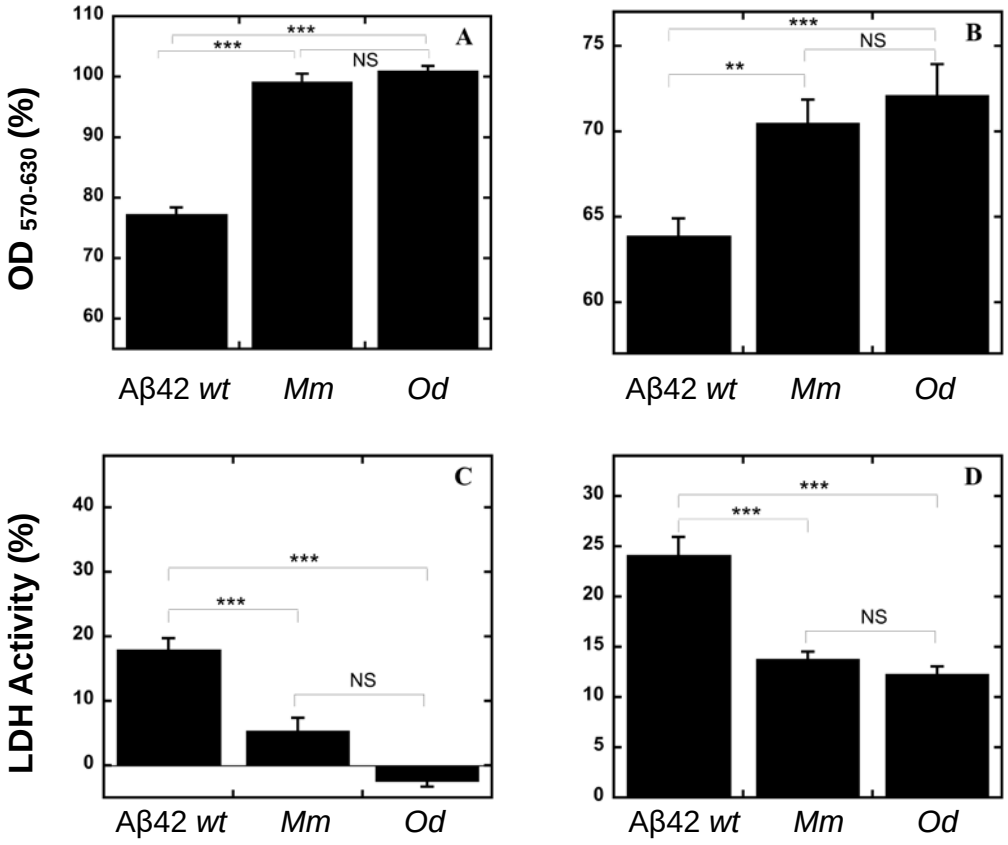

Figure 8.12 Peptide neurotoxicity. To determine the effects of the different peptides on cellular metabolism, MTT assays were performed using (A) differentiated PC12 cells or (B) rat primary cortical neurons. Freshly prepared peptides were added to the cultures for 24h at 37°C, after which MTT was added and incubated for 4h at 37°C, stop solution was added to the cultures, the cultures were incubated overnight, and then formazan optical absorbance was measured at 570-630 nm ($OD_{570-630}$). Data are representative of that obtained in three independent experiments (6 wells per data point). The data are normalized to the media control group and expressed as mean ± the standard error of the mean (SEM). Statistical significance between samples is indicated by asterisks (*** and ** indicate *p* values < 0.001 and <0.01 respectively). NS is "not significant." To determine cell death, LDH activity was measured in the media from (C) differentiated PC12 cells or (D) rat primary cortical neurons after 48 h of incubation of the cells with the different peptides. Data are representative of that obtained in three independent experiments (6 wells per data point). The data are normalized to the media control group and expressed as mean ± the standard error of the mean (SEM). Statistical significance between samples is indicated by asterisks (*** and ** indicate *p* values < 0.001 and <0.01 respectively). NS is "not significant."

To measure the level of apoptosis induced by freshly prepared Aβ, SHSY-5Y cells were stained for phosphatidylserine using Annexin-V conjugated FITC[50-51]. Propidium iodide (PI) staining was done concurrently to reveal cell nuclei. Negative control samples displayed only red nuclei, but no cell surface Annexin-V fluorescence. Positive control samples incubated with 1 µM staurosporine, showed complete disruption of membrane integrity (data not shown). All peptides produced green fluorescence, indicating binding of Annexin-V (Figure 8.13). Quantitative analysis of the number of Annexin-V-positive (fluorescent) cells per 100 μm^2 field (Figure 8.13B, bar graph) revealed an average of 4.7 for Aβ42 and 4.2 for *Od*, a difference that was not statistically significant. *Mm* showed significantly lower numbers (3.3; $p<0.01$) than did Aβ42. The difference in fluorescence between *Od* and *Mm* was not significant.

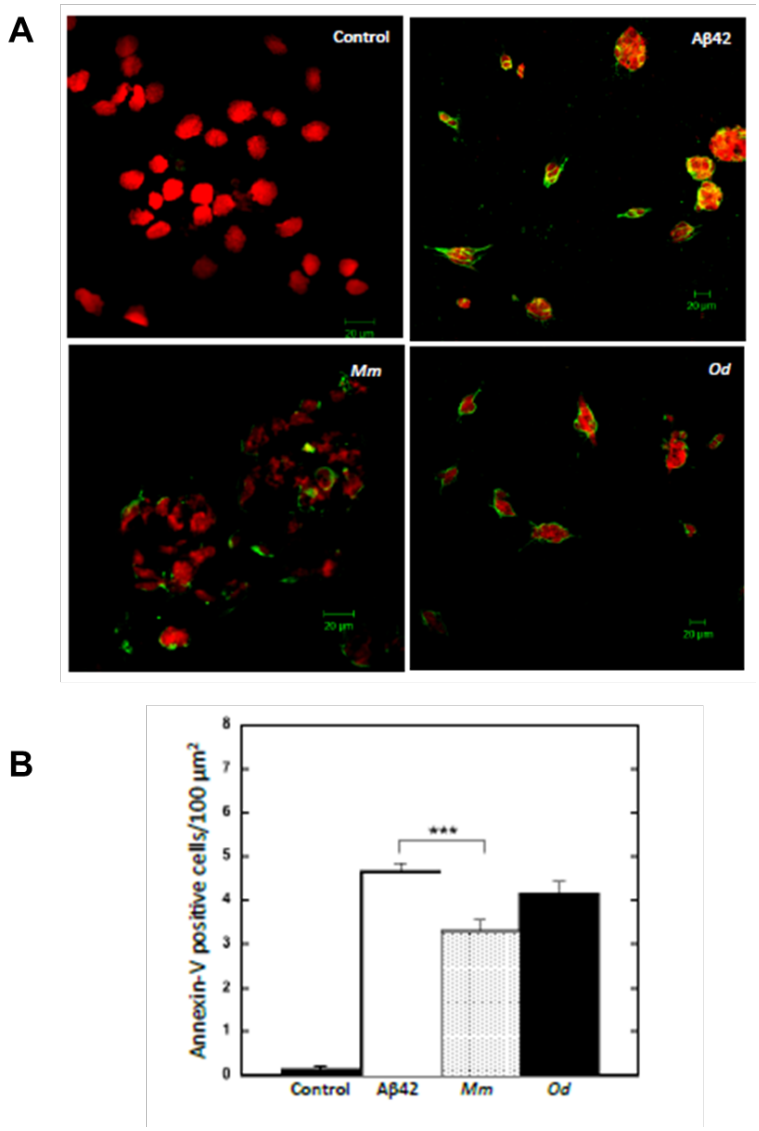

Figure 8.13 Monitoring apoptosis. (A) Annexin-V staining of human SH-SY5Y cells treated with each of the peptides was performed to estimate apoptosis levels. The SH-SY5Y cells were grown on cover slips and treated with freshly prepared Aβ42 peptides for 24h, after which they were stained with Annexin V-FITC. Images were recorded using confocal laser scanning microscopy. (B) Bar graph: Quantitation of Annexin-V staining. The number of apoptotic cells was counted in a 100 µm^2 area using Image-J software. A minimum of 30 microscopic fields was used in each of two independent experiments. Significance between groups is indicated by asterisks (*** and ** indicate *p* values of <0.001 and <0.01, respectively). No significant difference existed between *Mm* and *Od*, although it is possible that *Od* trended towards greater apoptotic activity.

Taken together, the results among these assays were consistent and showed a rank order of toxicity of Aβ42 >> *Mm* ≥ *Od*. An identical rank order was observed in our Annexin-V fluorescence apoptosis assay. This rank order was the opposite of the rank order observed in our biophysical studies. Considered from the broad perspective of assembly rate/size versus toxicity, our data suggest that assembly populations comprising smaller assemblies are relatively more toxic than are those containing larger assemblies. This result agrees with the hypothesis that the most important neurotoxin in AD are the small, presumably oligomeric, assemblies[52-53,54]. However, our data extend this hypothesis by providing evidence, through the use of peptides from different species (and of different primary structure), that assembly state, rather than primary structure *per se*, is likely to contribute most significantly to peptide neurotoxicity.

It is important to note that we do *not* argue that primary structure is irrelevant with respect to determining peptide neurotoxic activity[55], as some have with respect to the existence of "generic" amyloid structures[56-59]. Instead, we suggest that it is the combination of at least three factors that control peptide neurotoxicity: (1) primary structure; (2) assembly structure; and (3) cellular responses. Primary structure determines the intrinsic propensity of a peptide sequence to fold into an energetically determined distribution of tertiary structures, according to Anfinsen[60]. It is the basis of Factor #2, which encompasses the vast and complex folding landscape of Aβ and other amyloid proteins [58] that includes assemblies such as oligomers (irregular, globular, annular, worm-like), protofibrils, and fibrils. Factor #3 encompasses how distinct cell types (e.g., neurons, glia, microglia, or non-neuronal) respond to extracellular or intracellular (including cytoplasmic and intra-organellar or intramembranous (plasma, endosomal, lysosomal, mitochondrial, nuclear)) Aβ

assemblies. This response includes components of the unfolded protein response, chaperones, and lysosomal activities. It also includes anabolic features of Aβ metabolism, which help to determine steady state concentrations of Aβ in different anatomic sites). Factors #1 and #2 are intrinsic to the Aβ peptide *per se*. Factor #3 is specific to each type of organism and falls under the rubric of specific organismal responses to neurotoxins, such as Aβ. Organismal responses determine both the assembly space of Aβ aggregates as well as their biological half-lives. An excellent example of "organismal control" comes from recent studies of superoxide dismutase 1 (SOD1) aggregation in transgenic mouse models of amyotrophic lateral sclerosis. Bergh *et al.*[61] report that SOD1 aggregates formed in the brains and spinal cords of these animals differ in structure from those produced *in vitro*—a clear example of how organismal factors mediate the intrinsic assembly propensities of amyloid proteins and thus may affect their neurotoxic activities.

8.4 Conclusions

Taken together, these data do *not* support long-standing hypotheses that the primary factor controlling development of AD-like neuropathology in rodents is Aβ sequence. If it were, then we would *not* expect, *a priori*, to observe the folding and assembly of rodent peptides into intrinsically toxic oligomeric, protofibrillar, and fibrillar structures. Instead, our data support the hypothesis that the factors of *assembly quaternary structure* and *organismal response* control development of neuropathology. The implication of this hypothesis is that a valid understanding of disease causation within a given system (organism, tissue, etc.) requires the co-evaluation of both biophysical and physiologic properties of that system. One obvious property that might contribute to amyloid formation

is life span. AD amyloidosis in humans is a neuropathologic phenomenon that is age-dependent. Rats of the species *O. degus*, like the naked mole rat, live substantially longer than do animals of the species *M. musculus* (≈6-8 in captivity versus ≈2 years) and thus they may be more likely to develop amyloid and experience its attendant effects. Another interesting possibility, although one beyond the scope of study at this time, is that *O. degus* neurons are more susceptible to Aβ-induced toxicity.

References

1. Selkoe, D. J. Alzheimer's disease: Genes, proteins, and therapy. *Physiol. Rev.* **2001,** *81,* 741-766.

2. Selkoe, D. J. SnapShot: Pathobiology of Alzheimer's disease. *Cell* **2013,** *154,* 468-468.

3. Albert, M. S. Changes in cognition. *Neurobiology of aging* **2011,** *32 Suppl 1,* S58-63.

4. Selkoe, D. J. The genetics and molecular pathology of Alzheimer's disease - Roles of amyloid and the presenilins. *Neurol Clin* **2000,** *18,* 903-922.

5. Selkoe, D. J. Alzheimer's disease: genotypes, phenotypes, and treatments. *Science* **1997,** *275,* 630-631.

6. Johnstone, E. M.; Chaney, M. O.; Norris, F. H.; Pascual, R.; Little, S. P. Conservation of the sequence of the Alzheimer's disease amyloid peptide in dog, polar bear and five other mammals by cross-species polymerase chain reaction analysis. *Brain Res Mol Brain Res* **1991,** *10,* 299-305.

7. Selkoe, D. J. Biochemistry of altered brain proteins in Alzheimer's disease. *Annu Rev Neurosci* **1989,** *12,* 463-490.

8. Selkoe, D. J.; Bell, D. S.; Podlisny, M. B.; Price, D. L.; Cork, L. C. Conservation of brain amyloid proteins in aged mammals and humans with Alzheimer's disease. *Science* **1987,** *235,* 873-877.

9. Inestrosa, N. C.; Reyes, A. E.; Chacon, M. A.; Cerpa, W.; Villalon, A.; Montiel, J.; Merabachvili, G.; Aldunate, R.; Bozinovic, F.; Aboitiz, F. Human-like rodent amyloid-β-peptide determines Alzheimer pathology in aged wild-type Octodon degu. *Neurobiology of aging* **2005,** *26,* 1023-1028.

10. van Groen, T.; Kadish, I.; Popovic, N.; Popovic, M.; Caballero-Bleda, M.; Bano-Otalora, B.; Vivanco, P.; Rol, M. A.; Madrid, J. A. Age-related brain pathology in Octodon degu: Blood vessel, white matter and Alzheimer-like pathology. *Neurobiology of aging* **2011,** *32,* 1651-1661.

11. Ardiles, A. O.; Tapia-Rojas, C. C.; Mandal, M.; Alexandre, F.; Kirkwood, A.; Inestrosa, N. C.; Palacios, A. G. Postsynaptic dysfunction is associated with spatial and object recognition memory loss in a natural model of Alzheimer's disease. *Proc Natl Acad Sci U S A* **2012,** *109,* 13835-13840.

12. Tarragon, E.; Lopez, D.; Estrada, C.; Ana, G. C.; Schenker, E.; Pifferi, F.; Bordet, R.; Richardson, J. C.; Herrero, M. T. Octodon degus: A model for the cognitive impairment associated with Alzheimer's disease. *CNS Neurosci Ther* **2013,** *19,* 643-648.

13. Edrey, Y. H.; Medina, D. X.; Gaczynska, M.; Osmulski, P. A.; Oddo, S.; Caccamo, A.; Buffenstein, R. Amyloid beta and the longest-lived rodent: the naked mole-rat as a model for natural protection from Alzheimer's disease. *Neurobiology of aging* **2013,** *34*, 2352-2360.

14. Edrey, Y. H.; Oddo, S.; Cornelius, C.; Caccamo, A.; Calabrese, V.; Buffenstein, R. Oxidative damage and amyloid-β metabolism in brain regions of the longest-lived rodents. *J Neurosci Res* **2014,** *92*, 195-205.

15. Otvos, L., Jr.; Szendrei, G. I.; Lee, V. M.; Mantsch, H. H. Human and rodent Alzheimer β-amyloid peptides acquire distinct conformations in membrane-mimicking solvents. *Eur J Biochem* **1993,** *211*, 249-257.

16. Hilbich, C.; Kisters-Woike, B.; Reed, J.; Masters, C. L.; Beyreuther, K. Human and rodent sequence analogs of Alzheimer's amyloid βA4 share similar properties and can be solubilized in buffers of pH 7.4. *Eur J Biochem* **1991,** *201*, 61-69.

17. Fung, J.; Frost, D.; Chakrabartty, A.; McLaurin, J. Interaction of human and mouse Aβ peptides. *J Neurochem* **2004,** *91*, 1398-1403.

18. Janssen, J. C.; Beck, J. A.; Campbell, T. A.; Dickinson, A.; Fox, N. C.; Harvey, R. J.; Houlden, H.; Rossor, M. N.; Collinge, J. Early onset familial Alzheimer's disease: Mutation frequency in 31 families. *Neurology* **2003,** *60*, 235-239.

19. Ono, K.; Condron, M. M.; Teplow, D. B. Effects of the English (H6R) and Tottori (D7N) familial Alzheimer disease mutations on amyloid β-protein assembly and toxicity. *J Biol Chem* **2010,** *285*, 23186-23197.

20. De Strooper, B.; Simons, M.; Multhaup, G.; Van Leuven, F.; Beyreuther, K.; Dotti, C. G. Production of intracellular amyloid-containing fragments in hippocampal neurons expressing human amyloid precursor protein and protection against amyloidogenesis by subtle amino acid substitutions in the rodent sequence. *Embo J* **1995,** *14*, 4932-4938.

21. Dyrks, T.; Dyrks, E.; Masters, C. L.; Beyreuther, K. Amyloidogenicity of rodent and human βA4 sequences. *FEBS Lett* **1993,** *324*, 231-236.

22. Fraser, P. E.; Nguyen, J. T.; Inouye, H.; Surewicz, W. K.; Selkoe, D. J.; Podlisny, M. B.; Kirschner, D. A. Fibril formation by primate, rodent, and Dutch-hemorrhagic analogues of Alzheimer amyloid β-protein. *Biochemistry* **1992,** *31*, 10716-10723.

23. Walsh, D. M.; Lomakin, A.; Benedek, G. B.; Condron, M. M.; Teplow, D. B. Amyloid β-protein fibrillogenesis. Detection of a protofibrillar intermediate. *J Biol Chem* **1997,** *272*, 22364-22372.

24. Rahimi, F.; Maiti, P.; Bitan, G. Photo-induced cross-linking of unmodified proteins (PICUP) applied to amyloidogenic peptides. *J Vis Exp* **2009**.

25. Wyttenbach, T.; Kemper, P. R.; Bowers, M. T. Design of a new electrospray ion mobility mass spectrometer. *Int. J. Mass Spectrom.* **2001,** *212*, 13-23.

26. Einstein, A. Über die von der molekularkinetischen Theorie der Wärme geforderte Bewegung von in ruhenden Flüssigkeiten suspendierten Teilchen. *Annalen der Physik und Chemie* **1905,** *17*, 549-560.

27. Roychaudhuri, R.; Yang, M.; Deshpande, A.; Cole, G. M.; Frautschy, S.; Lomakin, A.; Benedek, G. B.; Teplow, D. B. C-terminal turn stability determines assembly differences between Aβ40 and Aβ42. *Journal of Molecular Biology* **2013,** *425*, 292-308.

28. Maiti, P.; Piacentini, R.; Ripoli, C.; Grassi, C.; Bitan, G. Surprising toxicity and assembly behaviour of amyloid β-protein oxidized to sulfone. *Biochem J* **2011,** *433*, 323-332.

29. Fradinger, E. A.; Monien, B. H.; Urbanc, B.; Lomakin, A.; Tan, M.; Li, H.; Spring, S. M.; Condron, M. M.; Cruz, L.; Xie, C. W.; Benedek, G. B.; Bitan, G. C-terminal peptides coassemble into Aβ42 oligomers and protect neurons against Aβ42-induced neurotoxicity. *Proc Natl Acad Sci U S A* **2008,** *105*, 14175-14180.

30. Ono, K.; Condron, M. M.; Teplow, D. B. Structure-neurotoxicity relationships of amyloid β-protein oligomers. *Proc Natl Acad Sci U S A* **2009,** *106*, 14745-14750.

31. Bernstein, S. L.; Wyttenbach, T.; Baumketner, A.; Shea, J.-E.; Bitan, G.; Teplow, D. B.; Bowers, M. T. Amyloid β-Protein: Monomer Structure and Early Aggregation States of Aβ42 and Its Pro19 Alloform. *J. Am. Chem. Soc.* **2005,** *127*, 2075-2084.

32. Baumketner, A.; Bernstein, S. L.; Wyttenbach, T.; Bitan, G.; Teplow, D. B.; Bowers, M. T.; Shea, J.-E. Amyloid β-protein monomer structure: A computational and experimental study. *Protein Science* **2006,** *15*, 420-428.

33. Bernstein, S. L.; Dupuis, N. F.; Lazo, N. D.; Wyttenbach, T.; Condron, M. M.; Bitan, G.; Teplow, D. B.; Shea, J.-E.; Ruotolo, B. T.; Robinson, C. V.; Bowers, M. T. Amyloid-β protein oligomerization and the importance of tetramers and dodecamers in the aetiology of Alzheimer's disease. *Nat. Chem.* **2009,** *1*, 326-331.

34. Lesné, S.; Koh, M. T.; Kotilinek, L.; Kayed, R.; Glabe, C. G.; Yang, A.; Gallagher, M.; Ashe, K. H. A specific amyloid-β protein assembly in the brain impairs memory. *Nature* **2006,** *440*, 352-357.

35. Lomakin, A.; Teplow, D. B. Quasielastic light scattering study of amyloid β-protein fibrillogenesis. In *Meth Mol Biol*, Sigurdsson, E. M.; Calero, M.; Gasset, M. a., Eds. Springer Science + Business Media: New York, 2012; pp 69-83.

36. Naiki, H.; Nakakuki, K. First-order kinetic model of Alzheimer's β-amyloid fibril extension in vitro. *Lab Invest* **1996,** *74*, 374-383.

37. LeVine, H., 3rd. Quantification of β-sheet amyloid fibril structures with thioflavin T. *Meth Enzymol* **1999,** *309,* 274-284.

38. Groenning, M. Binding mode of Thioflavin T and other molecular probes in the context of amyloid fibrils—current status. *J Chem Biol* **2009,** *3,* 1-18.

39. Stryer, L. The interaction of a naphthalene dye with apomyoglobin and apohemoglobin: A fluorescent probe of non-polar binding sites. *Journal of Molecular Biology* **1965,** *13,* 482-495.

40. Rosen, C. G.; Weber, G. Dimer formation from 1-anilino-8-naphthalenesulfonate catalyzed by bovine serum albumin. A new fluorescent molecule with exceptional binding properties. *Biochemistry* **1969,** *8,* 3915–3920.

41. Semisotnov, G. V.; Rodionova, N. A.; Razgulyaev, O. I.; Uversky, V. N.; Gripas, A. F.; Gilmanshin, R. I. Study of the "molten globule" intermediate state in protein folding by a hydrophobic fluorescent probe. *Biopolymers* **1991,** *31,* 119-128.

42. Shi, L.; Palleros, D. R.; Fink, A. L. Protein conformational changes induced by 1,1'-Bis(4-anilino-5-naphthalenesulfonic acid): preferential binding to the molten globule of DnaK. *Biochemistry* **1994,** *33,* 7536-7546.

43. Hawe, A.; Sutter, M.; Jiskoot, W. Extrinsic fluorescent dyes as tools for protein characterization. *Pharm. Res.* **2008,** *25,* 1487–1499.

44. Lansbury, P. T., Jr. Evolution of amyloid: what normal protein folding may tell us about fibrillogenesis and disease. *Proceedings of the National Academy of Sciences of the United States of America* **1999,** *96,* 3342-3344.

45. Fezoui, Y.; Teplow, D. B. Kinetic studies of amyloid β-protein fibril assembly. Differential effects of α-helix stabilization. *J Biol Chem* **2002,** *277,* 36948-36954.

46. Drake, A. F. Circular Dichroism. In *Methods in Molecular Biology: Microscopy, Optical Spectroscopy, and Macroscopic Techniques.*, Christopher Jones, B. M., and Adrian H. Thomas, Ed. Humana Press Inc: New Jersey, 1994; Vol. 22, pp 219-244.

47. Fasman, G. D. *Circular dichroism and the conformational analysis of biomolecules*. Plenum Press: New York, London, 1996.

48. Matsuo, K.; Sakurada, Y.; Yonehara, R.; Kataoka, M.; Gekko, K. Secondary-structure analysis of denatured proteins by vacuum-ultraviolet circular dichroism spectroscopy. *Biophys J* **2007,** *92,* 4088-4096.

49. Broersen, K.; Rousseau, F.; Schymkowitz, J. The culprit behind amyloid beta peptide related neurotoxicity in Alzheimer's disease: oligomer size or conformation? *Alzheimer's research & therapy* **2010,** *2,* 12.

50. Vermes, I.; Haanen, C.; Steffens-Nakken, H.; Reutelingsperger, C. A novel assay for apoptosis. Flow cytometric detection of phosphatidylserine expression on early apoptotic cells using fluorescein labelled Annexin V. *J Immunol Methods* **1995,** *184*, 39-51.

51. Aubry, J. P.; Blaecke, A.; Lecoanet-Henchoz, S.; Jeannin, P.; Herbault, N.; Caron, G.; Moine, V.; Bonnefoy, J. Y. Annexin V used for measuring apoptosis in the early events of cellular cytotoxicity. *Cytometry* **1999,** *37*, 197-204.

52. Dahlgren, K. N.; Manelli, A. M.; Stine, W. B., Jr.; Baker, L. K.; Krafft, G. A.; LaDu, M. J. Oligomeric and fibrillar species of amyloid-β peptides differentially affect neuronal viability. *J Biol Chem* **2002,** *277*, 32046-32053.

53. Klein, W. L.; Stine Jr., W. B.; Teplow, D. B. Small assemblies of unmodified amyloid β-protein are the proximate neurotoxin in Alzheimer's disease. *Neurobiology of aging* **2004,** *25*, 569-580.

54. Larson, M. E.; Lesne, S. E. Soluble Aβ oligomer production and toxicity. *J Neurochem* **2012,** *120 Suppl 1*, 125-139.

55. Teplow, D. B. On the subject of rigor in the study of amyloid β-protein assembly. *Alzheimer's Res Ther* **2013,** *5*, 39.

56. Knowles, T. P.; Vendruscolo, M.; Dobson, C. M. The amyloid state and its association with protein misfolding diseases. *Nature reviews. Molecular cell biology* **2014,** *15*, 384-396.

57. Baglioni, S.; Casamenti, F.; Bucciantini, M.; Luheshi, L. M.; Taddei, N.; Chiti, F.; Dobson, C. M.; Stefani, M. Prefibrillar amyloid aggregates could be generic toxins in higher organisms. *The Journal of neuroscience : the official journal of the Society for Neuroscience* **2006,** *26*, 8160-8167.

58. Eichner, T.; Radford, S. E. A diversity of assembly mechanisms of a generic amyloid fold. *Molecular cell* **2011,** *43*, 8-18.

59. Auer, S.; Meersman, F.; Dobson, C. M.; Vendruscolo, M. A generic mechanism of emergence of amyloid protofilaments from disordered oligomeric aggregates. *PLoS computational biology* **2008,** *4*, e1000222.

60. Anfinsen, C. B. Principles that govern the folding of protein chains. *Science* **1973,** *181*, 223-230.

61. Bergh, J.; Zetterström, P.; Andersen, P. M.; Brännström, T.; Graffmo, K. S.; Jonsson, P. A.; Lang, L.; Danielsson, J.; Oliveberg, M.; Marklund, S. L. Structural and kinetic analysis of protein-aggregate strains in vivo using binary epitope mapping. *Proceedings of the National Academy of Sciences* **2015,** *112*, 4489-4494.